

Electron Impact Ionisation of Ground-State and Laser-Excited Atoms

A thesis submitted to the University of Manchester for the degree of
Doctor of Philosophy in the Faculty of Science and Engineering

2022

Manish Patel

Photon Science Institute
Department of Physics and Astronomy

Contents

Contents	2
List of Figures	6
List of Tables	9
List of Acronyms	10
List of Publications	13
Abstract	14
Declaration	16
Copyright Statement	17
Acknowledgements	18
1 Introduction	20
1.1 Electron-Atom Interactions	21
1.1.1 Elastic Scattering	21
1.1.2 Inelastic Scattering	22
1.1.3 Superelastic Scattering	23
1.1.4 Ionisation	24
1.2 Scattering Theory	25
1.2.1 Rutherford Scattering	25
1.2.2 Modern Scattering Theory	26
1.3 (e, 2e) Experiments	31
1.4 Laser-aligned (e,2e)	33
1.5 Layout of this Thesis	34
2 Laser Interaction with Atoms	36
2.1 The Density Matrix	37
2.2 Equations of Motion for Atoms in a Laser Field	40
2.3 LASED: A Laser-Atom Interaction Simulator	46
2.3.1 Introduction	46
2.3.2 Computation of the Time Evolution	47
2.3.3 Gaussian Laser Beam Profile	51
2.3.4 Atomic Doppler Profile	53

2.3.5	Rotation of the Frame of Reference	53
2.3.6	Polarisation	55
2.3.7	Angular Shape	56
2.3.8	Examples	56
2.3.9	Summary	63
3	The (e, 2e) Spectrometer	65
3.1	Overview	66
3.2	The Scattering Chamber	68
3.2.1	The ‘Old’ (e, 2e) Spectrometer	68
3.2.2	The ‘New’ (e,2e) Spectrometer	70
3.2.3	The Pressure Gauges	72
3.3	The Electron Gun	72
3.3.1	The Electron Cathode Source	74
3.3.2	The Electron Optics	74
3.4	The Faraday Cup	75
3.5	Electron Energy Analysers	76
3.5.1	Analyser Elements	76
3.5.2	Hemispheres	78
3.5.3	The Channel Electron Multipliers	79
3.6	Analyser and Gun Power Supplies	79
3.6.1	The Old (e,2e) Power Supplies	80
3.6.2	The New (e,2e) Power Supplies	83
3.7	The Stepper Motor System	87
3.7.1	The Old (e,2e) Stepper Motor System	87
3.7.2	The New (e,2e) Stepper Motor System	88
3.8	Atomic Beams	90
3.8.1	The Atomic Beam Oven	90
3.8.2	The New (e,2e) Cold Trap	92
3.8.3	Gas Jets	94
3.9	The Coincidence Timing Electronics	96
3.10	Summary	99
4	Laser & Optics	100
4.1	The Laser System	101
4.1.1	Laser Optics	101
4.1.2	Laser Interlocks	102
4.2	New (e, 2e) Optics	105
4.3	Summary	107
5	Experimental Control Firmware & Software	108
5.1	Overview of the Main Program	109
5.2	Arduino-LabVIEW Serial Protocol	112
5.3	Faraday Cup Current & Pressure Measurements	115
5.4	Analyser Movement	117
5.4.1	The New (e, 2e) Analyser Angle Controller	118
5.5	Gun & Analyser Power Supply Control System	123
5.6	Half-Wave Plate Control	126
5.7	Laser Locking	128

5.8	Multi-Channel Analyser	132
5.9	Experiment Types & Data Handling	133
5.9.1	Gun Energy Scan	133
5.9.2	Tracking Scan	135
5.9.3	Angular Scan	135
5.9.4	Half-Wave Plate Scan	138
5.9.5	Data Handling	138
5.10	Summary	139
6	The Evolution of the TDCS of Xenon	140
6.1	Introduction	141
6.2	Binding Energy Spectrum of Xenon	143
6.3	The Measured TDCS from Xenon	145
6.3.1	60 eV above the IP	145
6.3.2	80 eV above the IP	146
6.3.3	100 eV above the IP	147
6.4	Xenon-Helium Coincidence Ratio	148
6.5	Summary	152
7	The Evolution of the TDCS of Argon	154
7.1	Introduction	155
7.2	The Measured DCS of Argon	155
7.2.1	5 eV to 200 eV above the IP	156
7.2.2	Detailed Measurements around 50 eV above the IP	157
7.3	Summary	159
8	Laser-Excited Strontium	161
8.1	Introduction	162
8.2	Fluorescence Spectrum of Strontium	163
8.3	Calibration using the He 2^2S Resonance	164
8.4	Proposed Experiments to Measure the QDCS of Strontium	165
8.5	Summary	166
9	Conclusions and Suggestions for Future Work	168
9.1	Conclusions	168
9.2	Suggestions for Future Work	170
9.2.1	Improvements to LASED	170
9.2.2	Improvements to the (e, 2e) Spectrometers and Control System	170
9.2.3	Future (e,2e) Experiments	174
	Bibliography	175
A	Laser-Atom Interaction Calculations	188
A.1	Calculation of the Generalised Decay Constants	188
A.2	Calculation of the Half-Rabi Frequency	189
A.2.1	The Half-Rabi Frequency in a Circular Basis	191
B	LASED Installation & Benchmarking	193
B.1	Installation of LASED	193

B.2	Computation Time	193
C	Knudsen Number Calculations	195
C.1	Calcium	196
C.2	Magnesium	197
C.3	Strontium	198
D	Control Software	199
D.1	ASCII characters	199
D.2	Tables of API commands	200

Final word count: 47282

List of Figures

1.1	Types of electron-atom interactions	21
1.2	The atomic collision parameters in an electron-photon coincidence experiment	22
1.3	Electron impact ionisation mechanisms	24
1.4	Rutherford scattering	26
1.5	Wave nature of scattering	27
1.6	Geometry of an (e, 2e) experiment at Manchester	32
1.7	Laser-aligned (e, 2e) geometry	34
2.1	The natural and collision frames of reference	38
2.2	A general laser-atom system	47
2.3	Flowchart of the calculation of the time evolution of a laser-atom system in LASED	48
2.4	The representation of a P-state as a flattened density matrix	49
2.5	A Gaussian laser beam profile	51
2.6	A coordinate system for elliptically polarised light	55
2.7	Simulation of the calcium 4^1S_0 to 4^1P_1 laser excitation	57
2.8	Rotation of the laser-excited calcium simulations	58
2.9	Simulation of the helium 3^1D_2 to 10^1P_1 laser-excitation for various decay parameters	59
2.10	Simulation of the helium 3^1D_2 to 10^1P_1 laser-excitation for various laser polarisation angles	60
2.11	Simulation of the helium 3^1D_2 to 10^1P_1 laser-excitation after electron-impact excitation from the S_0^1 state	60
2.12	Level diagram for the Cs D_2 transition.	61
2.13	Simulation of the excitation of Cs via the D_2 transition	62
3.1	Block diagram colour key	65
3.2	Overview of hardware for the (e, 2e) spectrometer	66
3.3	Photographs and geometry of the Old (e,2e) spectrometer	69
3.4	Photographs and geometry of the New (e, 2e) spectrometer	71
3.5	Pressure gauge pinout	72
3.6	Photographs and diagram of the electron gun	73
3.7	Block diagrams of hardware for the Faraday cup current measurement.	75
3.8	Photograph and diagram of the electron energy analysers.	77
3.9	Circuit diagram of the channel electron multiplier low pass filter.	79
3.10	Photograph of the Old (e, 2e) gun and analyser power supplies	80

3.11	Block diagram of the Old (e, 2e) electron gun and electron energy analyser power supplies	82
3.12	Photograph of the New (e,2e) electron gun power supplies and relay box	84
3.13	Photograph of the front panel of the New (e,2e) spectrometer electron energy analyser power supplies	84
3.14	Block diagram of the New (e, 2e) electron energy analyser power supplies	85
3.15	Diagram of the Old (e, 2e) stepper motors and rotary feedthroughs	87
3.16	Diagram of the side and top-down view of the New (e, 2e) spectrometer showing the analyser movement system.	89
3.17	Scaled drawing of the New (e, 2e) atomic beam oven	90
3.18	Atomic beam oven beam divergence testing	91
3.19	Graphs of the temperature of the atomic beam oven measured over time and the final equilibrium temperature as Thermocoax current is varied.	93
3.20	Diagram of the New (e, 2e) spectrometer cold trap	95
3.21	Photograph and diagram of the coincidence timing electronics.	97
3.22	Time-to-amplitude converter pulse duration and modification	98
4.1	Diagram of the optics contained inside the Matisse laser system	101
4.2	Arrangement of the laser system on an optical bench and safety interlock system diagrams	103
4.3	Laser interlock system circuit schematic	104
4.4	Optics in the New (e, 2e) spectrometer and block diagram of the half-wave plate rotator	106
5.1	A screenshot of the main control program	109
5.2	A block diagram showing an overview of the main control program	110
5.3	A block diagram of the Arduino-LabVIEW serial communication protocol	113
5.4	A block diagram of the Spellman MPS and Readable Characters checksums	114
5.5	A block diagram of the Faraday cup current and pressure measurement in the LabVIEW control program	115
5.6	A block diagram of the Arduino-based Faraday cup current monitor's firmware	116
5.7	A block diagram of the main program's analyser movement software	117
5.8	Main program analyser angle control tab screenshot	118
5.9	Pinout for the New (e, 2e) Arduino-based stepper controller	118
5.10	Flowchart of the Arduino-based New (e, 2e) analyser angle controller firmware	120
5.11	Crenelation detection logic	121
5.12	Analyser stepper controller calibration graphs	122
5.13	A block diagram of the control of the gun and analysers power supplies	123
5.14	Main program electron gun tab screenshot	124
5.15	Screenshot of the main program analyser power supply controls	125
5.16	Flowchart of the Arduino-based electron energy analyser and gun power supplies firmware	126
5.17	Half-wave plate rotator control block diagram	127
5.18	Histogram of the time between crenelation interrupts for the rotation of the New (e, 2e) half-wave plate	128
5.19	Screenshot of the half-wave plate controls in the main control program	129
5.20	Laser locking program screenshot	130

5.21	Flowchart of the laser locking program	131
5.22	Flowchart of the multi-channel analyser software	132
5.23	Screenshot of the NM optimisation tab in the main control program . . .	134
5.24	Main control program gun energy scan screenshot	134
5.25	Main control program tracking scan screenshot	136
5.26	Main program angular scan screenshot	137
5.27	Flowchart of the experimental data processing	138
6.1	TDCS measurements for the first five noble gases in the perpendicular plane	141
6.2	Xenon binding energy spectrum	144
6.3	TDCS of xenon from coplanar to the perpendicular plane at 60 eV	145
6.4	TDCS of xenon from coplanar to the perpendicular plane at 80 eV	146
6.5	TDCS of xenon from coplanar to the perpendicular plane at 100 eV	148
6.6	Diagram of the mixing chamber	149
6.7	Xe:He coincidence ratio at 100 eV above the ionisation potential	151
7.1	Evolution of the TDCS of argon in the perpendicular plane from 5 eV to 200 eV above the ionisation potential	156
7.2	Detailed survey of the TDCS of argon in the perpendicular plane from 40 eV to 55 eV above the ionisation potential	158
8.1	Strontium sample fluorescence spectrum	163
8.2	Measurement of the elastic scattering He 2^2S resonance	164
8.3	Flowchart of proposed experiments leading to measurement of the QDCS from strontium	165
9.1	New design for a Faraday cup current detector	172
9.2	Design of an atomic beam oven temperature controller	173
C.1	Knudsen number variation with temperature for Ca	197
C.2	Knudsen number variation with the New (e, 2e) atomic beam oven tem- perature for Mg.	198
C.3	Knudsen number variation with the New (e, 2e) atomic beam oven tem- perature for Sr.	198
D.1	The first 128 ASCII characters and their corresponding decimal, hexidec- imal, and binary values.	199

List of Tables

B.1	Execution times in LASED	193
C.1	Calcium Knudsen number data	197
C.2	Magnesium Knudsen number data	197
C.3	Strontium Knudsen number data	198
D.1	The Arduino-controlled analyser stepper API	200
D.2	The Arduino-controlled electron energy analyser power supplies API . . .	201
D.3	The Old (e, 2e) Arduino-controlled electron gun power supply unit API .	201

List of Acronyms

ACPs atomic collision parameters

RHC right-hand circular

LHC left-hand circular

PCI post collisional interaction

DCS differential cross section

IP ionisation potential

TDSE time dependent Schrödinger equation

TISE time independent Schrödinger equation

DWBA distorted wave Born approximation

PWA plane wave approximation

CCC convergent close-coupling

DDCS double differential cross section

TDCS triple differential cross section

QDCS quadruple differential cross section

QED quantum electrodynamics

LASED laser-atom simulator derived from quantum electrodynamics

QA quantisation z-axis

RWA rotating wave approximation

CEM channel electron multiplier

CFDs constant fraction discriminators

NIM nuclear instrumentation module

TTL transistor-transistor logic

DAQ NI PCI-6221 data acquisition

TAC time-to-amplitude converter

ADC analogue-to-digital converter

MCA multi-channel analyser

FC Faraday cup

USB Universal Serial Bus

RE residual energy

LE lens

AM analyser mean

IH inner hemisphere

OH outer hemisphere

DAC digital-to-analogue converter

EEPROM electrically erasable programmable read-only memory

SPI serial peripheral interface

MOSFET metal-oxide-semiconductor field-effect transistor

PCB printed circuit board

VC valid conversion

SHG single harmonic generation

HWP half-wave plate

Ti:Sa Titanium:Sapphire

BiFi birefringent filter

TGG Terbium-Gallium-Garnet

GUI graphical user interface

JSON JavaScript Object Notation

CSV comma-separated value

ASCII American Standard Code for Information Interchange

API application programming interface

NM Nelder-Mead

PWM pulse-width modulated

List of Publications

1. Harvey, M., A. Sakaamini, M. Patel, S. Amami, D. Madison, and A. J. Murray (2019), ‘Triple differential cross-section measurements for electron-impact ionization of methane from a coplanar geometry to the perpendicular plane’, *The Journal of Chemical Physics*, 151:19, 194305, <https://doi.org/10.1063/1.5127121>
2. Patel, M., A. Sakaamini, M. Harvey, and A. J. Murray (2020), ‘An experimental control system for electron spectrometers using Arduino and LabVIEW interfaces’, *Review of Scientific Instruments*, 91:10, 103104, <https://doi.org/10.1063/5.0021229>
3. Patel, M., M. Harvey, A. Sakaamini, and A. J. Murray (2022), ‘Evolution of the xenon ($e, 2e$) differential cross section from a coplanar geometry to the perpendicular plane in the intermediate-energy regime’, *Physical Review A*, 105:3, 032818, <https://doi.org/10.1103/PhysRevA.105.032818>
4. Patel, M., and A. J. Murray (2022), ‘Measurement of argon ($e, 2e$) differential cross sections in the perpendicular plane from 5 to 200 eV above the ionization threshold’, *Physical Review A*, 105:4, 042815, <https://doi.org/10.1103/PhysRevA.105.042815>
5. Patel, M., M. Harvey, and A. J. Murray (2022), ‘Laser-atom interaction simulator derived from quantum electrodynamics’, *Physical Review A*, 105:5, 053117, <https://doi.org/10.1103/PhysRevA.105.053117>

Abstract

(e, 2e) experiments test our understanding of collision dynamics in the electron impact ionisation process. These experiments use coincidence techniques to ascertain a triple differential cross section (TDCS) for the ionisation process, by measuring the angular correlation between the electron scattered from the target and the bound electron that is produced during ionisation. Almost all measurements conducted so far have been from atoms and molecules in their ground state. The original aim of this work was to measure (e, 2e) processes from laser-excited and aligned atoms, since this provides additional information on the collision from these targets. By aligning the atoms initially using a laser, the spherical symmetry of the atom is reduced, so that a quadruple differential cross section must be measured which depends on the scattering geometry as well as the alignment angle of the atom. Results from this type of experiment are expected to aid in our understanding of collisions involving molecules, since these targets also have reduced symmetry compared to atoms.

An open-source laser-atom interaction simulator derived from quantum electrodynamics (LASED) has been built to allow the simulation of the dynamics of any atom excited by continuous wave, narrow bandwidth laser radiation. Simulation results for the 4^1S_0 to 4^1P_1 laser-excitation of Ca, 3^1D_2 to 10^1P_1 laser-excitation of He after electron-impact excitation from the 1S_0 ground state, and the laser-excitation of the Cs D_2 line are hence presented in this thesis as examples of the application of LASED.

Two different (e, 2e) spectrometers were used to make measurements presented in this thesis from ground state noble gas targets. A modular, customisable, and low-cost experimental control system for these spectrometers using LabVIEW and Arduino interfaces has been built and is described in this thesis. This control system, combined with a new LabVIEW laser locking program will allow laser-aligned (e, 2e) experiments to be performed without an operator present in the future. A laser interlock system required to satisfy new health and safety regulations is also detailed.

Measurements of the TDCS of Xe as the scattering geometry was varied from a coplanar geometry to the perpendicular plane are detailed in this thesis. These measurements were taken from 60 eV to 100 eV above the ionisation potential (IP). Data for the TDCS of Ar in the perpendicular plane from 5 eV to 200 eV above the IP are also presented in this thesis. These data confirm the results of previous measurements at Manchester and reveal a trend in the flattening of the TDCS as the incident energy increases. A new technique for mapping the measurements of the relative TDCS of Xe to an absolute scale using a He-Xe mixture is presented. The new Ar data also reveals a deep minimum in the TDCS at 50 eV above the IP, which may be due to a nearby quantum vortex. Preliminary

experiments to measure laser-aligned $(e, 2e)$ from strontium are also outlined, so that future research using this target has guidance as to where to search for signal.

Declaration

I hereby declare that no portion of the work referred to in the thesis has been submitted in support of an application for another degree or qualification of this or any other university or other institute of learning.

Copyright Statement

1. The author of this thesis (including any appendices and/or schedules to this thesis) owns certain copyright or related rights in it (the “Copyright”) and s/he has given the University of Manchester certain rights to use such Copyright, including for administrative purposes.
2. Copies of this thesis, either in full or in extracts and whether in hard or electronic copy, may be made only in accordance with the Copyright, Designs and Patents Act 1988 (as amended) and regulations issued under it or, where appropriate, in accordance with licensing agreements which the University has from time to time. This page must form part of any such copies made.
3. The ownership of certain Copyright, patents, designs, trademarks and other intellectual property (the “Intellectual Property”) and any reproductions of copyright works in the thesis, for example graphs and tables (“Reproductions”), which may be described in this thesis, may not be owned by the author and may be owned by third parties. Such Intellectual Property and Reproductions cannot and must not be made available for use without the prior written permission of the owner(s) of the relevant Intellectual Property and/or Reproductions.
4. Further information on the conditions under which disclosure, publication and commercialisation of this thesis, the Copyright and any Intellectual Property and/or Reproductions described in it may take place is available in the University IP Policy (see <http://documents.manchester.ac.uk/DocuInfo.aspx?DocID=24420>), in any relevant Thesis restriction declarations deposited in the University Library, the University Library’s regulations (see <http://www.library.manchester.ac.uk/about/regulations/>) and in the University’s policy on Presentation of Theses.

Acknowledgements

Undertaking a PhD is a daunting and lonely task but the people around me have made it a fulfilling and enjoyable process. I would like to thank them here. First and foremost, thank you to my supervisor Professor Andrew Murray whose guidance, passion, and unfailing patience has made all of this possible. His technical knowledge and wizard-like ability in problem solving is inspirational. My only regret was my poor timekeeping abilities!

Thank you to fellow tinkerers Dr Ahmad Sakaamini, Dr Parinya Udommai, and Dr Josh Rogers for their companionship in the lab. Thank you to Dr Pawita Boonrat for all her support, especially at the beginning. A special thank you to Dr Matthew Harvey whose mentorship has been invaluable throughout this project. Working and learning with everyone in the Atomic and Molecular Physics Group at Manchester has been a joy.

Thank you to my co-supervisor Professor George King and advisor Dr Paul Campbell for their advice, interest in my project, and their concern for my well-being.

A huge thank you to all of the people over the course of these years for being able to remind me that life is not all about work. Thank you to Ana Tigan for bringing her extroverted energy into an introverted household (and for teaching me how to use a drill). Thank you to Jake Jones who I could always trust to brighten my day. Thank you to Raoul Hidalgo Charman for always keeping things new and weird. A huge thank you to Danielius Banys, Debra Bligh-Wall, Emily Cuffin-Munday, Dr Eunseong Lee, Guuske Tiktak, Dr Harry Waring, Luna Noguera, Dr Nialh McCallum, Sam Bateman, Tom Sweetnam, and Valerio Gilles for making this PhD a lot less lonely. Lunch time is a sacred hour.

Thank you to Dr Tommy Smith and Sankarshana Srinivasan for their help with some of the theoretical aspects of my work and for being excellent housemates and friends. Thank you to Adrian Parisi for his help with programming and whose enlightening conversations and friendship have impacted this project in more ways than he knows.

Thank you to my parents and family for their support and affection throughout this project, notably my brother Vikesh who sparked my interest in physics.

Lastly, thank you to my favourite person, Priya, whose constant cheerleading has kept me going, especially in these last few months. I am incredibly lucky.

*"Remember kids, the only difference between
science and screwing around is writing it down."*
- Adam Savage (MythBusters)

Chapter 1

Introduction

The ionisation of atoms via electron impact is a fundamental physical process in which an electron interacts with an atom and produces an ionised and scattered electron. This electron impact ionisation process is a many-body problem which cannot be analytically solved and approximations must be made to obtain a solution. Various theoretical approaches have hence been taken to find a computable solution. To test these different scattering theories, experimental data which fully characterises the electron-impact ionisation process is essential. Coincidence electron impact ionisation (e, 2e) experiments are used to provide information about this process as these techniques deliver the most precise data for the study of ionisation by electron impact [1]. The University of Manchester's Atomic Physics Group has been producing new (e, 2e) data for several decades with increasing sophistication of experiments and more complex targets. The computational tools, newly-built instrumentation, and new experimental data detailed in this thesis aim to further the longstanding output and sophistication of (e, 2e) data.

In this chapter, electron-atom scattering processes which are integral to this work are discussed. Thereafter, scattering theory is explored, and two modern theoretical approaches to the scattering problems that arise are examined. (e, 2e) experiments and the current accuracy of scattering theories to predict the data from these experiments is also reviewed. The (e, 2e) spectrometers and experiments conducted at Manchester are then outlined and a case is laid out for the research work in this thesis.

1.1 Electron-Atom Interactions

Electron impact ionisation is one of many fundamental processes which occur when electrons interact with atoms. To perform experiments which investigate this type of ionisation, it is also necessary to consider other types of electron-atom interactions, including elastic, inelastic, and superelastic scattering processes.

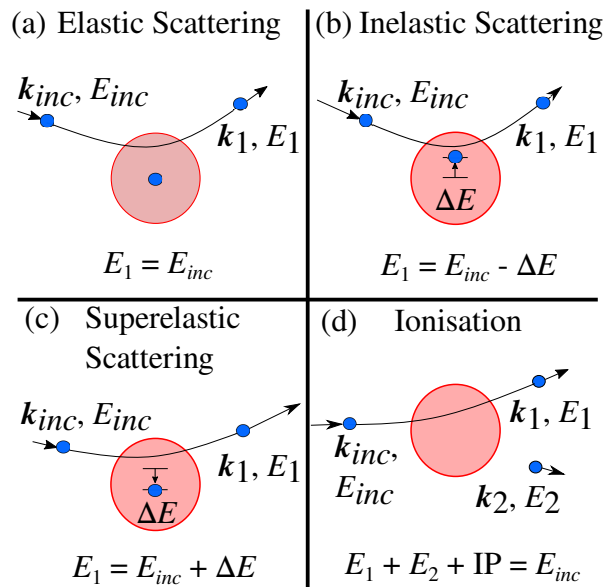


Figure 1.1: A diagram showing an electron with momentum \mathbf{k}_{inc} and energy E_{inc} scattering from a target via various processes: (a) elastic scattering, (b) inelastic scattering, (c) superelastic scattering, and (d) ionisation.

1.1.1 Elastic Scattering

Elastic scattering of an electron from an atom is shown in figure 1.1(a). It is the most common electron-atom scattering process for almost all atomic targets [2]. In this process, an electron impacts the atom with momenta \mathbf{k}_{inc} and energy E_{inc} and scatters with outgoing momentum and energy \mathbf{k}_1 and E_1 respectively. In this *elastic* interaction, energy is conserved so that $E_1 = E_{inc}$. However, the momentum of the outgoing electron may not equal the incident electron's momentum, hence the momentum of the atom will also change. Since the atom is much heavier than the electron, this change in momentum of the target is usually neglected in these collisions.

An example of a well-studied process involving elastic scattering is the 2^2S resonance of He [3–5]. In this interaction, an electron elastically scattering from a He atom and producing a negative ion is in resonance with the process of the incoming electron being captured by the atom. The interaction between these two processes produces a dip in the scattering cross section at 19.34 eV. This resonance can be used to calibrate the energy scale of experiments, as found in chapter 8.

1.1.2 Inelastic Scattering

An *inelastic* scattering process is shown in figure 1.1(b). In this case the energy of the incident electron is not conserved and the outgoing electron's energy decreases to $E_1 = E_{inc} - \Delta E$, where the atom is left in an excited state with an increased energy ΔE . Inelastic scattering is used in experiments to reach excited states via electron impact. As an example, electron impact excitation can be used to reach the D-state of He from the ground state, as discussed in chapter 2.

The first experiment to use inelastic scattering was Frank and Hertz in 1914 [6], where the change in energy of the scattered electrons after interacting with the target was measured i.e. an energy loss spectrum. This experiment provided one of the first pieces of evidence of the quantum nature of atoms. In modern experiments, an energy loss spectrum provides precise information about the electronic and vibrational states of targets [7]. This lends itself to being a tool used in studying surfaces [8] and material properties [9].

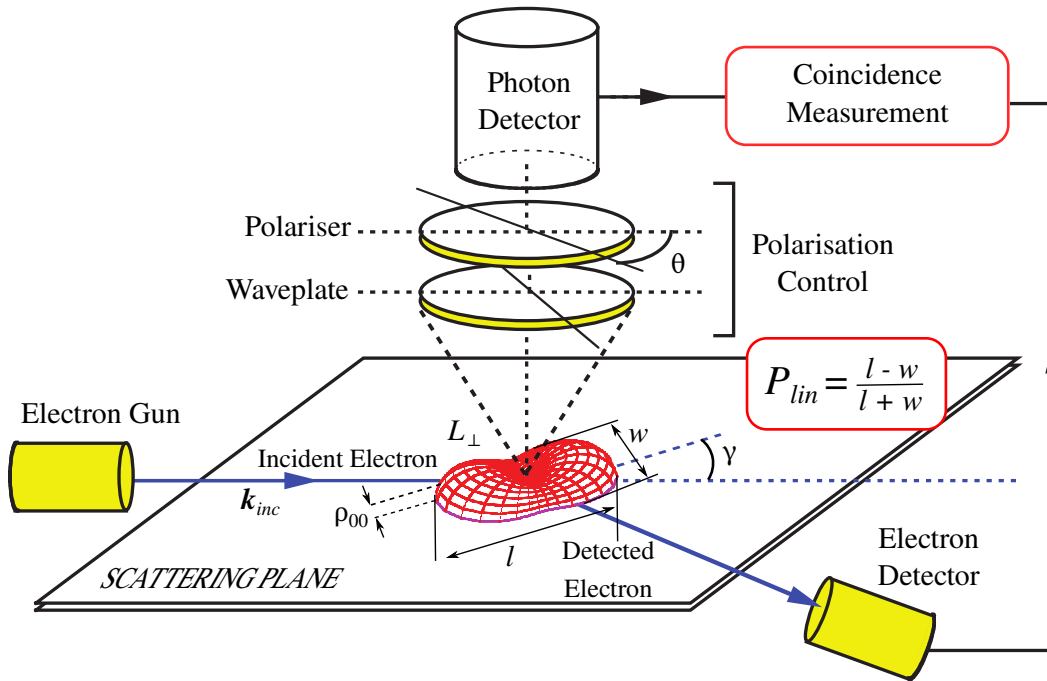


Figure 1.2: Diagram of an electron-photon coincidence experiment. An electron with momentum \mathbf{k}_{inc} excites the target to a P-state with alignment angle γ , angular momentum transferred to the atom L_{\perp} , charge cloud height ρ_{00} and charge cloud length and width l and w respectively. The detected electron and photon are measured in coincidence. Detection of photons is fixed to a polarisation angle of θ by a waveplate in combination with a polariser. This figure has been adapted from one produced by Professor Andrew Murray at the University of Manchester.

The decay of the excited target produces a photon which can be measured in coincidence with the scattered electron to provide a complete description of the scattering process. This is known as an electron-photon coincidence experiment [2, 10]. In these experiments, the atomic collision parameters (ACPs) L_{\perp} , P_{lin} , γ , and ρ_{00} fully characterise the excited target state [2], as shown in figure 1.2. L_{\perp} is defined as the expectation value of the angular momentum perpendicular to the scattering plane transferred to the atom in the collision. The linear polarisation of the charge cloud is described by

$$P_{lin} = \frac{l - w}{l + w}, \quad (1.1)$$

where l and w are the ‘length’ and ‘width’ of the charge cloud respectively. γ is the angle which the major symmetry axis of the charge cloud in the scattering plane makes with the incident electron momentum \mathbf{k}_{inc} . ρ_{00} is the ‘height’ of the charge cloud which describes the negative reflection symmetry component of the charge cloud. To measure the ACPs from an electron-photon coincidence experiment, the Stoke’s parameters are measured [11]

$$P_1 = \frac{I(0^\circ) - I(90^\circ)}{I(0^\circ) + I(90^\circ)} \quad (1.2)$$

$$P_2 = \frac{I(45^\circ) - I(135^\circ)}{I(45^\circ) + I(135^\circ)} \quad (1.3)$$

$$P_3 = \frac{I(RHC) - I(LHC)}{I(RHC) + I(LHC)}, \quad (1.4)$$

where $I(\theta)$ is the integrated number of electron-photon coincidence events detected with the polarisation of the detected photon at angle θ with respect to \mathbf{k}_{inc} . $I(RHC)$ and $I(LHC)$ are the number of coincidence events detected with right-hand circular (RHC) and left-hand circular (LHC) photon polarisation. These Stoke’s parameters can be related to the ACPs by [11]

$$P_{lin} = \sqrt{P_1^2 + P_2^2} \quad (1.5)$$

$$\gamma = \frac{1}{2} \tan^{-1} \left(\frac{P_2}{P_1} \right) \quad (1.6)$$

$$L_\perp = -P_3. \quad (1.7)$$

To measure ρ_{00} , the Stoke’s parameters must be re-measured with the experimental geometry described in figure 1.2 changed so that the laser is injected along the scattering plane [12].

1.1.3 Superelastic Scattering

Figure 1.1(c) shows a *superelastic* scattering process. In this process, the outgoing electron energy is increased as it de-excites the atom by energy ΔE . When a laser is used to prepare the target atom in an excited state followed by superelastic scattering from this excited target, this process can be considered as the ‘time-reversal’ of the electron-photon coincidence experiment. Superelastic scattering can be used as a more efficient electron-photon coincidence experiment. In these coincidence experiments, the atom which scatters the detected electron may not radiate a photon to the detector, in which case no event registers. In the superelastic scattering experiment, only the scattered electron needs to be detected and therefore the superelastic scattering technique is more efficient than electron-photon coincidence. In these superelastic scattering experiments, the ACPs are measured in a similar way to the electron photon coincidence experiment, except the measured $I(\theta)$ in equations 1.2 to 1.4 denotes the number of detected electrons with a laser polarisation angle of θ with respect to \mathbf{k}_{inc} . Superelastic scattering can also be used as an experimental calibration technique as noted in chapter 8.

1.1.4 Ionisation

The process of electron impact *ionisation* is shown in figure 1.1(d). In this process, the incident electron scatters from the atom and a second electron is ejected from the target. Energy is conserved so that the scattered and ejected electron both have energies E_1 and E_2 with an incident electron energy

$$E_{inc} = E_1 + E_2 + IP, \quad (1.8)$$

where the ionisation potential (IP) is the energy required to eject a bound electron.

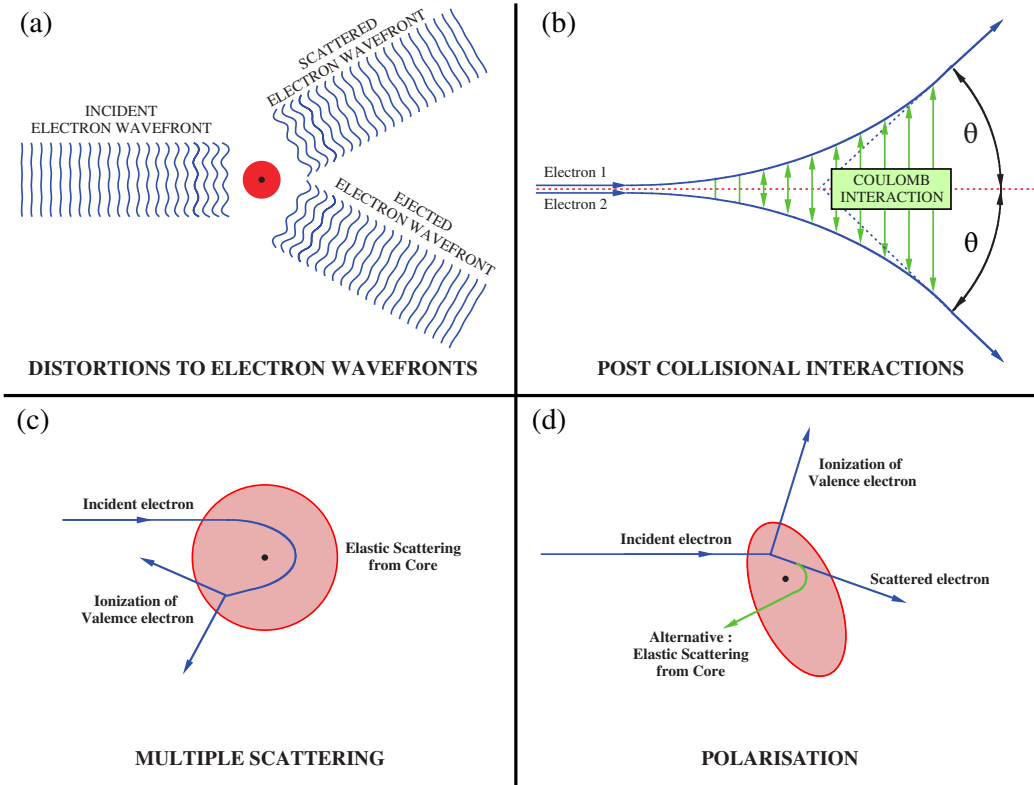


Figure 1.3: A diagram of electron-impact ionisation showing various scattering mechanisms that can play a role in the interaction: a) distortions to the electron wavefronts due to the Coulomb interaction between the electrons as well as from the ionic core, b) post-collisional interactions, c) multiple scattering, and d) polarisation. This figure has been adapted from one produced by Professor Andrew Murray at the University of Manchester.

The focus of this thesis is the process of electron impact ionisation of atomic targets. This is important in many physical systems, such as in the behaviour of stellar and planetary atmospheres [13, 14] and industrial plasmas [15–17]. Electron impact ionisation is a complex interaction between many bodies: the bound electrons of the target atom, the incident electron, the scattered electron, and the ionised electron. Therefore, there is no analytical solution to this system [18] without making approximations. Several theoretical approaches to address this problem have evolved over the years. These include R-matrix theory [19], the Generalised Sturmian Function approach [20], the convergent close-coupling (CCC) method [21], the distorted wave Born approximation (DWBA) method [22], and many more. These scattering models consider different physical mechanisms such as: the distortion to electron wavefronts as seen in figure 1.3(a), the post collisional interaction (PCI) between outgoing electrons as shown in panel (b), multiple

scattering events as seen in panel (c), and the polarisation of the target atom as seen in panel (d). These processes have different degrees of importance, depending on the energetics of the system under study. At high energies, the distortion of the electron wavefronts has the highest importance, whereas as the energy is lowered the other factors play an increasingly important role. When the energy is close to threshold, PCI is the dominant mechanism. In the intermediate energy regime where most of the work is carried out in Manchester, all of these processes must be considered. This makes the collision models in this energy regime challenging.

1.2 Scattering Theory

1.2.1 Rutherford Scattering

Scattering theories and experiments have been used to understand fundamental physical processes since the early 1900s. The original scattering experiment was performed by Geiger and Marsden between 1908 and 1913 at Manchester under the direction of Rutherford [23]. In this experiment alpha particles were scattered from gold foil. This experiment produced two key results: firstly that the positive charge of an atom is concentrated in the nucleus, and secondly that the nucleus is very small when compared to the size of an atom [24]. The measured scattering of alpha particles from gold foil is an example of elastic scattering. The probability of a scattering event can be characterised by a cross section σ which is defined as the scattering rate per unit flux of the incident particles. Usually, the differential cross section (DCS)

$$\frac{d\sigma}{d\Omega} = \frac{N}{j} \quad (1.9)$$

is quoted. This quantity is easily experimentally measured for a scattered particle scattering through solid angle $d\Omega$ steradians, number of particles per unit time detected N , and number of incident particles per unit area per unit time (flux) j . Hence, the total scattering cross section can be calculated by integrating over all solid angles.

A diagram of the Rutherford experiment for a scattering event is shown in figure 1.4. Here, the gold atom has a central Coulomb potential of $V(r) = \kappa/r$. The scattering angle θ is determined by the incident particle's perpendicular distance to the direction of incidence, which is called the impact parameter b . Applying conservation of flux, the number of particles scattered between θ to $\theta + d\theta$ equals the number of incident particles between b and $b + db$ and so

$$Nd\Omega = 2\pi b db j, \quad (1.10)$$

where we have used the fact that j is the flux on the surface perpendicular to the direction of incidence. Using $d\Omega = 2\pi \sin\theta d\theta$, an expression for the DCS can be derived as

$$\frac{d\sigma(\theta)}{d\Omega} = \frac{b}{\sin\theta} \left| \frac{db}{d\theta} \right|. \quad (1.11)$$

For a central potential $V(r)$, and assuming that the charge is located at a point, the DCS

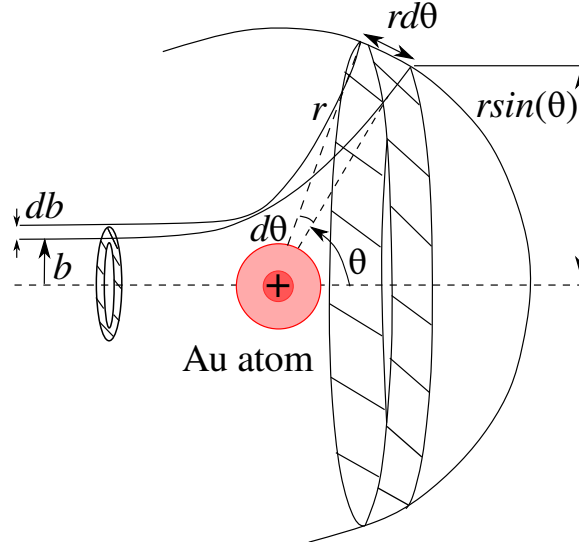


Figure 1.4: A diagram of Rutherford scattering showing two different trajectories of scattered particles from a gold atom. Particles with impact parameter b have an angle of scattering θ and scattering trajectory following radius r from the centre of the atom. The small changes in impact parameter and scattering angle are labelled as db and $d\theta$. The differential cross section can be derived from this geometry as discussed in the text.

can be re-written [25]

$$\frac{d\sigma}{d\Omega} = \frac{\kappa^2}{16E^2} \frac{1}{\sin^4(\theta/2)}, \quad (1.12)$$

where E is the energy of the incident particle. This is an important result which describes many phenomena [1, 26]. Rutherford scattering does not however model the quantum nature of particles and therefore is lacking when it comes to describing modern experimental data. In the next section, quantum scattering theory is discussed.

1.2.2 Modern Scattering Theory

When the quantum nature of electrons and atoms are taken into account, the scattering problem becomes more complicated. Since there are no analytical solutions to even simple scattering between a hydrogen atom and an electron [27], approximations must be made. Therefore, there are many competing modern scattering theories. Only those which are pertinent to the work carried out in this thesis will hence be outlined.

The wave nature of particles, as shown in figure 1.5, must be considered when solving scattering problems. The incoming particles can be represented by the wavefunction $\Psi(\mathbf{r}, t)$ and the time dependent Schrödinger equation (TDSE) [28]

$$i\hbar \frac{\partial \Psi(\mathbf{r}, t)}{\partial t} = \left(-\frac{\hbar^2}{2m} \nabla^2 + V(\mathbf{r}) \right) \Psi(\mathbf{r}, t) \quad (1.13)$$

can be used to calculate the probability amplitudes for the outgoing waves. If the incident beam of particles has been ‘switched on’ for a long time compared with the interaction time then the system is in a steady state. If an incoming wave has well-defined energy E

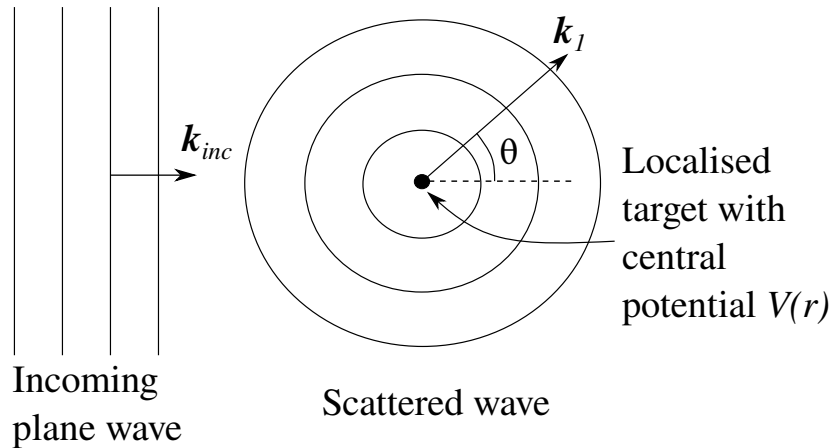


Figure 1.5: A diagram showing the wave nature of an incoming particle with momentum \mathbf{k}_{inc} impacting upon a target with central potential $V(r)$, resulting in an outgoing scattered wave with momentum \mathbf{k}_1 making an angle θ with respect to \mathbf{k}_{inc} .

then it may be considered a plane wave with separable solution [28]

$$\Psi(\mathbf{r}, t) = \psi(\mathbf{r})e^{-\frac{iEt}{\hbar}} \quad (1.14)$$

and therefore the time independent Schrödinger equation (TISE)

$$E\psi(\mathbf{r}) = \left[-\frac{\hbar^2}{2m}\nabla^2 + V(\mathbf{r}) \right] \psi(\mathbf{r}) \quad (1.15)$$

can be used to obtain a solution for $\psi(\mathbf{r})$. This solution is subject to boundary conditions of an incident plane wave $\psi \sim e^{i\mathbf{k}\cdot\mathbf{r}}$, where \mathbf{k} is the momentum of the incoming wave. The incoming wave scatters from the central potential and produces reflected and outgoing waves. All of these waves may interfere with each other. Approximations can be made using partial waves to describe the wavefunction of this system [28]

$$\psi(\mathbf{r}) \approx e^{i\mathbf{k}\cdot\mathbf{r}} + f(\theta)\frac{e^{i\mathbf{k}\cdot\mathbf{r}}}{r} \quad (1.16)$$

where $f(\theta)$ is the amplitude of the scattered wave in the direction θ . It can be shown that this scattering amplitude is directly related to the DCS as

$$\frac{d\sigma}{d\Omega} = |f(\theta)|^2 \quad (1.17)$$

and that the scattering amplitude can be decomposed into a summation of partial waves [28]. The scattering amplitudes can therefore characterise a scattering system.

The Born Approximation

In this section, the Born approximation is discussed. This approximation leads to the Born series expansion of the scattering amplitude [28, 29]. To obtain the Born expansion the TISE must be written in integral form. The scattering wavefunction can be written as

$$(\nabla^2 + k^2)\psi(\mathbf{r}) = U(\mathbf{r})\psi(\mathbf{r}), \quad (1.18)$$

where $U(\mathbf{r})$ is a modified potential, $V(\mathbf{r}) = (\hbar^2/2m)U(\mathbf{r})$ [28]. The general solution of equation 1.18 can be expressed as

$$\psi(\mathbf{r}) = \phi(\mathbf{r}) + \int G_0(\mathbf{r}, \mathbf{r}')U(\mathbf{r}')\psi(\mathbf{r}')d^3\mathbf{r}', \quad (1.19)$$

where G_0 is a Green's function which satisfies

$$(\nabla^2 + k^2)G_0(\mathbf{r}, \mathbf{r}') = \delta^3(\mathbf{r}, \mathbf{r}') \quad (1.20)$$

and $\phi(\mathbf{r})$ satisfies the free particle TISE

$$(\nabla^2 + k^2)\phi(\mathbf{r}) = 0. \quad (1.21)$$

Using the plane-wave solution to the TISE $\phi(\mathbf{r}) = e^{i\mathbf{k}\cdot\mathbf{r}}$ equation 1.19 can be written as [28]

$$\psi(\mathbf{r}) = e^{i\mathbf{k}\cdot\mathbf{r}} - \frac{1}{4\pi} \int \frac{e^{ik|\mathbf{r}-\mathbf{r}'|}}{|\mathbf{r}-\mathbf{r}'|} U(\mathbf{r}')\psi(\mathbf{r}')d^3\mathbf{r}'. \quad (1.22)$$

The approximation that the potential is localised at the scattering target centre $V(r = r' = 0)$ can be made as the wavefunction where the outgoing particle is detected is far away from the target. This leads to the approximation that $|\mathbf{r} - \mathbf{r}'| \approx r - \hat{\mathbf{r}}\cdot\mathbf{r}'$ which can be used to make the approximation [28]

$$\frac{e^{ik|\mathbf{r}-\mathbf{r}'|}}{|\mathbf{r}-\mathbf{r}'|} \approx \frac{e^{ikr}}{r} e^{-i\mathbf{k}\cdot\mathbf{r}'}. \quad (1.23)$$

By invoking the Born approximation that incoming plane waves are not altered by the localised central potential [29] and using equations 1.23, 1.16, and 1.19 the scattering amplitude can be approximated as

$$\begin{aligned} f(\theta, \phi) &\approx -\frac{1}{4\pi} \int e^{i(\mathbf{k}')\cdot\mathbf{r}'} U(\mathbf{r}')\psi(\mathbf{k}, \mathbf{r}')d^3\mathbf{r}' \\ &= -\frac{m}{2\pi\hbar^2} \langle \phi(\mathbf{k}') | V | \psi(\mathbf{k}) \rangle. \end{aligned} \quad (1.24)$$

The differential cross section can now be re-written as

$$\frac{d\sigma}{d\Omega} = |f(\theta, \phi)|^2 = \frac{m^2}{(2\pi)^2\hbar^4} |T(\mathbf{k}, \mathbf{k}')|^2, \quad (1.25)$$

where $|T(\mathbf{k}, \mathbf{k}')| = \langle \phi(\mathbf{k}') | V | \psi(\mathbf{k}) \rangle$ is the transition matrix element. The zeroth order Born approximation occurs when the scattering wavefunction $\psi_0(\mathbf{r})$ translates to an unperturbed incident plane wave and has the same expression as equation 1.19. In the first-order Born approximation

$$\psi_1(\mathbf{r}) = \phi(\mathbf{r}) + \int G_0(\mathbf{r}, \mathbf{r}')U(\mathbf{r}')\psi_0(\mathbf{r}')d^3\mathbf{r}' \quad (1.26)$$

and in the second-order

$$\psi_2(\mathbf{r}) = \phi(\mathbf{r}) + \int G_0(\mathbf{r}, \mathbf{r}')U(\mathbf{r}')\psi_1(\mathbf{r}')d^3\mathbf{r}'. \quad (1.27)$$

Therefore, the n^{th} order Born approximation can be expressed as a series expansion

$$\begin{aligned} |\psi(\mathbf{k})\rangle &= |\phi(\mathbf{k})\rangle + G_0U |\phi(\mathbf{k})\rangle + G_0UG_0U |\phi(\mathbf{k})\rangle + \dots \\ &= \sum_{n=0}^{\infty} (G_0U)^n |\phi(\mathbf{k})\rangle \end{aligned} \quad (1.28)$$

and the scattering amplitude can be calculated as

$$f(\theta, \phi) = -\frac{1}{4\pi} \langle \phi(\mathbf{k}) | U + UG_0U + UG_0UG_0U + \dots | \phi(\mathbf{k}) \rangle. \quad (1.29)$$

This is known as the Born series expansion. Physically, the higher order terms are contributions to the scattering cross section from higher order scattering events i.e. multiple successive scattering events by the central potential before the particle is detected. The Born approximation can be used with fairly high accuracy in high energy scattering events [30].

Distorted Wave Born Approximation

The DWBA is a theoretical approach to solving scattering problems which is an extension to the Born approximation. The use of this approach has been successful in modelling electron impact ionisation of light molecules [22] and atoms [31].

The many-body problem of electron-atom interactions can be reduced to a two-body problem by introducing a complex potential called the optical potential [1]. This is sometimes referred to as an effective potential V_{effect} . The effective potential can be calculated in different ways depending on the scattering system. As an example, a reasonable V_{effect} for electron impact ionisation can be found by combining the Coloumb potential between each electron in the interaction. If the V_{effect} is constructed to be spherically symmetric then the wavefunction describing the free electrons in the system, known as the continuum wavefucntion, can be separated from the wavefunction describing the orbital electron, target atom, and residual ion. A continuum wavefunction calculated in any effective potential is a distorted wave [22]. It can be shown [1] that the T-matrix for all continuum wavefunctions can be expressed as [32]

$$T_{DWBA} = \left\langle \chi_a^{(-)}(\mathbf{k}_a, \mathbf{r}_a) \chi_b^{(-)}(\mathbf{k}_b, \mathbf{r}_b) \phi \left| V_{int} \right| \chi_0^{(+)}(\mathbf{k}_0, \mathbf{r}_0) \psi \right\rangle \quad (1.30)$$

where $\chi_a^{(-)}$, $\chi_b^{(-)}$, and $\chi_0^{(+)}$ are distorted waves for the scattered, ionised, and incident electron respectively. These distorted waves are calculated in the effective potential of the target and residual ion. The potential V_{int} incorporates the interaction potentials of the scattered, ionised, and incident electron with the residual ion. The neutral target and residual ion wavefunctions are described by ψ and ϕ respectively.

The DWBA theory has the advantage that mechanisms can be ‘switched’ on or off to investigate their relative effects. However, there is no inherent inclusion of PCI or polarisation in this theoretical approach. These effects can be included in the DWBA in a variety of ways. For the inclusion of PCI, the Gamow factor N_{ee} is sometimes used [33,34] where the DCS is modified to become

$$(DCS)_{\text{PCI, DWBA}} = N_{ee} (DCS)_{\text{DWBA}} \quad (1.31)$$

and

$$N_{ee} = \frac{\gamma}{e^\gamma - 1} \quad (1.32)$$

$$\gamma = \frac{2\pi}{|\mathbf{k}_1 - \mathbf{k}_2|}, \quad (1.33)$$

where \mathbf{k}_1 and \mathbf{k}_2 denote the momenta of the two outgoing electrons. This inclusion of N_{ee} forces the DCS to be zero if \mathbf{k}_1 is parallel to \mathbf{k}_2 and $|\mathbf{k}_1 = \mathbf{k}_2|$, which is a physical condition which must be met [35]. Miller et al. [36] uses the DWBA theory and the Gamow factor to model data from experiments conducted at Manchester involving argon, which is discussed in detail in chapter 7. In this modelling, the usual Gamow factor is replaced with the Ward-Macek factor [37]

$$M_{ee} = N_{ee} |{}_1F_1(-iv_3, 1, -2ik_3r_{3av})|, \quad (1.34)$$

where the function ${}_1F_1$ is Kummer's confluent hypergeometric function [38] and

$$k_3 = \frac{1}{2}|\mathbf{k}_2 - \mathbf{k}_1| \quad (1.35)$$

$$v_3 = -\frac{1}{|\mathbf{k}_2 - \mathbf{k}_1|} \quad (1.36)$$

$$r_{3av} = \frac{3}{\epsilon} \left[\frac{\pi}{4\sqrt{3}} \left(1 + \frac{0.627}{\pi} \sqrt{\epsilon \ln \epsilon} \right) \right]^2, \quad (1.37)$$

where ϵ is the total energy of the outgoing electrons and \mathbf{k}_1 and \mathbf{k}_2 are the momenta of the outgoing electrons. The argon data is also modelled by these authors using a plane wave approximation (PWA). In this approximation the distorted wave $\chi_0^{(+)}(\mathbf{k}_0, \mathbf{r}_0)$ in equation 1.30 is replaced by a plane wave $\phi_0 \propto e^{i\mathbf{k}_0 \cdot \mathbf{r}}$.

The Convergent Close Coupling Method

The CCC theoretical approach to solving scattering problems is newer than the DWBA approach and was introduced by Stelbovics in 1990 [39] and expanded upon by Bray [21]. The CCC method has been successful at predicting scattering cross sections for light atoms such as He [40], the lighter alkali-earth atoms [41], and also light molecules such as H₂ [42].

The CCC theory is based on the close-coupling method, which solves a set of coupled equations in momentum-space [43] generated from a set of coupled target states. These coupled states are obtained by diagonalising the target Hamiltonian of the system and decomposing the wavefunction into N orthogonal, square, and integrable basis states. These basis states ϕ_n^N have associated energies ϵ_n^N , where $n = 1, 2, \dots, N$ [40]. The energies ϵ_n^N can be positive or negative. For negative values of ϵ_n^N , the corresponding basis states provide a representation of the discrete target spectrum where $\phi_n^N \rightarrow \phi_n$ as $N \rightarrow \infty$. The positive energy states discretise the target continuum, where adding more of these pseudostates increases the accuracy of the model but increases the complexity of the calculations.

For electron-atom interactions, the total wavefunction is expanded in terms of the basis states

$$\left| \Psi_i^{(+)} \right\rangle \approx \mathcal{A} \sum_{n=1}^N \phi_n^N f_{ni}^{N(+)}, \quad (1.38)$$

where \mathcal{A} is the antisymmetrisation operator for space and spin and $f_{ni}^{N(+)}$ are the unknown single-electron space-projectile functions to be determined by solving the resulting coupled equations with spherical boundary conditions [40]. The basis states ϕ_n^N can be composed of Laguerre polynomials which can be used to calculate the electron-impact excitation T-matrix elements [40]

$$T_{fi} = \langle \mathbf{k}_f \phi_f^N | T^N | \phi_i^N \mathbf{k}_i \rangle = \langle \mathbf{k}_f \phi_f^N | T^N | \Psi_i^{N(+)} \rangle, \quad (1.39)$$

where \mathbf{k}_f is the momentum of an incoming plane wave. Equation 1.39 leads to the calculation of scattering amplitudes using equation 1.24. The CCC method has been used to calculate the scattering amplitudes for the electron impact excitation of He used in chapter 2 of this thesis.

1.3 (e, 2e) Experiments

Whilst the DCS, as described in equation 1.17, is a desirable quantity to measure, it does not fully characterise the electron-impact ionisation process, as the cross section varies with energy, as shown for classical Rutherford scattering. A double differential cross section (DDCS) can be measured to provide more information about the ionisation process [44]

$$\text{DDCS} = \frac{d^2\sigma}{dE_{inc}d\Omega_1}, \quad (1.40)$$

where E_{inc} is the incoming electron energy and Ω_1 is the solid angle through which one of the emitted electrons scatters through. However, to fully characterise the interaction, information must be known about *both* scattered and ionised electron. Thus, an electron impact ionisation experiment must be performed where both outgoing electrons are detected in coincidence to fully characterise the ionisation interaction. This experiment is known as an (e, 2e) experiment (1 electron in, 2 electrons out). Experiments using the (e, 2e) coincidence technique have been performed for more than 50 years [45]. These experiments provide important cross sectional data for electron impact ionisation and provide a testing ground for scattering models. All the information regarding the target atom and the fundamental interactions between the electrons and the atom, such as those described in section 1.1.4, can be extracted from these experiments in the form of measuring the triple differential cross section (TDCS) [1, 46]

$$\text{TDCS} = \frac{d^3\sigma}{d\Omega_1\Omega_2E_2}, \quad (1.41)$$

where Ω_1 and Ω_2 are the solid angles for the scattered and ionised electron and E_2 is the energy of the ionised electron. Only a single outgoing electron energy needs to be used here as E_{inc} is known. All energies can hence be calculated by using the conservation of energy as seen in equation 1.8.

The effectiveness of theoretical models to predict the TDCS varies with the energy of the interaction. Different energy regimes are usually defined with respect to the IP. In the threshold regime, where $\text{IP} \lesssim E_{inc} \lesssim \text{IP}+2 \text{ eV}$, the outgoing electrons are moving so slowly that post-collision interactions are dominated by the Coulomb force between the two electrons. Interactions in this regime have been successfully modelled using different theories [47, 48]. In the high energy regime (above $\sim 100 \text{ eV}$) only a small fraction of the kinetic energy of the incident electron is transferred to the target atom and therefore the wave functions of the incident and emitted electrons can be well-approximated by plane waves [49]. Modelling this regime using the plane-wave approximation agrees well with experiment. This model has been so successful it is used in spectroscopy as a tool to probe the electronic structure of molecules or atoms [50]. In the intermediate energy regime, where $\text{IP}+2 \text{ eV} \lesssim E_{inc} \lesssim \text{IP}+100 \text{ eV}$, all of the mechanisms shown in figure 1.3 significantly contribute to the scattering cross section [51]. These mechanisms include electron exchange, electron capture and all short and long range interactions between all electrons and the atomic core [52]. For this regime, there are several competing models which have been successful in describing the ground states of light atoms such as helium [53] and simple molecular systems such as hydrogen [54, 55].

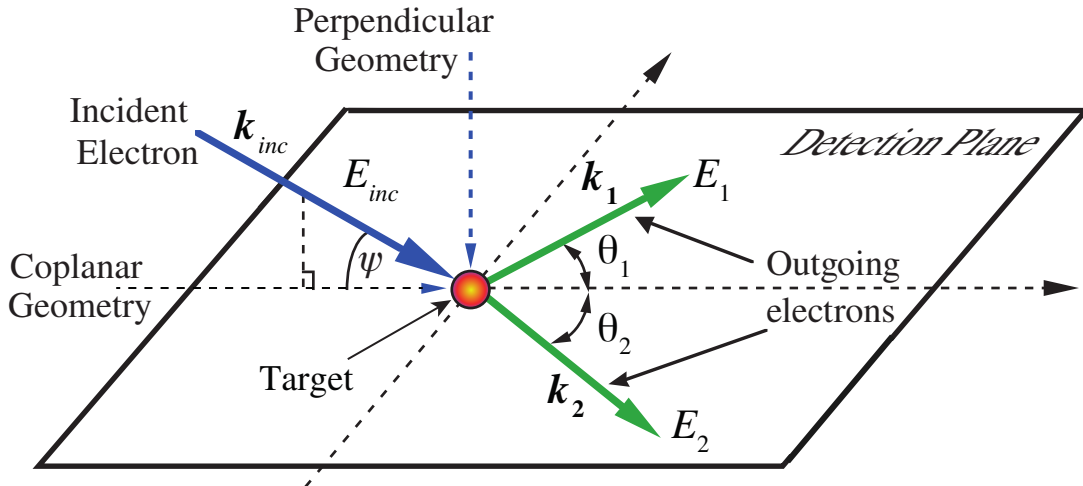


Figure 1.6: Geometry of an (e,2e) experiment at Manchester showing the incident electron, with energy and momentum E_{inc} and \mathbf{k}_{inc} respectively, impacting upon a target. The outgoing electrons have energies E_1 , E_2 and momenta \mathbf{k}_1 , \mathbf{k}_2 . This experiment is unique in that it can access all geometries from a coplanar geometry through to the perpendicular regime.

One of the first (e, 2e) experiments at Manchester was performed in 1992 [56]. This was performed in a spectrometer which was built in 1984 [57]. This spectrometer, referred to in this thesis as the Old (e, 2e) spectrometer, is still in operation today and has been used to provide new experimental data in this thesis in chapters 6 and 7. The experimental geometry in Manchester (e, 2e) experiments can be seen in figure 1.6. The outgoing electrons with momenta \mathbf{k}_1 and \mathbf{k}_2 span the detection plane. The incident electron makes an angle ψ with respect to the detection plane. The outgoing electrons' momenta make angles θ_1 and θ_2 with respect to the incident electron's momentum \mathbf{k}_{inc} projected onto the detection plane. The angle ψ can be varied out of the detection plane in the Old (e, 2e) spectrometer. At $\psi = 90^\circ$, the (e, 2e) experiment is in the perpendicular plane geometry and when $\psi = 0^\circ$, the experiment is in the coplanar geometry. This allows (e, 2e) experiments to be performed in non-coplanar geometries [51]. Measurements made in these non-coplanar geometries are more selective for higher order scattering

processes [58, 59]. This provides a sensitive test of different scattering theories. A further advantage of this configuration is that a common point exists for all angles ψ when $\theta_1 = \theta_2 = 90^\circ$ and so collected data can be inter-normalized for a range of different values of \mathbf{k}_{inc} . Hence, theoretical models must emulate data from these experiments at all angles, not just for a single scattering geometry.

In 2006 a new (e, 2e) spectrometer was built at Manchester [60] to measure scattering from laser-excited targets. The optical windows on this spectrometer allow for fluorescence to be detected and for laser light to enter the chamber, which has allowed both super-elastic and laser excited (e, 2e) experiments to be performed [61, 62]. This spectrometer is referred to as the New (e, 2e) spectrometer in this thesis. This spectrometer has been used for the experiments presented in chapter 8.

(e, 2e) experiments at Manchester have historically focused on the low-to-intermediate energy regime. In this regime, theoretical models generally agree with experimentally-obtained cross sections for atoms such as H [63] and He [55, 64]. However, for heavier atoms [36, 65] the models do not always predict the cross sections well under different kinematic conditions. In chapters 6 and 7, experimental data is provided for heavy atomic targets, Xe and Ar, in the low to intermediate energy regimes in non-coplanar geometries. This new data has been published in [66] and [67].

Theoretical predictions of molecular (e, 2e) cross sections for heavy molecules do not agree well with experiment [68]. Molecular (e, 2e) cross sections are difficult to model as experimentally-obtained data averages over all molecular orientations [69]. If an experiment can be performed which fixes the orientation of the target then models can make predictions for each orientation-dependent cross section, which can then be compared to experimental data. Such experiments have only been performed on simple diatomic molecules using the COLTRIMS technique at the present time [70].

1.4 Laser-aligned (e,2e)

Laser excitation of atomic targets can fix the orientation and alignment of an atom. For example, an excited fully aligned P -state has a shape such as that described in figure 1.7. The alignment angle of the P -state θ_T depends on the linear polarisation direction of the incoming laser beam ϵ . (e, 2e) experiments performed on this laser-aligned target cannot be fully described by the TDCS, as the collision symmetry has been reduced due to the absence of a spherically-symmetric ground state atom. In this laser-aligned (e, 2e) experiment a quadruple differential cross section (QDCS) is introduced [71]

$$\text{QDCS} = \frac{d^4\sigma}{d\Omega_T \Omega_1 \Omega_2 E_2}, \quad (1.42)$$

where the atom alignment solid angle is $\Omega_T(\theta_T, \phi_T)$. The New (e, 2e) spectrometer was used to produce the first laser-aligned (e, 2e) measurements from magnesium in 2011 [71, 72]. This spectrometer has also produced results for superelastic scattering of laser-aligned Mg [73] and Ag [74]. These (e, 2e) experiments used magnesium as it is an alkaline-earth atom. This atomic group's main isotopes have no hyperfine structure and

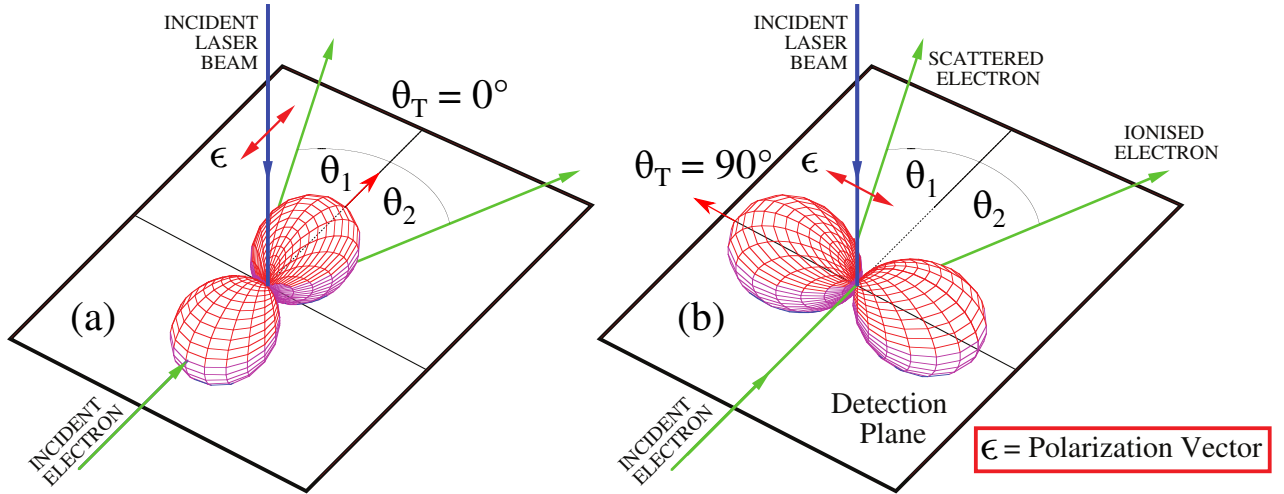


Figure 1.7: The geometry of laser-aligned (e, 2e) experiments where the incident laser beam polarisation ϵ is (a) parallel and (b) perpendicular to the incident electron beam. The shape of the excited P -state electron cloud is shown with alignment angle (a) $\theta_T = 0^\circ$ and (b) $\theta_T = 90^\circ$.

so they can be aligned into a pure P -state fully using linearly polarised continuous wave radiation.

Laser-excited scattering experiments require careful consideration of which target states to investigate. Factors to consider include: the electronic structure of the atom, whether an atomic beam can easily be formed, and achievable laser wavelengths to reach the target excited state with a large enough population to provide a strong scattering signal. Modelling of the laser-excitation of the target atom can aid in the design of these experiments. A computational package to aid in simulating laser-atom interactions for use in scattering experiments is hence presented in section 2.3. This work has been published in [75]. Laser-excited (e, 2e) experiments have smaller signals than ground state (e, 2e) experiments as only a proportion of the target atoms are in the excited state. Another difficulty with performing these experiments is that the laser needs to be locked onto a specific wavelength for weeks at a time. Therefore, a reliable and automated experimental control system has been built and detailed in this thesis, in chapter 5, to fulfill these requirements. This work has also been published and can be found in [76].

1.5 Layout of this Thesis

This introduction is followed by a full quantum electrodynamical treatment of atoms excited in a laser field in chapter 2. The density matrix formalism is introduced and the equations of motion for a laser-excited atomic system are derived. A laser-atom simulator derived from quantum electrodynamics (**LASED**) is detailed in this chapter, to generate and solve these equations of motion.

In chapter 3, the Old and New (e, 2e) spectrometers' hardware are detailed and compared. In this chapter, the testing of a new atomic beam oven for the New (e, 2e) spectrometer is also given. In chapter 4, the laser systems used at Manchester are described, as well as the new laser safety interlock system that has been developed to satisfy the new health and

safety regulations required at the University of Manchester. In this chapter, the control of a half-wave plate for use in laser-aligned experiments in the New (e, 2e) spectrometer is detailed. In chapter 5, the experimental control software and firmware using Arduino [77] and LabVIEW [78] interfaces for use in both spectrometers is detailed.

In chapter 6, new experimental data for the evolution of the TDCS of xenon as the scattering geometry changes from coplanar to the perpendicular plane at incident energies of 60 eV, 80 eV, and 100 eV above the IP is presented. A new technique for mapping these relative cross sectional measurements to absolute values using a He-Xe mixture is described here. In chapter 7, new data for the evolution of the TDCS of argon in the perpendicular plane is detailed as the incident energy is increased from 5 eV to 200 eV above the IP. Chapter 8 details calibration of the New (e, 2e) spectrometer using measurements of the He 2^2S resonance and fluorescence of Sr. Proposed experiments to measure laser-aligned (e, 2e) from Sr are also discussed in this chapter.

Chapter 9 summarises the work presented in this thesis and suggests future work which expands upon the research presented here.

Chapter 2

Laser Interaction with Atoms

This chapter presents a theoretical treatment of laser radiation interacting with atoms. It is divided into three sections. In the first section, the density matrix formalism for describing an atomic system is introduced along with a description of the natural and collision frames of reference (as has been introduced in chapter 1). Density matrices are also used to describe the process of electron-impact excitation. In the second section, the equations of motion for atoms in a coherent laser field are derived from the theory of quantum electrodynamics (QED). Expressions are given for calculating the half-Rabi frequency and decay constants as well.

In the last section, a laser-atom interaction simulator (LASED) is presented, which has been developed in the python programming language [79]. LASED allows a user to automatically generate the required equations of motion for a laser-excited atomic system and then calculate the time evolution of this system. The model allows for any laser polarisation, a Gaussian laser beam profile, a rotation of the reference frame chosen to define the states, and an averaging over the Doppler profile of an atomic beam. Examples of simulations using LASED are presented for excitation of calcium from the 4^1S_0 state to the 4^1P_1 state, for excitation from the helium 3^1D_2 state excited by electron impact to the 10^1P_1 state, and for laser excitation of caesium via the D_2 line. This work has been published in [75].

2.1 The Density Matrix

The density matrix is a useful representation of a quantum state and will be used extensively in this chapter to describe the state of an atomic system. The total wavefunction for any quantum system can be expanded into a linear combination of orthogonal basis states [11]

$$|\Psi\rangle = \sum_i a_i |i\rangle, \quad (2.1)$$

where $|i\rangle$ are the orthogonal basis states and a_i are complex coefficients. The probability of the system to occupy state $|i\rangle$ is $|a_i|^2$. As an example, the atomic wavefunction of a P-state can be represented as

$$|\Psi\rangle = \sum_{J,m} a_{J,m} |J, m\rangle = a_{1,-1} |1, -1\rangle + a_{1,0} |1, 0\rangle + a_{1,+1} |1, +1\rangle, \quad (2.2)$$

where J is the angular momentum quantum number, m is the projection of the angular momentum along the quantisation z-axis (QA), and $a_{J,m}$ are the complex coefficients which determine the probability of an electron occupying the substate $|J, m\rangle$. The coefficients also contain phase relationships between each substate. The density matrix can be defined as [80]

$$\rho = |\Psi\rangle \langle\Psi|. \quad (2.3)$$

Defining the basis for the P-state as $\langle+1| = (1, 0, 0)$, $\langle 0| = (0, 1, 0)$, and $\langle-1| = (0, 0, 1)$, the density matrix for a P-state, as given by equation 2.2, is then

$$\rho = \begin{pmatrix} |a_{+1}|^2 & a_{+1}a_0^* & a_{+1}a_{-1}^* \\ a_0a_{+1}^* & |a_0|^2 & a_0a_{-1}^* \\ a_{-1}a_{+1}^* & a_{-1}a_0^* & |a_{-1}|^2 \end{pmatrix}. \quad (2.4)$$

The diagonal terms $|a_m|^2$ in equation 2.4 are the *populations* of the substates $|J, m\rangle$, which correspond to the probability of the state occupying that particular substate. As these diagonal terms are probabilities, the condition that $\text{tr}(\rho) = 1$ is a property of all normalised density matrices. The *atomic coherences* between substates $|J, m\rangle$ and $|J, m'\rangle$ in the density matrix representation correspond to the off-diagonal terms $a_m a_{m'}^*$, where $m \neq m'$. Note that $\rho_{ij} = \rho_{ji}^*$ as ρ is Hermitian.

In a scattering experiment, a P-state density matrix can be simplified by changing reference frame. A typical reference frame to be used in a collision experiment is where the quantisation axis lies in the same direction as the incident electron's momentum, as shown in figure 2.1(b). This is known as the collision frame Z^{Coll} [2]. The reference frame can be changed to the natural frame Z^{Nat} , where the quantisation axis is perpendicular to the scattering plane, as shown in figure 2.1(a). A target excitation from an S-state to a P-state in Z^{Nat} would have zero transfer of momentum out of the scattering plane, unless a spin-flip of the electron occurs [11]. Under these conditions, a_0 can be set to 0 and the P-state density matrix can be defined as

$$\rho^{\text{Nat}} = \begin{pmatrix} |a_{+1}|^2 & 0 & |a_{+1}||a_{-1}|e^{-i\delta} \\ 0 & 0 & 0 \\ |a_{-1}||a_{+1}|e^{i\delta} & 0 & |a_{-1}|^2 \end{pmatrix}, \quad (2.5)$$

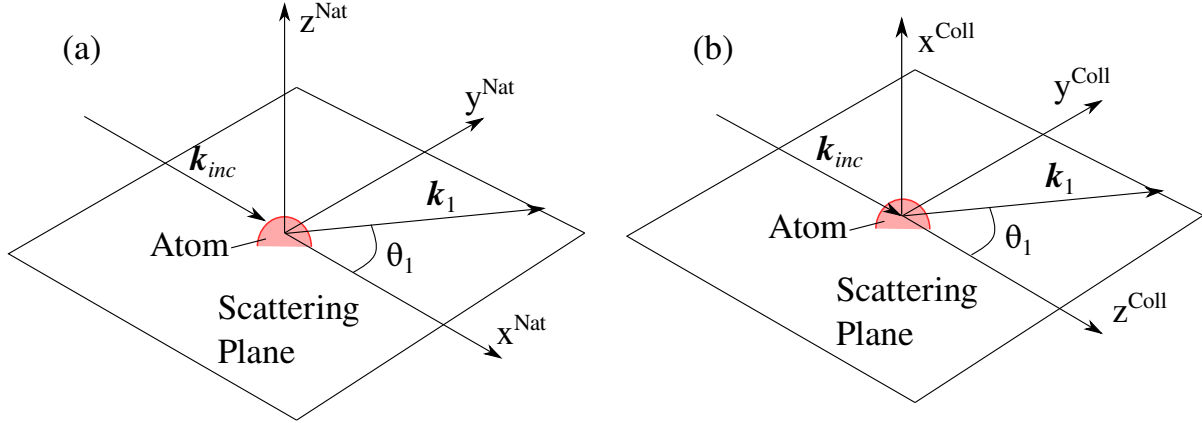


Figure 2.1: (a) The axes used for the natural frame Z^{Nat} and (b) the axes used for the collision frame Z^{Coll} . In both frames, an incident electron with momentum \mathbf{k}_{inc} scatters from a target at the origin and has outgoing momentum \mathbf{k}_1 which makes angle θ_1 with respect to the direction of \mathbf{k}_{inc} . The plane spanned by \mathbf{k}_{inc} and \mathbf{k}_1 is called the scattering plane.

where the coefficients have been written in their explicit complex form $|a_m|e^{i\phi_m}$ and $\delta = \phi_{-1} - \phi_{+1}$ is the phase difference between a_{-1} and a_{+1} . This simplified density matrix can be used to calculate the ACPs directly. In the natural frame the density matrix can be written in terms of the ACPs [11]

$$\rho = \frac{1}{2} \begin{pmatrix} 1 + L_{\perp} & 0 & -P_{lin}e^{-2i\gamma} \\ 0 & 0 & 0 \\ -P_{lin}e^{2i\gamma} & 0 & 1 - L_{\perp} \end{pmatrix}. \quad (2.6)$$

By relating equation 2.6 to 2.5, the ACPs can be directly related to the coefficients describing the basis states as

$$P_{lin} = 2|a_{-1}||a_{+1}| \quad (2.7)$$

$$\gamma = \frac{\delta}{2} \pm \frac{\pi}{2} \quad (2.8)$$

$$L_{\perp} = |a_{+1}|^2 - |a_{-1}|^2. \quad (2.9)$$

The addition of $\pm\frac{\pi}{2}$ in equation 2.8 is from a choice of phase to constrain P_{lin} to be positive [11]. In the natural frame, the height of the charge cloud ρ_{00} represents the relative amplitude for a spin-flip for an S to P-state excitation. Since we have defined the momentum transfer out of the scattering plane to be zero, no spin-flip occurs and ρ_{00} is zero.

The density matrix can also be used to calculate the final state from an electron-impact experiment given the scattering amplitudes, as is done when calculating the helium electron-impact excited 3^1D_2 state in section 2.3.8. The initial atom is represented by a density matrix in the collision frame given by [80]

$$\rho^{\text{atom}} = \frac{1}{2J+1} \sum_M |\alpha_i J_i M_i\rangle \langle \alpha_i J M_i|, \quad (2.10)$$

where J_i is the initial total angular momentum of the atom, M_i is the initial projection of the total angular momentum along the QA, and α_i describes all other quantum numbers

necessary for fully characterising the initial atomic state. The incident electron can be represented by the density matrix [80]

$$\rho^{\text{electron}} = \frac{1}{2} |\mathbf{p}_i m_i\rangle \langle \mathbf{p}_i m_i|, \quad (2.11)$$

where \mathbf{p}_i is the initial momentum of the incident electron and m_i is the electron's initial spin component. Since the atom and incident electron are uncorrelated prior to the collision, the initial density matrix of the atom-electron system is the product of ρ^{atom} and ρ^{electron}

$$\rho^{\text{initial}} = \frac{1}{2(2J+1)} \sum_{M_i m_i} |M_i m_i\rangle \langle M_i m_i|, \quad (2.12)$$

where the fixed quantum numbers have been suppressed so $|M_i m_i\rangle = |\alpha_i J_i M_i \mathbf{p}_i m_i\rangle$. The atom and electron states after the collision are given by $|\alpha_f J_f M_f\rangle$ and $|\mathbf{p}_f m_f\rangle$ respectively. The density matrix after the collision is given by

$$\begin{aligned} \rho^{\text{final}} &= T \rho^{\text{initial}} T^\dagger \\ &= \frac{1}{2(2J_i+1)} \sum_{M_i m_i} T |M_i m_i\rangle \langle M_i m_i| T^\dagger, \end{aligned} \quad (2.13)$$

where T is the transition operator. As in equation 1.25, the T -matrix can be defined in terms of the scattering amplitudes

$$\langle M_i m_i| T |M_f m_f\rangle = f(M_i m_i, M_f m_f), \quad (2.14)$$

where $f(M_i m_i, M_f m_f)$ is the scattering amplitude for the transition between initial state $|M_i m_i\rangle$ and final state $|M_f m_f\rangle$. By combining equations 2.13 and 2.14, the matrix elements of the final state density matrix can be written as

$$\langle M_f m_f| \rho^{\text{final}} |M'_f m'_f\rangle = \frac{1}{2(2J_i+1)} \sum_{M_i m_i} \langle M_f m_f| T |M_i m_i\rangle \langle M_i m_i| T^\dagger |M'_f m'_f\rangle. \quad (2.15)$$

As the spin of the scattered electron is not detected, ρ^{final} is an average over the undetected spin states. The observed density matrix is hence calculated by taking the trace of the matrix elements of ρ^{final} which are diagonal in the unobserved spins m'_f [80]. Equation 2.15 can therefore be written in reduced form as

$$\begin{aligned} \rho_{MM'}^{\text{final}} &= \sum_{m'_f} |M m'_f\rangle \rho^{\text{final}} |M' m'_f\rangle \\ &= \frac{1}{2(2J_f+1)} \sum_{M_i m_i m'_f} \langle M m'_f| T |M_i m_i\rangle \langle M_i m_i| T^\dagger |M' m'_f\rangle \\ &= \langle f(M) f(M')^* \rangle, \end{aligned} \quad (2.16)$$

where here $\langle \dots \rangle$ denotes the averaging over spins and M_f is replaced by M . The final state density matrix can be normalised by the condition that $\text{tr}(\rho^{\text{final}}) = 1$. If the scattering amplitudes are known, then a full description of the atomic density matrix for the electron-impact excited state can be calculated using equation 2.16. In section 2.3.8, the normalised density matrix of the electron-impact excited 3^1D_2 state of He is calculated using scattering amplitudes.

2.2 Equations of Motion for Atoms in a Laser Field

The general equations of motion using the QED approach for continuous wave laser irradiation of atoms are derived in this chapter. The derivation will follow in the same method as [81–84]. The equations are derived using the Heisenberg formulation, where the operators are chosen to evolve in time. The Hamiltonian of the laser-atom system is hence given by

$$H = H_{\text{Atom}} + H_{\text{Field}} + H_{\text{Int}} \quad (2.17)$$

where H_{Atom} describes the atom evolving freely over time

$$H_{\text{Atom}} |i\rangle = \hbar\omega_i |i\rangle. \quad (2.18)$$

Here $\hbar\omega_i$ is the energy of the i 'th level. By applying the closure theorem $\sum_i |i\rangle \langle i| = 1$ [85] twice to equation 2.18, H_{Atom} can be written as

$$H_{\text{Atom}} = \sum_i |i\rangle \langle i| H_{\text{Atom}} \sum_j |j\rangle \langle j|. \quad (2.19)$$

Equation 2.19 can be simplified by applying the orthonormality condition $\langle i| H_{\text{Atom}} |j\rangle = \hbar\omega_i \delta_{ij}$, where δ_{ij} is the Kronecker delta, resulting in

$$H_{\text{Atom}} = \sum_i \hbar\omega_i |i\rangle \langle i|. \quad (2.20)$$

The Hamiltonian for the field is represented quantum mechanically by

$$H_{\text{Field}} = \sum_q \hbar\omega_q a_q^\dagger a_q, \quad (2.21)$$

where a_q^\dagger, a_q are the creation and annihilation operators for the mode q of the field, with q representing both the wave vector and its polarisation. The interaction Hamiltonian [85] is expressed in normal ordering [86] as

$$H_{\text{Int}} = \hbar \sum_{e'g'q'} g_{e'g'q'}^{q'} \hat{\sigma}_{e'g'} a_{q'} e^{ik_{q'}z} + g_{e'g'q'}^{q'*} a_{q'}^\dagger e^{-ik_{q'}z} \hat{\sigma}_{g'e'}, \quad (2.22)$$

where

$$g_{e'g'q'}^{q'} = i \sqrt{\frac{\omega_{q'}}{2\epsilon_0 \hbar V}} \hat{\mathbf{e}}_{q'} \cdot \mathbf{D}_{e'g'} \quad (2.23)$$

is a coupling coefficient between the mode of the laser field and the lower atomic state $|g'\rangle$ and upper state $|e'\rangle$. V is the mode volume, $\mathbf{D}_{e'g'}$ is the dipole moment, and $\hat{\mathbf{e}}_{q'}$ is the polarisation unit vector. The atomic operators between laser-coupled states are defined by the outer product between the atomic states so that

$$\hat{\sigma}_{eg} = |e\rangle \langle g|, \quad (2.24)$$

where $|g\rangle$ represents the manifold of all lower states of the system and $|e\rangle$ represents the manifold of upper states that are coupled to $|g\rangle$ by the laser. The atomic operators evolve over time using the Liouville equation [87]

$$\begin{aligned} \frac{d\hat{\sigma}_{eg}}{dt} &= -\frac{i}{\hbar} [\hat{\sigma}_{eg}, H] \\ &= -\frac{i}{\hbar} [\hat{\sigma}_{eg}, H_{\text{Atom}}] - \frac{i}{\hbar} [\hat{\sigma}_{eg}, H_{\text{Int}}]. \end{aligned} \quad (2.25)$$

H_{Field} does not contribute here as it commutes with the atomic operator. The first term in equation 2.25 can be simplified using the orthonormality relations $\langle e|e\rangle = \langle g|g\rangle = 1$ and $\langle e|g\rangle = \langle g|e\rangle = 0$ so that

$$-\frac{i}{\hbar}[\hat{\sigma}_{eg}, H_{\text{Atom}}] = -i(\omega_g - \omega_e) |e\rangle \langle g|. \quad (2.26)$$

The second term in equation 2.25 can be expanded using equation 2.22 so that

$$-\frac{i}{\hbar}[\hat{\sigma}_{eg}, H_{\text{Int}}] = -i \sum_{e'q'} g_{e'g}^{q'*} a_{q'}^\dagger(t) e^{-ik_{q'}z} \hat{\sigma}_{ee'} + i \sum_{g'q'} g_{e'g}^{q'*} a_{q'}^\dagger e^{-ik_{q'}z} \hat{\sigma}_{gg'}. \quad (2.27)$$

As the time evolution of the annihilation and creation operators depends on the field coupling to the atomic states, the time evolution of $a_{q'}$ is explicitly derived from the Heisenberg equation of motion for operators [81]

$$\begin{aligned} \frac{da_{q'}}{dt} &= -\frac{i}{\hbar}[a_{q'}, H] \\ &= -\frac{i}{\hbar}[a_{q'}, H_{\text{Field}}] - \frac{i}{\hbar}[a_{q'}, H_{\text{Int}}], \end{aligned} \quad (2.28)$$

where the commutation relation $[a_{q'}, H_{\text{Atom}}] = 0$ has been used to simplify. This equation consists of the first field term and the second interaction term. Equation 2.21 can be used to rewrite the field term in equation 2.28 as

$$\begin{aligned} -\frac{i}{\hbar}[a_{q'}, H_{\text{Field}}] &= -\frac{i}{\hbar} \left[a_{q'} \left(\sum_{q''} \hbar\omega_{q''} a_{q''}^\dagger a_{q''} \right) - \left(\sum_{q''} \hbar\omega_{q''} a_{q''}^\dagger a_{q''} \right) a_{q'} \right] \\ &= -i\omega_{q'} a_{q'}, \end{aligned} \quad (2.29)$$

where the bosonic commutation relation $[a_{q'}, a_{q''}^\dagger] = \delta_{q'q''}$ is used to simplify [85]. By using equation 2.22, the interaction term in equation 2.28 can be rewritten as

$$\begin{aligned} -\frac{i}{\hbar}[a_{q'}, H_{\text{Int}}] &= -\frac{i}{\hbar} \left[a_{q'} \hbar \sum_{e''g''q''} (g_{e''g''}^{q''*} \hat{\sigma}_{e''g''} a_{q''} e^{ik_{q''}z} + g_{e''g''}^{q''*} a_{q''}^\dagger \hat{\sigma}_{g''e''} e^{-ik_{q''}z}) \right] \\ &\quad + \frac{i}{\hbar} \left[\hbar \sum_{e''g''q''} ((g_{e''g''}^{q''*} \hat{\sigma}_{e''g''} a_{q''}) e^{ik_{q''}z} + g_{e''g''}^{q''*} a_{q''}^\dagger \hat{\sigma}_{g''e''} e^{-ik_{q''}z}) \right] a_{q'} \\ &= -i \left(\sum_{e''g''q''} (g_{e''g''}^{q''*} [a_{q'}, \hat{\sigma}_{e''g''} a_{q''}] e^{ik_{q''}z} + g_{e''g''}^{q''*} [a_{q'}, a_{q''}^\dagger \hat{\sigma}_{g''e''}] e^{ik_{q''}z}) \right). \end{aligned} \quad (2.30)$$

Using the commutation relations $[a_{q''}, \hat{\sigma}_{e''g''}] = 0$, $[a_{q'}, a_{q''}] = 0$, equation 2.30 can be simplified as

$$\begin{aligned} -\frac{i}{\hbar}[a_{q'}, H_{\text{Int}}] &= -i \sum_{e''g''q''} g_{e''g''}^{q''*} \underbrace{[a_{q'}, a_{q''}^\dagger]}_{\delta_{q'q''}} \hat{\sigma}_{g''e''} + a_{q''}^\dagger \underbrace{[a_{q'}, \hat{\sigma}_{g''e''}]}_0 e^{-ik_{q''}z} \\ &= -i \sum_{e''g''} g_{e''g''}^{q''*} \hat{\sigma}_{g''e''} e^{-ik_{q''}z}. \end{aligned} \quad (2.31)$$

Now, using equations 2.29 and 2.31, equation 2.28 can be written as

$$\frac{da_{q'}}{dt} = -i\omega_{q'}a_{q'} - i \sum_{e''g''} g_{e''g''}^{q'*} \hat{\sigma}_{g''e''} e^{-ik_{q''}z}. \quad (2.32)$$

Multiplication of equation 2.32 by the integrating factor $e^{-i\omega_{q'}t}$ yields the solution

$$a_{q'}(t) = a_{q'}(0)e^{-i\omega_{q'}t} - i \sum_{e''g''} g_{e''g''}^{q'*} e^{-ik_{q'}z} \int_0^t \hat{\sigma}_{g''e''}(t') e^{-i\omega_{q'}(t-t')} dt', \quad (2.33)$$

where the boundary condition $\sigma_{g''e''}(t=0) = 0$ is used. The Hermitian conjugate of equation 2.33 is hence given by

$$a_{q'}^\dagger(t) = a_{q'}^\dagger(0)e^{i\omega_{q'}t} + i \sum_{e''g''} g_{e''g''}^{q'} e^{ik_{q'}z} \int_0^t \hat{\sigma}_{e''g''}(t') e^{i\omega_{q'}(t-t')} dt'. \quad (2.34)$$

To continue with the derivation, the harmonic approximation must be discussed where the atomic operator can be removed from the integral [88]

$$\sum_{q'} \int_0^t \hat{\sigma}_{e''g''}(t') e^{i\omega_{q'}(t-t')} dt' \approx \sum_q \hat{\sigma}_{e''g''}(t) \int_0^t e^{i\omega_{q'}(t-t')} dt'. \quad (2.35)$$

This approximation is valid in equation 2.35 as the exponential inside the integral is oscillating at light frequency $\omega_{q'}$ and the sum runs over all frequency modes q' so we can assume destructive interference after a few optical periods. Thus, only the values of t' close to t will make a significant contribution to the integral. The effects of the atomic operator interacting with the field, such as spontaneous emission, are much longer than the optical period so we can assume that the atomic operator is constant over the time interval being integrated over and can be taken outside of the integral. The time evolution of the atomic operator is then given by

$$\begin{aligned} \frac{d\hat{\sigma}_{eg}}{dt} &= -\frac{i}{\hbar} [\hat{\sigma}_{eg}, H_{\text{Atom}}] \\ &= -i(\omega_g - \omega_e)\hat{\sigma}_{eg}. \end{aligned} \quad (2.36)$$

Integrating 2.36 between t' and t yields

$$\hat{\sigma}_{eg}(t') = \hat{\sigma}_{eg}(t) e^{i(\omega_g - \omega_e)(t-t')}. \quad (2.37)$$

Now, equation 2.34 can be substituted into equation 2.27 and the harmonic approximation can be used to yield

$$\begin{aligned} -\frac{i}{\hbar} [\hat{\sigma}_{eg}, H_{\text{Int}}] &= -i \sum_{q'e'} g_{e'g}^{q'*} a_{q'}^\dagger(0) e^{i(\omega_{q'}t - k_{q'}z)} \hat{\sigma}_{e'e'} \\ &+ \sum_{q'e'e''g''} \left(g_{e'g}^{q'*} g_{e''g''}^{q'} \hat{\sigma}_{e''g''} \int_0^t e^{i(\omega_{q'} - \omega_{e''} + \omega_{g''}(t-t'))} dt' \right) \hat{\sigma}_{e'e'} \\ &+ i \sum_{q'g'} g_{eg'}^{q'} a_{q'}^\dagger(0) e^{i\omega_{q'}t - k_{q'}z} \hat{\sigma}_{g'g} \\ &- \sum_{q'g'e''g''} \left(g_{eg'}^{q'*} g_{e''g''}^{q'} \hat{\sigma}_{e''g''} \int_0^t e^{i(\omega_{q'} - \omega_{e''} + \omega_{g''}(t-t'))} dt' \right) \hat{\sigma}_{g'g}. \end{aligned} \quad (2.38)$$

The term in equation 2.38 can be solved directly as

$$\int_0^t e^{i(\omega_{q'} - \omega_{e''} + \omega_{g''})(t-t')} dt' = i \left(\frac{1 - \cos[(\omega_{q'} - \omega_{e''} + \omega_{g''})t]}{\omega_{q'} - \omega_{e''} + \omega_{g''}} \right) + \frac{\sin[(\omega_{q'} - \omega_{e''} + \omega_{g''})t]}{\omega_{q'} - \omega_{e''} + \omega_{g''}}. \quad (2.39)$$

This integral term can be simplified for time periods much larger than the inverse of oscillation frequency $t \rightarrow \infty$ and when the laser frequency $\omega_{q'}$ is close to the transition frequency $\omega_{e''} - \omega_{g''}$ [85, 86]

$$\lim_{\omega_{q'} - \omega_{e''} + \omega_{g''} \rightarrow 0} \left(\lim_{t \rightarrow \infty} i \left(\frac{1 - \cos[(\omega_{q'} - \omega_{e''} + \omega_{g''})t]}{\omega_{q'} - \omega_{e''} + \omega_{g''}} \right) \right) = 0 \quad (2.40)$$

$$\lim_{\omega_{q'} - \omega_{e''} + \omega_{g''} \rightarrow 0} \left(\lim_{t \rightarrow \infty} \left(\frac{\sin[(\omega_{q'} - \omega_{e''} + \omega_{g''})t]}{\omega_{q'} - \omega_{e''} + \omega_{g''}} \right) \right) = \pi \delta(\omega_{q'} - \omega_{e''} + \omega_{g''}), \quad (2.41)$$

where $\delta(\omega_{q'} - \omega_{e''} + \omega_{g''})$ is the Dirac delta function. The time evolution of the atomic operator can hence be written as

$$\begin{aligned} \frac{d\hat{\sigma}_{eg}}{dt} &= -i(\omega_g - \omega_e)\hat{\sigma}_{eg} \\ &\quad - i \sum_{q'e'} g_{e'g}^{q'} a_{q'}^\dagger(0) e^{i(\omega_{q'} t - k_{q'} z)} \hat{\sigma}_{e'e'} \\ &\quad + i \sum_{q'g} g_{eg}^{q'*} a_{q'}^\dagger(0) e^{i(\omega_{q'} t - k_{q'} z)} \hat{\sigma}_{g'g} \\ &\quad - \sum_{q'g'e'} g_{eg}^{q'*} g_{e'g}^{q'} \hat{\sigma}_{e'g} \pi \delta(\omega_{q'} - \omega_{e'} + \omega_{g'}). \end{aligned} \quad (2.42)$$

Equation 2.42 contains rapidly oscillating terms at the frequency of the driving radiation. In many experiments these cannot be measured, and so the rotating wave approximation (RWA) [88] is adopted. For a single mode continuous wave laser beam driving the transition, the RWA transforms the atomic operators into slowly varying operators $\hat{\chi}_{eg}$, by setting

$$\hat{\sigma}_{eg} = \hat{\chi}_{eg} e^{i(\omega_L t - k_L z)} \quad (2.43)$$

$$\hat{\sigma}_{gg'} = \hat{\chi}_{gg'} \quad (2.44)$$

$$\hat{\sigma}_{ee'} = \hat{\chi}_{ee'}, \quad (2.45)$$

where ω_L is the laser frequency and k_L is the associated wave vector. Equation 2.42 is hence transformed to slowly varying operators using equation 2.43. Expectation values are then taken, so that

$$\begin{aligned} \langle \dot{\hat{\chi}}_{eg} \rangle &= -i(\omega_L - k_L \dot{z} - \omega_{eg}) \langle \hat{\chi}_{eg} \rangle \\ &\quad - i \sum_{Le'} g_{e'g}^{L*} \langle a_L^\dagger(0) \rangle \langle \hat{\chi}_{ee'} \rangle \\ &\quad + i \sum_{Lg'} g_{eg}^{L*} \langle a_L^\dagger(0) \rangle \langle \hat{\chi}_{g'g} \rangle \\ &\quad - \sum_{qg'e'} g_{eg}^{q*} g_{e'g}^q \langle \hat{\chi}_{e'g} \rangle \pi \delta(\omega_L - \omega_{e'} + \omega_{g'}). \end{aligned} \quad (2.46)$$

The slowly varying operators are directly related to the density matrix elements ρ_{eg} that are commonly used to describe the populations and coherences of an atomic system, since

$$\langle \hat{\chi}_{eg} \rangle = \langle \psi | e \rangle \langle g | \psi \rangle = (\langle e | \psi \rangle \langle \psi | g \rangle)^* = (\rho_{eg})^* = \rho_{ge}. \quad (2.47)$$

The half-Rabi frequency is input to equation 2.46 using the relation [81]

$$\Omega_{eg}^L = g_{eg}^{L*} \langle \hat{a}_L^\dagger(0) \rangle. \quad (2.48)$$

Physically, the half-Rabi frequency is half of the oscillation frequency between the populations of the excited and ground laser-coupled states. This is set to be real by an appropriate choice of phase [81].

The time evolution of $\langle \hat{\chi}_{gg''} \rangle$ and $\langle \hat{\chi}_{ee''} \rangle$ can be derived in an identical way to that of $\langle \hat{\chi}_{eg} \rangle$ in equation 2.46. These can then be written in the density matrix formalism using equation 2.47. The general equations of motion for the populations, optical and atomic coherences are then given by:

$$\begin{aligned} \dot{\rho}_{gg''} = & -i\Delta_{gg''}\rho_{gg''} + i\sum_{Le}(\Omega_{eg''}^L\rho_{ge} - \Omega_{eg}^L\rho_{eg''}) \\ & + \sum_{qe'e''} g_{e'g''}^q g_{e''g}^{q*} \pi \delta(\omega_q - \Delta_{e''g}) \rho_{e'e''} \\ & + \sum_{qe'e''} g_{e''g''}^q g_{e'g}^{q*} \pi \delta(\omega_q - \Delta_{e''g''}) \rho_{e'e''} \end{aligned} \quad (2.49)$$

$$\begin{aligned} \dot{\rho}_{ee''} = & -i\Delta_{ee''}\rho_{ee''} + i\sum_{Lg}(\Omega_{e''g}^L\rho_{eg} - \Omega_{eg}^L\rho_{ge''}) \\ & - \sum_{qg'e'} g_{eg'}^q g_{e'g''}^{q*} \pi \delta(\omega_q - \Delta_{e'g'}) \rho_{e'e''} \\ & - \sum_{qg'e'} g_{e'g'}^q g_{e''g''}^{q*} \pi \delta(\omega_q - \Delta_{e'g'}) \rho_{ee'} \end{aligned} \quad (2.50)$$

$$\begin{aligned} \dot{\rho}_{ge} = & -i\Delta_{L,eg}\rho_{ge} - i\sum_{Le'}\Omega_{e'g}^L\rho_{e'e} + i\sum_{Lg'}\Omega_{eg'}^L\rho_{gg'} \\ & - \sum_{qg'e'} g_{e'g'}^q g_{eg'}^{q*} \pi \delta(\omega_q - \Delta_{e'g'}) \rho_{ge'} \end{aligned} \quad (2.51)$$

with $\dot{\rho}_{eg}$ given by the complex conjugate of equation 2.51.

The population equations for the lower and upper states are derived by setting $g = g'$ and $e = e'$ respectively in equations 2.49 and 2.50. The atomic coherence equations (which describe the phase relationship between sub-states in each manifold) are formulated by setting $g \neq g'$ and $e \neq e'$ in these equations. The optical and non-optical terms between the lower and upper states manifolds are described by equation 2.51. This equation hence is used to derive both the optical coherence terms generated directly by the laser, as well as the atomic coherence terms generated between upper and lower states. The term

$$\Delta_{L,eg} = \omega_L - \frac{2\pi v_z}{\lambda_L} + \omega_e - \omega_g \quad (2.52)$$

is the detuning from resonance, where v_z is the velocity component of the atoms in the direction of the laser beam (which gives rise to the Doppler shift). λ_L is the wavelength of the laser mode L . The term $\Delta_{eg} = \omega_e - \omega_g$, whereas $\Delta_{gg'} = \omega_g - \omega_{g'}$ and $\Delta_{ee'} = \omega_e - \omega_{e'}$. The half-Rabi frequency can be calculated in rad/s using the expression

$$\Omega_{eg}^q = C_{eg}^q \sqrt{\frac{3\lambda_L^3 I_L}{8\pi\hbar c\tau}} = C_{eg}^q \Omega, \quad (2.53)$$

where τ is the lifetime of the transition, I_L is the laser intensity, Ω is the maximum value of the Rabi frequency, and C_{eg}^q is a coupling coefficient given by [89]

$$\begin{aligned} C_{eg}^q &= (-1)^{\frac{q(1+q)}{2} + F' + F + J' + J + I' + L' + S' - m'_F + 1} \\ &\times \sqrt{(2F' + 1)(2F + 1)(2J' + 1)(2J + 1)(2L' + 1)} \\ &\times \begin{pmatrix} F' & 1 & F \\ -m'_F & q & m_F \end{pmatrix} \begin{Bmatrix} J' & F' & I' \\ F & J & 1 \end{Bmatrix} \begin{Bmatrix} L' & J' & S' \\ J & L & 1 \end{Bmatrix}, \end{aligned} \quad (2.54)$$

where L, S, J, I , and F are the quantum numbers describing the lower states $|g\rangle$ and their primed equivalents are the quantum numbers describing the upper states $|e\rangle$. Here, the (\dots) term describes a Wigner-3j symbol and $\{\dots\}$ describes a Wigner-6j symbol. C_{eg}^q always has a value between 0 and 1 and q is set to be either +1, 0, or -1 for RHC laser polarisation, linear laser polarisation, or LHC laser polarisation respectively. A full derivation of the half-Rabi frequency and the coupling coefficients can be seen in appendix A.2.

The triple summations in equations 2.49, 2.50, and 2.51 describe spontaneous emission. They produce decay of the atomic excitation even if there is no driving laser field. These terms can be calculated by relating them to the generalised decay rate given in [81]

$$\Gamma_{ege'g'} = \sum_q [g_{eg'g}^q g_{e'g}^{q*} \pi \delta(\omega_q - \Delta_{e'g'}) + g_{e'g'}^q g_{eg}^{q*} \pi \delta(\omega_q - \Delta_{eg})]. \quad (2.55)$$

Equation 2.55 is then used to derive the decay rate between an excited substate $|e\rangle$ to a lower substate $|g\rangle$ with

$$\Gamma_{eg} = \Gamma_{egeg} = 2 \sum_q |g_{eg}^q|^2 \pi \delta(\omega_q - \Delta_{eg}). \quad (2.56)$$

The total decay rate of state $|e\rangle$ is then given by

$$\Gamma_e = \sum_g \Gamma_{eg}. \quad (2.57)$$

The transition probability for spontaneous emission is proportional to the square of the dipole matrix element and so the decay constants Γ_{eg} can be calculated using

$$\Gamma_{eg} = \frac{(\Omega_{eg})^2}{\sum_{g'} (\Omega_{eg'})^2} \Gamma_e = \frac{|C_{eg}^q|^2}{\tau \sum_{g'} |C_{eg'}^q|^2}, \quad (2.58)$$

where the summation in the denominator is over all coupled ground states and τ is the lifetime of the excited state. Here, q is the required polarisation for the decay from $|e\rangle$ to $|g\rangle$.

2.3 LASED: A Laser-Atom Interaction Simulator

2.3.1 Introduction

Deriving the equations of motion by hand and solving the laser-atom interaction is time-intensive, complex, and is prone to mistakes. As an example, for transitions with hyperfine structure such as excitation of the Cs $6^2S_{1/2}$ state to the $6^2P_{3/2}$ state, a total of 48 individual substates are involved in the interaction. There are hence 2304 coupled differential equations that must be generated and solved simultaneously to fully characterise the dynamics of the system. A computational method of systematically generating and solving these equations is hence advantageous, so that the time evolution of the populations, optical coherences and the atomic coherences can be obtained.

This section presents an open-source python package that solves this problem: a laser-atom interaction simulator derived from quantum electrodynamics ([LASED](#)). LASED allows a user to automatically set up a laser-atom system and generate all the equations of motion for that system. The package then solves the dynamics of the system over a given time, outputting the evolution of all lower and upper state populations, their atomic coherences and the optical coherence terms that couple the states together. LASED can also model the system using laser beams that have different polarisations. It can model a rotation of the frame of reference of the system both prior to the interaction, as well as after the laser interaction has occurred. This rotation technique can simplify the calculation, thereby reducing the time required for computation. LASED can further include integration over the Gaussian profile of the laser beam (assuming a TEM₀₀ beam) and also allows integration over the Doppler profile of an atomic beam, should this be required for the experiment that is being modelled. The angular ‘shape’ of the electron charge cloud for both excited and lower atomic states can also be modelled and plotted as the system evolves over time.

LASED has been developed to describe scattering experiments which combine laser interactions with electron collisions and that use an atomic beam [71, 81, 90]. It is designed to be easy-to-use and has comprehensive online documentation (available in [91]) to aid users in creating the required laser-atom system they wish to model. This documentation also demonstrates how to run simulations by solving examples of the differential equations automatically generated by LASED. Details on how to install LASED can be found in this documentation and in appendix B.1.

In sections 2.3.2 to 2.3.7, the computational method for generating the coupled differential equations to solve the time evolution of the laser-atom system is discussed. This section also shows how averaging over the Gaussian and Doppler profiles is approximated, and it details how the reference frame is rotated. The method used to model a general polarisation state of the laser is also described.

Section 2.3.8 demonstrates the outcome from the model for three selected targets. In the first example excitation of calcium from the ground $4S$ state to the $4P$ state is discussed, since this is one of the simplest systems that can be solved. These results are presented for both linear and elliptic excitation, and includes integration over both Doppler and

Gaussian profiles. An example of the technique of rotating the frame of reference is then discussed, with the calcium target again being used. In the second example, laser excitation of helium initially excited by electron impact to a D -state is presented. This is a considerably more complex problem to solve, since the lower state is then in a coherent superposition of substates due to the collision, as has been discussed in section 2.1. Both the populations and atomic coherences are hence non-zero prior to laser excitation and these must be included as initial conditions. Finally, a discussion of laser excitation of the Cs atom from the ground state via the D_2 transition is presented for circular excitation, as would be used in a Magneto Optical Trap (MOT) [92].

2.3.2 Computation of the Time Evolution

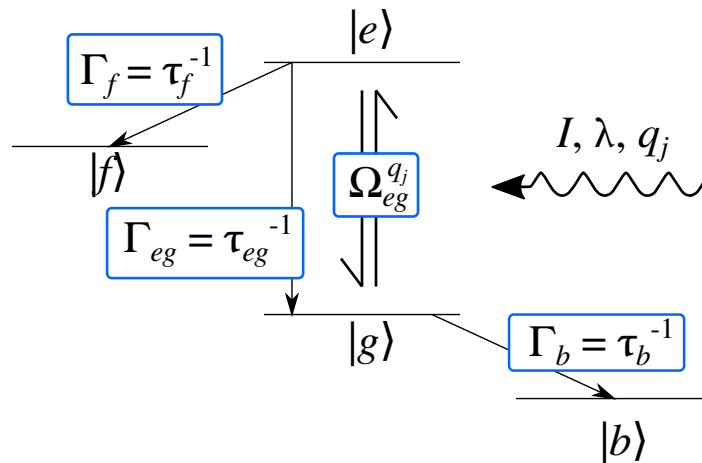


Figure 2.2: The model of a general laser-atom system as used by LASED. The laser excites lower state $|g\rangle$ to the excited state $|e\rangle$. The half-Rabi frequency $\Omega_{eg}^{q_j}$ couples these states, where q_j is the polarisation of the incoming laser radiation with intensity I and wavelength λ . The index j denotes that the incoming laser can be in a superposition of multiple polarisations in this model. The decays to states $|f\rangle$ and $|b\rangle$, which may exist but are not directly coupled by the laser, can also be included in the model. For details see the text.

LASED enables a user to define a general atomic system by creating the states and substates of the atom that are coupled by the laser. Their relative energy separation, angular momenta, and the projection of the total angular momentum associated with each state are also input to the model as initial parameters. The substates are labelled as either an upper state $|e\rangle$ or a lower state $|g\rangle$, as shown in figure 2.2. The resonant transition laser wavelength between upper and lower states is defined as λ . The user then enters the laser parameters by defining the laser polarisation q and the intensity I . This sets up the initial laser-atom system to be solved. The time steps t_i over which the simulation is run is also defined before the system evolves. At the initial time step $t = t_0$ the laser is turned on.

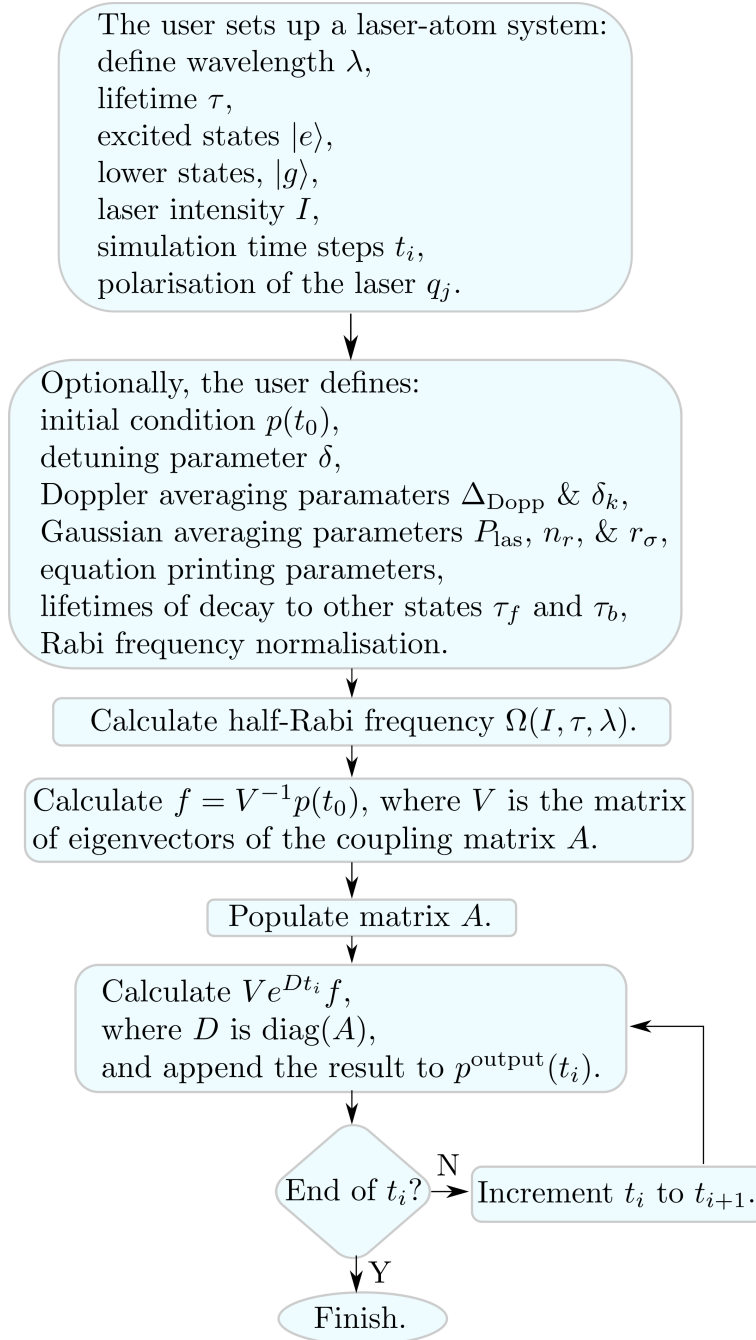


Figure 2.3: A flowchart of the algorithm used to compute the time evolution of a laser-atom system in LASED. See the text for details.

The process of setting up a laser-atom system and finding the solutions to the equations of motion is outlined in figure 2.3. To solve the user-defined laser-atom system, equations 2.49, 2.50 and 2.51 are used to automatically generate the complete set of coupled differential equations which are solved numerically. LASED uses a matrix method by writing the equations in the form

$$\dot{p} = Ap(t) \quad (2.59)$$

where p is a column vector containing all the populations and coherences defined within the density matrix for the coupled system i.e. a flattened density matrix. The density matrix has n^2 elements, where n is the number of substates in the system. p is hence

a column vector of n^2 elements. A is an $n^2 \times n^2$ coupling matrix that contains all of the coefficients of the interaction. This includes all half-Rabi frequencies generated from equation 2.53, the detuning terms and all decay constants. The matrix A can become very large, and so to reduce computation time equation 2.59 is solved by diagonalising the matrix and calculating the eigenvectors and eigenvalues. The solution of p using this technique then gives

$$p(t) = V e^{Dt} V^{-1} p(t_0) \quad (2.60)$$

where $A = V D V^{-1}$, D is the diagonalised form of A that contains the complex eigenvalues, and V is the matrix of eigenvectors of A . All real terms in the eigenvalues generated by the calculation must be negative for the solutions to converge. The initial condition $p(t_0)$ can be defined by the user when setting up the laser-atom system. If the initial conditions are not defined by the user, it is assumed that all lower substates have equal populations and that all atomic coherences are identically zero prior to the laser being turned on as would occur if the atomic beam was generated from an oven or from a gas jet, such as in the experiments presented in chapter 8.

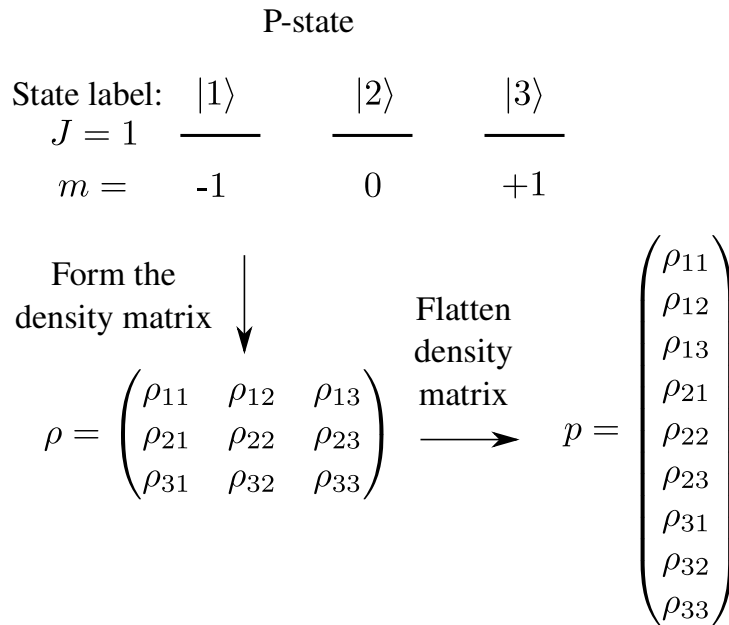


Figure 2.4: The conventional representation of a P-state in LASED with $|Jm\rangle$ eigenstate labels $|1, -1\rangle = |1\rangle$, $|1, 0\rangle = |2\rangle$, $|1, +1\rangle = |3\rangle$. The P-state density matrix ρ is flattened to column vector p .

Using this matrix method requires the populations and coherences to be in a strict order within p . The user hence has to define the substate with a number that labels it, e.g. $|1\rangle$, $|2\rangle$, and $|3\rangle$ for a lower P -state with $m = -1, 0, +1$ respectively, as shown in figure 2.4. The convention used throughout LASED is that the first element in the vector p is the element ρ_{11} , which is the lower state population with the lowest projection of angular momentum $-m_F$. The labelling continues until the excited substate population with the largest projection of total angular momentum $+m_F$ is set to be the n^{th} substate. The vector p would hence have the form: $[\rho_{11} \ \rho_{12} \ \dots \ \rho_{1n}, \ \rho_{21} \ \rho_{22} \ \dots \ \rho_{2n}, \ \rho_{n1} \ \rho_{n2} \ \dots \ \rho_{nn}]$. The matrix A is then populated using the coefficients generated using equations 2.49 to 2.51.

These can be modified to give a set of equations with computable variables:

$$\begin{aligned}\dot{\rho}_{gg''} = & -\left(i\Delta_{gg''} + \frac{1}{\tau_b}\right)\rho_{gg''} \\ & + i\Omega \sum_{qe} (C_{eg''}^q \rho_{ge} - C_{eg}^q \rho_{eg''}) \\ & + \frac{1}{2\tau} \sum_{qe'e''} \gamma_{e'e''}^q \rho_{e''e'} + \gamma_{e''e'}^q \rho_{e'e''}\end{aligned}\quad (2.61)$$

$$\begin{aligned}\dot{\rho}_{ee''} = & -\left(i\Delta_{ee''} + \frac{1}{\tau} + \frac{1}{\tau_f}\right)\rho_{ee''} \\ & + i\Omega \sum_{qg} (C_{e''g}^q \rho_{eg} - C_{eg}^q \rho_{ge''})\end{aligned}\quad (2.62)$$

$$\begin{aligned}\dot{\rho}_{ge} = & -i\left(\Delta_{eg}^q + \delta + \frac{1}{2\tau} + \frac{1}{2\tau_f} + \frac{1}{2\tau_b}\right)\rho_{ge} \\ & - i\Omega \sum_{qe'} C_{e'g}^q \rho_{e'e} + i\Omega \sum_{qg'} C_{eg'}^q \rho_{gg'}.\end{aligned}\quad (2.63)$$

The decay constants in $\dot{\rho}_{gg''}$ are contained in the term

$$\gamma_{e'e''}^q = \begin{cases} \frac{|C_{e'g''}^q C_{e''g}^q|}{\sum_{g'} |C_{e''g'}^q C_{e'g'}^q|}, & \text{if } e' = e'' \\ \Gamma_{e'ge''g}, & \text{if } e' \neq e'' \text{ AND } \sum_q C_{e'g}^q C_{e''g}^q \neq 0, \end{cases}\quad (2.64)$$

where the sum over q is the sum of all values over which spontaneous emission can occur: +1, 0, and -1. The second case in equation 2.64 only appears when there is hyperfine splitting leading to vertical coherences [81].

The calculation of the generalized decay constants and their phase relationships is shown in appendix A.1. The coupling coefficients are calculated using equation 2.54 and the maximum half-Rabi frequency Ω is calculated as defined in equation 2.53. The detuning term is calculated using equation 2.52 as discussed in section 2.2. The laser-atom system modelled using equations 2.61 to 2.63 are more general than the system modelled using equations 2.49 to 2.51 as these also include extra decay terms that describe the process of relaxation to states which are not directly coupled by the laser, as shown in figure 2.2. These include states that $|e\rangle$ and $|g\rangle$ may decay to that are not included in equations 2.49 to 2.51, as well as any non-radiative decay routes that may occur. The decay from a laser-excited state $|e\rangle$ to a non-coupled state $|f\rangle$ is modelled by the lifetime τ_f and the decay from a lower state $|g\rangle$ to a non-coupled state $|b\rangle$ is modelled by the lifetime τ_b . Equation 2.63 also includes a detuning term δ , which allows the user to add a constant detuning from resonance if required (e.g. for laser-cooling of atoms).

Whilst the matrix A is being generated, the equations of motion can be printed out in a numeric or symbolic format depending on the user's preference. The Sympy package [93] is used to generate the symbolic equations, which can be output as LaTeX.

Once the matrix A has been generated, the NumPy package [94] is used to diagonalise the matrix to form D . NumPy is also used to perform all matrix multiplication in LASED. The SciPy package [95] is used to generate the matrix of eigenvectors V from A and is also used in LASED to perform matrix exponentials and the inversion of matrices. For every element of the time array t_i , the column vector $p(t)$ of the laser-atom system is calculated numerically. Before looping over every element in t_i , $V^{-1}p(t_0)$ is calculated to save computation time. During the loop over t_i , the matrix exponential e^{Dt} is calculated by taking the exponent of each diagonal element of Dt . Finally, $\rho(t)$ is calculated using equation 2.60. Once the calculation of the time evolution is completed, the user can access any element of $p(t)$ for analysis, the data can be saved as a csv file, or it can be plotted.

2.3.3 Gaussian Laser Beam Profile

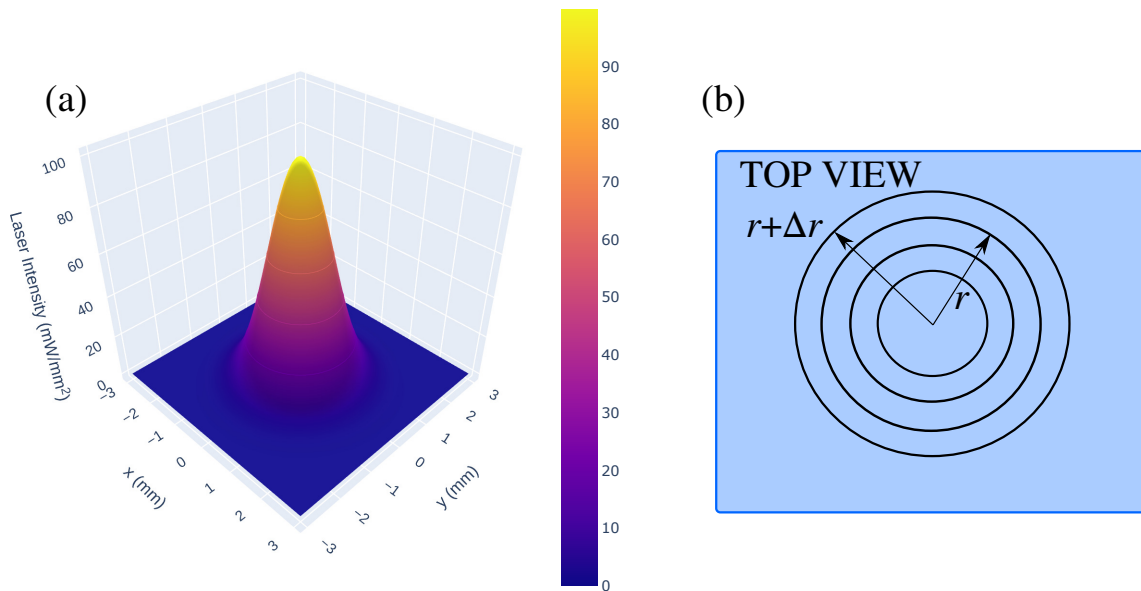


Figure 2.5: (a) A Gaussian laser beam profile with a 2D standard deviation of 0.75 mm and a peak intensity of 100 mW/mm². (b) A top-view of the laser beam profile split into concentric rings of radius r and distance between each ring Δr (see equation 2.68). The time evolution of a laser-atom system is calculated for atoms in each ring and then summed to model the effects of a Gaussian beam profile. A user defines the number of rings which split the laser beam profile, with an increasing number of rings giving higher accuracy but increased computational time.

When a laser-atom system is modelled in LASED the default setting is that the spatial intensity profile of the laser beam is uniform. The user can however also specify a two-dimensional (2D) Gaussian laser beam profile, so as to emulate a TEM₀₀ mode [96]. For a Gaussian beam the intensity as a function of the radial distance from its beam axis r is given by

$$I(r) = I_0 e^{-\frac{r^2}{2r_\sigma^2}}, \quad (2.65)$$

where I_0 is the intensity at the peak $r = 0$ and r_σ is the radial distance equivalent to the 2D standard deviation. An example of a 2D Gaussian intensity profile with $I_0 = 100$ mW/mm² and $r_\sigma = 0.75$ mm is shown in figure 2.5(a). To obtain the total laser power

P_{las} as measured by a power meter, equation 2.65 is integrated so that

$$\begin{aligned} P_{\text{las}} &= \int_0^{\infty} 2\pi r I_0 e^{-\frac{r^2}{2r_\sigma^2}} dr \\ &= 2\pi r_\sigma^2 I_0. \end{aligned} \quad (2.66)$$

The intensity at any given radius is hence given by

$$I(r) = \frac{P_{\text{las}}}{2\pi r_\sigma^2} e^{-\frac{r^2}{2r_\sigma^2}}, \quad (2.67)$$

from which the equivalent Rabi frequency can be generated using equation 2.53. To model the effect of a Gaussian beam profile on the system, the beam profile is divided into a series of concentric rings, as shown in figure 2.5(b), with the populations and coherences generated for each ring then summed incoherently to obtain the total density matrix for the ensemble. LASED assumes that the atoms are uniformly distributed throughout the laser beam profile with a density given by ν_A and that the atoms are stationary during the interaction. Hence the number of atoms in any ring between r and $r + \Delta r$ is given by

$$N_A^{\Delta r} = \nu_A (2\pi r \Delta r h), \quad (2.68)$$

where the laser beam is assumed to be parallel through the interaction region, which has a height along the laser beam of h . Equation 2.68 then provides a weighting term to calculate the total number of atoms in the interaction region, up to a given radius. The laser beam diameter is approximated as $6r_\sigma$ ($\pm 3r_\sigma$) and so the total number of atoms in the interaction volume is given by

$$N_{\text{total}}^{6r_\sigma} = \int_0^{3r_\sigma} 2\pi \nu_A h r dr = 9\pi \nu_A h r_\sigma^2. \quad (2.69)$$

For n_r equal rings and a beam diameter of $6r_\sigma$ the ring radius will be $\Delta r = 3r_\sigma/n_r$. The density matrix elements can then be calculated for averaging over the Gaussian laser profile, by performing a discrete sum of all n_r rings and dividing by the total number of atoms:

$$\begin{aligned} p^{\text{av}}(I(r_\sigma), t) &= \frac{\sum_{j=0}^{n_r-1} \nu_A ((2j+1)\pi \Delta r^2 h) p(I(r_j, r_\sigma), t)}{9\pi \nu_A h r_\sigma^2} \\ &= \frac{\sum_{j=0}^{n_r-1} (2j+1) \left(\frac{9r_\sigma^2}{n_r^2}\right) p(I(r_j, r_\sigma), t)}{9r_\sigma^2} \\ &= \frac{1}{n_r^2} \sum_{j=0}^{n_r-1} (2j+1) p(I(r_j, r_\sigma), t) \\ &= \frac{1}{n_r^2} \sum_{j=0}^{n_r-1} (2j+1) p(\Omega(r_j, r_\sigma), t). \end{aligned} \quad (2.70)$$

The half-Rabi frequency is introduced in place of the intensity in equation 2.70 since this is what is required when combining equations 2.53 and 2.67. To model a Gaussian beam profile in LASED, the user must enter the number of rings n_r as well as the 2D standard deviation of the beam profile r_σ in millimetres. When performing the time evolution, an array of ring radii is created up to the maximum beam profile radius $3r_\sigma$. For each r_j in the array, the time evolution of the laser-atom system is calculated and then averaged as given by equation 2.70. A value of $n_r \approx 50$ gives reasonably precise simulation results, as seen in section 2.3.8.

2.3.4 Atomic Doppler Profile

LASED also includes a functionality to model the effect of the Doppler profile of atoms within the interaction region, as would occur in an atomic beam from an oven or gas jet. The Doppler profile of the atoms is input to the model as a detuning term δ in units of 10^9 rad/s. For numerical purposes the Doppler profile is again split up into discrete values across the profile and the density matrix elements are calculated for each detuning term. The results are then averaged in a similar way to that adopted for representation of a TEM₀₀ laser beam. This Doppler averaging requires a weighting factor of the atoms given by [97]

$$F_{\text{Dopp}}(\delta) = \frac{1}{\sqrt{2\pi\Delta_{\text{Dopp}}^2}} e^{-\frac{\delta^2}{2\Delta_{\text{Dopp}}^2}}, \quad (2.71)$$

where Δ_{Dopp} is the Doppler width. The averaged density matrix elements across the atomic Doppler profile are then given by

$$\begin{aligned} p^{\text{av}} &= \sum_i p(\delta_i) F_{\text{Dopp}}(\delta_i) \Delta\delta_i \\ &= \frac{1}{\sqrt{2\pi\Delta_{\text{Dopp}}^2}} \sum_i p(\delta_i) \Delta\delta_i e^{-\frac{\delta_i^2}{2\Delta_{\text{Dopp}}^2}}, \end{aligned} \quad (2.72)$$

where $\Delta\delta_i$ is the angular frequency spacing between the discrete detunings that are used to represent the Doppler profile. Hence, to model a Doppler profile using LASED the user must declare a value for the Doppler width and create an array which contains discrete detuning values. Equation 2.72 is then used to calculate the Doppler averaged density matrix elements for the system.

2.3.5 Rotation of the Frame of Reference

It is often advantageous to define an atomic system in a particular reference frame that makes the calculation easier, or that decreases the computation time. As an example, excitation by linearly polarised light can adopt a quantisation z-axis QA along the direction of the electric field vector, so that the change in m_F values between upper and lower substates is $\Delta m_F = 0$. An alternative and equally valid representation for linear excitation may choose the QA along the direction of the laser beam, in which case simultaneous $\Delta m_F = \pm 1$ excitation occurs. In the former case for an S to P transition, this leads to $n = 4$ differential equations that must be solved. By contrast, in the latter case, nine equations must be generated and then solved. Both calculations lead to the same results and can be related to each other using a suitable rotation from one frame to the other. Since the computational speed scales as n^2 , choosing the QA along the electric field vector in this example hence produces results more than 5 times faster than when the QA is chosen along the beam.

An example where the rotation technique has been adopted to simplify the calculation can be found in [98], where electron excited mercury atoms in the 6^1P_1 state were further excited by a laser beam to the 6^1D_2 state using linearly polarised light. In this case the

atomic system in the collision frame was first rotated into the natural frame along the electric field of the laser and the laser interaction was calculated in this new frame. The Natural and collision frames are as seen in figure 2.1. The resulting atomic system was then rotated back to the collision frame to determine the evolved atomic structure in that frame. This required 36 differential equations to be solved for the laser interaction, compared to 64 equations that would need to be generated and solved simultaneously if the calculation had been carried out directly in the collision frame. A further advantage of moving to the laser frame was that the 12 equations for the populations and optical coherences decoupled from the 24 equations for the non-optical and atomic coherences, so that the matrix A was block diagonal. This led to a 5.7 fold increase in computational efficiency.

It is not however always possible to apply this technique, since there may be constraints on the system due to additional interactions. An example is found in [61, 84], where an external magnetic \mathbf{B} -field was imposed on the system. In these experiments the \mathbf{B} -field direction was co-linear with the direction of the laser beam, and so the QA was chosen along this axis for excitation by both circular and linearly polarised laser beams, with the linear beam being considered as a superposition of right-hand and left-hand circularly polarised beams.

LASED can incorporate rotation between reference frames within its structure, so that these advantages can be exploited. The rotation is performed by rotating the density matrix for each atomic state using the Wigner rotation matrices [99], so that

$$\rho_{Jm,J'm'} = \sum_{\mu=-J}^{+J} \sum_{\mu'=-J'}^{+J'} D_{\mu m}^{J*}(\omega) \rho_{J\mu,J'\mu'} D_{\mu' m'}^{J'}(\omega) \quad (2.73)$$

where $\rho_{J\mu,J'\mu'}$ and $\rho_{Jm,J'm'}$ are the atomic state density matrix elements in the new and old reference frame respectively, J is the total angular momentum of the state (which will be F if there is non-zero isospin), m is the projection of angular momentum onto the QA, and ω denotes the Euler angles for the rotation (α, β, γ) . In LASED, the Euler angles are defined as three angles of rotation performed in succession from Cartesian reference frame Z to Z' , and then to a final Z'' . α then rotates around the z -axis, β rotates around the new y' -axis, and γ finally rotates around the new z'' -axis. The Wigner-D matrix is calculated using [100]

$$D_{m'm}^J(\omega) = e^{-im'\alpha} d_{m'm}^J(\beta) e^{-im\gamma}, \quad (2.74)$$

where d is determined using

$$\begin{aligned} d_{m'm}^J(\beta) &= \sqrt{(J+m')!(J-m')!(J+m)!(J-m)!} \\ &\times \sum_{s=s_{\min}}^{s_{\max}} \frac{(-1)^{m'-m+s} \left(\frac{\cos\beta}{2}\right)^{2J+m-m'-2s} \left(\frac{\sin\beta}{2}\right)^{m'-m+2s}}{(J+m-s)!s!(m'-m+s)(J-m'-s)!}. \end{aligned} \quad (2.75)$$

The summation over s is constrained to $s_{\min} = \max(0, m-m')$ and $s_{\max} = \min(J+m, J-m')$ so that the factorials remain non-negative. Hence, if a rotation matrix is required to rotate a state with angular momentum J , it will be a square matrix of size $2J+1$. If required, LASED uses equation 2.73 to rotate any density matrix set up by the user to a new reference frame.

2.3.6 Polarisation

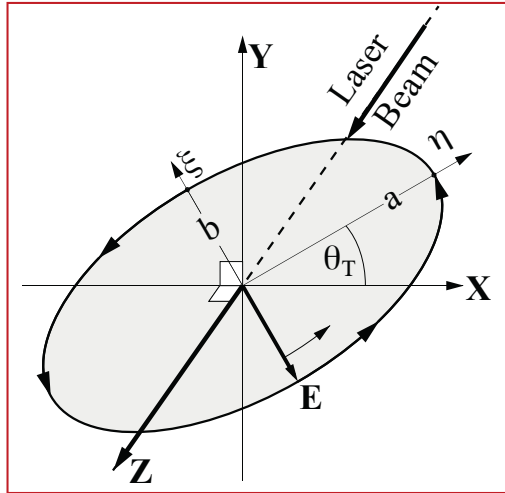


Figure 2.6: A coordinate system for elliptically polarised light travelling in the $+z$ -direction. The electric field vector \mathbf{E} traces out an ellipse with major axis a and minor axis b . The polarisation angle θ_T is shown as the angle that the major axis makes with respect to the x -axis. The vector rotates in an anti-clockwise direction so is right-hand circular polarised.

In many experiments the laser beam interacting with the atoms is chosen to have either circular or linearly polarisation. This makes the generation of the equations of motion and subsequent computation of the dynamics relatively straightforward, as discussed above. It is also important for LASED to model the interaction using a laser which has elliptic polarisation, since this is the most general form for any beam. An elliptically polarised beam can be considered as one that has its \mathbf{E} -field vector tracing out an ellipse, as shown in figure 2.6. The ellipse has major and minor axes, with the major axis being rotated from the x -axis at an angle θ_T as shown. The direction of rotation of the \mathbf{E} -field also must be defined to fully characterise the radiation.

Any elliptically polarised beam can be described as a superposition of right-hand and left-hand circular components with different complex amplitudes, the relative phase between the amplitudes producing the rotation of the major axis from the x -axis. These amplitudes then feed into the Rabi frequencies through equations 2.23 and 2.53. Since the QED model has been developed for the Rabi frequencies being real, it is necessary to first rotate the QA through the angle θ_T so that the new x -axis is aligned along the major axis of the ellipse. This rotation sets the relative phase to zero and so the elliptically polarised light can then be described using two real amplitudes, as given by

$$|P\rangle = \frac{1}{\sqrt{a_{-1}^2 + a_{+1}^2}}(a_{-1}|\sigma_{-1}\rangle + a_{+1}|\sigma_{+1}\rangle). \quad (2.76)$$

Here $|\sigma_{-1}\rangle$ and $|\sigma_{+1}\rangle$ are the LHC and RHC polarisation unit vectors and a_{-1} and a_{+1} are real amplitudes. The computation then proceeds in the same way as described above, however two weighted Rabi frequencies are now required to describe the interaction. From equation 2.76 it follows that the half-Rabi frequency for elliptically polarised light in this frame is given by

$$\Omega_{\text{elliptic}} = \frac{1}{\sqrt{a_{-1}^2 + a_{+1}^2}}(a_{-1}\Omega_{-1} - a_{+1}\Omega_{+1}), \quad (2.77)$$

where the negative sign arises from the definition of the half-Rabi frequency in a circular basis, as seen in appendix A.2.1. Once the interaction has been modelled in this frame, the QA can be rotated back into the original frame to calculate the final density matrix elements.

LASED uses the procedure detailed above to model excitation by elliptically polarised light, if this is required. The user can enter any polarisation state into the model, however they must also include the normalisation factor to ensure the correct Rabi frequency is calculated. As an example, if the minor axis of the ellipse has $b = 0$, the ellipse represents linearly polarised light and so the half-Rabi frequency in this frame is represented by an equal weighting of the circular basis states. In this case $a_{-1} = a_{+1} = 1$ and so the normalisation factor to be input is $1/\sqrt{2}$.

2.3.7 Angular Shape

In LASED, the three dimensional angular shape of the charge cloud for the lower and upper states can be visualised as given in [84, 101], using the expression

$$W(\theta, \phi, t) = \sum_{mm'} \rho_{Jm, Jm'}(t) Y_{Jm}(\theta, \phi) Y_{Jm'}^*(\theta, \phi) \quad (2.78)$$

where Y_{Jm} are spherical harmonics, J is the total angular momentum of the state and m is the projection of J onto the selected quantization axis. $\rho_{Jm, Jm'}(t)$ is the time dependent density matrix element for the atomic state that is being visualised. In LASED, the user can generate the angular shape of the states $W(\theta, \phi, t)$ in the laser-atom system as the system evolves over time. Images of the charge cloud can then be created using an appropriate plotting package. These images can then be displayed sequentially as a function of time, using software that creates a video from the image sequence. The generated videos can be instructive to demonstrate how the states evolve under different experimental conditions. Examples of the generated charge clouds at different times for both the lower and upper states are shown in figure 2.11 in section 2.3.8.

2.3.8 Examples

Example systems are simulated below with increasing complexity to display the features of LASED. More examples can be found at [91].

Calcium Excitation

The simplest system to simulate is from an S -state to a P -state and so as an example, laser excitation from the 4^1S_0 to the 4^1P_1 state in calcium is considered. A level diagram is shown in figure 2.7(a) for this transition. The lifetime and transition wavelength are 4.6 ns [102] and 422.8 nm [103] respectively. In figure 2.7(b) the time evolution of the upper state population ρ_{33} is presented under different conditions. These include a fixed laser detuning of $\delta = 300$ MHz, a Doppler atomic beam profile with $\Delta_{\text{Dopp}} = 300$ MHz, a

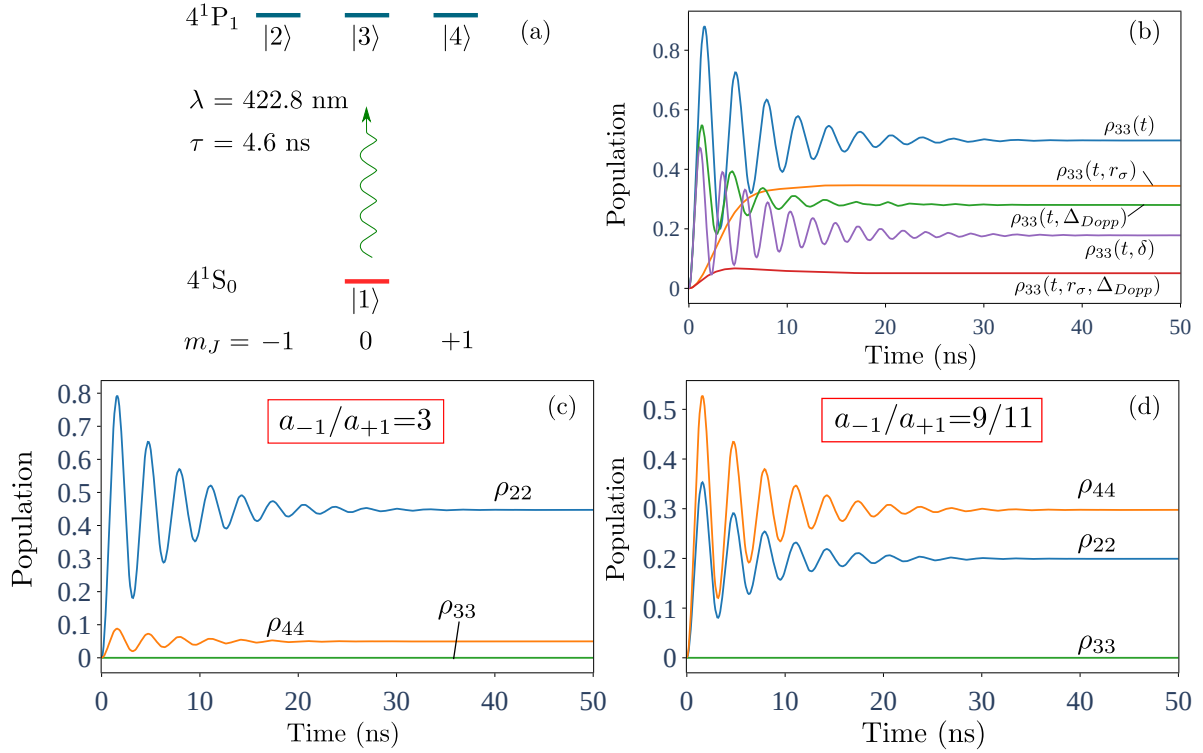


Figure 2.7: (a) A level diagram for the 4^1S_0 to 4^1P_1 excitation of calcium using linearly polarised light, with the QA co-linear with the \mathbf{E} -field of the laser beam so that $\Delta m_J = 0$. (b) The simulated time evolution of the population of substate $|3\rangle$, showing the effect of various simulation parameters, including a Doppler profile for the atomic beam and a Gaussian laser profile. (c) and (d) show the excited state populations using elliptically polarised light for different weightings a_{-1} and a_{+1} (see equation 2.76). In this case the atom is described with the QA along the laser beam direction and so substate $|3\rangle$ remains unpopulated. All simulations used a laser intensity of 100 mW/mm^2 .

Gaussian laser beam profile with $P_{\text{las}} = 100 \text{ mW}$, $r_\sigma = 0.75 \text{ mm}$, and $n_r = 50$, and when both Doppler and Gaussian averaging processes are included together. The simulation time was from 0 to 50 ns using 501 time steps. These simulations are in agreement with the calculations presented in [104].

Results for the same system with elliptically polarised light are shown in figure 2.7(c) and (d). In panel (c) the weightings are set to $a_{-1}/a_{+1} = 3.0$ whereas in panel (d) $a_{-1}/a_{+1} = 0.8$. As expected, the population of the $m_J = -1$ state is much larger in panel (c) due to the favoured $|\sigma_{-1}\rangle$ weighting. By contrast in panel (d) where the weighting for the $|\sigma_{+1}\rangle$ basis state is higher, the $m_J = +1$ substate population dominates. The population of substate $m_J = 0$ is identically zero for the entire simulation as the laser cannot couple to state $|3\rangle$ in this frame with σ^+ and σ^- polarisation.

An example of using rotations in LASED can be seen in figure 2.8. To check that LASED is valid in all reference frames, the calcium system described in figure 2.7(a) is once again considered. This system is now excited using linear-polarised light with the QA along the \mathbf{E} -field of the laser, for a laser intensity of 100 mW/mm^2 and a detuning of 100 MHz. The results from this simulation are shown in panel 2.8(a). Under these conditions, four differential equations are required to describe the populations of substates $|1\rangle$ and $|3\rangle$ as well as the optical coherences generated between them. An equally valid representation is to choose the QA along the direction of the laser beam. In this frame substates $|2\rangle$ and $|4\rangle$

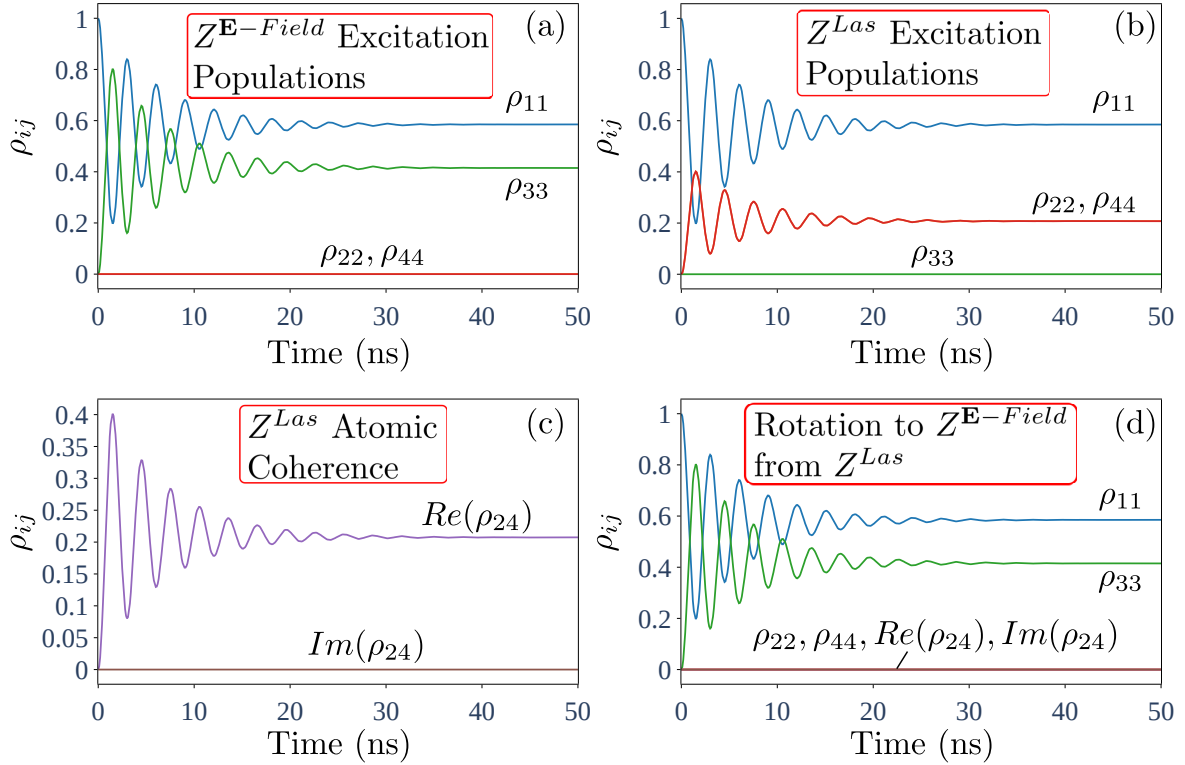


Figure 2.8: Figure showing the use of rotations in LASED to check that the general equations of motion are consistent in all reference frames using the calcium system described in figure 2.7(a). In panel (a) excitation occurs in the frame $Z^{\mathbf{E}\text{-Field}}$ with the QA along the \mathbf{E} -field of the linearly polarised laser beam. An intensity of 100 mW/mm^2 is used and the laser is detuned by 100 MHz from resonance. The populations of the states $|1\rangle$ and $|3\rangle$ in the frame are shown. In (b) excitation is now using simultaneous σ^- and σ^+ radiation with the reference frame Z^{Las} where the QA is along the laser beam direction. The populations ρ_{11} , ρ_{22} and ρ_{44} are shown. Panel (c) shows the real and imaginary components of the atomic coherence ρ_{24} . The data from (b) and (c) are then rotated back to $Z^{\mathbf{E}\text{-Field}}$ in panel (d). This produces results identical to those in panel (a).

are excited using simultaneous σ^- and σ^+ radiation. Substate $|3\rangle$ in this frame remains unpopulated. It is important to realise that the states represented in the different frames are not the same. In this representation nine equations must be generated and solved. Three equations represent the populations of substates $|1\rangle$, $|2\rangle$ and $|4\rangle$, four equations represent the optical coherences between them and two equations represent the atomic coherences generated between substates $|2\rangle$ and $|4\rangle$. The results from this calculation are shown in figure 2.8(b) for the populations ρ_{11} , ρ_{22} and in figure 2.8(c) for the atomic coherence ρ_{24} . Note that $\text{Im}(\rho_{24}) = 0$ here due to the choice of axes in both reference frames. The results from this calculation are then rotated back to the reference frame where the QA is along the \mathbf{E} -field of the laser in figure 2.8(d), which reproduces the results in figure 2.8(a) exactly. This shows that LASED produces the same result independent of the reference frame chosen, as long as the initial conditions are rotated before excitation.

Helium D to P Excitation

A more complex system to model using LASED is presented in this section, where laser excitation is from the 3^1D_2 state to the 10^1P_1 state, as shown in figure 2.9(a). This transition is of interest as experiments are in preparation in Manchester to study this

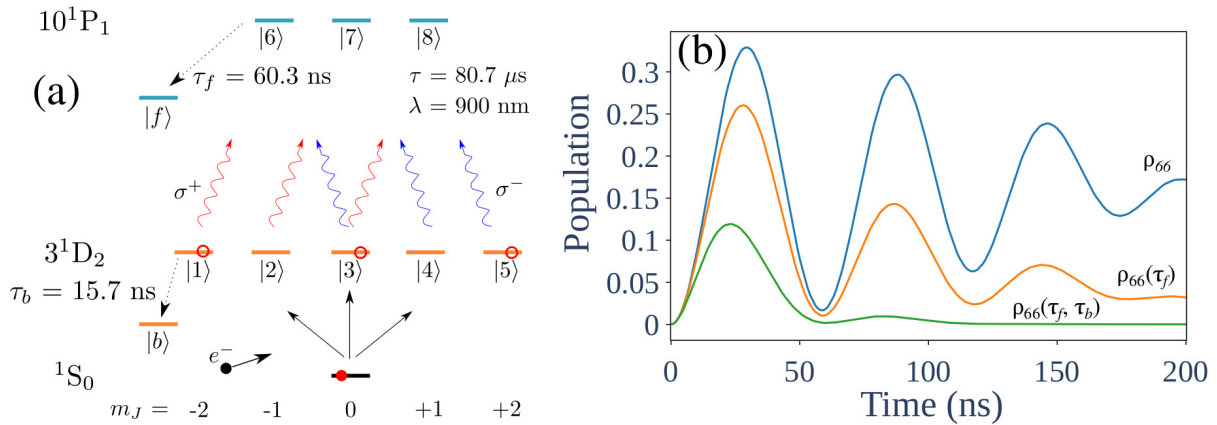


Figure 2.9: (a) A level diagram of step-wise He excitation in the Z^{Nat} frame from the ground $1S_0$ state to the 3^1D_2 state via electron impact and then to the 10^1P_1 state by laser excitation with simultaneous σ^+ and σ^- light. Atomic data for the collisionally excited D -state is taken from [105]. (b) The He system in (a) is simulated with different decay parameters. The laser is on-resonance with an intensity of 1500 mW/mm^2 and ρ_{66} is plotted.

stepwise excitation process. Excitation from the the 1^1S_0 state to the 3^1D_2 state is via electron collision and so the system is presented in the natural frame Z^{Nat} . The laser beam is then injected along the quantization axis and is linearly polarised along the incident beam direction, with an incident intensity of $1,500 \text{ mW/mm}^2$. The beam is set to be on-resonance with the transition at a vacuum wavelength of 900 nm . In this frame, only the substates $m_J = -2, 0, +2$ in the 3^1D_2 -state are excited due to reflection symmetry in the scattering plane [106]. Since the laser beam is linearly polarised, the interaction must be represented by simultaneous σ^+ and σ^- excitation with equal weighting in this frame, as discussed above. The collision excites the atom into a superposition of $|J, m_J\rangle$ eigenstates $|2, -2\rangle = |1\rangle$, $|2, 0\rangle = |3\rangle$, and $|2, +2\rangle = |5\rangle$. The states $|2, -1\rangle = |2\rangle$ and $|2, +1\rangle = |4\rangle$ are not initially populated. Simultaneous σ^+ and σ^- laser excitation is used to represent linear excitation in the natural frame. The 10^1P_1 states are excited by $\Delta m_J = \pm 1$ radiation so as to populate the eigenstates $|1, -1\rangle = |6\rangle$ and $|1, +1\rangle = |8\rangle$, with the state $|1, 0\rangle = |7\rangle$ remaining unpopulated. Both 3^1D_2 and 10^1P_1 states can decay to states that are not coupled by the laser. The excited 3^1D_2 state decays to lower states $|b\rangle$ with a total lifetime of 15.7 ns . The upper 10^1P_1 state decays to states $|f\rangle$ with a lifetime of 59.6 ns , whereas the lifetime for decay back to the 3^1D_2 state is $80.7 \mu\text{s}$ [105]. These decay routes are not shown in figure 2.9(a) for clarity.

Figure 2.9(b) shows simulations of the He system described by figure 2.9(a), where the upper-state population ρ_{66} is displayed using different decay parameters. Due to symmetry, the population of ρ_{88} is the same as ρ_{66} throughout the simulation. The decay routes to $|f\rangle$ and $|b\rangle$ leak both populations and atomic coherences away from the system. The population ρ_{77} for the upper 10^1P_1 state remains zero throughout the simulation, since the laser does not couple to this state in the natural frame. The decays to other states $|f\rangle$ and $|b\rangle$ are added for each simulation. As τ_f has a smaller lifetime than τ , the effect of adding this decay is a smaller upper-state population. Adding τ_b has an even greater effect as $\tau_b < \tau_f$ for this system.

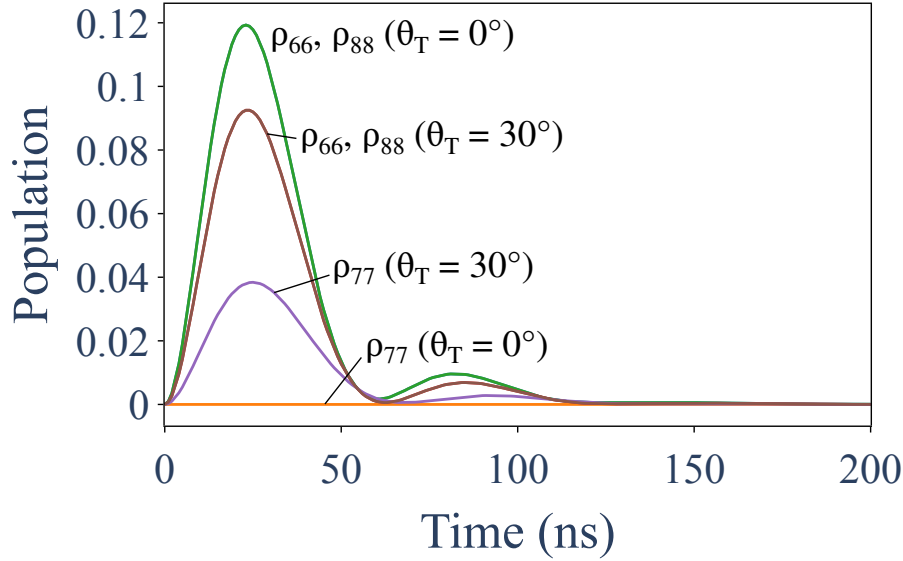


Figure 2.10: A simulation of the He system presented in figure 2.9(a) for laser polarisation angles of $\theta_T = 0^\circ$ and $\theta_T = 30^\circ$ with respect to the x-axis. The upper state populations are shown.

The He system described in figure 2.9(a) has been simulated in LASED using a polarisation angle of $\theta_T = 30^\circ$, as shown in figure 2.10. The angle of polarisation is modelled by rotating the system to the frame where the polarisation angle is 0° and performing the time evolution in this frame and then rotating the resulting time-evolved density matrix back to the original frame. When $\theta_T = 30^\circ$, state $|7\rangle$ gains some excited population as the system evolves and states $|6\rangle$ and $|8\rangle$ have less excited population compared to the $\theta_T = 0^\circ$ case, due to the weaker coupling to these states when $\theta_T = 30^\circ$.

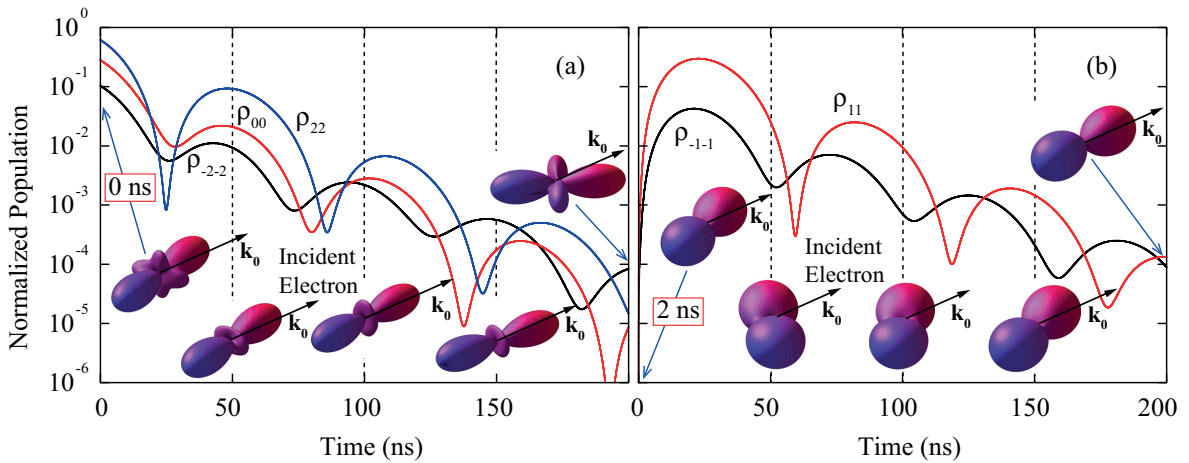


Figure 2.11: The time evolution of the He system in figure 2.9 in the natural frame using electron-impact excitation data showing the (a) 3^1D_2 state populations and (b) the 10^1P_1 state, both presented on a logarithmic scale. The structure of the associated charge clouds have been calculated at various times during the evolution of the states as shown. This is given for the 10^1P_1 state at 2 ns, since this state is unpopulated at 0 ns when the laser is switched on. The incident electron direction \mathbf{k}_0 is also shown for reference. The atomic coherences are not shown, however they are calculated in LASED to allow the charge cloud models to be generated.

Figure 2.11 shows the simulation results of the He system in figure 2.9(a) with the 3^1D_2 initialised with electron-impact excitation data. The scattering amplitudes for the excitation of the ground 1^1S_0 state to the 3^1D_2 state were given by a CCC calculation performed by Bray at Curtin University [107]. The scattering amplitudes given were for an array of

scattering angles and energies. The scattering amplitudes for an electron impact energy of 40 eV and a scattering angle of 45° are used here to calculate the substate populations and atomic coherences at $t = 0$ ns by using equation 2.16. Since the decay routes to $|b\rangle$ and $|f\rangle$ are relatively rapid, the populations of the 3^1D_2 and 10^1P_1 states are presented on a logarithmic scale in figure 2.11. The atomic and optical coherences are not shown, however these are also calculated.

The full density matrices representing the 3^1D_2 and 10^1P_1 states are calculated by LASED, including the time evolution of both populations and atomic coherences. This allows the charge clouds associated with each state to be modelled as a function of time, as discussed in section 2.3.7. Examples of these charge cloud models are shown at different times throughout the evolution of the system in figure 2.11, for both the 3^1D_2 state and the 10^1P_1 state. It is seen that both the angle and shape of the D -state and P -state charge clouds evolve in a complex way, and so must be considered carefully in the associated experiments studying this system.

Caesium D₂ Line

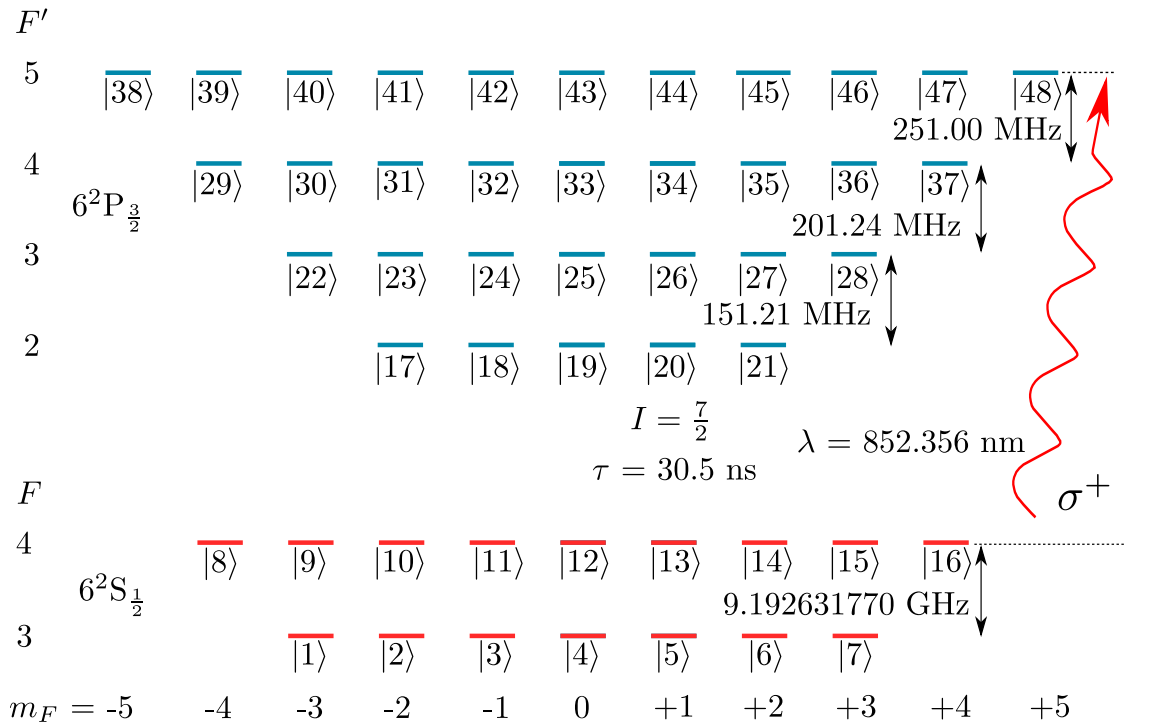


Figure 2.12: A level diagram of the $6^2S_{1/2}$ to $6^2P_{3/2}$ excitation in caesium. σ^+ exciting laser radiation is represented by a wiggly arrow and is set to be on-resonance between the $F = 4$ lower state and the $F' = 5$ upper state.

LASED can also simulate the time evolution of systems with hyperfine structure, such as the caesium transition from the $6^2S_{1/2}$ state to the $6^2P_{3/2}$ state, commonly called the D_2 line. A level diagram for this system is shown in figure 2.12. In this example, the laser is on resonance between the $F = 4$ and $F' = 5$ states and is set to have σ^+ polarisation. The lifetime and wavelength of this transition are taken from [108] and [109] respectively. The hyperfine splittings for the upper and lower substates are taken from [110].

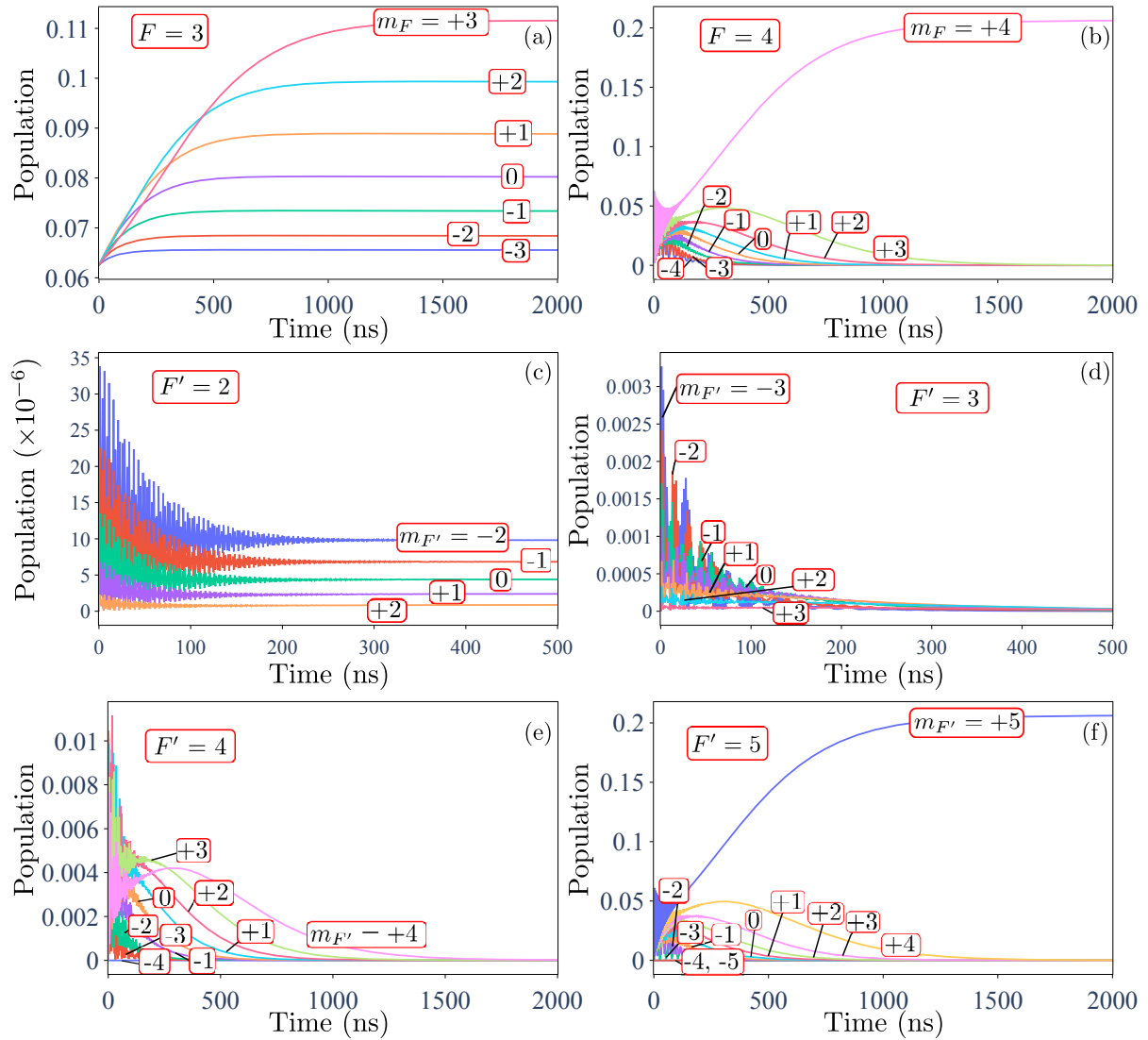


Figure 2.13: The time evolution of the populations of substates in the ground states (a) $F = 3$, (b) $F = 4$, the upper states (c) $F' = 2$, (d) $F' = 3$, (e) $F' = 4$, and (f) $F' = 5$ for the system described in figure 2.12. The laser is σ^+ -polarised with an intensity of 50 mW/mm^2 .

The time evolution of a subset of the populations in the caesium manifold described in figure 2.12 is shown in figure 2.13. This simulation was run with all ground states populated equally at $t = 0$ ns and with no atomic coherences in the initial state, as would be produced for atoms emitted from an oven. Since the laser is tuned from the $F = 4$ state, selection rules prohibit excitation from this state to the $F' = 2$ state, which hence remains essentially unpopulated as shown in figure 2.13(c). The very small change in the population of these states in figure 2.13(c) arises due to pumping from the $F = 3$ state by the laser radiation red-detuned by 9,193 MHz. Selection rules allow the states $F' = 3$ and $F' = 4$ to be populated from the $F = 4$ state, however since they are detuned from resonance by 251 MHz and 452.24 MHz respectively, they are excited with only a small probability as the interaction proceeds.

In figure 2.13(a) the evolution of the population over time for the $F = 3$ ground state is shown. This is the lowest state in the system and is not coupled directly by the laser beam. Since the $F' = 4$ and $F' = 3$ states can however decay to this state via spontaneous emission, its population slowly increases with time as shown, until the substates reach a steady state at around 1500 ns. As the interaction progresses, the states to the left of figure 2.12 decrease in population since spontaneous emission feeds their population to the right, due to pumping with σ^+ radiation. This feeding to the right and subsequent decrease in population is seen in the substates of the $F' = 3$ and $F' = 4$ upper states in figures 2.13(d) and 2.13(e). Each of these states is effectively emptied within around 1500 ns. By contrast, the populations of the $F' = 5$, $m_{F'} = +5$ and $F = 4$, $m_F = +4$ substates shown in figures 2.13(b) and 2.13(f) are seen to rise steadily after the Rabi oscillations have decayed, which occurs at around 150 ns. The substate populations rise quickly until they reach a steady state, after which they remain unchanged. This is a direct consequence of the system evolving towards the closed 2-level system between substates $|16\rangle$ and $|48\rangle$. After this time the interaction can then be approximated to a 2-level system between these substates, with spontaneous and stimulated emission from $|48\rangle$ always feeding back into substate $|16\rangle$. This simplified system is often used to simulate laser interactions in atom cooling and trapping experiments in a Magneto Optical Trap (MOT).

LASED can easily simulate these large and complex systems and can generate all the equations of motion that are required. As noted above the computation time increases considerably as the number of states increases. As an example, simulation of the calcium system in figure 2.7 required less than 1 second of computing time. The model for the D -state to P -state transition in figure 2.9 took a few seconds to generate the data. By contrast, the caesium system required around 9,000 seconds of computing time to generate the results shown in figure 2.13. A table of typical times to run simulations can be found in appendix B.2.

2.3.9 Summary

LASED is an open source package available to researchers, that is written in the python programming language. The general equations of motion used in LASED have been described in this section. LASED allows the user to model different aspects of the interaction, including the Doppler profile of an atomic beam, the Gaussian profile of a

TEM₀₀ laser beam, an arbitrary polarisation of the beam, any rotation between different frames of reference, and the angular shape of the atomic electron cloud. Examples of these techniques have been described here, using different atomic systems.

To further extend the usefulness of LASED the source code is freely accessible, so that other researchers can contribute to its development and further extend its functionality. The source code is hence available and can be edited at [\[111\]](#).

Chapter 3

The (e, 2e) Spectrometer

The ‘Old’ (e,2e) and ‘New’ (e,2e) spectrometers are detailed in this chapter. First, an overview of the common components in both spectrometers is presented. Then, the scattering chambers which house each spectrometer are detailed along with an overview of the gauges used to monitor the high vacuum inside these chambers. The electron gun and electron energy analysers used in both spectrometers are then described. The power supplies for the electron gun and electron energy analysers for each spectrometer are also discussed. The different stepper motor systems to change the experimental geometry in each spectrometer are then outlined. The atomic beam oven in the New (e, 2e) spectrometer is then detailed and results for testing the beam divergence and thermal properties of the oven are presented. The New (e, 2e) cold trap and liquid nitrogen filling system are also described here. The gas jet used in both spectrometers is then discussed. Finally, the detection of an (e, 2e) event using the associated timing electronics is discussed.

In this chapter and subsequent chapters, block diagrams are used extensively to describe hardware, software, and processes. These diagrams are colour coded, as shown in figure 3.1. This colour scheme is used throughout this thesis.

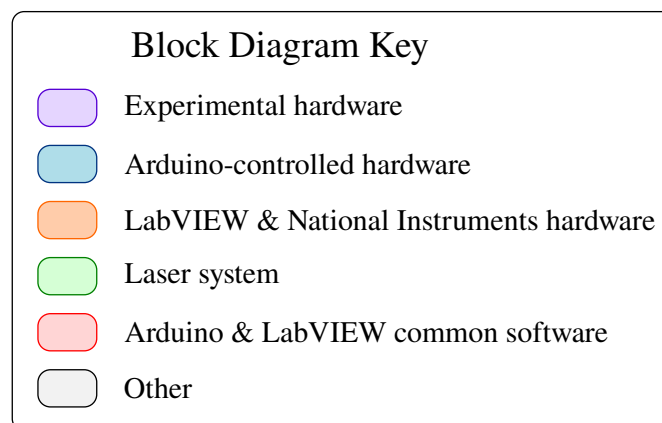


Figure 3.1: A key for the colour scheme used in the preceding figures in this thesis.

3.1 Overview

This section presents a brief overview of the (e, 2e) spectrometers that are in operation at Manchester and the components used in both systems. In subsequent sections, each component is then detailed.

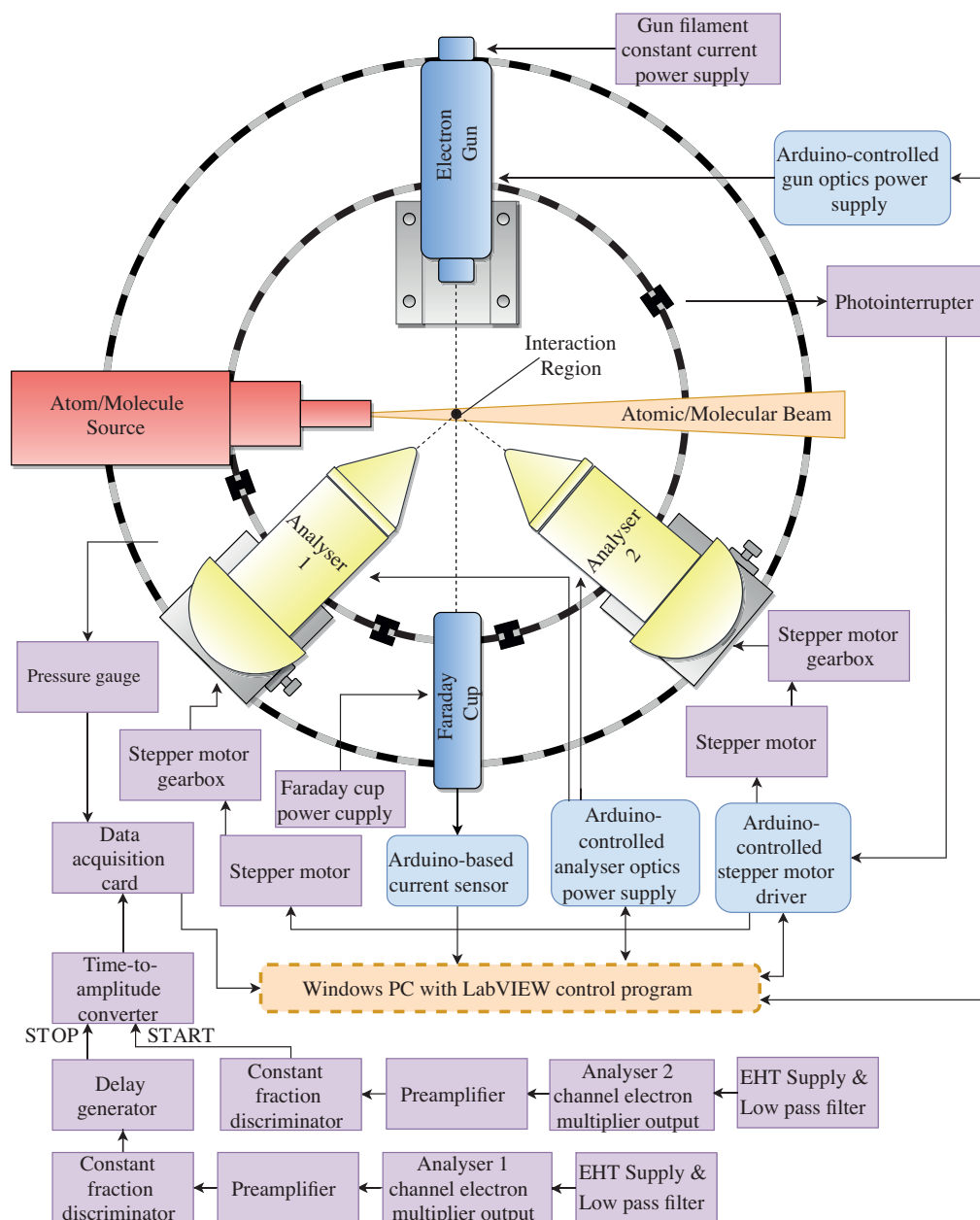


Figure 3.2: A top-down view of key components which comprise one of the (e, 2e) spectrometers at Manchester. The electron gun, analysers, beam source and Faraday cup are housed inside a vacuum chamber. The analysers can rotate around the interaction region on independent turntables. The text blocks represent interacting hardware elements located outside the vacuum chamber. The blocks are colour coded with the key shown in figure 3.1. The arrows represent data flows to and from these components.

A top-down view of one of the (e, 2e) spectrometers at Manchester is shown in figure 3.2. Experiments take place inside a μ -metal lined stainless steel vacuum chamber which is

evacuated to pressures below 10^{-4} Pa using a turbo-molecular pump and a backing scroll pump. An electron gun produces a continuous beam of electrons via thermionic emission from a tungsten filament, which is heated with a current of around 2 A delivered from an external constant current power supply. The electron beam (operating at a current of up to $4 \mu\text{A}$) is steered and focused onto the interaction region at the centre of the chamber by a series of computer controlled electrostatic deflectors and focusing elements within the gun. Electrons that pass through the interaction region without deflection are collected by a Faraday cup which is used to measure the beam current. The bias potential on the Faraday cup is set by an external power supply and the beam current is monitored by the control systems as shown. The target beam of atoms or molecules is provided by an atomic beam oven or gas jet. This beam intersects with the electron beam at the interaction region. Two independent hemispherical energy-selective electron analysers are focused onto the interaction region using electrostatic lenses, to collect electrons emitted following the collision. The analysers can be rotated independently around the interaction region, so that electron impact cross section data can be obtained. Each analyser uses a three element cylindrical lens and a pair of deflectors to image electrons from the collision onto the entrance of their respective hemispherical energy selectors. All voltages on these elements are under computer control.

The electrons that pass around the hemispheres are detected by channel electron multipliers (CEMs) located at their exit. The outputs of the CEMs are amplified by either Philips Scientific Model 6954 pre-amplifiers in the New (e, 2e), or by using custom built pre-amplifiers [112] in the Old (e, 2e). The amplified negative-going signals from each pre-amplifier are directed to ORTEC 473A constant fraction discriminators (CFDs), which filter out noise produced during the amplification process. Each CFD produces two nuclear instrumentation module (NIM) pulses, one of which is buffered to give a transistor-transistor logic (TTL) pulse. The TTL signals from each analyser are sent to the NI PCI-6221 data acquisition (DAQ) card for counting. The second NIM signals from the CFDs are directed to an Ortec 567 time-to-amplitude converter (TAC) for coincidence measurements. The TAC outputs a pulsed signal whose amplitude is proportional to the time difference between the fast NIM pulses that arrive at its start and stop inputs. For (e, 2e) studies, the TAC receives start pulses from one analyser and stop pulses from the second analyser. The stop pulses are usually delayed in time using an Ortec 416A delay generator so that correlated events occur midway within the TAC output. The output of the TAC feeds into the DAQ card which uses an on-board high-speed, 16-bit, analogue-to-digital converter (ADC) to measure the amplitude of the TAC output pulse. The LabVIEW program then stores the result into different bins using a custom-designed multi-channel analyser (MCA) LabVIEW virtual instrument. The MCA signal then builds up over time, with the correlated results from individual events producing a coincidence signal that can then be further analysed.

In both spectrometers the vacuum system pressure is monitored using an Ionivac ITR90 combination Pirani and ion gauge. Analogue readings from this gauge are sent to an ADC on the DAQ card and are converted and displayed in the appropriate units (usually mBar) by the LabVIEW-based control program.

The lens and deflector voltages used to focus and steer the electron gun beam are adjusted using an Arduino-controlled power supply which communicates with the control program. The control system can automatically focus, steer and optimise the incident beam by

monitoring either the Faraday cup current, the electron counts from the analysers or by monitoring the (e, 2e) coincidence counts. The electron beam current readings from the Faraday cup monitor are sent to the LabVIEW program in real time.

The analysers are rotated around the interaction region by an Arduino-controlled stepper motor/gearbox unit which is interfaced by the program. A series of internal opto-interrupters are distributed around the turntables to prevent collisions between internal components should a software malfunction occur. The signals from the opto-interrupters are sent to the Arduino to immediately shut down the stepper motors before a collision can take place, and these signals are also directed to the program for monitoring by the user. Two further Arduino-controlled power supplies interfaced to the control program are used to set the nine lens and deflector voltages that are required for each analyser.

The PCI-interfaced DAQ card is used by the program to monitor and log the electron count rates. Pulses from the CFDs and TAC are sent to this card as noted above, so that the LabVIEW-based MCA can produce coincidence signals.

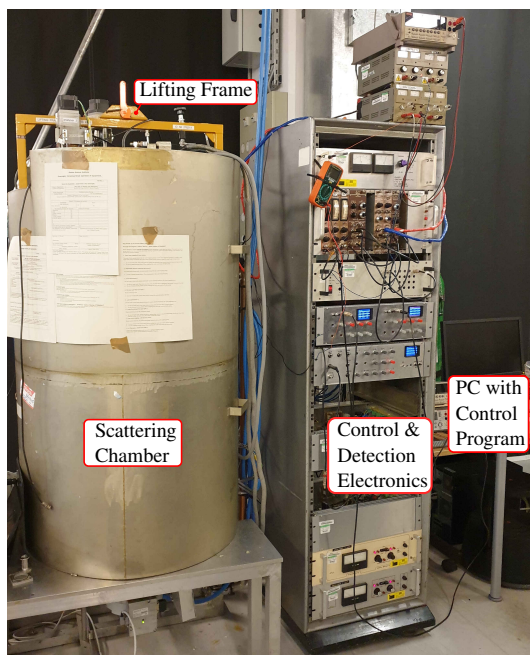
In both spectrometers, experiments are conducted using similar procedures. The target beam is initially turned on either by injecting gas through a needle or by heating the oven to the required temperature to emit atoms. The electron gun filament current and the voltages to the electrostatic lenses and deflectors are then adjusted to maximise the electron beam current into the Faraday cup. The analysers are rotated to set angles and their lens and deflector voltages are optimised under computer control by detecting electrons scattered from the interaction region. The beam from the electron gun is then steered and focused onto the interaction region so that the electron count rates detected by the analysers are maximised. Electron counts and coincidence counts from the interaction are then accumulated for a set period of time at different analyser angles so as to build up the TDCS for the set experimental configuration.

3.2 The Scattering Chamber

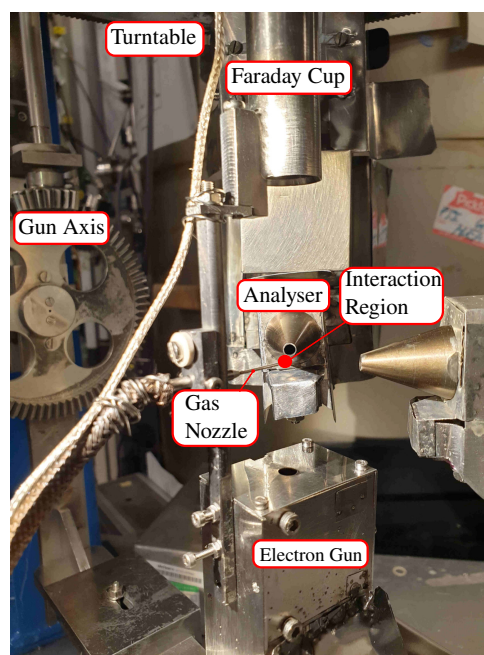
In this section the scattering chamber and vacuum systems for the Old and New (e, 2e) spectrometers are discussed.

3.2.1 The ‘Old’ (e, 2e) Spectrometer

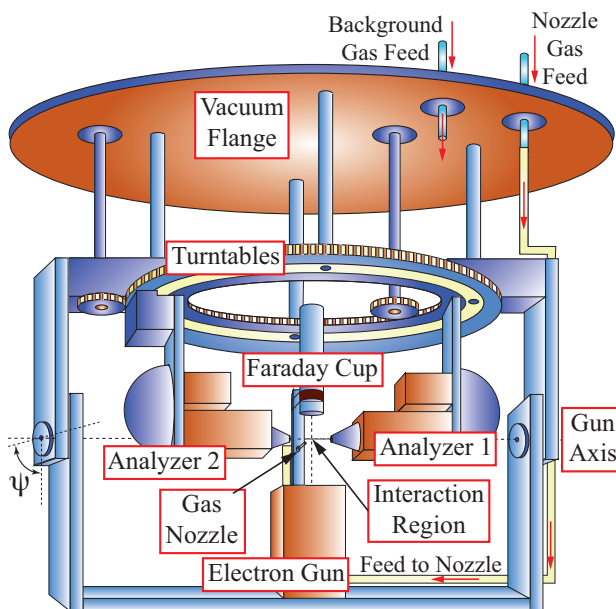
Photographs of the outside and inside of the Old (e, 2e) scattering chamber are shown in figures 3.3(a) and 3.3(b). A detailed diagram of the spectrometer inside the scattering chamber is also shown in figure 3.3(c). The cylindrical scattering chamber is multi-layered. The outside of the chamber is made from non-magnetic type 304 stainless steel, lined externally with 3mm-thick μ -metal. The inside of the chamber is also lined with 3mm-thick μ -metal. This double μ -metal screen reduces the effect of external magnetic fields on the experiments within the chamber [113] to a level where the spectrometer can operate at low electron energies down to ≈ 100 meV.



(a) A photograph of the outside of the Old (e,2e) scattering chamber showing: the lifting frame attached to the scattering chamber, the control PC, and control electronics.



(b) A photograph of the inside of the Old (e, 2e) scattering chamber with the gun axis set to the perpendicular plane geometry.



(c) The geometry of the Old (e,2e) spectrometer, shown in the perpendicular plane where $\psi = 90^\circ$. This diagram is taken from [66].

Figure 3.3

A 25mm-thick stainless steel flange sits on top of the spectrometer, supporting the gun axis and turntable with four support struts. The gun axis supports the electron gun, Faraday cup, and gas nozzle whilst the turntable struts support the analysers. The flange also houses multiple feedthroughs for signals to be carried in and out of the spectrometer. The stepper motors to control the movement of the gun axis and turntable are placed on top of the flange and are coupled to rotary feedthroughs. A background gas feed is also placed on top of the flange and lets gas flow into the spectrometer's background through a CF70 flange. A lifting frame is attached to the top flange to enable an overhead crane to lift the spectrometer out of the scattering chamber and onto a bench for modification and/or alignment.

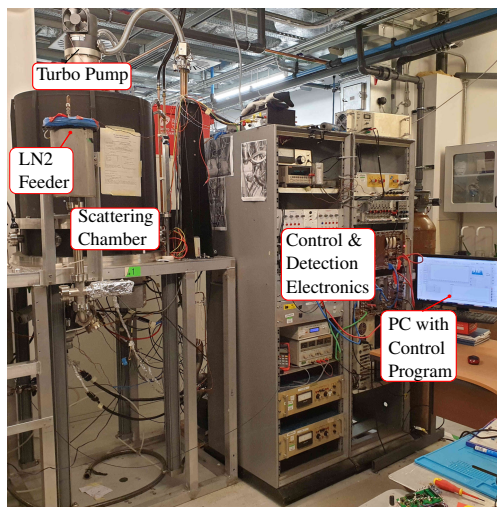
The chamber is pumped to high vacuum using a Balzers TPU 510 500 l/s turbo pump backed by an Edwards XDS35i scroll pump. The vacuum flange sits on top of a Viton O-ring on the upper lip of the chamber to ensure a vacuum tight seal. A minimum pressure of around 5×10^{-7} mBar can be achieved in this spectrometer without baking.

3.2.2 The 'New' (e,2e) Spectrometer

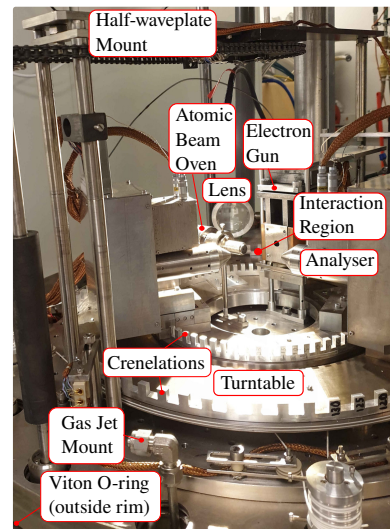
Photographs of the inside and outside of the New (e, 2e) scattering chamber can be seen in figures 3.4(a) and 3.4(b). A detailed diagram showing the geometry of the spectrometer is shown in figure 3.4(c). The New (e, 2e) spectrometer is similar to the Old (e, 2e) spectrometer with a few key differences. The cylindrical scattering chamber is made out of type 310 stainless steel and is lined with a double layer of μ -metal inside of the chamber. The outside of the chamber is lifted using a pneumatic system. The outer chamber also sits on a Viton O-ring to ensure a good vacuum seal, as shown in figure 3.4(b). The New (e, 2e) spectrometer can only access coplanar geometries, unlike the Old (e, 2e) where the gun can be moved out of the plane (see figure 3.3).

Inside this chamber, the electron gun remains in a fixed position and each analyser sits on top of an inner or outer turntable. The turntables have crenelations every 5° which are used to provide a measurement of the angle of the analysers by blocking or unblocking internal opto-interrupters. Rotation of the turntables is performed by stepper motors which sit underneath the chamber. These are coupled to the turntables via rotary feedthroughs. Feedthroughs to carry electrical signals in and out of the chamber are located underneath the bench which the chamber sits on. Inside the chamber, the feedthroughs are spaced around the outside of the outer turntable.

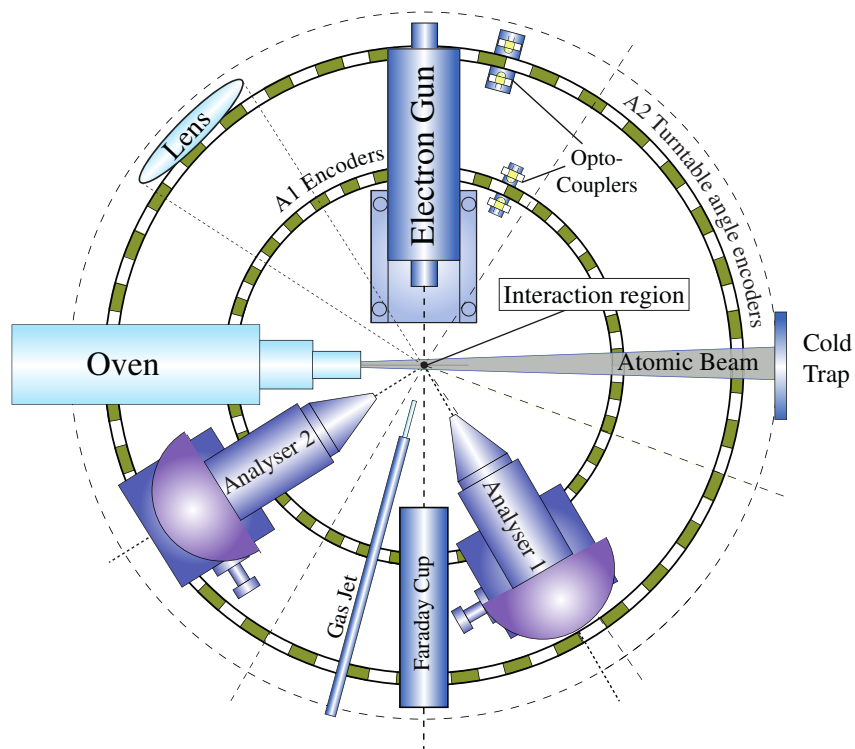
The additional components inside the New (e, 2e) spectrometer include the optical windows, atomic beam oven, and cold trap. Optical windows are placed around the scattering chamber to allow laser light to enter the chamber and fluorescence to be detected from the interaction region using an external photodiode. A lens is placed inside the chamber to image the interaction region to detect this fluorescence. The cold trap is placed directly opposite the atomic beam oven inside the chamber. A liquid nitrogen (LN₂) reservoir is supplied with LN₂ outside the chamber and gravity-feeds the cold trap continuously with LN₂. Target metal atoms produced by the atomic beam oven hence stick onto the surface of the cold trap to ensure that they do not contaminate the spectrometer.



(a) A photograph of the outside of the New (e,2e) scattering chamber showing: the liquid nitrogen feeder for the cold trap, turbomolecular pump, and control PC and electronics.



(b) A photograph of the spectrometer inside the New (e, 2e) scattering chamber.



(c) The geometry of the New (e, 2e) spectrometer. This diagram is taken from [73].

Figure 3.4

A Leybold TurboVAC 361 turbo-molecular pump backed by a Varian Triscroll scroll pump is used to evacuate the chamber so as to reach a minimum pressure of $\sim 5 \times 10^{-7}$ mBar. When the cold trap is active, the pressure will drop to $\sim 9 \times 10^{-8}$ mBar, due to the freezing of water vapour inside the spectrometer onto the trap.

3.2.3 The Pressure Gauges

The vacuum pressure inside each of the scattering chambers is monitored by an Ionivac ITR90 combination ion and Pirani gauge, which takes pressure readings through a CF70 flange. A 15-pin D-Sub connector is fitted onto the gauge to provide power and read the pressure from the gauge. All voltages supplied and read from the pressure gauge are shown in figure 3.5. The voltage output by the gauge is measured by an ADC on the DAQ card and is converted to a pressure reading by the main LabVIEW-based control program, as is detailed in section 5.3.

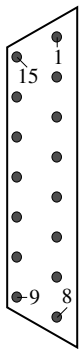
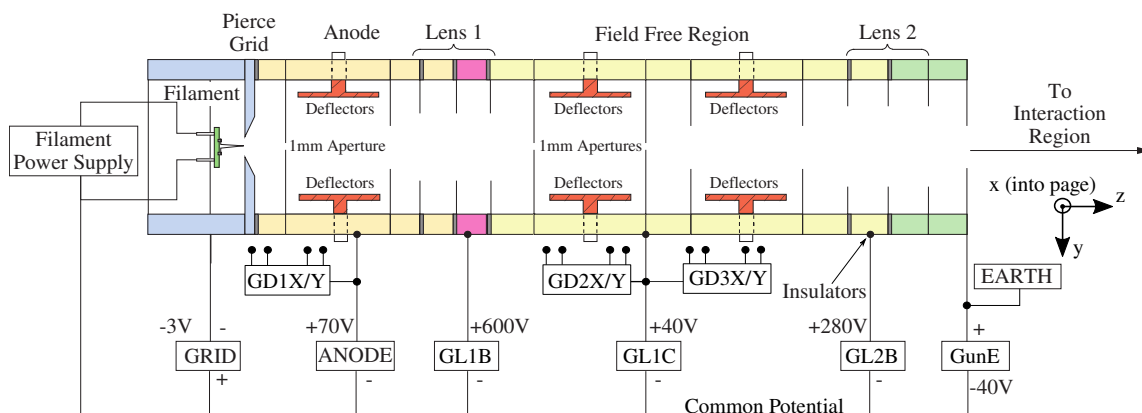
D-Sub 15 Pinout	Pin Number	Description
	2	Pressure reading, 0 to +10V, referenced to 'signal common'
	5	Supply common, GND
	8	Supply, +24V, referenced to 'supply common'
	12	Signal common, GND
	15	Shielding housing, GND

Figure 3.5: The pinout of the 15 pin D-Sub connector for the Ionivac ITR90 pressure gauge used in both the Old and New (e, 2e) spectrometers.

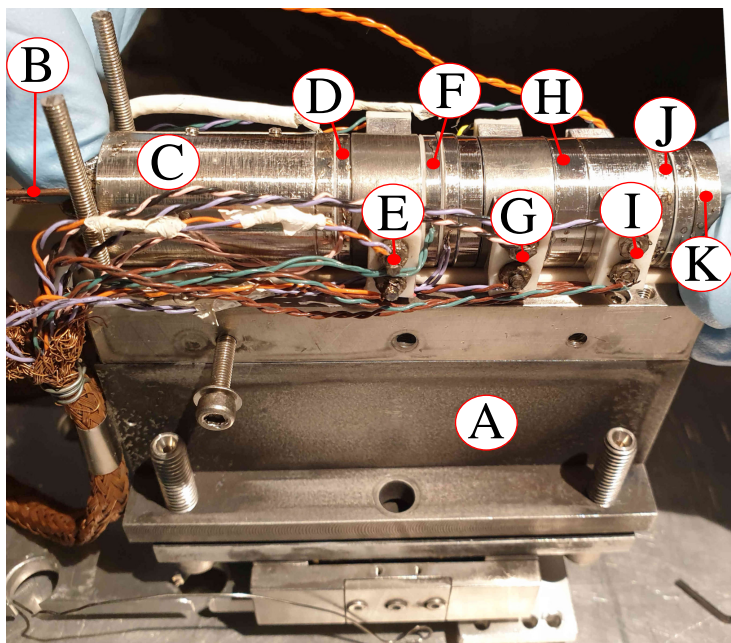
The Ionivac ITR90 measures the pressure using a Pirani measurement system above 5.5×10^{-3} mBar and for pressures below 2.0×10^{-2} , a Bayard Alpert hot cathode ionisation measurement system is used. For pressures in the region between 2.0×10^{-2} mBar and 5.5×10^{-3} mBar, the pressure reading output is measured using a mixed signal derived from both measurements systems. In practice, when the scattering chamber is pumped down from atmospheric pressure the pressure gauge is turned off at 10^{-2} mBar and turned on at a later time, when the chamber pressure drops below 10^{-4} mBar. This prevents the ion gauge's filament from burning out thereby increasing time between failures of the gauge.

3.3 The Electron Gun

The source of electrons in the (e, 2e) experiments comes from an electron gun. The design of the electron gun is the same in both Old and New (e, 2e) spectrometers, and is detailed in this section.



(a) A diagram of the cross section of the electron gun. The filament produces electrons which are accelerated and extracted by a Pierce grid and anode. The electrons are then steered through the gun and to the interaction region by: xy -deflectors GD1X/Y, GD2X/Y, GD3X/Y, lenses GL1B, GL2B, and field-free region of potential GL1C. The electron leaves the gun with energy GunE. Typical operating voltages for each element of the gun are also shown.



(b) A photograph of the electron gun showing the: A) mount, B) connection to the cathode filament, C) grid, D) anode, E) deflectors GD1X/Y, F) lens GL1B, G) deflectors GD2X/Y, H) field-free region with defining apertures GL1C, I) final deflector GD3X/Y, J) final lens GL2B, K) the grounded element defining energy GunE.

Figure 3.6

A diagram and photograph of the electron gun can be seen in figures 3.6(a) and 3.6(b) respectively. The design of the gun was first specified by Woolf [114]. The electron gun consists of an electron source, two 1 mm apertures for defining the electron beam pencil and beam angles at the interaction region, two triple-element lenses for focussing the beam, three xy -deflectors for steering the beam, and a field-free region. A dedicated computer-controlled power supply provides voltages to all the elements, as detailed in section 3.6. Each electrostatic element is separated by a PTFE spacer. The entire system is fixed to a stainless steel block and is encased in a shield to ensure that the voltage on the gun does not affect the electrons in the chamber.

The electron gun produces a beam with a pencil angle of $\sim 2^\circ$ and a 0° beam angle. The gun can produce electrons with energies from around 10 eV to 300 eV with a beam current of up to $4\mu\text{A}$.

3.3.1 The Electron Cathode Source

The electron source is a triode composed of a heated cathode, Pierce grid [115], and anode. Electrons are emitted from the tungsten hairpin element, which is heated to a temperature $>2000^\circ\text{C}$ by a current of typically 2 A provided by an external power supply. Due to the thermionic emission of the electrons, the electrons have an energy spread of around 600 meV. The emitted electrons are accelerated towards the positive anode. The anode is a thin molybdenum plate with a 1 mm aperture in the centre. The voltage on the anode is chosen to efficiently extract the electrons from the filament.

The Pierce grid consists of a 3 mm stainless steel circular conical aperture which sits after the filament. The filament protrudes 0.5 mm through the aperture and the grid is usually biased negative to the filament at around -3 V. The purpose of the grid is to shape the electrostatic field so that electrons emitted at a wide angular range are steered through the 1 mm anode aperture. This allows the electron cloud to be shaped towards the aperture, allowing a higher output beam current. If the grid is decreased by a large amount ~ 10 V, all the electrons are repelled backwards. The grid therefore allows fast switching of the electron beam at the interaction region.

3.3.2 The Electron Optics

The configuration of electrostatic lenses and deflectors used to steer the electron beam through the gun and to the interaction region are shown in figure 3.6(a). The lenses GL1B and GL2B focus the electron beam so that the beam angle at the exit aperture of the gun is 0° . Each lens voltage is referenced to the voltage GunE, which is referenced to real earth. Typical voltages for GL1B and GL2B are +600 V and +280 V respectively. The electron beam is defined by 1 mm apertures which sit in a field-free region of high potential of +40 V to +100 V. This potential is defined by the voltage GL1C. The purpose of the field-free region is to allow the electrons to travel along a straight path to lens GL2B. Each deflector GD1, GD2, and GD3 consist of a pair of parallel plates fixed in the axis perpendicular to the gun axis and hence deflect the electron beam path in

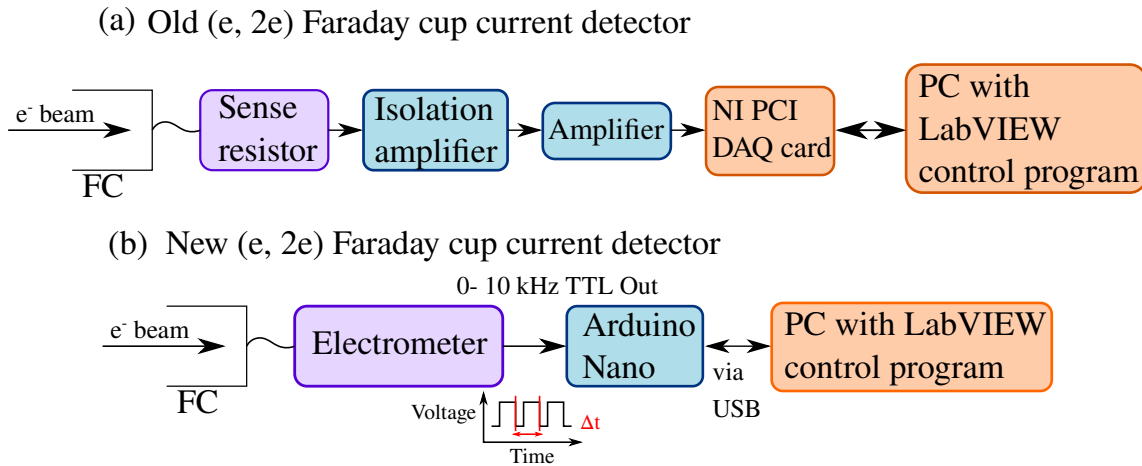


Figure 3.7: Block diagrams showing the measurement of the Faraday cup current for the (a) Old (e, 2e) and (b) New (e, 2e) spectrometer. A colour key can be found in figure 3.1.

the $x - y$ direction. The voltage applied on each deflector plate is equal and opposite to the other e.g. a voltage of $+3$ V is applied to one plate and -3 V is applied to the other plate. The voltages on the deflectors range from $+15$ V to -15 V. The deflectors correct for any misalignment in the beam as it passes through the gun. The voltages on GD1 are referenced to the anode and deflector voltages GD2 and GD3 are referenced to GL1C. The grid, anode, and filament supplies are also referenced to the GunE voltage to ensure that the electron exits the gun with gun energy GunE.

The electron gun is aligned using an alignment laser which passes through the gun and onto the interaction region. The Faraday cup is also aligned with this laser to catch the electrons from the beam which are not deflected in the interaction region.

3.4 The Faraday Cup

The Faraday cup (FC) is a stainless steel cup designed to catch electrons. A shielding cup (~ 60 mm in length) surrounds a smaller inner cup (~ 10 mm in length) which catches the electrons. The inner cup is attached to the shielding via a screw which allows the cup to be aligned to catch electrons coming from the interaction region. The current measured from the FC provides feedback on the alignment and current of the electron beam from the gun. The cup sits at a high positive voltage of around $+200$ V with respect to earth, resulting in a field which attracts electrons which have not been deflected in the interaction region. The cup shielding reduces the effect of this high voltage on electron paths in the chamber.

Figure 3.7(a) shows how the FC current is measured in the Old (e, 2e) spectrometer. The current produced by the FC is run through a 1 M Ω sense resistor. The voltage generated from this sense resistor is fed into an ISO124 isolation amplifier followed by an OPA277 amplifier set to have unity gain. The resulting voltage is then measured by an ADC on the DAQ card and displayed in the main control program. For a detailed schematic of the detection electronics see Sakaamini's thesis [116]. The resistor values were chosen to produce 1 V for every 1 μ A of FC current. The power supply for the cup and detection

electronics comes from a computer controlled power supply as detailed in section 3.6.1.

Figure 3.7(b) shows the FC measurement system in the New (e, 2e) spectrometer. The FC current is fed into an electrometer built by the Manchester electronics workshop (job number EW672). Inside the electrometer, the FC current is fed into an OPA104BM amplifier, which produces a voltage with a gain set by a feedback resistor whose value is controlled by a rotary switch on the front panel. The amplifier's output is then fed into a voltage-to-frequency converter followed by a TIL117 optical isolator and a buffer. The electrometer then outputs TTL pulses with a frequency proportional to the measured current. This pulsed output is measured by a digital input pin on an Arduino Nano which is programmed to measure the frequency, as detailed in section 5.3. This frequency measurement is then sent to the control PC via a Universal Serial Bus (USB) and is displayed in the main control program.

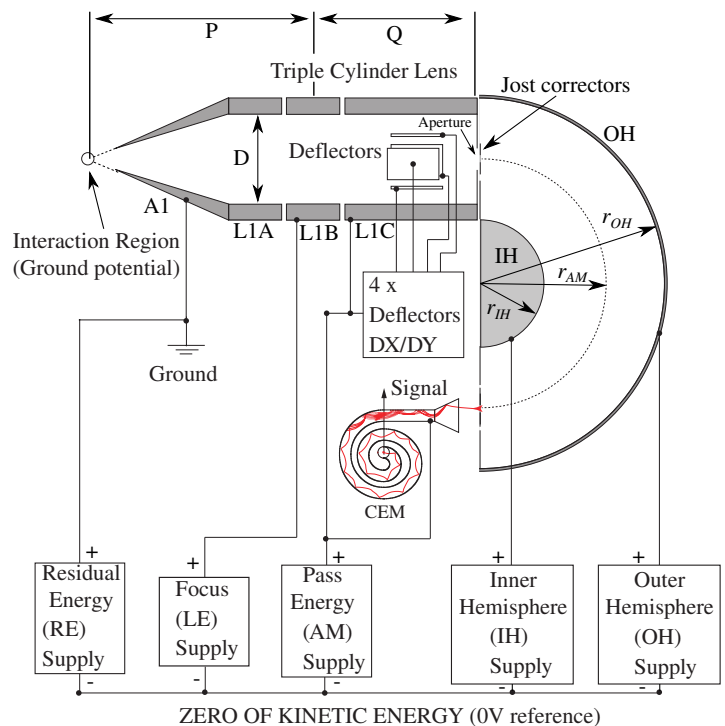
3.5 Electron Energy Analysers

The design of the electron energy analysers use hemispherical deflectors to select and detect scattered and ejected electrons of the required energy. The design of the analysers are identical in both spectrometers.

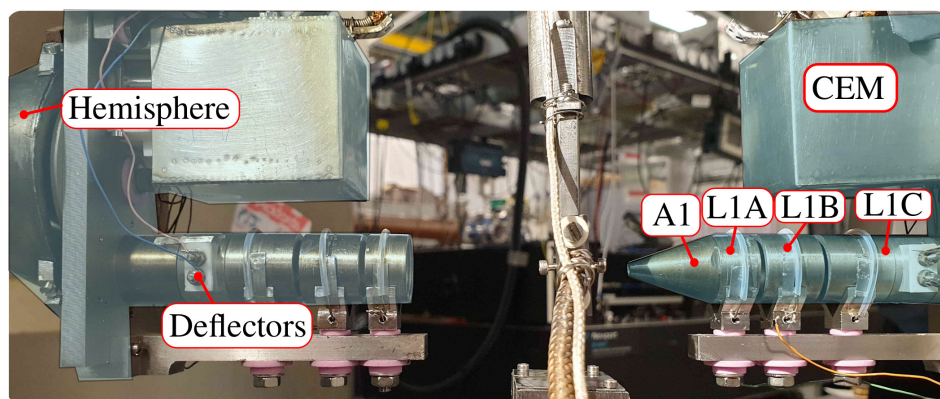
Figure 3.8(a) shows a diagram of one of the electron energy analysers and figure 3.8(b) shows a photograph of both analysers in the Old (e, 2e). The conical element A1 defines a 5° acceptance angle for the electrons to enter the analyser. This aperture is referenced to real earth and the voltage residual energy (RE), which defines the energy of the detected electrons, is referenced to the aperture. The electron is then focussed onto a 1 mm aperture by the cylindrical lens elements L1A, L1B, and L1C. The deflectors correct for any physical defects (e.g. lens aberrations) and for stray fields which may cause the electron beam to veer off the central path. The electron then enters the hemisphere and is imaged onto the exit aperture, if it has energy equal to the pass energy, and then enters the CEM to be detected.

3.5.1 Analyser Elements

The cylindrical lens elements are made from molybdenum and have a diameter D of 16.25 mm. The lengths D , P , and Q , in figure 3.8(a), are made so that $P = Q = 4D$. The first lens element L1A is electrically connected to the front cone A1 and is set to the ground of the interaction region. This lens is connected to the residual energy (RE) supply, which defines the kinetic energy of the detected electrons. All other potentials are referenced to RE. The second lens element L1B images the interaction region onto the entrance aperture to the hemispheres. The focus or lens (LE) voltage is used to change the focal length of this lens element by modifying the electrostatic fields which bend the electron beam path towards the lens axis. The third lens element L1C is set to accelerate or decelerate electrons to the pass energy eV_{AM} , where V_{AM} is the voltage set by the pass energy supply, often called the analyser mean (AM) voltage. There is an xy -deflector electrically referenced to L1C to correct for any misalignment of the electron path from



(a) A cross section of the electron energy analysers, showing the lenses, deflectors, and power supplies which guide an electron into a channel electron multiplier (CEM). Voltages are set to image the interaction region onto a 1 mm entrance aperture and around the hemispherical detector then through an exit aperture. P is the distance between the interaction region and the centre of L1B and Q is the distance between the centre of L1B and the entrance aperture of the hemisphere. D is the diameter of the lenses.



(b) A photograph of the electron energy analysers in the Old (e, 2e) spectrometer showing: A1) the conical cover referenced to ground, L1A) the first lens element connected to ground and A1, L1B) the focussing lens element, L1C) a field-free region defined by two apertures, the deflectors, the shielded CEM, and a hemisphere.

Figure 3.8

the interaction region to the hemisphere entrance aperture. The deflectors are set up as two pairs of parallel plates similar to that of the electron gun. These plates are placed in the field-free region of L1C and are enclosed by 6 mm apertures to minimise stray fields from the deflector plates, which influence the focus of the lens.

3.5.2 Hemispheres

The energy selecting components in the analyser are composed of an inner and outer hemisphere and entrance and exit apertures. Two Jost correctors surround the entrance and exit apertures. These are referenced to AM and have the effect of correcting the potential around the apertures, leading to a more central trajectory [117]. A high energy electron entering the hemisphere will have a path radius along the hemisphere so large that it will be absorbed by the outer hemisphere and a low energy electron will be deflected into the inner hemisphere. An electron with energy eV_{AM} however, is deflected along the mean path radius of the analyser r_{AM} . Additionally, electrons which enter the hemisphere with an angular spread from the central trajectory are re-focussed onto the exit aperture. To produce the deflection along r_{AM} , the voltages on the inner hemisphere (IH) and outer hemisphere (OH) are given by [118]

$$V_{IH} = V_{AM} \left(\frac{2r_{AM}}{r_{IH}} \right) \quad (3.1)$$

$$V_{OH} = V_{AM} \left(\frac{2r_{AM}}{r_{OH}} \right), \quad (3.2)$$

where r_{IH} and r_{OH} are the radii of the inner and outer hemisphere respectively. For the analysers in operation in the New and Old (e, 2e), the hemisphere radii are given by $r_{OH} = 33.6$ mm, $r_{IH} = 17.2$ mm, and $r_{AM} = 25.4$ mm. Due to physical and electrostatic imperfections in the analysers, the voltages set on the analysers are only approximated by equations 3.1 and 3.2. The exact voltages set on the hemispheres are determined by tuning IH and OH for a given AM to maximise the detected and energy selected electron rate in an experiment. These are then set for the duration of the experiment.

The energy spread of the detected electrons at the exit of the hemispheres can be approximated by [118]

$$\frac{\Delta E}{E_{AM}} = \frac{w}{2r_{AM}}, \quad (3.3)$$

where $E_{AM} = eV_{AM}$ and w is the diameter of the entrance and exit apertures. As the parameters r_{AM} and w are fixed, the variable which changes the energy resolution of the detected electrons is hence given by V_{AM} . A lower V_{AM} reduces the energy spread of the detected electrons but decreases the number that will pass through the analyser successfully. There is therefore a trade-off between high resolution and high detection rates. A value of $V_{AM} = 15$ V is found to be a good balance between the two and hence has been used throughout the experiments in this thesis. For $V_{AM} = 15$ V and w of 1 mm, the energy resolution of the analysers is ≈ 0.3 eV.

3.5.3 The Channel Electron Multipliers

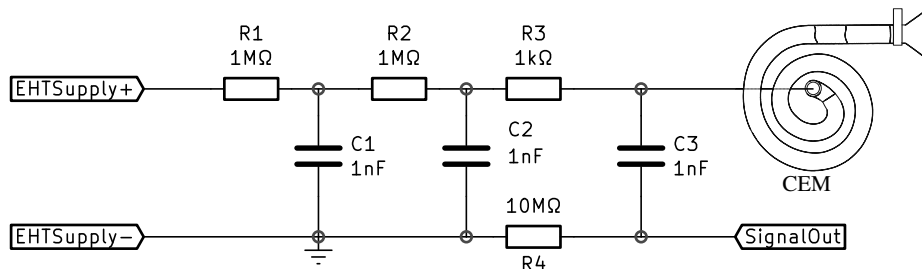


Figure 3.9: A circuit diagram of the second order low pass filter in-between the EHT supply and the CEM. The output signal from the CEM is input to a preamplifier.

The energy selected electrons which pass through the analyser are detected by a Mullard X919BL channel electron multiplier (CEM). These devices amplify a single electron to produce a current pulse with a gain of $\sim 10^8$. The amplification is performed by the lead glass internal surface of the CEM which has a high coefficient of emitting secondary electrons if supplied by a high voltage. Each CEM is supplied with 2.7 kV by a Brandenburg EHT power supply. The CEM emits a negative pulse of around 25 - 40 mV into the 50 Ω input of a preamplifier, which is followed by timing electronics detailed in section 3.9.

A second order low pass filter is placed in-between the EHT supply and CEM to reduce pick-up noise from the power supply, as shown in figure 3.9. A 10 M Ω resistor R4 protects the preamplifier from sudden high voltage transients, if the supply is suddenly disconnected.

3.6 Analyser and Gun Power Supplies

Low noise and reliable computer-controlled voltages are required for the experiments detailed in this thesis. Custom-made power supplies are hence in use to supply voltages for the analysers in the New (e, 2e) and the analysers, gun, and FC in the Old (e, 2e). The design of these custom-made power supplies uses Arduino [77] microcontroller units, which have the advantage of being low-cost and easy-to-use.

The design of the power supplies consist of two main parts: the variable voltage units which directly connect to and supply gun and analyser elements and the voltage rails which provide power to the variable voltage units. The voltages on the voltage rails are produced by rectifying and smoothing the output of a transformer connected to the mains power supply. The variable voltage units usually consist of a digital-to-analogue converter (DAC) connected to a series of buffers and amplifiers which supply a computer-controllable voltage to the given gun or analyser element. The output voltage of the DACs are set by an optically-isolated digital signal from the Arduino, which in turn is controlled by a Windows PC with a LabVIEW-based control program. Chapter 5 details the firmware running on the Arduino and the main control program software. Each power supply also has rotary encoders and potentiometers for manual control of voltages, should this be required.

3.6.1 The Old (e,2e) Power Supplies

In the Old (e, 2e) all but two gun and analyser voltages are supplied by an Arduino-based power supply. The coarse gun energy (GunE coarse) and the lens element GL2B are set by external power supplies after the internal supplies had failed. The DAC on the DAQ card provides fine control of the gun energy via the main control program.

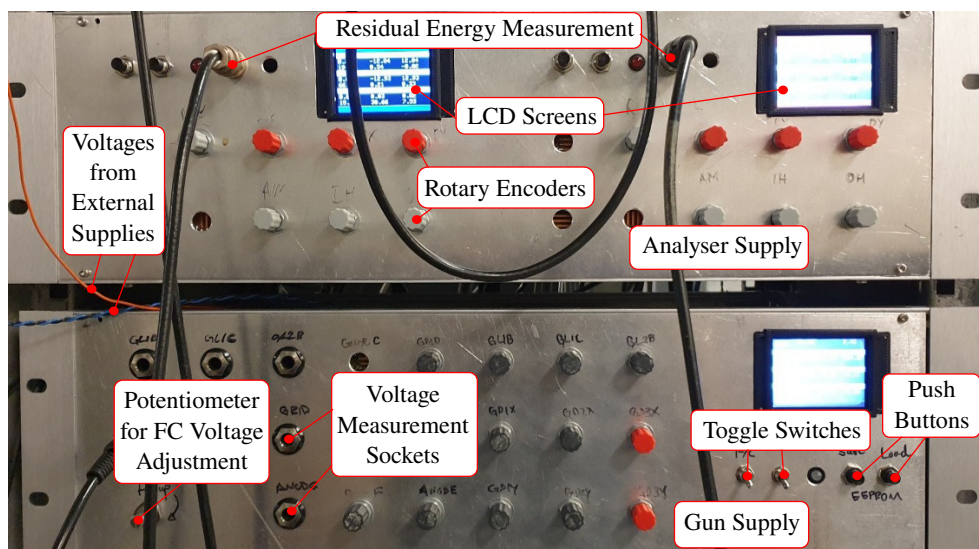


Figure 3.10: A photograph of the front panel of the Old (e, 2e) Arduino-based power supply. The variable voltage units are contained inside the two 19-inch boxes shown. The top box provides units supplying the analysers and the bottom box supplies the gun elements and FC. The bottom box also houses part of the FC current detector shown in figure 3.7(a). Rotary encoders, potentiometers, toggle switches, push buttons, LCD screens, and sockets are used to interface with the supply units. Two voltages from external supplies are wired into the gun supply box to supply elements GunE coarse and GL2B.

The power supply is split into four 19-inch rack-mounted boxes. The top two boxes, as shown in figure 3.10, provide the variable voltage units supplying the analyser and gun elements. The bottom two boxes contain the voltage rails supplying the variable voltage units via two 25-pin D-Sub connectors. LCD screens on the variable voltage supply boxes show set and measured voltages. Rotary encoders mounted on the front panel of the variable voltage supply are used to manually control each voltage. A USB connected to an Arduino Mega 2560 is mounted on the back of the analyser variable voltage supply box. Female jack plugs are connected to each gun element and two BNC sockets connect to the residual energy of the analysers, for measurement using an external voltmeter. The supply also provides the high voltage for the FC and one of the supply boxes contains the sense resistor, isolation amplifier, and amplifier for the FC current monitor. As the isolation amplifier's output is unreliable at times, power is disconnected and re-connected to the amplifier using toggle switches mounted onto the front panel.

The Arduino usually resets its firmware and loses all saved voltages when it is powered on and voltages must be reset back to previous values. The resetting of the firmware is triggered by the 'RESET' pin experiencing a TTL LOW pulse. A 100 nF capacitor is placed between the 'RESET' pin and ground of the power supply to prevent this from happening and ensuring that voltages are saved when the device is powered off. This

reset capacitor also prevents the Arduino from being re-programmed. A toggle switch has hence been placed in-between the reset capacitor and ground to allow re-programming of the Arduino. This toggle switch is located on the back of the supply. Set voltages can also be saved and loaded on the Arduino's electrically erasable programmable read-only memory (EEPROM) by pressing the push buttons on the front panel of the supply, as seen on figure 3.10.

A block diagram describing the Old (e, 2e) gun and analyser power supply is shown in figure 3.11. (a) shows the design of the voltage rails supplying the variable voltage supply units. The voltages of ± 15 V, ± 12 V, and ± 5 V are supplied by using the 78xx and 79xx series of fixed linear regulators to regulate a smoothed output from a bridge rectifier connected to a step-down transformer. The voltages of +30 V and +60 V are provided by a pair of TL783 adjustable positive voltage regulators. The voltage of +120 V is again supplied by a TL783 regulator from the smoothed and rectified output of a step-down transformer. The output of a 1:1 transformer is fed into a bridge rectifier and smoothed to provide a high voltage of +380 VDC.

The variable voltage units supply twelve different voltages to the gun and analyser elements. The power supply is computer-controlled by the main LabVIEW control program which sends serial commands to an Arduino Mega 2560. To control the voltage level of each element, the Arduino sends optically-isolated TTL signals to the MCP4822 DACs via the serial peripheral interface (SPI) protocol. After optical-isolation and inversion by the HCPL2630 optical couplers, the signals are re-inverted by an SN7F4F04N hex inverter. The deflectors DX/Y on the gun and analysers are set by buffering and amplifying the signal from a dual-DAC with a series of TL084 quad operational amplifiers. One DAC sets the coarse voltage level and the other DAC sets a finer voltage level within each coarse level. Each DAC has 12 bits of precision so this dual-DAC system provides a total level of precision of up to 24 bits. The control of the grid is similar to the control of the deflectors. The control of the analyser elements AM, IH, and OH is similar to that of the deflectors except after the TL084s, a single OPA445 is used for amplification. A single TL084 followed by a high voltage LTC6090 amplifier provides the buffering and amplification for GL1C, anode gun elements, and analyser elements RE and LE. The analyser's RE is referenced negative with respect to earth. The high voltage lens element is supplied by an isolated THV12-1000P DC/DC converter. This converter's output is controlled by the buffered output of a single DAC. The Faraday cup is also supplied by a voltage from this power supply. A +5 V reference from a REF02 is buffered and set by a manually-controlled potentiometer and fed into a metal-oxide-semiconductor field-effect transistor (MOSFET) which controls the voltage on the Faraday cup from the +380 V rail. The voltage supplied by the rail is protected by a 1N4007 diode.

Rotary encoders connected to ATtiny85 microcontrollers give manual control of all the digitally-set voltage elements. The ATtiny chips are used here as the Arduino Mega 2560 does not have enough I/O pins to interface with rotary encoders for each element. Additionally, the ATtiny chips provide quick sensing of any changes to the state of the rotary encoders. Each ATtiny has an I/O pin connected to the Arduino's receiver (RX) line, transmission (TX) line, rotary encoder push button, and two rotary encoder signal lines. When a rotary encoder is turned, the ATtiny senses the changes in each signal line and calculates the direction and acceleration of turning which is sent via the RX line to the Arduino, where a signal is sent out to change the corresponding voltage. The Arduino

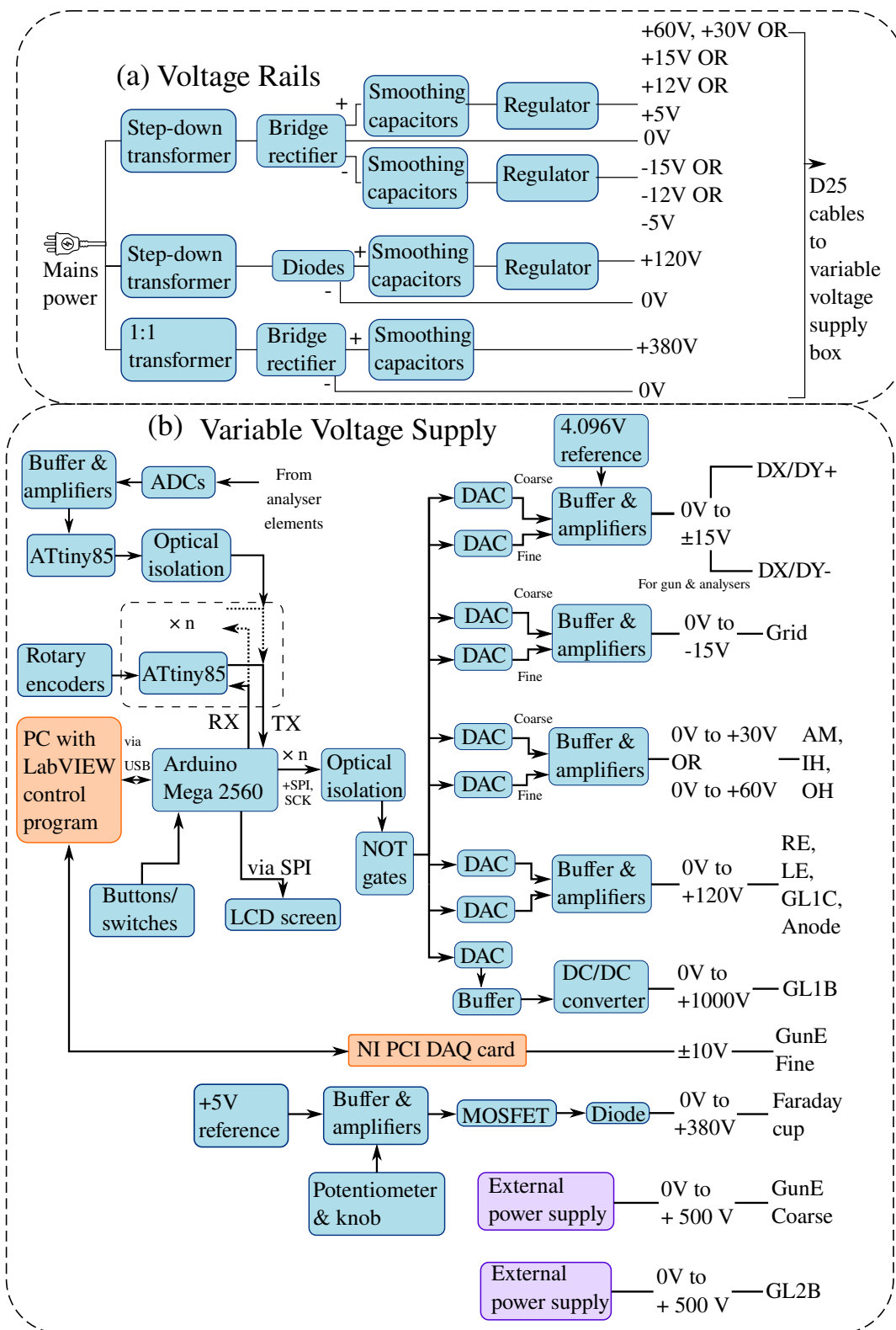


Figure 3.11: Block diagram describing the Old (e, 2e) gun and analyser power supplies. A circuit schematic can be found in [116]. A colour key can be found in figure 3.1. For details, see the text.

can also send messages and commands to the ATtinys via the TX line. The ATtiny85 does not have dedicated TX and RX pins so these pin types must be set in the firmware for each individual chip.

Custom-built [ADC](#) boards are used to monitor the voltages on the analyser elements. A full schematic can be found at [119]. A fraction of the analyser voltages are measured by a potential divider and fed into a buffer amplifier. This is then followed by an MCP3208 ADC, which is referenced to +5 V provided by a REF02. The digital signal produced by the ADC is sent to an ATtiny85, which communicates to the Arduino Mega via the RX line using serial commands. This signal is converted to a measured analyser element voltage by using the known potential divider resistor values for each element. Two LCD screens display the set voltages for the gun and set and measured voltages for the analysers. The LCD screens are sent data by the Arduino Mega via the I²C protocol.

Two Lambda LPD-421A-FM power supplies provide the coarse level of the gun energy and GL2B. These power supplies can run from 0 to +500 V. Fine control of the gun energy by -10 V to +10 V is provided by the 16-bit DAC of the [DAQ](#) card which is connected in series with the Lambda supply.

3.6.2 The New (e,2e) Power Supplies

In the New (e, 2) spectrometer, all analyser voltages are supplied by an Arduino-based power supply. The ADC on the [DAQ](#) card is used to finely control the gun energy via the main control program and all other gun voltages are supplied by manually-controlled power supplies.

The Electron Gun Supplies

A photograph of the New (e, 2e) electron gun power supplies can be seen in figure 3.12(a). These supplies provide all of the voltages for the gun elements and the Faraday cup via plug-in modules. Each module is slotted into a rail which connects to the mains supply. In each module, the AC mains supply is rectified, buffered, and amplified to provide a voltage. The gain for amplification of the voltage is controlled by a potentiometer and therefore manual control of each voltage is provided by the adjustment knobs on the front panel of each module. Each deflector module provides two voltages for the x and y deflectors and switches on each module controls the polarity of each deflector voltage. For fine control of the gun energy, the output of a DAC on the [DAQ](#) card is connected in series with the gun energy voltage provided by the power supply module. This gives fine control of the gun voltage by ± 10 V with 16-bit precision.

The low voltages provided by the deflector supplies and the high voltages provided by the lens, gun energy, Faraday cup, and anode supplies are fed out to a separate switch box via two 25-pin D-sub connectors. Figure 3.12(b) shows a photograph of the front panel of this box. A constant-current power supply is also fed into the box to provide current to the gun filament. The switch box provides a connection to the gun elements and Faraday cup via a printed circuit board ([PCB](#)) and another D-sub connector. The box consists

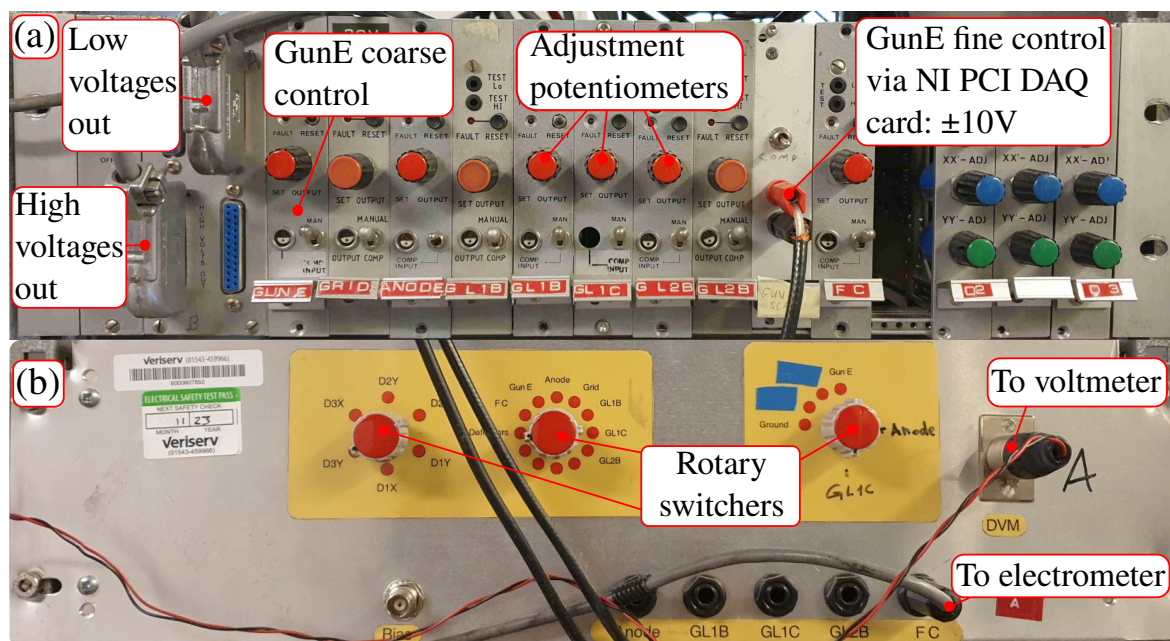


Figure 3.12: Photograph of the (a) electron gun power supplies for the New (e, 2e) spectrometer. Each voltage element is provided by a plug-in circuit board with an adjustment potentiometer for control. Fine control of the gun energy is provided by a connection to the DAQ card. Two 25-pin D-sub connectors connect the high and low voltages generated for each element to the gun elements via the (b) switchbox which provides monitoring for each element.

of three sets of rotary switchers on the front panel. These switches control the voltage which is connected to a socket monitored by a Keithley voltmeter. The anode, GL1B, GL1C, GL2B, and the Faraday cup currents can also be monitored via sockets which can be connected to the electrometer as shown.

Electron Energy Analyser Power Supplies

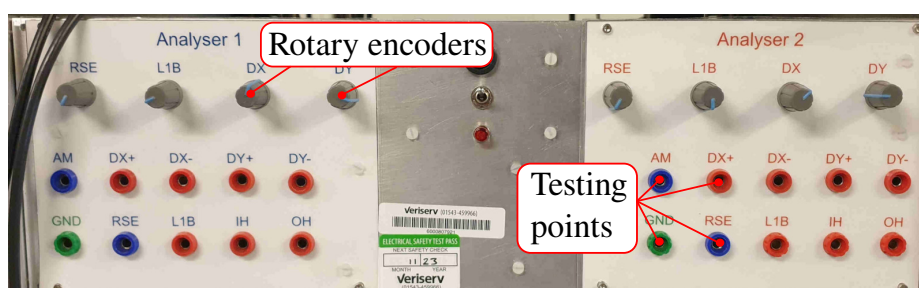


Figure 3.13: A photograph of the front panel of the New (e, 2e) electron energy analyser power supplies. Rotary encoders provide manual control of each voltage element and 4 mm sockets can be connected to a digital voltmeter for testing. All voltages can be computer-controlled via a serial interface.

A photograph of the front panel of the New (e, 2e) electron energy power supplies can be seen in figure 3.13. The power supplies provide the analysers with voltages which can be manually controlled via rotary encoders or using computer-controlled serial commands via USB. Each voltage element can be monitored and tested using the 4 mm breakout sockets on the front panel of the power supply. A USB socket is on the back of the box which is connected to the Arduino Mega 2560 inside.

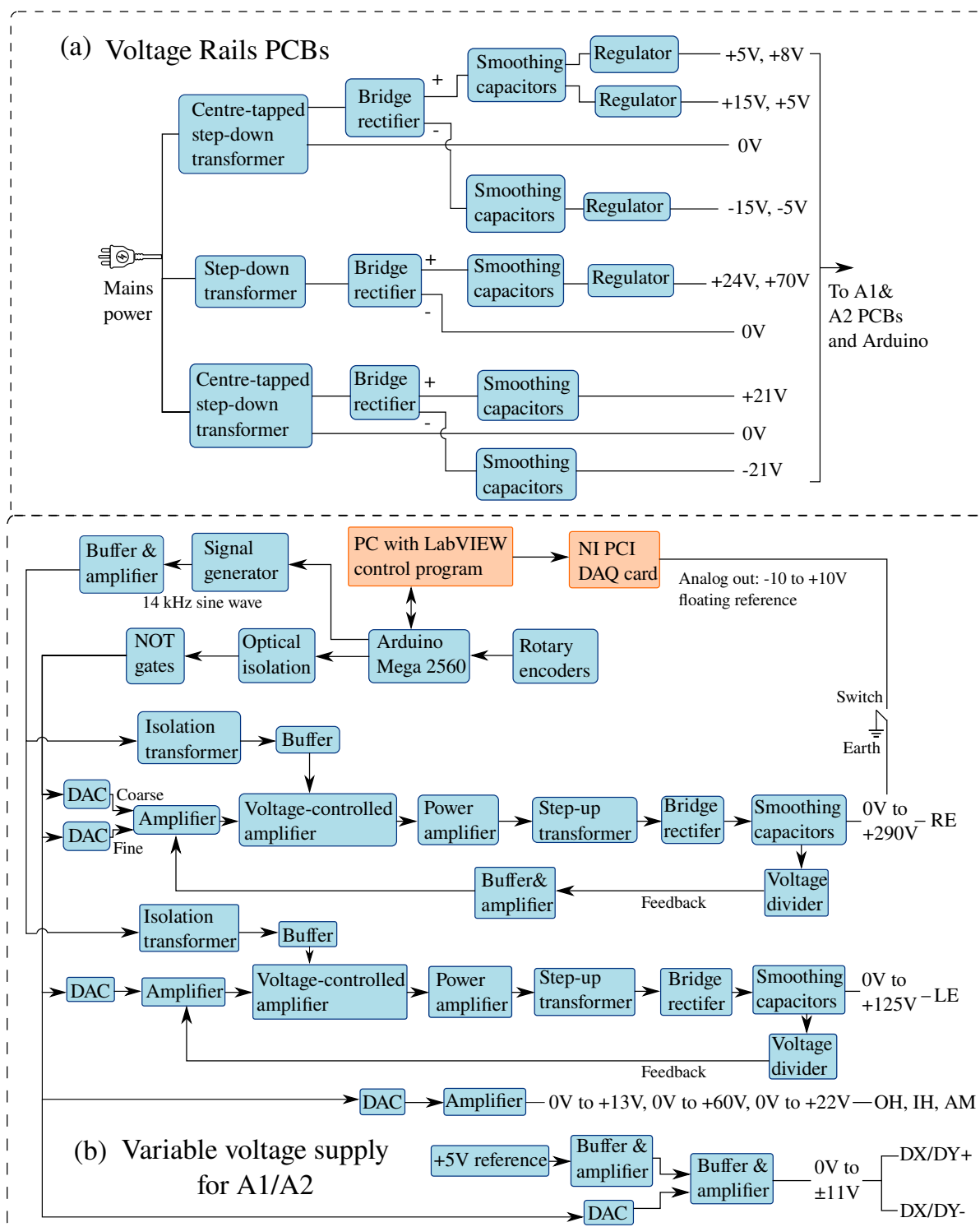


Figure 3.14: A block diagram of the New (e, 2e) electron energy analyser power supplies. A detailed schematic can be found at [120]. A colour key can be found in figure 3.1.

Figure 3.14 shows a block diagram describing the New (e, 2e) electron energy analyser power supplies. The components of the power supplies are contained within four PCBs with an Arduino Mega 2560 mounted on the inside of the front panel. Two PCBs provide the voltage rails to supply the other two PCBs which generate the voltages for each analyser element. Each voltage rail PCB provides voltages ranging from -21 V to +70 V to the variable voltage supplies for analyser 1 (A1) or analyser 2 (A2). The low voltages of ± 5 V, ± 15 V, and +8 V are provided by using a step-down transformer connected to mains AC power followed by a W08G bridge rectifier. The output of the rectifier is then smoothed and is then regulated by a 78xx or 79xx regulator to provide the respective voltages. The reference of these voltages comes from the centre-tap of the step-down transformer. The ± 21 V voltage rail is provided by a 15 V, 3.2 VA centre-tapped step-down transformer followed by a VSIB410 rectifier whose output is smoothed by capacitors. A step-down transformer followed by a W08G bridge rectifier into a 7824 linear regulator provides the +24 V rail. The +70 V rail is provided by a TL783 adjustable regulator which is supplied with the smoothed output from a W08G bridge rectifier.

There is one variable voltage supply PCB for each analyser. These PCBs provide all the voltages for each analyser element via a 15-pin D-sub connector located on the back of the box which house the power supplies. Each voltage element is controlled using an Arduino Mega 2560. For computer-control of the analyser voltages, serial messages are sent from the main LabVIEW control program to the Arduino, which then sends optically-isolated TTL signals (using HCPL2631 optical isolators) to 12-bit MCP4822 DACs via the SPI protocol. The TTL signal is inverted after optical isolation and is then re-inverted by a 74F04 Schottky hex-inverter. Rotary encoders also control the level of output of the DACs via the Arduino. New firmware has been written for the Arduino and is further discussed in section 5.5.

Control of the deflector elements DX/DY are provided by a DAC controlling the input into an OPA4277 amplifier. The output of a Ref02 is buffered and amplified to feed +2.048 V into the second input to the amplifier. The output of the amplifier is then the difference between the DAC output and the reference voltage. This gives a symmetric voltage around 0 V for the positive and negative deflector elements for DX and DY.

Each voltage for the hemispheres is generated by amplifying the voltage set by a DAC. The OPA445 is the amplifier used to generate voltages for AM and IH, with ranges of -15 V to +24 V and -15 V to +70 V respectively. The OPA277 is used to generate a voltage from -15 V to +15 V to supply OH.

The high voltages for LE and RE provided by these supplies are generated by using an isolation transformer whose input is an oscillating 14 kHz sine wave, generated from an ADS9850 signal generator. The ADS9850 output frequency is set by a command from the Arduino via the SPI protocol. The output of the signal generator is buffered and amplified then fed into a 1:1 isolation transformer. The output from this transformer is then buffered and amplified by a SM2018 voltage-controlled amplifier, where the amplifier's gain is set by the output of the DACs. The signal is then amplified by a LM1876 power amplifier followed by a step-up transformer, bridge rectifier, and smoothing capacitors which converts the AC voltage into a smooth DC voltage. A voltage divider provides feedback to the amplifier after the DAC to regulate the output. A high frequency signal is used to generate the DC voltages here, as low peak-to-peak ripple voltage can be

generated with high AC frequencies. This method also reduces the cost of the power supplies as inexpensive transformers can be used to generate the DC voltage required. With this method, the lens element (LE) voltage can be supplied with 0 V to +125 V and residual energy (RE) can be supplied with 0 V to +290 V. One DAC provides coarse control of the RE voltage and the other provides fine control, giving a total 24-bit precision over the voltage. The DAQ card can be connected to RE via a manual switch on top of the power supply. This gives control of the energy of the detected electron via the ADC of the DAQ card, which enables the gun energy and RE to be tracked together, as discussed in chapter 5.

3.7 The Stepper Motor System

Adjustment of the electron energy analyser angles around the interaction region is performed by a stepper motor system, which is detailed in this section. The control system for this varies slightly for each spectrometer.

3.7.1 The Old (e,2e) Stepper Motor System

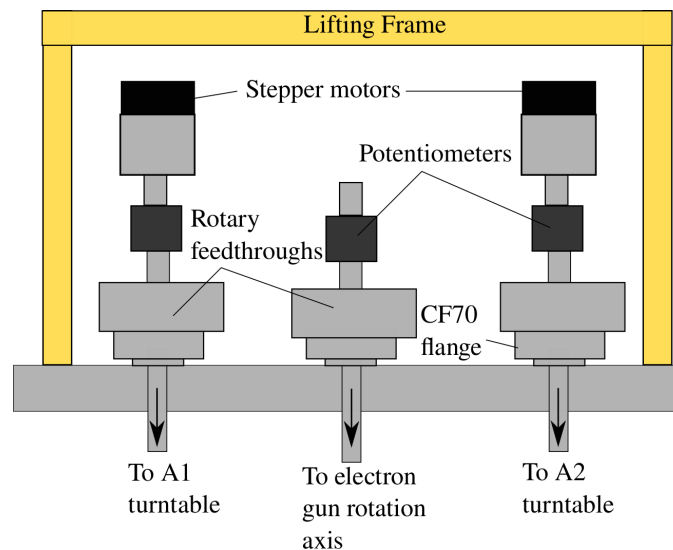


Figure 3.15: Diagram of the Old (e, 2e) stepper motors and rotary feedthroughs mounted on the top flange of the spectrometer. The analyser angles are adjusted by stepper motors whereas the electron gun is rotated manually.

The Old (e, 2e) has two RS PRO Unipolar stepper motors mounted on the top flange of the spectrometer which rotate the analysers. The stepper motors are coupled to the turntables inside the scattering chamber via rotary feedthroughs and an 18:1 gearbox. Turning the stepper motors hence rotates the analysers. The rotary feedthroughs are mounted through CF70 flanges. The rotation of the stepper motors are monitored by a potentiometer connected to an Arduino Mega 2560. The Arduino is also fed signals from opto-interrupter flags based on photodiode-phototransistor pairs. These flags provide signals to a software-based interlock system to avoid collisions when rotating the

analysers. The stepper motors are controlled by the Arduino via L298N drivers. The main control program sends and receives serial messages from the Arduino to control the stepper motors and therefore adjusts the analyser angles. The Arduino also sends the status of the opto-interrupter flags to the user via the LabVIEW interface. A more detailed description of the stepper motor system can be found in [116].

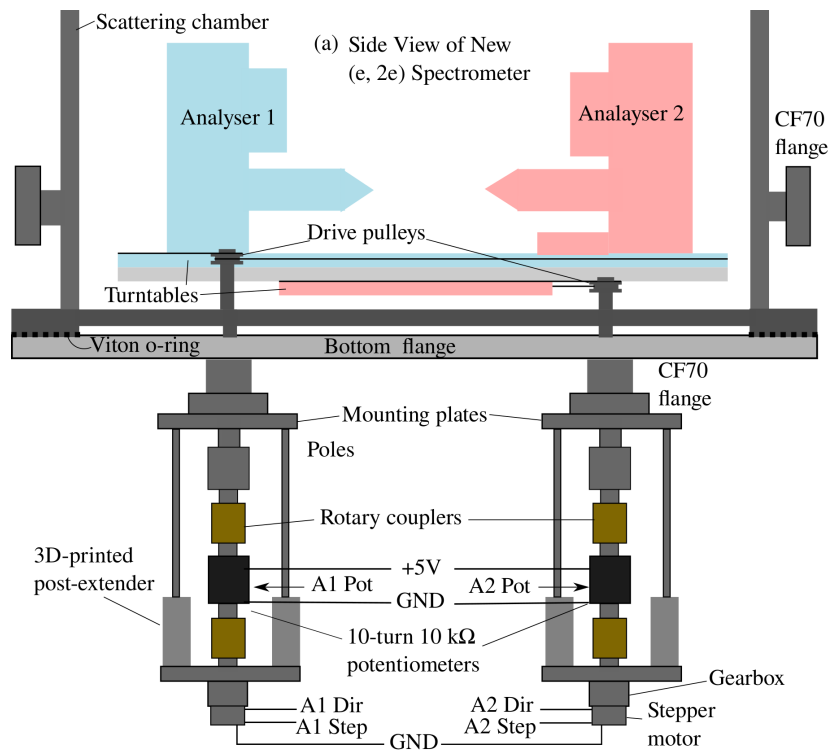
The electron gun is rotated manually using a rotary feedthrough attached to the electron gun axis through a CF70 flange. A potentiometer is used to monitor the electron gun angle in a similar manner to the analysers.

3.7.2 The New (e,2e) Stepper Motor System

In the New (e, 2e) spectrometer, the analysers are mounted on two concentric turntable rings which surround the interaction region. Figure 3.16(a) shows a side view of the turntables and analysers inside the scattering chamber and the stepper motor system underneath the experimental chamber. One analyser is fixed to the inner turntable and the other is fixed to the outer turntable. These turntables are coupled to drive pulleys via PTFE-coated wire, as shown in figure 3.16(b). The ratio of the radius of the drive pulley to the inner and outer turntable is 1:4 and 1:8 respectively. The wire is fixed onto the rim of each turntable at fixation points via two M1 screws. The wire can be put under an appropriate amount of tension by adjustment of the amount of wire wrapped around the drive pulley and the two tensioning wheels. The drive pulleys are coupled to rotary feedthroughs which extend underneath the scattering chamber and connect to rotary couplers. A stepper motor and gearbox can drive the rotation of each turntable through a rotary coupler. In-between the stepper motor and coupler is a 10-turn 10 k Ω potentiometer which monitors the turning of the motor. The stepper motor and gearbox are fixed by two poles and 3D-printed PLA plastic pole extenders, which connect to a mounting plate.

The outer rim of each turntable has a fixed series of crenelations separated by 5°. These crenelations rotate with the turntable and block the signal from opto-interrupter flags placed around the interaction region, as shown in figure 3.4(c). These opto-interrupters consist of a SHF401 and BPX43 infrared photodiode-phototransistor pair which produce a TTL HIGH signal when the diode has line-of-sight of the transistor. When a flag is blocked by a crenelation, a LOW signal is produced. The flags in combination with the crenelations provide a way to measure analyser angles. Signals from end-stop flags are measured by the stepper motor and provide hardware and software interrupts to ensure that the analysers do not crash into any internal instruments when rotating.

A new analyser angle controller system uses an Arduino Nano to control the motor and monitor the angle and the opto-interrupts. The Arduino supplies +5 V across the potentiometer with the wiper connected to the Arduino's ADC. This allows the rotation of the analysers to be monitored and calibrated. The direction and speed of the stepper motor is controlled via two digital pins on the Arduino, which are connected to a drive board. The main control program sends serial messages to the Arduino to control the motor and the Arduino sends serial messages to display the angle and status of the analysers and interrupts. The control firmware and software is detailed in section 5.4.



(b) Top-view of New (e, 2e) Spectrometer

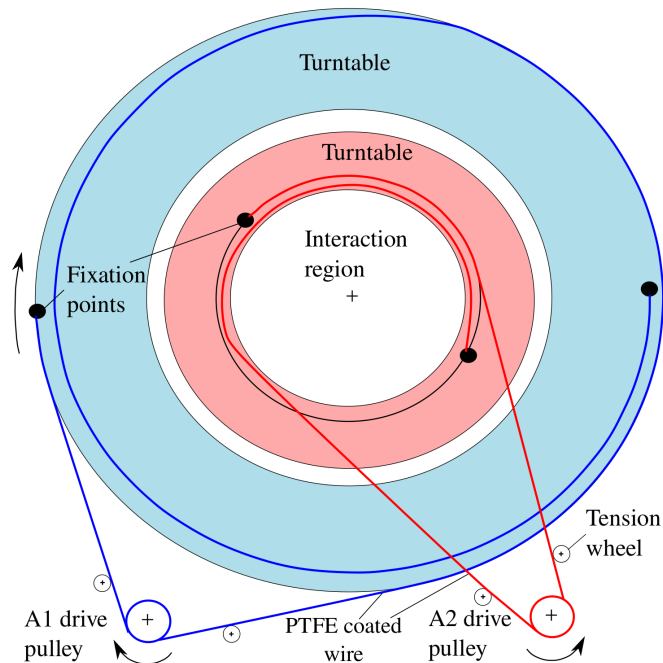


Figure 3.16: (a) shows a side view of the New (e, 2e) spectrometer, showing the components of the analyser movement system. (b) shows a top-down view of the turntables which the analysers are positioned on.

3.8 Atomic Beams

The delivery of a narrow beam of target atoms is essential to perform (e, 2e) experiments. The New (e, 2e) produces a beam of alkali-earth target atoms using an atomic beam oven. A cold trap is used to condense the metal atom beam onto its surface so that the internal surfaces of the spectrometer do not get coated in the target metal. The New and Old (e, 2e) also use a platinum-iridium needle to produce gas jets to study gaseous targets, such as those presented in chapters 6 and 7. In this section, the use of atomic beam ovens and needles to produce atomic beams is discussed.

3.8.1 The Atomic Beam Oven

The atomic beam oven in the New (e, 2e) is used to vaporise solid target elements into a gaseous collimated beam of atoms directed towards the interaction region. The oven is used to produce an atomic beam of strontium, as used in experiments detailed in chapter 8.

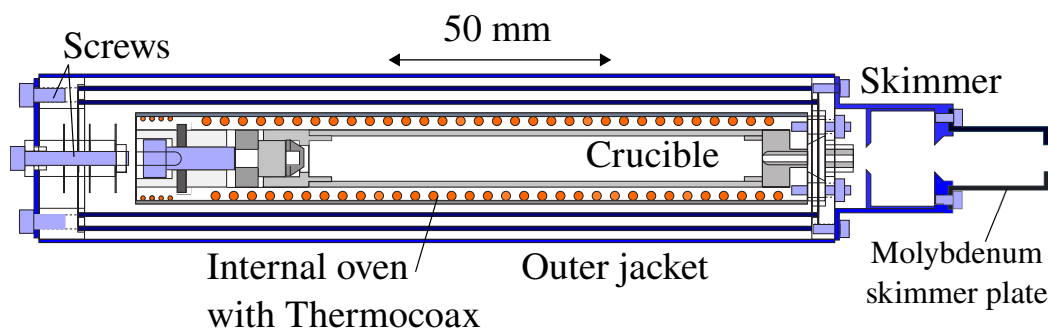


Figure 3.17: A scaled drawing of the atomic beam oven used in the New (e, 2e) spectrometer. A crucible containing a desired target is contained inside an internal cylinder which is heated using Thermocoax. Ceramic rods separate the inner cylinder from layers of heat shielding. A skimmer front-piece is used to direct the gaseous target atoms into a collimated beam.

The design of the atomic beam oven is based on a previous oven detailed in [60]. Figure 3.17 shows a scaled drawing of the atomic beam oven. The oven consists of three concentric, cylindrical, grade 310 stainless steel heat shields surrounding an internal copper jacket. The copper jacket has Thermocoax spiralled around its diameter to heat the entire oven. The internal copper jacket is thermally insulated from the first heat shield layer by ceramic rods and a MACOR piece. Ceramic bolts also secure the outer jacket to the internal oven. The internal oven is designed to be hollow to allow a crucible to slide inside the oven, which contains the target element to be vaporised. When the internal oven is heated, the target inside the crucible heats up to a gaseous state and pressure builds up inside the crucible. The pressure differential between the crucible and outside of the oven directs the gaseous target atoms out of the crucible's nozzle and towards the interaction region. The crucible is made from grade 310 stainless steel and is sealed with an end screw, once filled with the target element. This ensures that the gaseous atoms do not leak from the back of the oven. Once the crucible has been inserted into the oven, a ceramic spacer is placed afterwards and the oven is closed by screwing on a backplate.

A molybdenum skimmer plate is attached to the front of the oven to guide the gaseous atoms into an atomic beam with a narrow beam divergence.

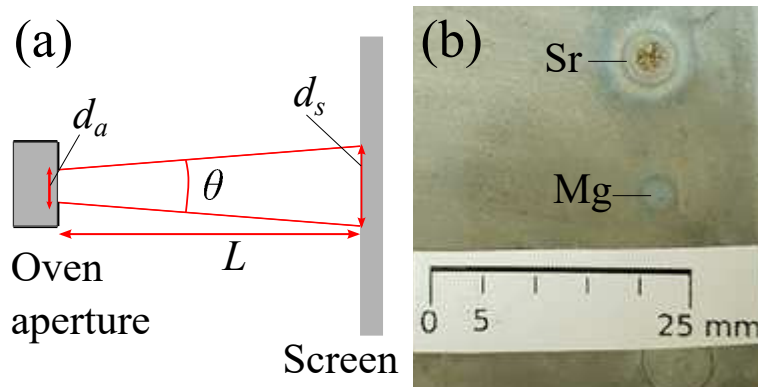


Figure 3.18: (a) shows a diagram of the experimental setup for testing the beam divergence produced by the atomic beam oven. The atomic beam oven has aperture diameter d_a and is length L away from a screen. The atomic beam, with beam divergence θ , makes a spot on the screen with diameter d_s . (b) shows a photograph of a aluminium screen with spots of Sr and Mg deposited by an atomic beam and a scale to make measurements of the diameter.

Figure 3.18(a) shows the experimental setup for measuring the beam divergence produced from the atomic beam oven for calcium, magnesium, and strontium. The oven effuses a beam onto a screen placed at a distance L from the oven. Atoms deposit onto the screen over the period of several days, resulting in a circular spot with diameter d_s . The spots are photographed beside a scale, as shown in figure 3.18(b), and pixels are counted to determine the diameter of the spot. The beam divergence is then estimated as

$$\theta = 2\arctan\left(\frac{d_s - d_a}{2L}\right), \quad (3.4)$$

where d_a is the aperture of the oven. Equation 3.4 assumes that the angular distribution of the atomic beam has a uniform beam profile rather than the more accepted cosine beam profile [121]. The beam divergence is calculated to be $3.7 \pm 0.2^\circ$ for calcium, $5.9 \pm 0.3^\circ$ for magnesium, and $6.7 \pm 0.5^\circ$ for strontium. The spot for calcium was deposited onto an acrylic surface but it was found that magnesium or strontium did not deposit well onto this surface so an aluminium screen was used for these elements. The spot size for magnesium can be measured easily as this appears as one circular spot however the spot for strontium has a halo around an inner spot, as seen in figure 3.18(b). In this case, the beam divergence is calculated from the size of the inner spot.

The temperature of the internal oven determines the evaporation rate of the target in the crucible and therefore the density of atoms in the atomic beam and interaction region. Increasing the temperature of the oven increases the evaporation rate until a maximum is achieved. After this maximum, a critical density is reached where the atomic mean free path decreases with an increase in temperature, hence decreasing the directionality and flow of the atoms effusing from the oven. The flow rate is dictated by the atomic beam flow regime. This can be parameterised by the dimensionless Knudsen number

$$K = \frac{\lambda}{L}, \quad (3.5)$$

where λ is the mean free path and L is the length of the oven aperture [122]. For an effusive flow of atoms from an atomic beam oven, $K \gtrsim 1$ gives a flow regime which increases the

density of atoms with temperature [121]. For lower Knudsen numbers, increasing the oven temperature decreases the atomic density in the beam. Therefore, the temperature to achieve the maximum density of atoms in the atomic beam can be approximated by equating the Knudsen number to 1. Calculations for the Knudsen number for calcium, magnesium, and strontium from the New (e, 2e) atomic beam oven with oven temperature variation can be found in appendix C.

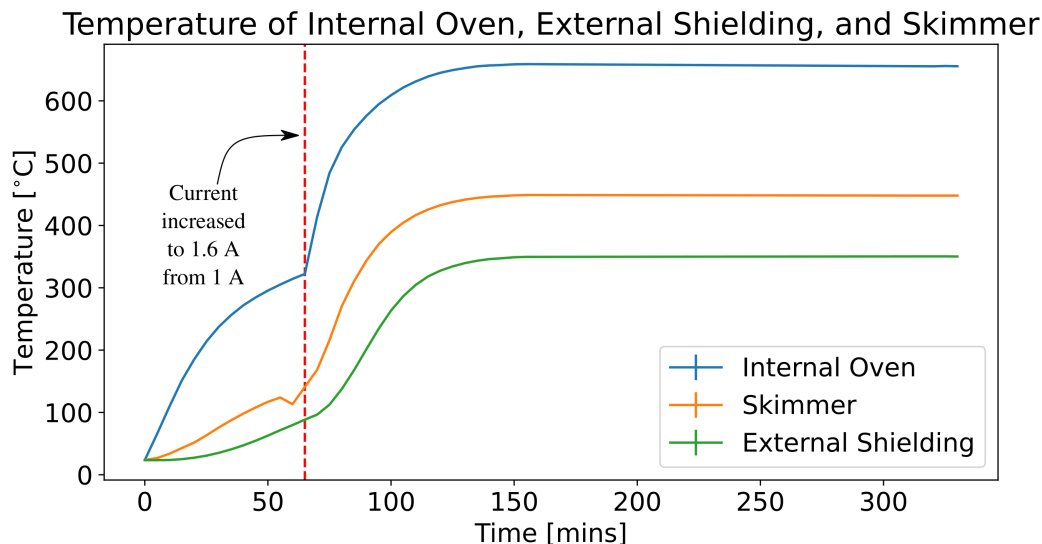
Testing of the thermal properties of the atomic beam oven was performed by attaching three type-K thermocouples to the internal heating cylinder, the surface of the outer jacket, and the front of the skimmer whilst applying varying amounts of current through the Thermocoax using a constant-current power supply. A graph showing the temperature measured over time by these three thermocouples as the current through the Thermocoax increases from 1 A to 1.6 A can be seen in figure 3.19(a). All three components of the oven display a rapid increase in temperature when the current increases and finally settle to an equilibrium temperature. The rapid increase in temperature over a short period of time can put stress on the ceramic parts inside the oven as the coefficient of expansion of ceramic is less than that of stainless steel. If the oven is heated rapidly, the expansion of the internal oven and outer jacket puts stress upon the ceramic rods, bolts, and pieces which can result in cracking. Care must hence be taken to heat the oven slowly over time to reduce the stress on the ceramics. During testing, the temperature was not increased by more than 6 °C per minute by adjusting the current slowly or allowing an equilibrium temperature to be approximately reached before increasing the current. The internal oven has a final equilibrium temperature of around 200 °C higher than the skimmer and around 300 °C higher than the external surface of the oven. This ensures that a pressure gradient is induced by the heating of the crucible, which allows an atomic beam to be directed through the front of the oven and out of the skimmer.

During experiments, the oven temperature is kept constant to ensure that the density in the interaction region is constant. The final equilibrium temperature with applied current can be seen in figure 3.19(b). The data in this figure was collected by monitoring the internal oven equilibrium temperature whilst applying varying currents from a constant-current power supply. A linear fit of the data shows a fairly linear response of final temperature with 338 ± 18 °C/A. The Thermocoax coil has a resistance of 37 Ω so requires a constant current supply which can deliver up to 2 A of current and a DC voltage of 75 V.

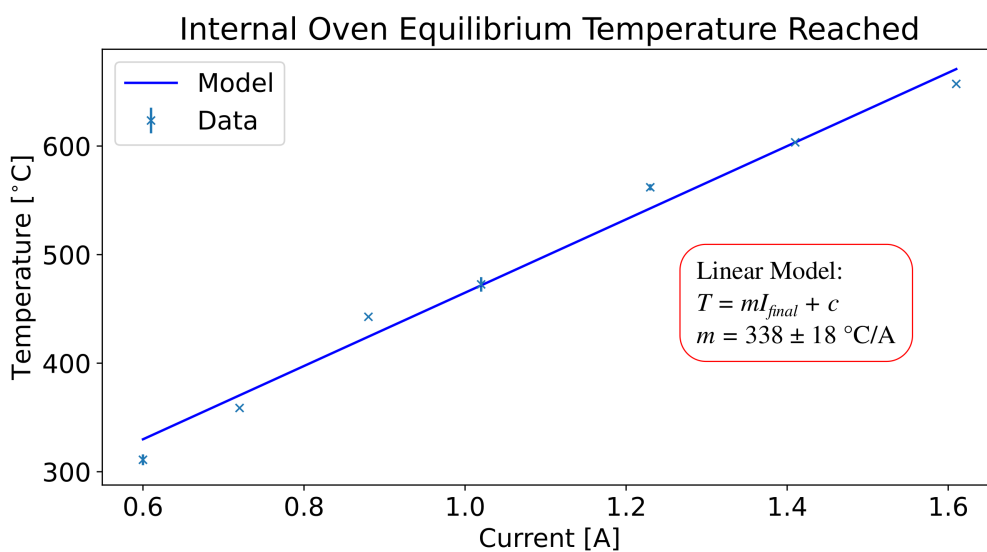
The temperature of the internal oven is monitored with a single type-K thermocouple to adjust the temperature to a value which maximises count rates when setting up an experiment. The type-K thermocouple is input into a handheld HH801A Omega thermometer for easy-readout.

3.8.2 The New (e,2e) Cold Trap

The New (e, 2e) cold trap consists of a stainless steel plate opposite the atomic beam oven, thermally connected to a liquid nitrogen reservoir. Free metal atoms condense onto the cold trap, ensuring that the surfaces of the spectrometer remain free of a coating of the target atom. Coating of the spectrometer with a layer of metal atoms is not desirable



(a) The temperature of the internal heating cylinder, external jacket, and skimmer of the atomic beam oven measured over time for a sudden increase in Thermocoax current.



(b) The internal oven final equilibrium temperature as applied Thermocoax current is varied in the atomic beam oven. A linear model is fit to the data yielding a gradient of 338 ± 18 °C/A. Error bars are present in this graph but are too small to be visible for some data points.

Figure 3.19

as stray charges can build up on the surface and effect the electrostatics in the chamber. Optical feedthroughs also become clouded over and become unusable over time. Another advantage of using a cold trap is that water vapour inside the chamber condenses onto the surface of the trap which decreases the overall pressure inside the chamber by a factor of ~ 2 . The cold trap is cooled by a gravity-fed liquid nitrogen system which is detailed in this section.

A photograph of the New (e, 2e) cold trap system can be seen in figure 3.20(a). The cold trap is located inside the scattering chamber and is thermally connected to the liquid nitrogen (LN₂) reservoir via gravity-fed pipes. A coil heats the dewar at the top flange to ensure that ice does not form on the reservoir, which can cause problems if the seal then freezes. Once filled and the reservoir is at equilibrium, liquid nitrogen slowly boils off from the reservoir and so is re-filled throughout an experiment.

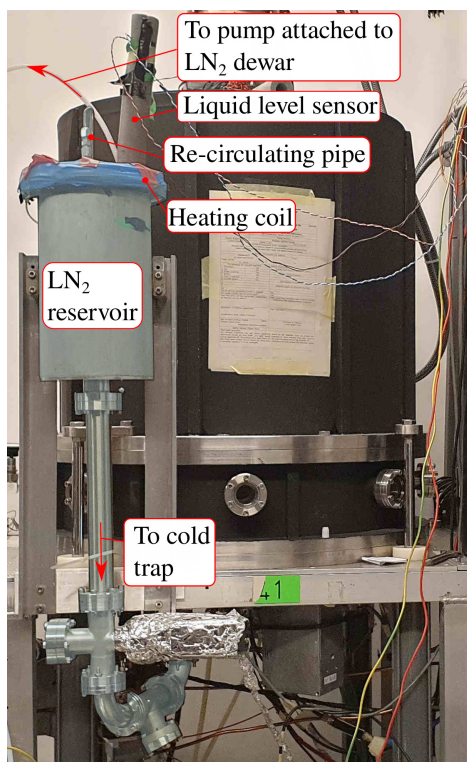
The liquid level of the LN₂ in the reservoir is automatically re-filled by a pump connected to a dewar full of LN₂ and a liquid-level sensing system, as shown in figure 3.20(b). The liquid-level sensor consists of two green LEDs attached to a thin ceramic rod at different positions. Full details of the control system can be found in [123]. The forward voltage of the LEDs V_b is a function of temperature: at room temperature $V_b = 2.5$ V and at LN₂ temperature $V_b = 8$ V. The change of voltage of the LEDs when submerged in LN₂ hence changes the output voltages into an amplifier. When neither LED is submerged in LN₂, the amplifier allows the transistor to turn on the relay to provide power to the filling pump's motor, which pumps LN₂ into the reservoir from the dewar. When both LEDs are submerged in LN₂, the amplifier provides a voltage which turns off the transistor and hence stops the pumping of LN₂, preventing spill-over of the LN₂ in the reservoir. Power is provided to the sensor by a step-down transformer connected to mains power followed by a bridge rectifier and smoothing capacitors, providing ± 12 V DC. A pump switch bypasses the relay and turns on the motor for manual filling of the reservoir, as required.

A dewar full of LN₂ lasts for a few days with this system so the dewar needs to be re-filled during an experiment, as the typical duration of an experiment is on the order of weeks. Running the atomic beam oven at a hotter temperature (e.g. using Ca instead of Mg) leads to larger evaporation of the LN₂, so the dewar must be re-filled more frequently.

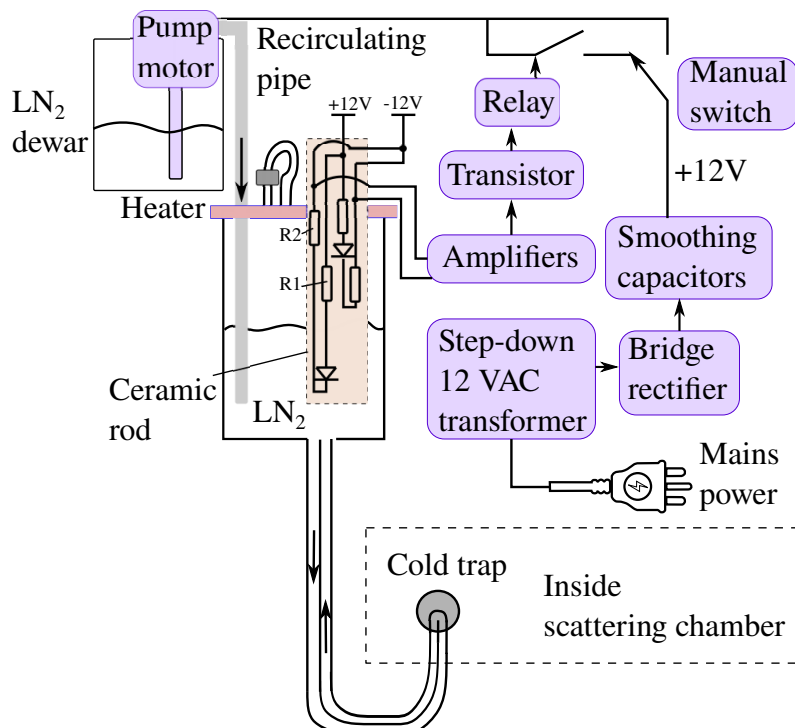
3.8.3 Gas Jets

A gas jet of atoms is supplied to the interaction region in both spectrometers using a platinum-iridium needle. The needle has a small nozzle with an inner diameter of ~ 0.5 mm and an outer diameter of ~ 1 mm, and is placed ~ 10 mm from the interaction region. The source of target atoms comes from a gas bottle outside the chamber, connected to the needle via a series of pipes and Swagelok connectors. The density of gas in the interaction region is controlled via a needle valve placed on the outside of the chamber, which controls the pressure which the gas exits the nozzle.

In the Old (e, 2e), the gas jet is used to supply the xenon and argon in experiments discussed in chapters 6 and 7 respectively. The Old (e, 2e) also has a needle valve which connects to the scattering chamber to provide a background density of gas. This



(a) Annotated photograph of the New (e, 2e) cold trap and liquid nitrogen (LN_2) reservoir.



(b) Diagram showing the gravity-fed, auto-refilling LN_2 cold trap. Resistors $R1 = 8.2 \text{ k}\Omega$ and $R2 = 12 \text{ k}\Omega$. A full schematic of the liquid level sensor can be found in [123].

Figure 3.20

background gas is used to perform (e, 2e) experiments on a xenon-helium mixture as detailed in section 6.4. In the New (e, 2e), the gas jet is principally used to provide a source of helium for calibration experiments as discussed in section 8.3.

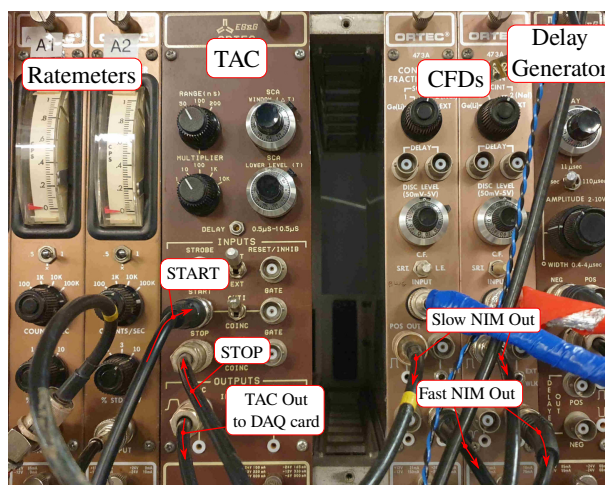
3.9 The Coincidence Timing Electronics

The electronics to detect a coincidence event are discussed in this section. Figure 3.21 shows a photograph and diagram of the timing electronics used in the Old and New (e, 2e) spectrometers. The output of the two CEMs are amplified by a Phillips Scientific 6954 preamplifier in the New (e, 2e) and custom-built preamplifiers in the Old (e, 2e) [112]. The output signal from the preamplifiers is then input into two constant fraction discriminators (CFDs), which outputs a NIM signal if the input is above a set threshold level. Background noise below this threshold value is not passed through the CFDs and is not detected. The CFDs also significantly decrease the final temporal spread of the coincidence signal that occurs due to variations in the height of the CEM pulses. Slow NIM pulses are sent to the two ORTEC 441 ratemeters from the CFDs, which convert the pulses to TTL pulses and send them to the timer/counters on the DAQ card to be counted. The count rates are then displayed and saved by the main program.

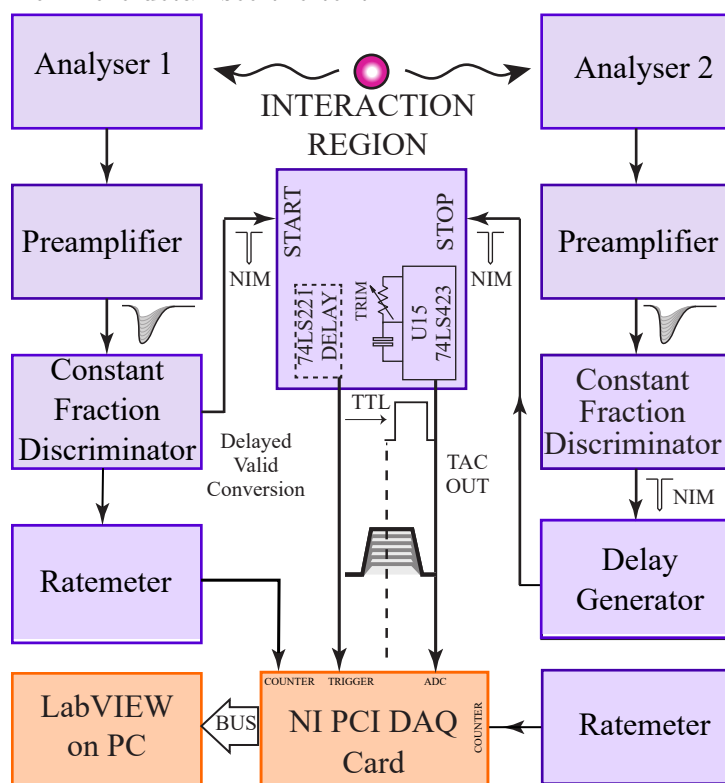
The fast NIM pulses from the CFDs are directed into the start and stop inputs of an ORTEC 567 TAC as shown in 3.21(b). The start pulse triggers a constant current source in the TAC that charges a capacitor C through a resistor R . The current feed is switched off when the stop pulse is received. Since a constant current source is used, the resulting voltage on the capacitor C that has been charged through the resistor R is then directly proportional to the time difference between start and stop inputs. The voltage across the capacitor is amplified to be in the range from 0 V to 10 V, with the timing window selected by both R and C . The TAC outputs this amplified voltage as a pulse of duration $\approx 5 \mu\text{s}$, along with additional TTL signals indicating if a valid start and valid conversion have occurred. Once a TAC output pulse is produced, the capacitor is discharged and the timing triggers are reset so a new timing event can be measured. The fast NIM output of one of the CFDs is delayed using an ORTEC 416A delay generator to position the coincidence peak centrally in the timing window since there is a propagation delay along each signal path due to the electronics and any transmission lines that are used. This delay also allows for different momenta (and hence flight times) of the detected particles.

The 0-10 V output of the TAC is measured by a 16-bit ADC on the DAQ card, which requires $7 \mu\text{s}$ to sample the signal and output a 16-bit level. To ensure the TAC output pulse is sampled at its peak, the DAQ card's ADC conversion process is hardware triggered by the TAC's valid conversion (VC) output. The VC pulse occurs around 320 ns before the peak of the TAC pulse, as can be seen in 3.22(a), and so it must be delayed to ensure conversion occurs at the centre of the TAC output pulse.

The width of the TAC pulse is controlled using the 74LS423 monostable multivibrator on the main TAC PCB. The on-board $20 \text{ k}\Omega$ trim potentiometer is adjusted so that the pulse width is set to a value of $3.2 \mu\text{s}$ as shown in 3.22(a). The positive-transitioning ADC trigger pulse is provided by the circuit in 3.22(b). A 74LS221 monostable multivibrator



(a) An annotated photograph of the timing electronics used in the Old and New (e, 2e) spectrometers. For more detail see the text.



(b) Diagram of the data transfer in the timing electronics. Electron events are detected by CEMs whose outputs are amplified and passed to constant fraction discriminators. A delay is incorporated into one of the signal paths so that the correlated signal is positioned centrally in the TAC timing window. The signals are sent to the start & stop inputs of the TAC which produces an output pulse whose height is proportional to the received signals time difference. The height of the pulse is measured by a LabVIEW-based MCA, which then produces a timing spectrum.

Figure 3.21

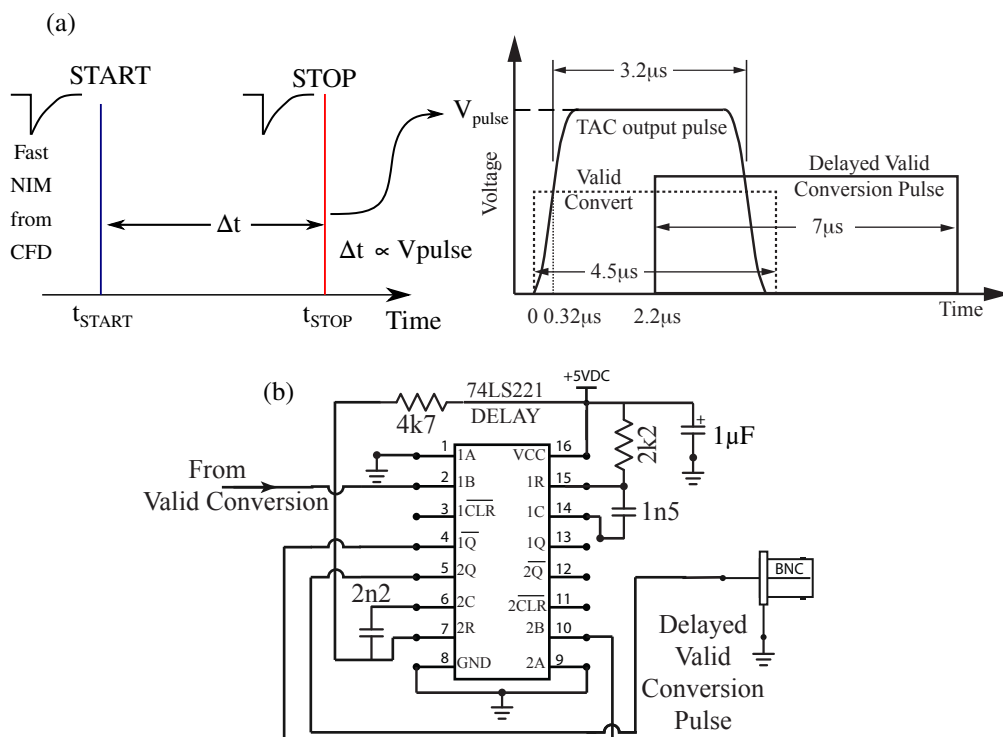


Figure 3.22: (a) shows a timing diagram of the different pulses. The valid conversion pulse arrives 320 ns prior to the TAC pulse and so must be delayed so that the ADC can be triggered by this pulse, which transitions around the centre of the TAC output pulse. (b) shows the circuit built around the 74LS221 that delays the valid conversion pulse so that the ADC samples the signal around the centre of the TAC pulse.

is used to produce a delayed TTL pulse at the output BNC on the rear panel of the TAC, in place of the VC pulse. A 2.2 k Ω resistor and 1.5 nF capacitor set the delay time to be $\sim 2.2\mu s$ as shown, so that this pulse transitions in the centre of the TAC output pulse. This monostable output then triggers the second monostable which delivers a $\sim 7\mu s$ pulse at the output BNC. This pulse width is set to match the ADC conversion time and is sent to the ADC trigger input, as shown in 3.21(b).

The circuit in 3.22(b) is built onto a small PCB directly fixed to the VC BNC on the rear panel of the NIM unit. +5 V DC is brought from the TAC supply rail to power this board. The TAC is then operated as normal. The TAC output is sent to the ADC input of the DAQ card, and the delayed VC pulse is directed to the ADC trigger input. The TAC pulse is read in differential mode so that a common-mode rejection ratio of 100 dB at frequencies up to 60 Hz is ensured. This reduces any noise that is present at mains frequencies on the input signal. The TAC output is connected to the analog input $AI0+$ via RG58 cable and the shield is connected to the $AI0-$ pin.

The analog input is hardware triggered in continuous sample mode. The sample clock is set to the rising edges of the delayed VC signal so readings are triggered as TAC events occur. Each reading is placed in a hardware buffer that can store up to 4095 samples. These are periodically transferred to memory on the PC via direct memory access. This technique allows TAC pulses to be measured at rates of up to 250 kS/s. In practice however the TAC output rate is much lower than this, with typical rates being less than 1 kHz. The 16-bit ADC on the DAQ card hence delivers a timing resolution of ~ 30 ps

when used with a 1000 ns TAC window.

3.10 Summary

In this chapter, the hardware and instruments for both the New (e, 2e) and Old (e, 2e) spectrometers have been detailed. The next chapter will cover the laser system used in experiments discussed in chapter 8, the newly-built laser interlock system, and the optics inside the New (e, 2e) spectrometer.

Chapter 4

Laser & Optics

In this chapter, the laser system used to supply the New (e, 2e) with tunable and stable laser radiation is detailed. First, the optics and sub-systems which comprise the laser are detailed. The newly-built laser interlock system for improving safety in the lab is then discussed. Finally, the half-wave plate rotator and optics inside the New (e, 2e) spectrometer are detailed.

4.1 The Laser System

The New (e, 2e) laser system is composed of a tunable Titanium:Sapphire (Ti:Sa) Matisse TX laser, pumped by a 15 W Millenia Pro 15s laser. The output of the Ti:Sa laser is input into a single harmonic generation (SHG) Matisse WaveTrain frequency-doubler to provide visible light for use in experiments. The laser light is then directed into a fibre-coupler, and then into the New (e, 2e) scattering chamber using multi-mode optical fibre. Due to new health and safety regulations, all laser beams have been enclosed in custom-made enclosures and new interlock systems have been built.

4.1.1 Laser Optics

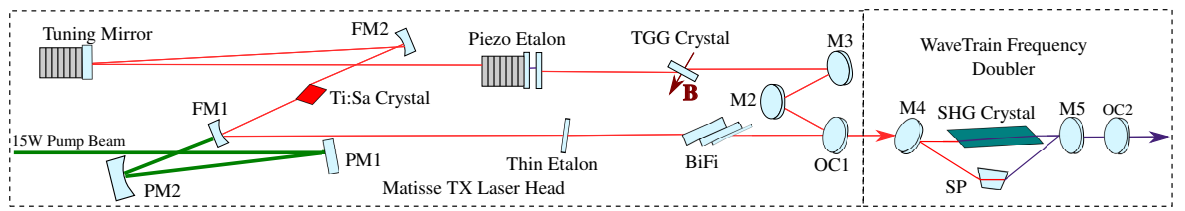


Figure 4.1: Diagram of the optics contained inside the Matisse laser system. A Ti:Sa crystal is pumped by a 15 W pump beam. The Ti:Sa laser cavity is tuned using a tuning mirror, piezo-controlled etalon, birefringent filter (BiFi), and a thin etalon. A Terbium-Gallium-Garnet (TGG) crystal in combination with mirror M2 form an optical diode to ensure the laser radiation only travels in one direction inside the cavity. The output of the Ti:Sa laser head is frequency doubled by a Matisse WaveTrain.

The optics contained inside the Matisse laser system can be seen in figure 4.1. A Millenia Pro 15s laser produces a 15 W pump beam which is steered by pump mirror PM1 onto mirror PM2, which then focusses the beam into the Ti:Sa crystal. The folding mirror FM1 directs a parallel beam after amplification by the Ti:Sa crystal and then FM2 focusses the laser beam back into the crystal after it has travelled around the ring cavity. The Ti:Sa crystal laser gain medium is cooled by temperature-controlled water provided by a Neslab KMC 100 chiller.

The tuning mirror changes the length of the laser cavity by using a long stroke piezoelectric actuator. This mirror is only adjusted when performing significant adjustment of the laser wavelength so is rarely moved during an experiment. The piezo etalon, thin etalon, and birefringent filter (BiFi) are used to finely control the laser wavelength to a desired value, by ensuring that losses occur in the cavity except at the wavelength set by the electronic systems. These elements are interfaced to the electronic systems using a LabVIEW-based control system, which is detailed in section 5.7. The piezo etalon is used to finely control the wavelength with a piezoelectric actuator. The thin etalon is attached to a stepper motor, which provides a coarser tunability by controlling the horizontal tilt angle of the etalon. Rotation of the BiFi assembly using a stepper motor provides additional, broader adjustment to the wavelength compared to the thin etalon.

The mirror M2 is mounted at a different beam height with respect to the main cavity beam and so introduces a rotation of the beam polarisation. The Terbium-Gallium-

Garnet (TGG) crystal lies in a magnetic field generated by two permanent magnets and therefore acts as a Faraday-rotator. This rotates the polarisation of the beam as it passes through the crystal. The mirror M2 and TGG crystal hence form an optical diode which supports lasing in a defined direction. The output coupler OC1 only allows a fraction of light to exit the cavity, the remainder is directed back into the cavity to ensure continuous lasing.

The Matisse Ti:Sa laser operates at its highest power output in the infra-red regime. For experiments detailed in this thesis, the first 1S_0 to 1P_1 transition of alkali-earth metals is investigated which have wavelengths in the optical blue region. A Matisse Wavetrain is therefore used to frequency double the high-power infra-red laser light from the Ti:Sa into visible light. The output of the Ti:Sa laser is focussed onto an SHG crystal by a series of lenses and mirrors, as shown in figure 4.1. The SHG crystal is a non-linear optical medium which generates frequency-doubled light from the input of a fundamental beam. The frequency-doubled beam generated by the crystal is reflected by mirrors M4 and M5 and a steering prism SP, creating a cavity within which resonance can be achieved. The mirrors of the resonant cavity can be adjusted using adjustment knobs on the outside of the cavity housing. The frequency-doubled light exits the cavity through the output coupler OC2, which has a high reflectivity for the fundamental Ti:Sa beam but which has low reflectivity for the frequency doubled beam.

4.1.2 Laser Interlocks

As the laser systems in the lab at Manchester (including the Ti:Sa laser) are high power class 3B and 4 lasers, physical infrastructure is required to protect all lab users. All laser beams have thus been enclosed and two interlock systems have been built for ‘open beam’ and ‘closed beam’ operation of these lasers.

Figure 4.2(a) shows the setup of the laser system and safety interlocks on an optical bench. The Millennia Pro pump laser’s output is fed into the Ti:Sa laser head through a connecting pipe, where an internal shutter is mounted. The output of the Ti:Sa laser then passes through a LaserMet shutter and into the Matisse frequency doubler, separated by a custom-made 3mm-thick aluminium enclosure. The output of the frequency doubler is directed into multi-mode optical fibre, via two mirrors and a fibre-coupler. Another aluminium enclosure fully encloses the fibre-coupler and output of the doubler. The enclosures have been spray-painted matt black to minimise reflections of any scattered laser radiation. An opening on top of the enclosures enables a power meter to be inserted into the path of the laser beam, so as to measure the power of the beam. The laser optics can then be adjusted to peak the power displayed by the power meter. The power meter is attached to an aluminium lid with two neodymium magnets on each side of the lid. When the lids are closed, reed switches on each side of the enclosure openings automatically close, thereby creating a circuit of low resistance. This circuit then enables power to be delivered to the LaserMet shutter via a manually-controlled shutter switch, as shown in figure 4.2(b). The magnetic-lid enclosures and LaserMet shutter form a ‘closed beam’ interlock system. If the magnetic lids are removed, power to the LaserMet shutter is cut and the shutter immediately closes, ensuring that no open beams can be present.

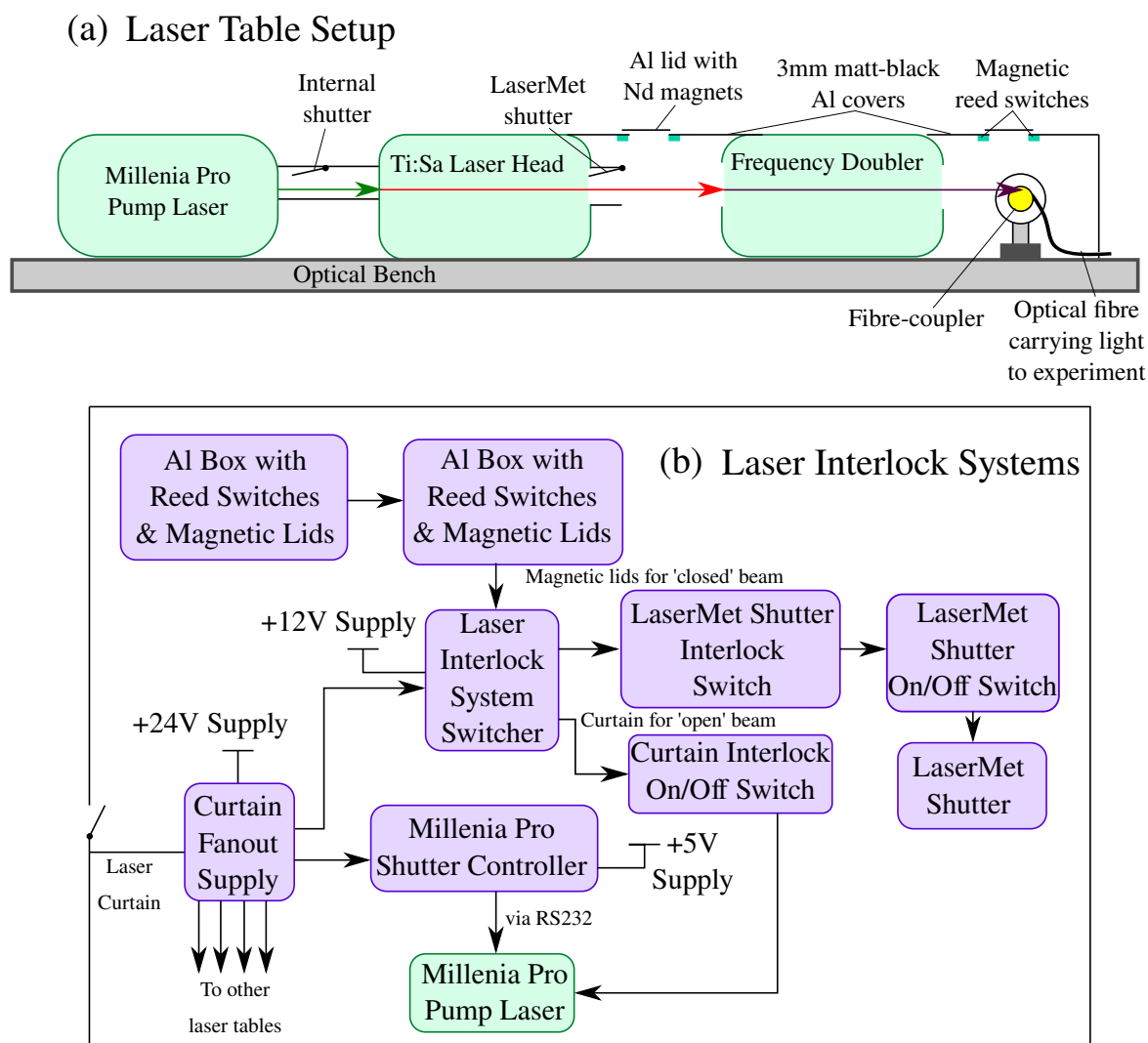


Figure 4.2: (a) shows a block diagram of the arrangement of the laser system on an optical bench. (b) shows a block diagram of the two laser safety interlock systems. For more details see the text. A colour key can be found in figure 3.1.

Sometimes optics inside the laser or on top of a laser table can only be adjusted when the laser beams are not enclosed. In these instances, the lasers are in ‘open beam’ operation and the interlock system is changed. Under open beam conditions, a laser safety curtain surrounding the lab area must be closed, thereby preventing access to the area. Closing this curtain, closes an interlock switch on the curtain. This then produces a short circuit, which is monitored by the curtain fanout supply. This enables magnetic relays in the supply to be closed, as seen in figure 4.3. The curtain signal is then passed onto the laser interlock system switcher circuit. This circuit is composed of a manual toggle switch which changes the laser interlock system from ‘closed’ beam to ‘open’ beam and vice versa. If open beam conditions are selected, the curtain short signal is passed onto the Millenia Pro laser, as seen in figure 4.2(b). The Millenia Pro’s power supply is shut off if the curtain is opened in open beam conditions.

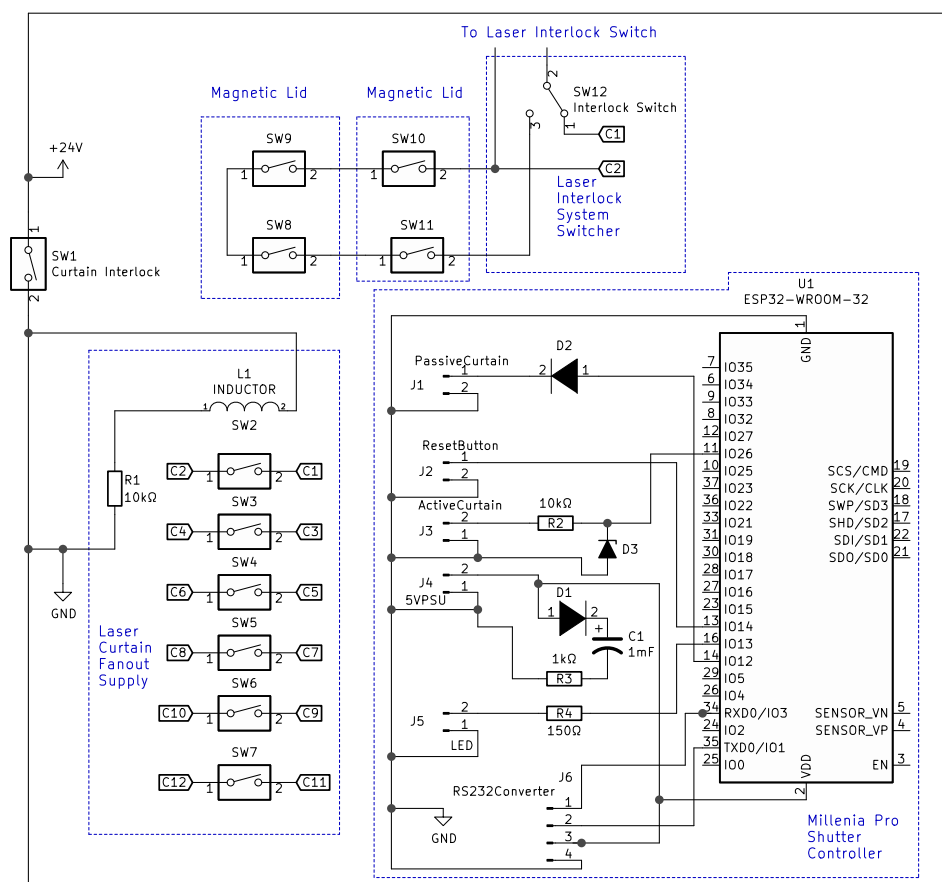


Figure 4.3: Interlock system circuit schematic. The laser curtain fanout supply feeds the laser curtain short circuit to the laser interlock system switcher and the ESP32-based Millenia Pro shutter controller. The magnetic lid interlock is used when under closed beam operation of the laser and the shutter controller is used under open beam operation. The connector J1 is connected to one of the fanout supply outputs for monitoring of the laser curtain. The ESP32 is powered by a +5 V power supply connected to the 5VPSU connector.

The Millenia Pro’s internal shutter provides a better way to interlock the pump laser to the curtain for open beam operation compared to directly shutting off the pump laser power supply. The shutter is operated via RS232 commands sent from an ESP32-based shutter controller, as detailed by the schematic in figure 4.3. The ESP32 [124] monitors the curtain short via I/O pins (connector J1 in figure 4.3) connected to one of the curtain

fanout supply outputs. If the laser curtain opens, the ESP32 detects an open circuit and reads a HIGH TTL signal from its I/O pins due to an internally set pull-up resistor. A LOW signal is hence detected when the circuit is closed. Upon reading a HIGH signal, the ESP32 sends a serial command to the Millenia Pro via a MAX3232 RS232 converter, immediately shutting the mechanical shutter in the laser head. When the curtain circuit is closed again, a reset button must be pressed by the user before the laser shutter opens again. A 20 ms loop continuously checks the status of the curtain interlock. The ESP32-based controller is supplied with a +5 V DC power supply external to the control unit, which is positioned close to the pump laser power supply. If the 5 V DC power is suddenly disrupted, the capacitor C1 provides current to the supply of the ESP32 to ensure that a final close command can be sent to the shutter. A more detailed discussion on this shutter controller can be found in reference [125].

4.2 New (e, 2e) Optics

A multi-mode optical fibre carries laser light through a CF70 flange and into the New (e, 2e) spectrometer. The fibre is directed through a fibre-coupler, fixed onto the top mounting plate, as seen in figure 4.4(a). The laser is collimated and directed into the interaction region and then travels through an optical CF70 window at the bottom of the chamber, where retro-reflection of the beam occurs by a lens and mirror. Retro-reflection of the beam provides up to twice the laser intensity at the interaction region. The lens and mirror are secured onto a matrix plate below the spectrometer as shown. A matt black, 3mm-thick, aluminium enclosure is bolted onto the matrix plate to ensure closed beam safety requirements.

A zero-order half-wave plate (HWP) is used to rotate the polarisation of the laser in the New (e, 2e) spectrometer. The HWP is made of a birefringent material which has a lower refractive index in one (fast) axis of the material, allowing light to travel through this axis faster. This material also has a higher refractive index in the (slow) axis orthogonal to the fast axis. As the incoming laser beam travels through the HWP the components of the beam along the fast and slow axes travel at different rates and the resultant beam's polarisation vector is hence rotated. A rotation of the HWP by an angle θ results in a rotation of the laser polarisation vector by 2θ .

The HWP is attached to a nylon gear, which is rotated by a nylon drive chain attached to a second gear via a rotary feedthrough, as seen in figure 4.4(a). The rotary feedthrough is connected to a 12 V DC motor by a pulley belt. The rotation of the HWP is controlled by the electronics detailed in figure 4.4(b). The main control program interfaces with an Arduino Mega 2560 via USB. The Arduino receives signals from two opto-interrupters surrounding the gear inside the chamber. The rim of the gear has holes every 10° to allow an opto-interrupter to detect the angle through which the HWP is rotated. A single hole is located around the rim of the gear to trigger a response from the second opto-interrupter, thereby defining the position of 0° . When an opto-interrupter is blocked by the gear, a HIGH TTL signal is detected by the Arduino and when unblocked, a LOW signal is detected. The Arduino is programmed to send the current HWP angle to the main controlling LabVIEW program, as detailed in section 5.6. The Arduino uses the

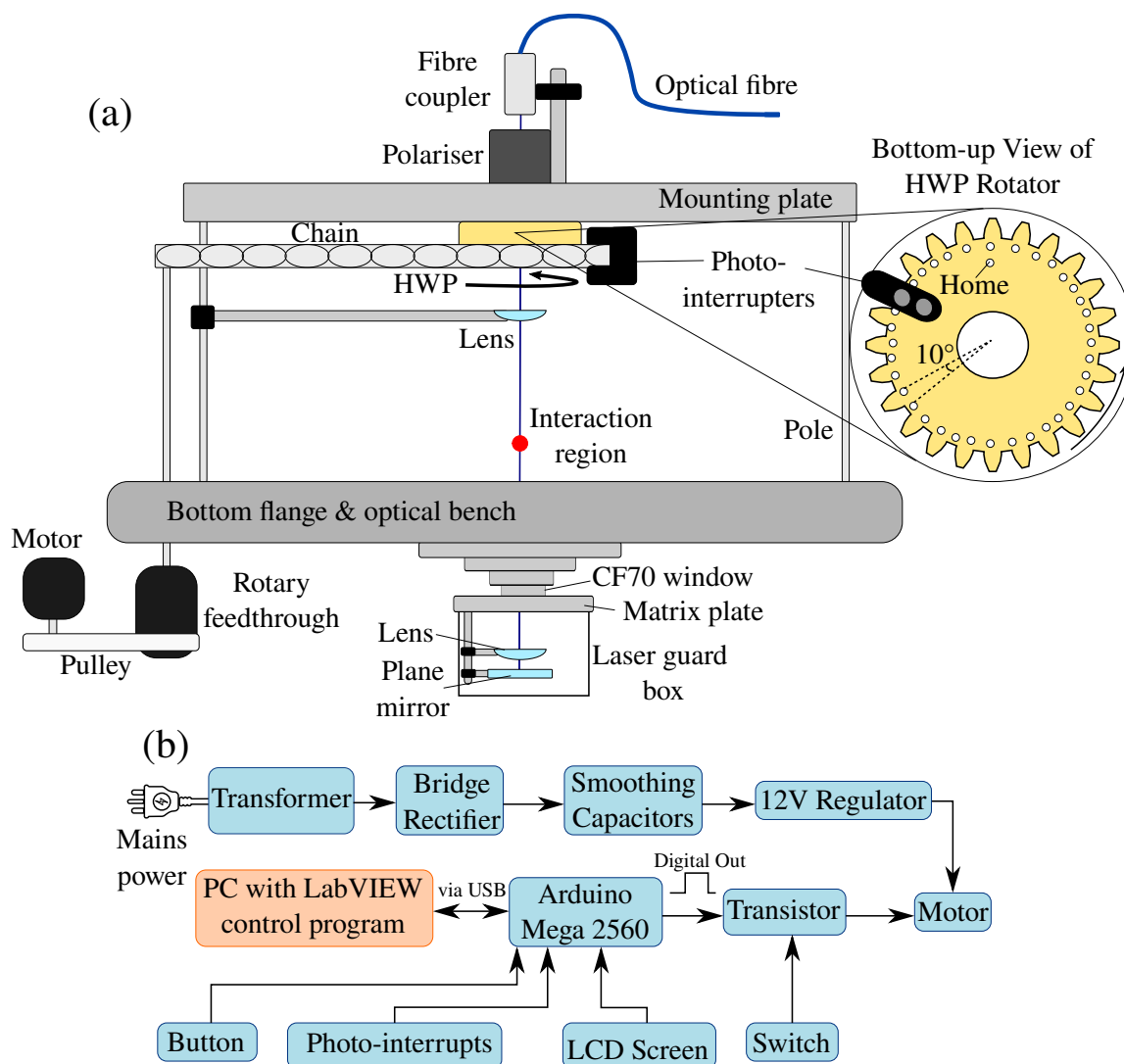


Figure 4.4: (a) shows a diagram of the optics used in the New (e, 2e) spectrometer. A laser is directed through an optical fibre, fibre coupler, and collimating lens, so as to be directed onto the interaction region. Retro-reflection of the laser beam is performed by a mirror and a lens mounted underneath the spectrometer. A half-wave plate (HWP) rotator and polariser control the polarisation of the incident laser. (b) shows a block diagram of the Arduino-based HWP rotator. For more details, see the text. A colour key can be found in figure 3.1. A full schematic can be found in reference [120].

I²C protocol to communicate with an LCD screen, which displays the current angle and any error messages. The Arduino also monitors the state of a push button, which can be used to manually increment the HWP angle. When the user pushes this button or gives a serial command to rotate the HWP, the Arduino produces a HIGH signal on the gate of a T1P121 Darlington power transistor. This transistor allows current from a +12 VDC supply to then activate the motor. The Arduino monitors the amount of time for which the motor is on and stops the motor when the desired angle is reached by producing a LOW signal at the gate of the transistor. The time taken to rotate the HWP by a given angle is measured using the calibration techniques presented in section 5.6. A manual switch allows power to bypass the transistor so as to operate the motor continuously. The +12 V rail is provided by a 7812 linear regulator, supplied from the smoothed and rectified output of a 3.2 VA transformer.

4.3 Summary

This chapter detailed the components in the laser system used in experiments in chapter 8 and also described the newly-built laser interlock system. The optics inside the New (e, 2e) chamber have also been detailed.

In the next chapter, the experimental control firmware and software is discussed. The control of both spectrometers using a LabVIEW-based program which communicates with the individual Arduino-controlled modules is also detailed.

Chapter 5

Experimental Control Firmware & Software

A modular, customisable and low-cost experimental control system for the Old (e, 2e) and New (e, 2e) spectrometers is described in this chapter. A LabVIEW-based main program is used to interface with the Arduino-controlled power supplies, detectors, and stepper motors enabling a variety of different types of experiments to be performed. The structure of the LabVIEW control system and the firmware running on each Arduino module is detailed.

An overview of the structure of the main program is given at the start of this chapter. The communication protocol between the Arduino modules and the LabVIEW main program is then detailed. Monitoring of the system pressure and Faraday cup (FC) current is then discussed. The movement of the analysers is also detailed, along with a discussion of the newly-built New (e, 2e) analyser angle controller system. Control of the power supplies for the gun and analysers is then discussed. Rotation of the half-wave plate (HWP) in the New (e, 2e) is then detailed. The LabVIEW-based laser-locking program is then presented, followed by a description of the software-based multi-channel analyser (MCA). Finally, the experiments which the main program can run are detailed, followed by a discussion of the experimental data-processing workflow.

The control system detailed in this chapter has been published in [76]. By using version-controlling tools, such as Git [126], the control software is easier to customise and multiple experimenters can edit the software concurrently. The control software is hence available in reference [119].

5.1 Overview of the Main Program

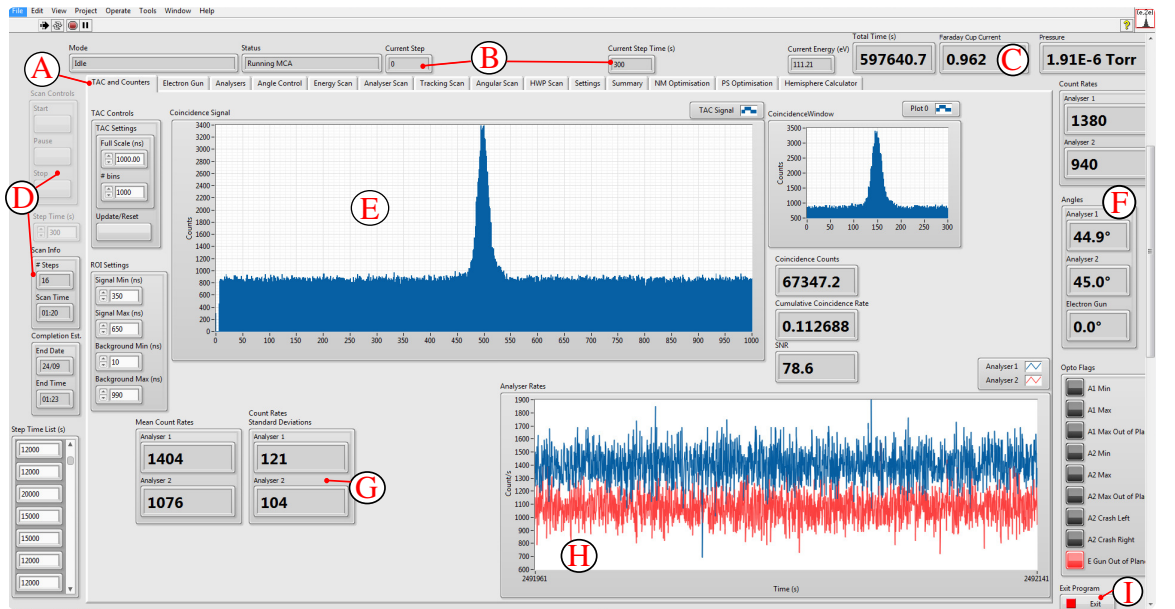


Figure 5.1: A screenshot of the main program under the TAC and counters tab. Label A shows the tab control, B shows the current experiment step and next action queue, C shows the Faraday cup current and pressure, D shows the scan information and step time controls, E shows the MCA histogram, F shows the analyser count rates and angles (and Old (e, 2e) electron gun angles), G shows the running mean and standard deviation of analyser counts, H shows analyser count rates plotted over time, and I shows the exit button to close the program safely.

Both spectrometers in Manchester are controlled by a program written in National Instruments' LabVIEW language [78] which runs on a PC with Microsoft Windows. Since each spectrometer is broadly similar and designed to perform an overlapping range of experiments, a single LabVIEW program was developed to control both spectrometers. All experiments carried out by the spectrometers are set up and automatically controlled from this program.

A graphical user interface (GUI) provides real time monitoring of the experimental parameters including vacuum pressure, FC current, all power supply voltages, electron gun and analyser angles, analyser count rates and the coincidence signal. To achieve this, the GUI is split across several tabbed screens. The most pertinent information such as count rates and their charted history, coincidence counts, analyser angles, the experiment dwell time, gun current and pressure are overlaid on all tabs. The TAC and counters tab (shown in figure 5.1) provides a real time display of coincidence events, as captured by the onboard MCA. The time-averaged count rates detected by both analysers are displayed. The MCA window settings can be adjusted in this tab to set the region of interest around the coincidence peak and the region within the timing window where the random background rate can be determined. The true coincidence count rate is then calculated by subtracting the background rate from the measured count rate in this region of interest.

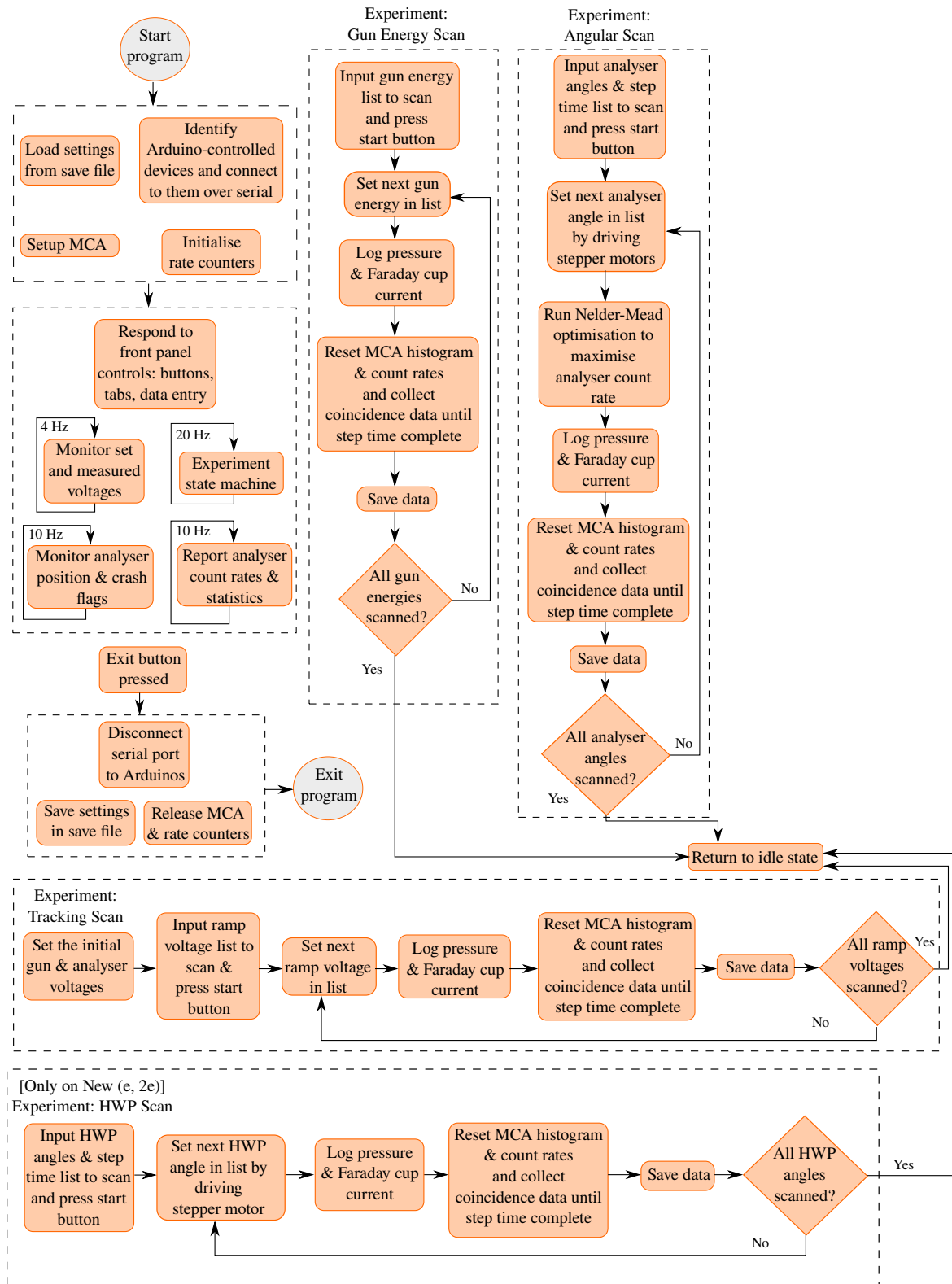


Figure 5.2: A block diagram showing the structure of the main LabVIEW program. After initialisation and setting up of devices, the program is run in a state machine architecture with several loops running concurrently. If an experiment is chosen by the user, the state machine runs the experiment in a loop until finished.

To enable real time data collection and control of the spectrometer, the program is designed as shown in figure 5.2. At commencement of the program, the settings from the

previous session are loaded. The PCI-6221 DAQ card is then configured to act as rate meters for the two electron energy analysers and to provide multi-channel analysis of the coincidence signal. The Arduino control modules are then identified and connected to the program via USB. This is implemented by opening connections to all serial peripherals and sending an 'ID' request. Each unit responds with a unique identifier, so that the LabVIEW program can establish which unit is located at each USB port. As an example, 'AN' is the identifier for the power supply for the analysers in the New (e, 2e).

After these initialisation steps, the program starts running five parallel loops as shown in figure 5.2. The first loop utilises an event structure which only loops in response to user interactions with the GUI. In this case, new voltages or angles are sent to the relevant Arduino, and experiments are started or stopped by queuing up a series of states to be carried out by the experiment state machine handling the 'while' loop. By handling GUI interactions in this separate loop, the user retains overriding control over the apparatus and can immediately amend, pause or cancel actions at any time. When the GUI's start button is pressed, a series of tasks are queued up to be implemented by the experiment state machine loop. This could be a gun energy scan, angular scan, tracking scan, or HWP scan as shown in figure 5.2 and depends on which tab is currently selected in the GUI.

The experiment state machine loop runs at 20 Hz and performs a variety of tasks depending on which mode the program is in. Unless an experiment is in process, the loop continuously executes an 'idle' state where the coincidence histogram is updated. During an energy scan or angular scan, the state machine iterates through a series of tasks until all the steps required by the experiment are completed. If the experiment needs to be paused or modified, appropriate pause states are injected into the state queue. As an example, in the case of an angular scan the initial state of the spectrometer is written to a save file and the analysers are moved to their start positions. The analyser focus lenses and steering deflector voltages are then automatically adjusted by a modified Nelder-Mead optimisation routine [127] in order to maximise the electron signal received from the interaction region. Each time this runs, all the voltages, count rates, electron gun current, and background pressure readings are written to the current-step section of the save file and the experiment is then started. This runs for the configured step dwell-time while the analyser count rates and coincidence counts are continuously monitored. These are also then written to the current-step section of the save file. These steps are repeated until the experiment is completed or the user intervenes.

The purpose of the optimisation technique is to ensure that the spectrometer remains at its optimum tuning condition as the experiments continue over multiple sweeps of the detection plane, without the need for operator intervention. This technique hence allows for any drift or changes in the operating conditions over the extended periods of time required for the experiments (up to several weeks of continuous running may be required to ensure a good signal to noise ratio in the coincidence cross section). By automatically tuning the spectrometer lens elements at each angle, the cross section is then built up over time to increase the statistical accuracy of the data.

The remaining three loops run continuously to provide real time information about the experimental conditions within the spectrometer. The 'monitor set and measured voltages' loop runs at 4 Hz and continuously polls the electron gun and analyser power

supplies in order to report the set and measured voltages on the LabVIEW GUI. This allows real-time values to be written to the save file. The ‘monitor analyser position and crash flags loop’ operates at 10 Hz and communicates the angles of the analysers and electron gun within the spectrometer. The status of the opto-interrupters are also displayed within the GUI at all times. The final loop, also operating at 10 Hz, reports the analyser real-time count rates, count rate history chart and count rate statistics. The history chart greatly aids in manual tuning of the electron gun and analyser voltages in order to optimise the electron counts from the interaction region, by providing immediate visual feedback to the user.

The program continues running until the exit program button is pressed. This triggers the PCI-6221 DAQ card hardware locks to be released, the serial connections to the various Arduinos to be closed, and the program state to be saved to a settings file for reuse on the next program start-up. In practice the program is only terminated when a Windows Update needs to restart the controlling PC, so that the spectrometer conditions can be ascertained at all times.

All experiments are logged to a JavaScript Object Notation ([JSON](#)) formatted save file. At the start of each experiment a summary section is written where all experimental parameters are logged, together with a plain-text description of the experiment. At each step in the experiment, all parameters including the voltages, beam current and count rates are again logged so that any long term drifts present in the operating conditions can be monitored, investigated and corrected. By comprehensively logging every parameter the experimental conditions can be fully recreated at a later date. A python script also creates a summary of the data in a comma-separated value ([CSV](#)) file, containing the most important scan information such as the scan variable and count rates. Real-time data analysis is performed from the JSON files using python in a Jupyter environment [[128](#)].

5.2 Arduino-LabVIEW Serial Protocol

The Arduino modules and LabVIEW main program communicate via a serial protocol, as shown in figure [5.3](#). The Arduino modules are connected to the LabVIEW main program by opening all the ports connected to the PC and identifying the serial-compatible devices. The serial command ‘ID’ and the corresponding checksum character is sent out to all these devices. The Arduino modules, upon receiving the ID message, send their unique identification strings. After waiting 5 ms for a response, the main program then reads the serial buffer and checks if the string sent by the Arduino matches with any valid IDs. If no ID is read after 50 tries, then the connected serial port is closed and an error is raised. If a valid ID is matched, the serial port to the matched Arduino is set up with a 250,000 bits/s baud rate with 8 data bits and a line feed as a termination character.

The LabVIEW program sends a command to the Arduino by sending a specific message followed by a checksum character, and is then terminated by a line feed. If the checksum at the end of the serial message matches with the checksum calculated by the Arduino, the message is then accepted. If the message corresponds to a recognised command, the Arduino accepts the command and shifts into the corresponding state and/or per-

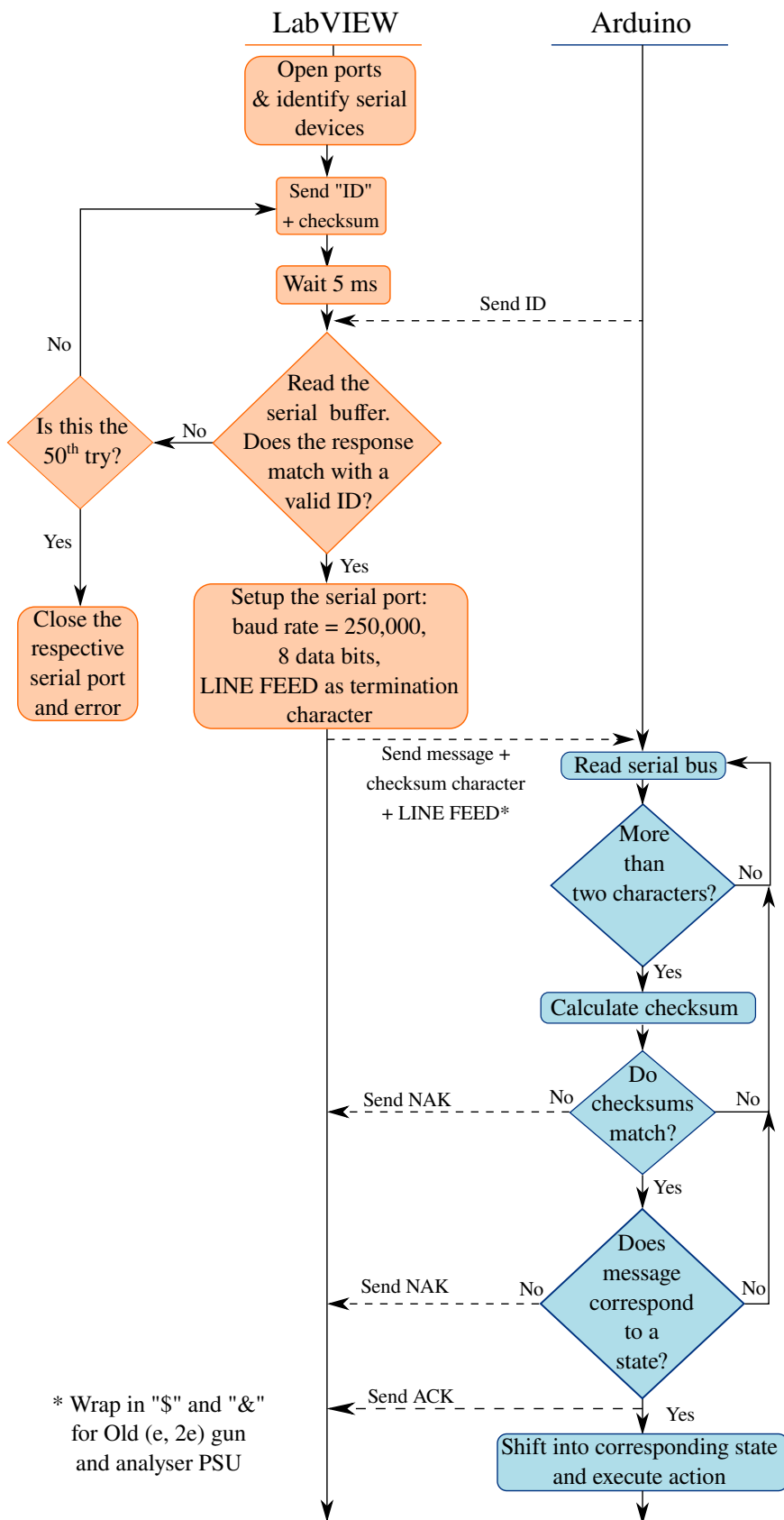


Figure 5.3: A block diagram showing the serial protocol for communication between the Arduino-controlled modules and the LabVIEW main program. A colour key can be found in figure 3.1.

forms the action required. An ‘ACK’ is sent to the LabVIEW program if a command is acknowledged and a ‘NAK’ is sent if the checksums do not match or the command is not acknowledged. The gun and analyser power supplies for the Old (e, 2e) require an extra ‘\$’ character to acknowledge the start of a message and an ‘&’ character as the termination character.

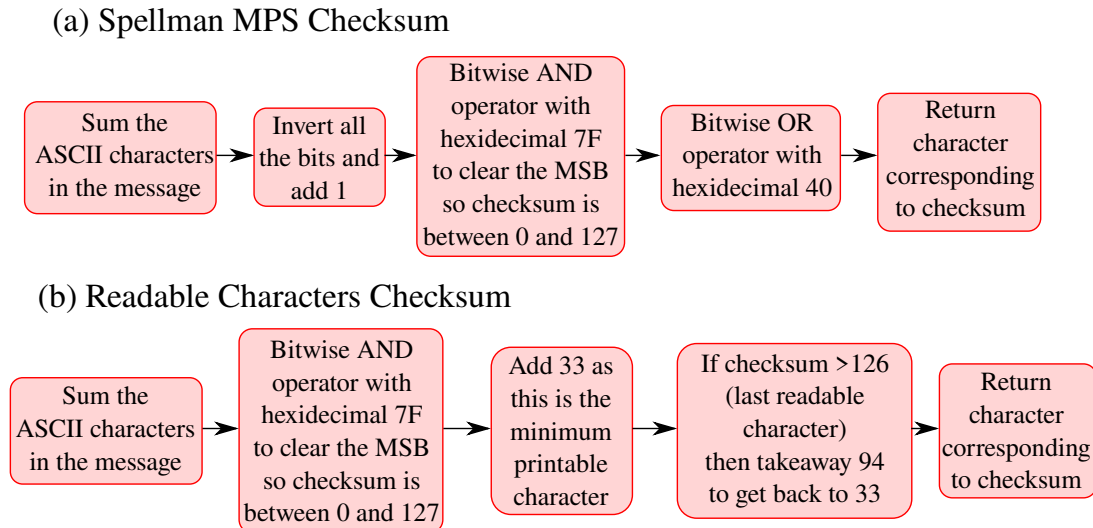


Figure 5.4: A block diagram showing the Spellman MPS and Readable Characters functions to calculate checksums. A checksum is calculated using the characters in a serial message and appended to the end of the message.

The checksum of a message is determined by a function which uses all of the characters in the message. Once the checksum is calculated it is appended to the end of the message. Any errors in these messages can cause critical failure of instruments, for example moving the analysers to an angle out of range can cause collisions inside the chamber. The checksum therefore ensures that errors in messages due to bit flips or noise are not accepted by the Arduino modules. The New (e, 2e) uses a ‘Readable Characters’ checksum whilst the Old (e, 2e) uses a checksum based on the Spellman MPS series of power supplies [129], as seen in figure 5.4. The Spellman MPS checksum is calculated by summing all of the American Standard Code for Information Interchange (ASCII) values of each character in the message (see appendix D), inverting the bits in the calculated sum, and performing a bitwise AND with the hexadecimal value 7F to clear the most significant bit (MSB). This ensures that the result is in decimal and is between 0 and 127. This result is then bitwise OR operated with the hexadecimal 40 and returned as the final checksum.

The Readable Characters checksum method is similar to the Spellman MPS method, where the characters in the message are summed and the MSB is cleared. The number 33 is then added to the result and if the checksum is larger than 126, 94 is taken away from the result. The character is then returned as the final checksum. This method constrains the checksum to human-readable characters, as 33 represents the minimum readable character in ASCII. Using this method makes manually sending and receiving serial commands to devices easier for the user.

5.3 Faraday Cup Current & Pressure Measurements

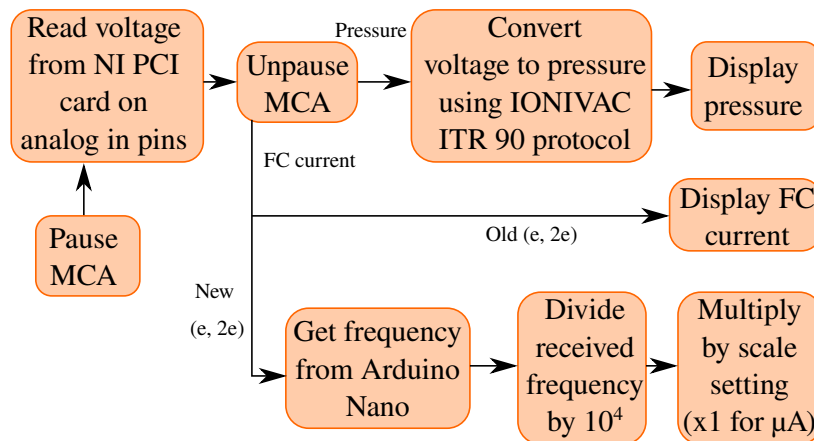


Figure 5.5: A block diagram of the Faraday cup current and pressure measurement in the LabVIEW control program for both Old (e, 2e) and New (e, 2e) spectrometers. A colour key can be seen in figure 3.1.

The FC current and pressure are monitored continuously in the ‘idle’ state of the main program. The Ionivac pressure gauge outputs a voltage to the DAQ card’s analog pin, which is read using the on-board 16-bit ADC. This voltage V is converted to a pressure P using

$$P = 10^{\left(\frac{V-7.75}{0.75} - 0.125\right)}, \quad (5.1)$$

which is found in the datasheet of the gauge [130]. The FC current in the Old (e, 2e) is calculated by multiplying the voltage on the DAQ card’s respective analog pin by $1 \mu\text{A}$, as noted in section 3.4. The ADC on the DAQ card cannot perform multiple readings at one time. The MCA is therefore paused before the voltages for the pressure and current are read and then unpaused after readings are taken, as seen in figure 5.5.

In the New (e, 2e), a custom-built electrometer outputs a TTL signal with a frequency of 10 kHz proportional to the FC current measured, multiplied by a manually-set scale setting. This signal is input into an I/O pin of an Arduino Nano to measure the frequency and to send the measurement to the main control program via USB. The frequency value sent by the Arduino is divided by 10^4 to convert the reading to μA and then is multiplied by the scale setting.

The firmware and application programming interface (API) of the New (e, 2e) Arduino-based current monitor is described in figure 5.6. An I/O pin on the Arduino is set up in the firmware as an interrupt pin and connected to the output of the electrometer. When the signal from the electrometer reaches a falling edge, the time t_1 is recorded by the Arduino’s in-built timer. The difference between this new time and an older time t_0 is calculated as Δt and the frequency $1/\Delta t$ is calculated. The new time t_1 is then set to the old time t_0 . A new reading flag is set to a binary TRUE value and a frequency value is sent to the main program if prompted with the get frequency command ‘GF’. The command to get the frequency from the Arduino is sent after the MCA is unpaused in the main program’s experimental state machine loop, as seen in figure 5.5. The current monitor can be set to print continuous current readings to the serial communication line

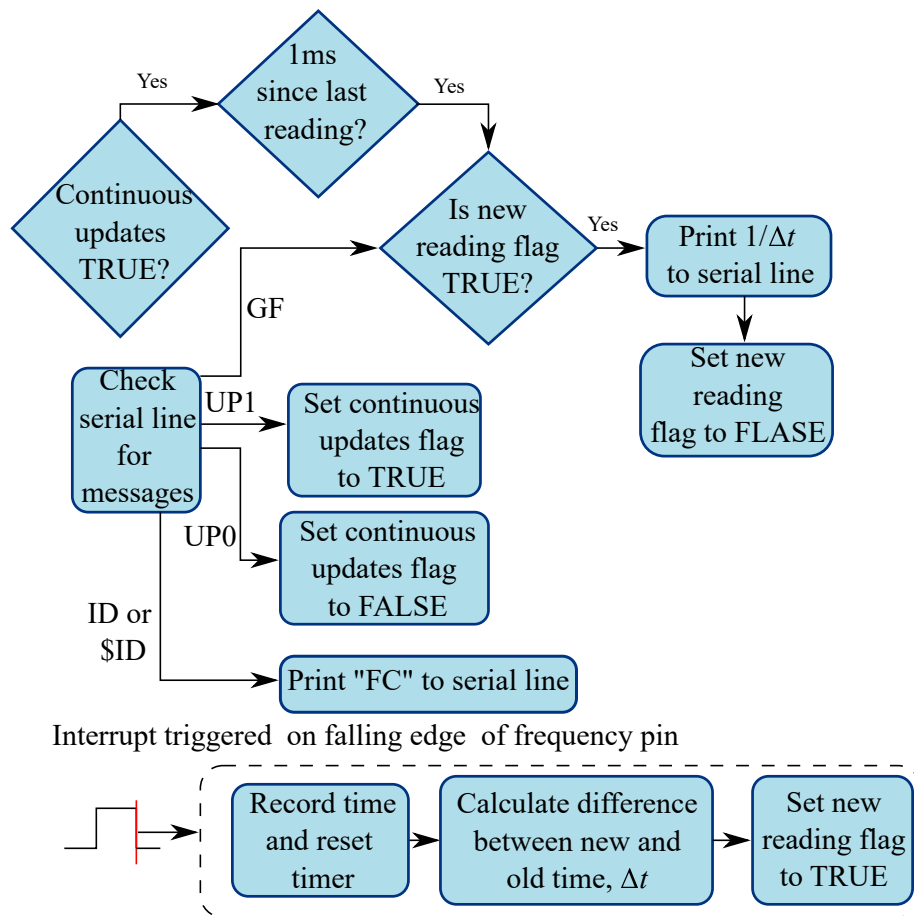


Figure 5.6: A block diagram showing the interfacing commands which can be sent to the Arduino-based FC current monitor in the New (e, 2e). The structure of the firmware which measures the frequency of the electrometer's output is also detailed.

if the command ‘UP1’ is given. This mode can be turned off by sending the command ‘UP0’. Sending the command ‘ID’ or ‘\$ID’ to the device prints ‘FC’ to the main control program via the serial line.

5.4 Analyser Movement

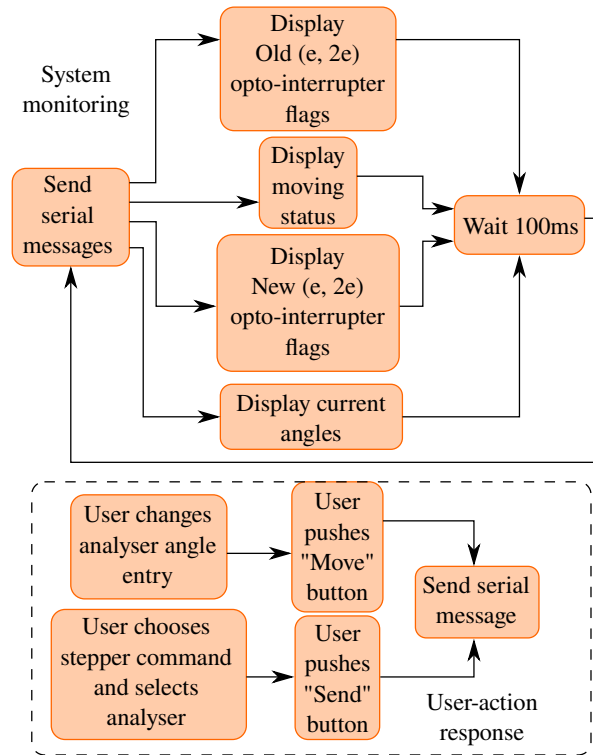


Figure 5.7: A block diagram showing the logic which monitors and controls the movement of the analysers in the main control program.

The main program monitors and controls the position of the analysers, as seen in figure 5.7. Every 100 ms, serial messages are sent to the Arduino unit which controls and monitor the stepper motors and opto-interrupter flags. The current analyser angles and moving status of the analysers are measured by the Arduino and sent to the main program via the serial line. This data is then displayed in the main program to the user. The New (e, 2e) and Old (e, 2e) spectrometers have opto-interrupters measuring different flags and so the displayed flags depend on the spectrometer in use. The New (e, 2e) flags are measured by the Arduino and sent via serial messages to the main program, whilst the Old (e, 2e) flags are measured by digital pins on the DAQ card.

The user of the main program can change the analyser angle and send serial commands to the Arduino under the ‘Angle Control’ tab, as seen in figure 5.8. Under this tab, the user can change the set angle for each analyser and send a command to move each analyser to their set angles. An interface box for sending direct commands over the serial line to the Arduino and the Arduino’s response to these commands are also shown in this tab. Serial messages can also be sent to adjust the minimum and maximum speed and acceleration of the stepper motors. The command to move the analysers to a preset ‘home’ angle can also be sent here. Commands setting the home angle and the angle limits can also be sent

over the serial line using this interface. The full [API](#) for the movement of the analysers can be found in [appendix D](#).

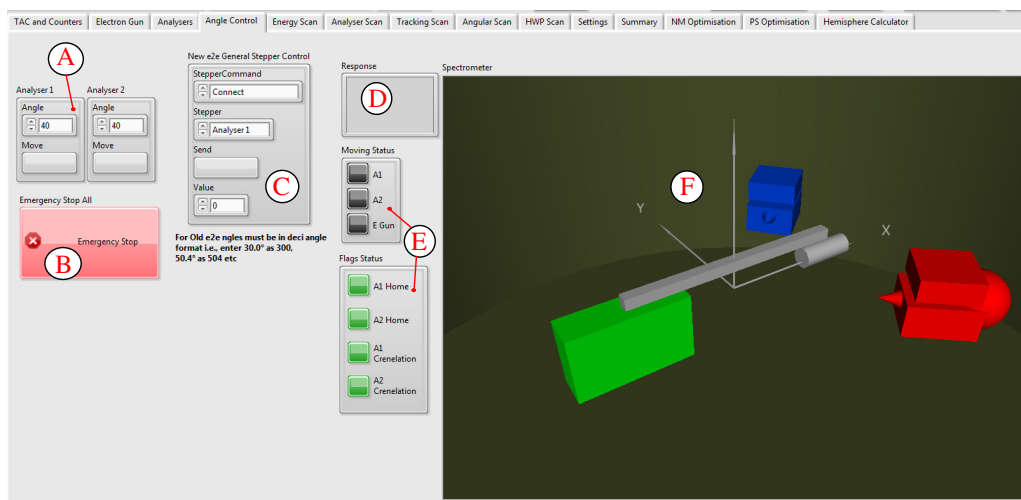


Figure 5.8: A screenshot showing the controls for the movement of the analysers. Label A shows where the user enters set angles and can push a ‘Move’ button to move the analyser to the set angle, B shows the emergency stop button, C shows an interface box to send commands to the Arduino, D shows a dialog box reading the response of the Arduino to serial commands, E is where the opto-interrupter flags status are shown, and F shows a 3D representation of the position of the analysers (blue and red) with respect to the electron gun (green).

In the angle control tab shown in [figure 5.8](#), the New (e, 2e) opto-interrupter flags show whether the analyser is at the ‘home’ angle and/or that a 5° crenelation has been detected. The moving status of both analysers and the Old (e, 2e) electron gun are shown. In the case where the opto-interrupters fail and the stepper motor keeps driving past safe angular limits, an emergency stop button can be pressed which exits the main program and stops the stepper motors immediately. A 3D representation of the geometry of the analysers and electron gun in the scattering chamber is also drawn in this tab.

5.4.1 The New (e, 2e) Analyser Angle Controller

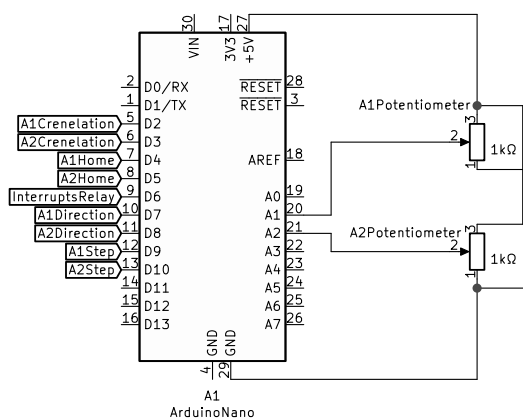


Figure 5.9: The pinout for the New (e, 2e) Arduino-based stepper controller.

A new analyser angle controller system has been built for the New (e, 2e) spectrometer using an Arduino Nano to control the stepper motors which move the analysers. The

pinout for the Arduino can be seen in figure 5.9. The opto-interrupters, which detect the crenelations passed by the analysers, are read by digital pins. Using only crenelations to detect analyser angles in the New (e, 2e) is prone to error. The tension in the turntable wire can slacken and introduce bounce on the opto-interrupter signal, resulting in false angle readings. A 1 k Ω potentiometer is hence coupled to the stepper motor and the analyser to provide a more reliable angle measurement. The +5 V supply from the USB connection which powers the Arduino is passed through the potentiometer, resulting in a voltage on the wiper which is measured by the Arduino's 10-bit ADC. The ADC is powered by the Arduino's +5 V supply so no analog reference needs to be provided. This potentiometer (pot) voltage can be mapped to the analyser angle through calibration. The opto-interrupter flags which detect the 'home' angle are also measured by using the digital pins of the Arduino. Pieces of advance metal are welded to each turntable at an analyser angle of 45° to block the opto-interrupter home flags, giving a TTL LOW reading when the analysers pass this angle. A digital pin switches a relay which must be turned on to connect power to the opto-interrupters. The stepper motor's direction and steps are controlled via digital pins on the Arduino.

The firmware running on the analyser angle controller is detailed in figure 5.10. Serial commands are sent to the Arduino from the main program via USB. The serial message starts with a '1' or '2' which correspond to a command for analyser 1 and analyser 2 respectively. Serial commands can be sent which request data from the Arduino e.g. 'GA' triggers the Arduino to read the pot voltage, converts this reading to an angle, and sends the calculated angle to the main program. Other commands send data or change the state of the Arduino e.g. the command 'SS' stops the movement of the stepper motor. A full list of commands is detailed in appendix D.

The analyser angle controller firmware is structured as a state machine, as seen in figure 5.10. The controller's MOVING state is initiated if the set angle does not equal the current angle. The set angle is converted to the set pot voltage by the calibration parameter. The difference between the set pot voltage and the measured pot voltage is then calculated and multiplied by the number of steps per volt to calculate the number of steps to move. The steps per volt is set as a constant for each analyser and is hard-programmed in the firmware. Once the number of steps to move has been calculated, the stepper motor's direction is calculated and a crenelation debounce timer is reset. The stepper motor is then stepped with a TTL HIGH followed by a LOW pulse with 1 ms duration. The stepping rate v (in steps/s) is then calculated as

$$v = v_0 + a, \quad (5.2)$$

where v_0 is the minimum stepping rate and a is the current stepping acceleration. The stepping acceleration is calculated using

$$a = a_0 + j, \quad (5.3)$$

where a_0 is the minimum stepping acceleration (units of steps/s²) and j is the stepping jerk (units of steps/s³). The stepper motor initially accelerates towards the set angle and then decelerates to the minimum rate once the halfway point to the set angle has been reached. This acceleration pattern decreases the time spent moving and reduces the stress on the turntable wire from the sudden stop of the motor from a high speed. After the stepping rate is calculated, the pot voltage is read by the Arduino's ADC. If

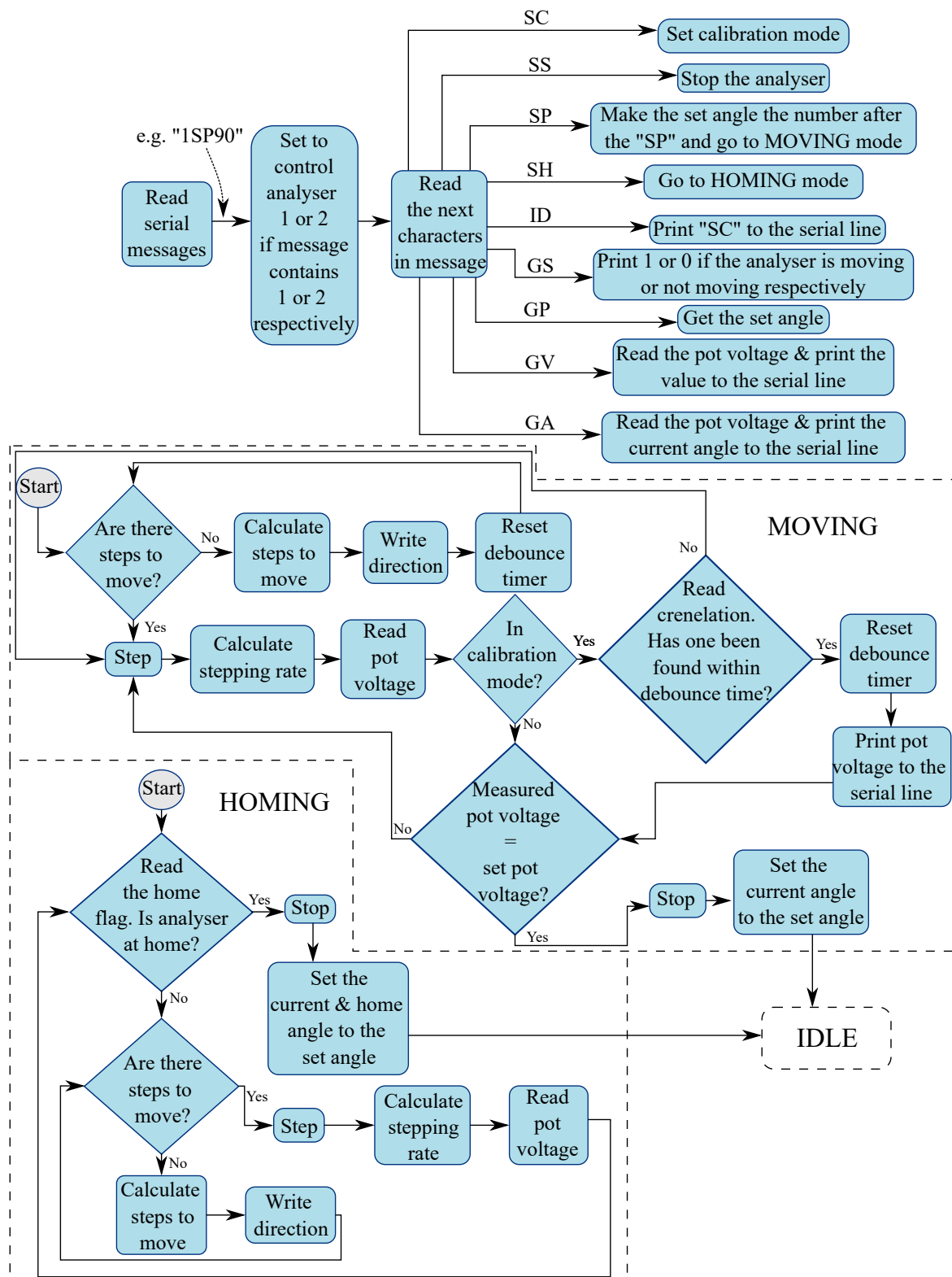


Figure 5.10: Flowchart of the firmware operating on the Arduino-based analyser angle controller. The full list of commands is not shown here and is detailed in appendix D. The source code can be viewed and downloaded at [119].

the set pot voltage is equal to the measured pot voltage, the stepper motor is stopped, the current angle is made the new set angle, and the Arduino is put in the IDLE state. If the set pot voltage has not been reached, the stepper motor is stepped again and the loop continues as seen in figure 5.10.

Opto output	Crenelations layout	Direction	Crenelation found sequence
0		+ve	010
1		direction	
0		-ve	101
1		direction	

Figure 5.11: A matrix showing the logic used to detect the left-hand side of the crenelations in the New (e, 2e) when rotating the analysers. The opto-interrupter’s output is a TTL LOW (0) when blocked or HIGH (1) when unblocked. The sequence required to detect a crenelation is different depending on the direction of rotation. Detection of sequential crenelations denotes a rotation by 5°.

Calibration of the stepper controller allows a user to calculate the conversion parameter of analyser angle to pot voltage. This mode is initiated by the serial command ‘SC’. In this mode, the crenelation opto-interrupters are measured when moving to a set angle. A direction-dependent sequence of opto-interrupt signals trigger the detection of the left-hand side of a crenelation, as seen in figure 5.11. These are used to mark rotation by 5°. A debounce timer is set to stop a reading from the crenelation bouncing from being detected. If the edge of a crenelation is detected within the debounce time, the debounce timer is reset and the pot voltage is printed to the main program via the serial communication line. The main program or serial monitor is used to read the pot voltages and so calibration of the angle controller can be performed by plotting the results and calculating a linear fit to the data.

Calibration curves for the stepper controller for both analysers can be seen in figure 5.12. The level of the ADC which measures the pot voltage for each data point is calculated by taking the average of two measured ADC levels for each detected analyser angle, reached by rotations from both clockwise and anti-clockwise directions. This eliminates bias from one direction of rotation. The data is fitted with a linear curve using the Levenberg-Marquardt method [131] and shows a strong linear relationship for analyser 1, with a reduced chi-squared of $\chi_{red}^2 = 0.36$. For the linear fit for analyser 2, the reduced chi-squared is $\chi_{red}^2 = 0.03$ which indicates that the errors have been over-estimated. The analyser angle (in degrees) per volt is calculated by taking the inverse of the gradient m of the linear fit and multiplying by the ADC level per pot voltage 2^{10} levels/5 V = 204.8 levels/V, yielding 81.9 °/V and 143.4 °/V for analysers 1 and 2 respectively. The precision of the analyser angle controller is the inverse of the gradient: 0.4°/level and 0.7°/level for analysers 1 and 2 respectively. The discrepancy between angular precision for both analysers is due to analyser 2 sitting on the smaller inner turntable in the spectrometer. Given the same stepper motor and gear ratio, a smaller turntable results in a higher final rotation for a single step of the motor. These uncertainties are below the 3° analyser acceptance angle but do make a contribution of around 13% and 23%

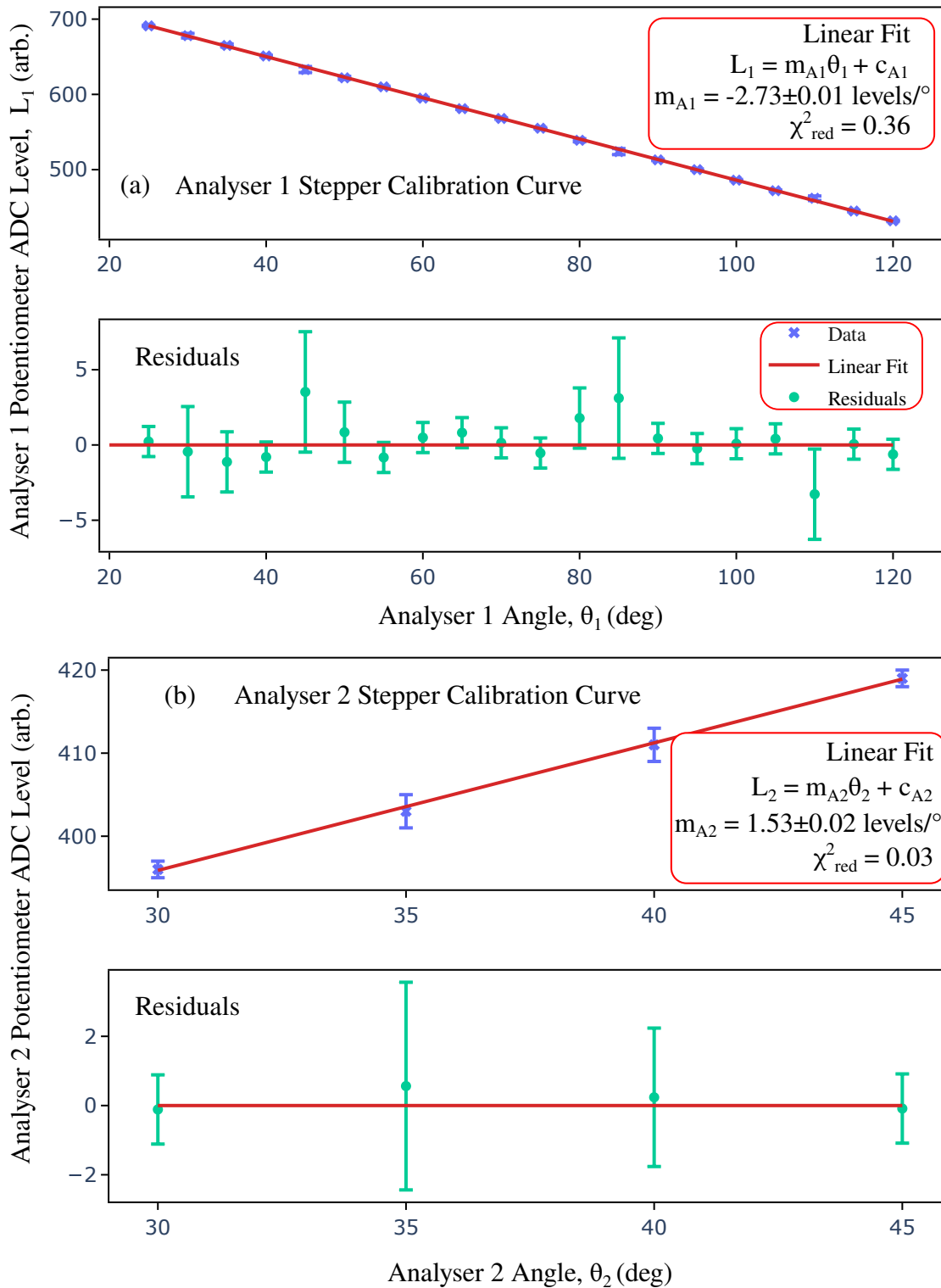


Figure 5.12: Calibration curves for the stepper controller for (a) analyser 1 and (b) analyser 2. The level of the ADC which measures the voltage on the potentiometer's wiper is recorded as the analyser angle is rotated. A linear fit using the Levenberg-Marquardt method is calculated and shown along with the residuals for each calibration curve. The fitted gradients for analysers 1 and 2 are $m_{A1} = -2.73 \pm 0.01 \text{ levels}/^\circ$ and $m_{A2} = 1.53 \pm 0.02 \text{ levels}/^\circ$ respectively.

to the final angular error for analysers 1 and 2 respectively. A higher precision ADC is recommended if future improvements to the system are made. A 12-bit ADC can reduce the experimental error by a factor of four, leading to more accurate and reliable angular control.

5.5 Gun & Analyser Power Supply Control System

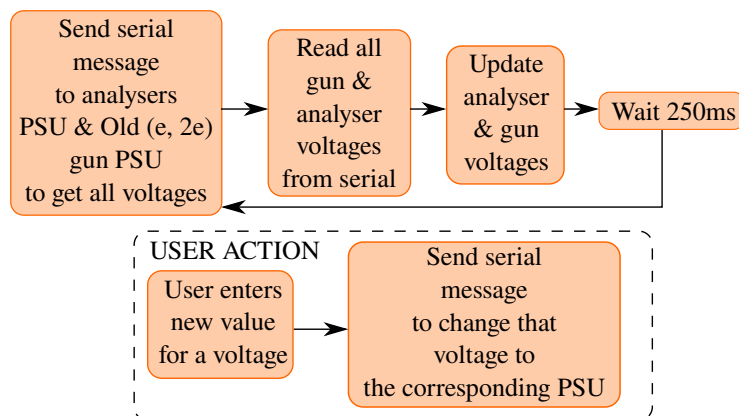


Figure 5.13: A block diagram of the control of the gun and analysers power supply units.

In the main control program, a loop sends serial messages to the Arduino which controls the analyser power supplies and the Old (e, 2e) electron gun power supply, as seen in figure 5.13. All voltages set on each of the elements in the power supplies (and measured voltages on the Old (e, 2e) analyser supply) are retrieved from the Arduino and displayed in the main program, as shown in figures 5.14 and 5.15. After retrieval and update of the gun and analyser voltages, the loop waits 250 ms before another cycle of retrieval occurs. A user entering a new set voltage on either the analyser or gun power supplies immediately triggers the sending of a serial message to the respective power supply, which sets the DACs to produce the new set voltage.

All analyser and gun voltages are saved in a file upon exiting of the main program. Voltages can be retrieved from this file upon starting of the main program again. The main program can also automatically change the set voltages on the analysers to maximise the analyser count rate. This is performed by a modified Nelder-Mead algorithm. The settings and manual running for this algorithm can be adjusted in the tab labelled ‘NM Optimisation’.

The controls for the electron gun can be found in the tab labelled ‘Electron Gun’ in the main control program, as seen in figure 5.14. Retrieved set electron gun voltages are displayed in this tab from the Old (e, 2e) power supply. In the New (e, 2e), there is no functionality to automatically retrieve electron gun voltages so these are manually entered by the user. The gun voltages in this tab are saved in experimental save files and the settings file. Fine control of the gun energy voltage is performed by entering a value (with range ± 10 V) into the interface labelled ‘Gun Fine’. The final gun energy is the sum of this value and the value inside the interface labelled ‘Gun Coarse’. There is functionality for measured gun voltages from the supply to be displayed on this tab

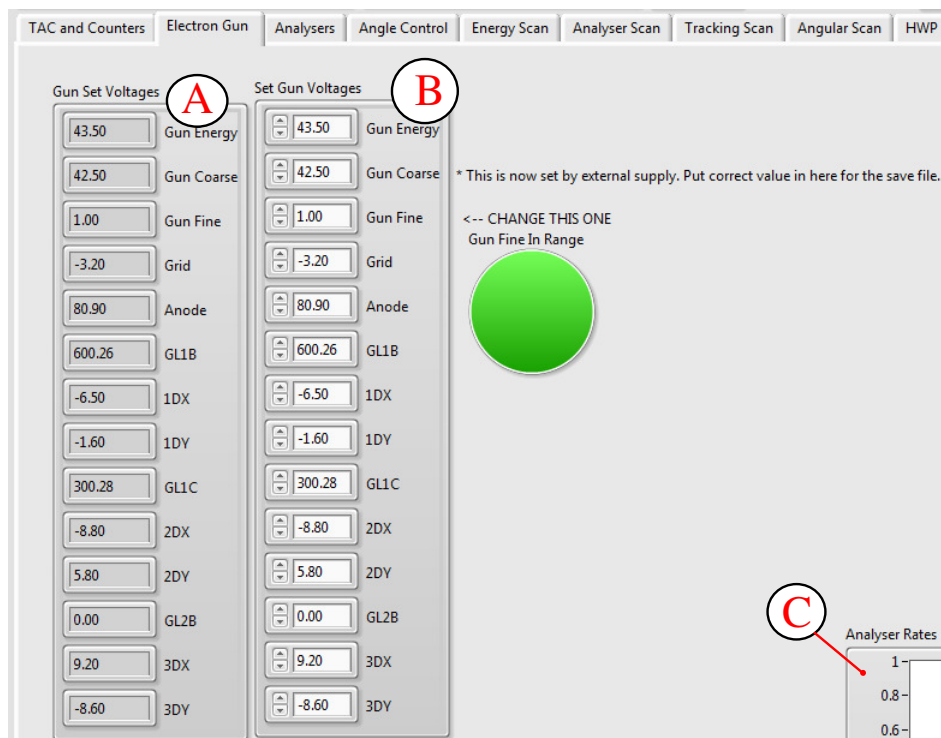


Figure 5.14: Screenshot of the controls of the main program’s electron gun tab. Label A shows the measured gun voltages, B shows the input gun voltages, and C shows the (off-screen) measured analyser count rate chart.

however this feature has not been built for either power supply. The set gun voltages are therefore displayed instead. A running analyser count rate graph is also shown in this tab so the user can instantly see the effect of changing the gun voltages on the analyser count rate and therefore can manually tune the electron gun voltages to maximise the count rate.

A user of the main program can control the analyser voltages in the tab labelled ‘Analysers’. This tab contains the user interface to enter set voltages on both analysers. When the main program is used for the Old (e, 2e), the measured and set voltages are retrieved from the power supply and displayed on this tab. The New (e, 2e) has no functionality to measure the analyser voltages so displays the user-set voltages instead.

The residual energy voltage (RE) for the New (e, 2e) analyser power supply is not well calibrated and the voltage offset increases with increasing set voltage. The voltage offset becomes ~ 1 V as the residual energy values become ~ 100 eV. This is a significant error as the residual energy determines the detected energy of the electrons in experiments which need to be resolved within at least 0.1 eV precision. Manual calibration of the voltage element RE is therefore performed by measuring the output voltage of the supply with recorded set voltages sent by the main program. These recorded and measured values are input into a table provided under the tab labelled ‘PS Optimisation’ which is saved by the main program. The main program then sends a set voltage to the power supply corresponding to the user-input voltage using linear interpolation of the saved data.

Charts displaying the running analyser count rates and the FC current are featured on this tab. These charts are used to manually tune the analyser voltages to maximise

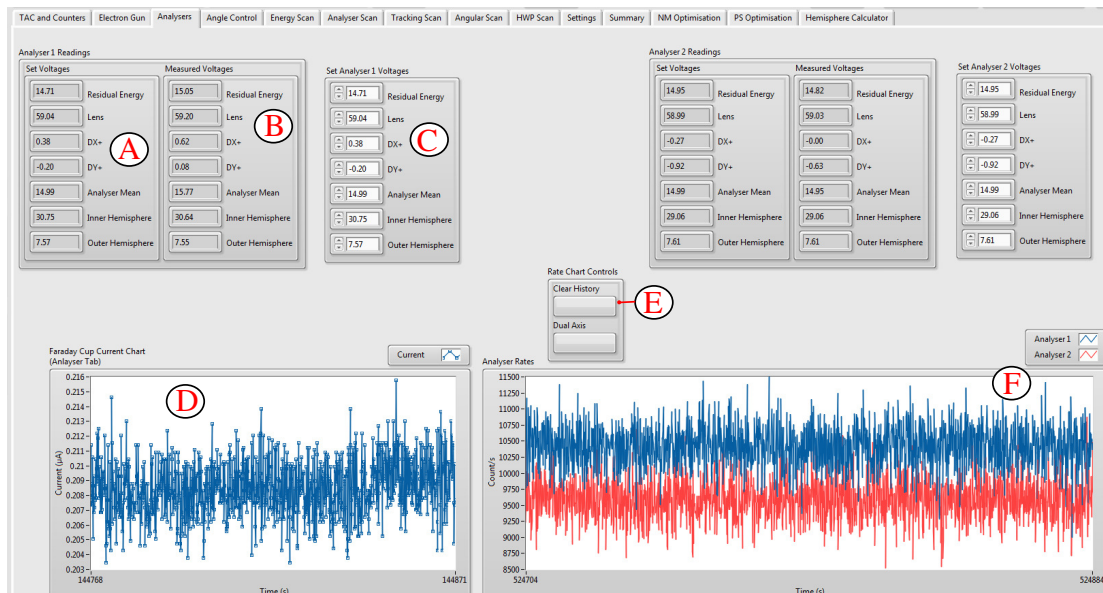


Figure 5.15: Screenshot of the controls for the analyser power supplies in the main control program. Label A shows the power supplies' set voltages, B shows the power supplies' measured voltages, and C shows the user-controlled set analyser voltages. Label D shows the **FC** current measured over time, E shows buttons to clear and reset the measured analyser rates graph or split the graph into a dual axis, which shows analyser 1 and 2 on different axes. Label F shows the measured analyser rates.

the analyser count rates. Due to imperfections in the construction of the analysers or experimental setup, the analyser count rates are not the same for the same set voltages. The rates may differ by a significant amount and identification of the analyser count rate peak becomes difficult to ascertain from an auto-scaled chart. Functionality is therefore built to split the chart into a dual-axis where the analyser count rate scales are on two y-axes, which make it easier to see trends in individual analyser rates. The chart can also be cleared of its history for a similar purpose.

The structure of the firmware running on the Arduinos which control the analyser and gun power supplies is shown in figure 5.16. Initialisation of devices and pins is first performed. The LCD screens (Old (e, 2e) only) are initialised and then interrupt pins are setup for detecting changes from the rotary encoders. For the New (e, 2e) analyser supplies only, the AD9850 signal generator is initialised to produce a 14 kHz signal and the timer for resetting the signal generator is initialised (see chapter 3 for details).

After initialisation, the main control loop is started by checking the state of all buttons and changes on all rotary encoder pins. If changes are detected, the firmware executes the desired action e.g. a turning of a rotary encoder triggers the firmware to increment or decrement the corresponding voltage. The serial line is then checked for messages. If a valid message is received, the firmware shifts into the corresponding state and executes the desired action e.g. setting the level of the **DACs** to the received set voltages. A table of all commands which can be sent to the power supplies is detailed in appendix D. In the New (e, 2e), the signal generator is reset if the timer measures that 1 s or more has passed since it was last reset. This was implemented since in testing the supply, no output was produced if the **DAC** controlling the residual energy is set to a new voltage without a reset of the signal generator. The control loop is then started again by checking the rotary encoders and buttons.

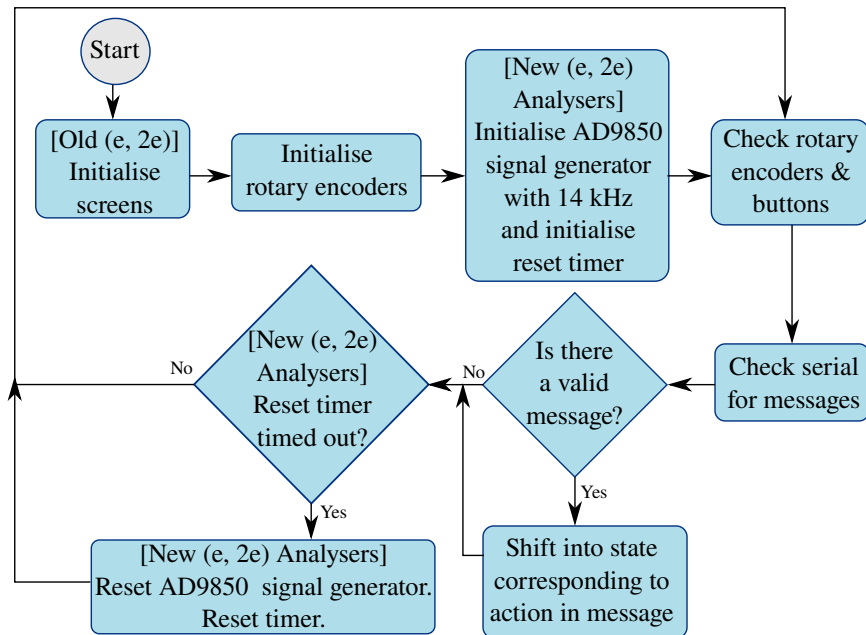


Figure 5.16: Flowchart of the firmware running on the Arduino which controls the analyser and gun power supplies.

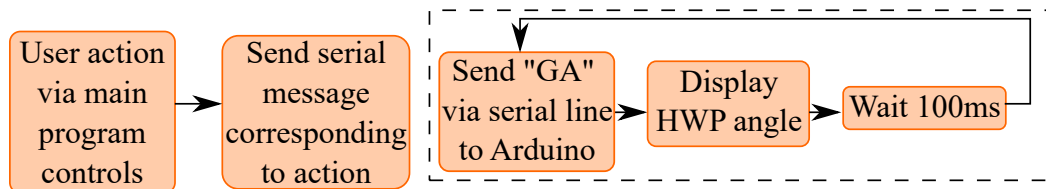
5.6 Half-Wave Plate Control

The New (e, 2e)’s Arduino-based [HWP](#) angle controller is interfaced with the main program, as detailed in figure 5.17(a). The main program retrieves the HWP angle by sending a serial message to the Arduino and displays the reading on the front panel. The program then waits 100 ms and loops, retrieving and displaying the HWP angle again. Any user action which requires interfacing with the Arduino triggers an event structure which executes the sending of the corresponding serial command.

The structure of the Arduino firmware and the [API](#) is detailed in figure 5.17. The Arduino is started or reset and the LCD screen, timers, and digital pin reading the state of a button are all then initialised. The HWP controller is then set to calibration mode, where the HWP is rotated 360° and the time taken between the 10° opto-interrupter signals is measured and saved. The average of all recorded times is halved to find the time taken to rotate the HWP by 5° . Figure 5.18 shows a histogram of measured times between interrupts for ten full 360° rotations of the HWP. A Gaussian fit over this data, set using the Levenberg-Marquardt method, yields a mean time between interrupts as 3.63 ± 0.14 s. This gives the time to rotate 5° in-between interrupt signals as 1.82 ± 0.07 s. Rotations to angles which are divisible by 10° are performed by turning on the motor until an interrupt is detected. Rotations by angles which are divisible by 5° are performed by turning on the motor for the 5° -rotation time calculated by the calibration mode.

If the timer measures that more than 6 s has passed since the last interrupt during calibration, the pulley belt may be slipping and therefore does not couple the DC motor to the rotary feedthrough well. In this case, an error is printed to the LCD screen. Calibration of the HWP controller is performed every time the Arduino resets or starts up in case the motor, pulley, or rotary feedthrough has changed.

(a) LabVIEW HWP Control



(b) Arduino HWP Control

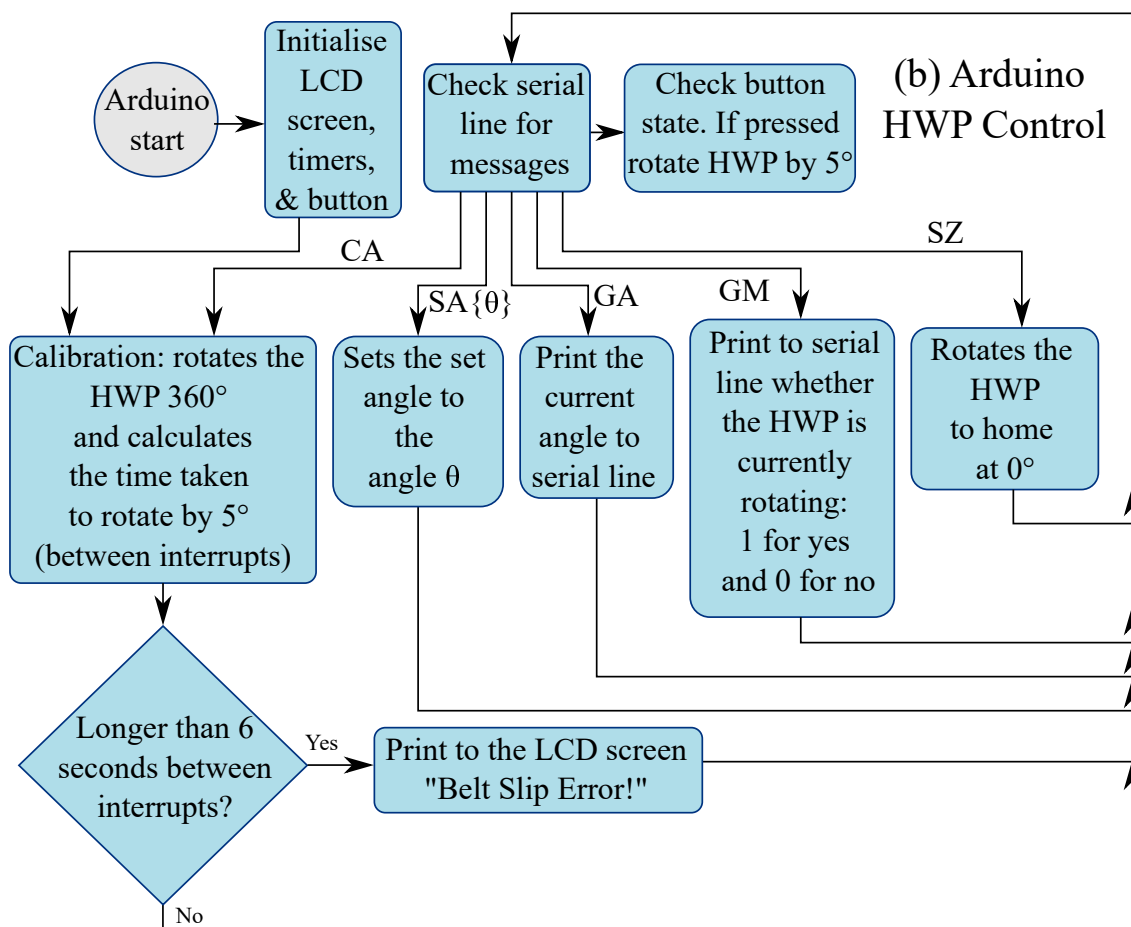


Figure 5.17: Block diagrams describing the control of the HWP rotator in the (a) LabVIEW-based main program and (b) the Arduino firmware. The firmware is available to download and edit at reference [119]. A colour key can be found in figure 3.1.

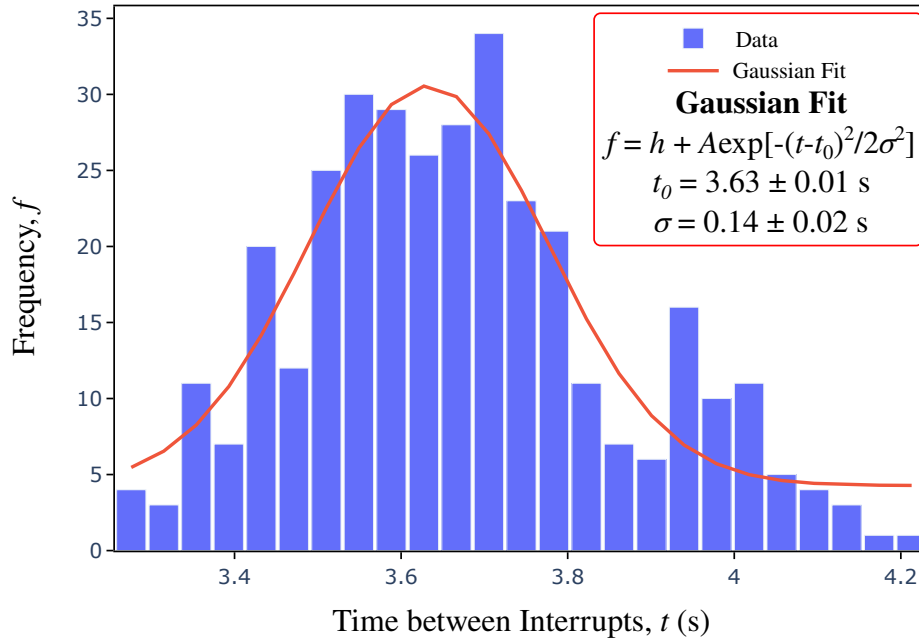


Figure 5.18: Histogram of the time between crenelation interrupts for the rotation of the New (e, 2e) half-wave plate. A Gaussian model is fitted to the data resulting in a mean time of 3.63 s with a standard deviation of 0.14 s.

After calibration, the Arduino firmware begins a loop which checks the serial interface for commands and checks the state of the button on the front panel of the HWP controller, as shown in figure 5.17. If the button is pressed, the DC motor is incremented by 5° . The serial command ‘CA’ puts the Arduino into calibration mode again. The command ‘SA θ ’, where θ is a number from 0 to 360, sets the HWP set angle to θ and initiates the HWP to move to this angle. The command ‘GA’ prints the current HWP angle to the main program via the serial communication line. The command ‘GM’ prints the moving status of the HWP to the serial line: 1 if the HWP is rotating (motor is on) and 0 if not rotating (motor is off). The command ‘SZ’ rotates the HWP until the ‘home’ opto-interrupter is detected i.e. the HWP’s zero angle. After executing a command, the control loop is initiated again where the serial line is checked for messages. The firmware is available to download and edit at [119].

The control of the HWP in the main program is under the tab labelled ‘HWP Scan’, as shown in figure 5.19. The HWP can be calibrated, set to the zero angle, and set to a user-input angle in the interface labelled ‘HWP Controls’. Under this tab, the HWP angle can also be scanned whilst taking measurements of the coincidence counts or analyser rates. The HWP angle controls the polarisation of the laser, which in turn controls the polarisation of the atom. This allows the main program to determine the QDCS (as detailed in chapter 1).

5.7 Laser Locking

The wavelength of the Matisse laser drifts due to thermal changes and vibrations of the laser cavity and defining optics. Since the wavelength of an atomic transition is extremely

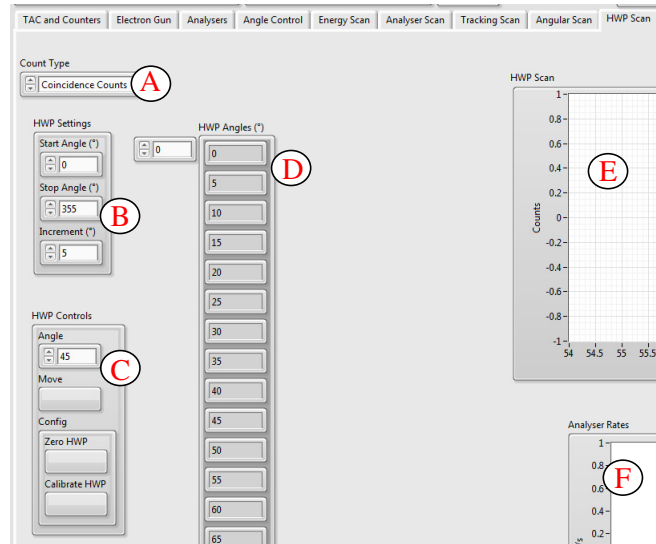


Figure 5.19: Screenshot of the main program in the ‘HWP Scan’ tab. Label A shows the count type selected to measure as the HWP rotates, B shows the interface to add HWP angles to the scan, C shows an interface to send serial messages to the HWP rotator, D shows a list of the HWP angles to be scanned, E shows a graph of the HWP scan, and F shows the analyser counts.

precise, any small drift of the laser wavelength can significantly change the excited atomic population. This results in an unstable environment for coincidence experiments. If the laser has detuned significantly, the experiment is stopped and the laser wavelength is usually stabilised by manually adjusting of the optics. As coincidence experiments run for weeks at a time, under these conditions an operator must be present during the whole experiment to manually adjust the laser wavelength. Coincidence data is also not collected during the time spent adjusting the wavelength. A LabVIEW-based laser locking program has hence been built to automatically adjust the optics inside the laser to lock the laser to a set wavelength.

The new laser locking program is an extension of the Spectra-Physics Matisse laser control program. The tunable optical elements contained inside the Matisse Ti:Sa laser (see figure 4.1) are therefore controllable from the laser locking program via a USB connection to the Matisse laser. The motor and piezoelectric actuator settings for each element can be adjusted from the program by a user, as shown in figure 5.20. User adjustment of these optical elements is performed to obtain a laser wavelength within the BiFi’s scanning range of the desired wavelength.

A WSU Ultimate wavemeter measures the wavelength and relative power of the laser, which is sent to the laser locking program via a USB connection. As the laser and wavemeter must communicate via USB, the program is run on a separate PC from the one running the main control program. Laser data is hence sent to the main control program via a network connection. A desired wavelength can be input by the user into the laser locking program and scans over the BiFi, thin etalon, and piezo etalon can be performed to reach the desired wavelength and lock to that wavelength. The resulting scans are displayed as graphs shown in figure 5.20. An auto-lock can also be run by the laser locking program to automatically re-lock the laser wavelength to the desired wavelength.

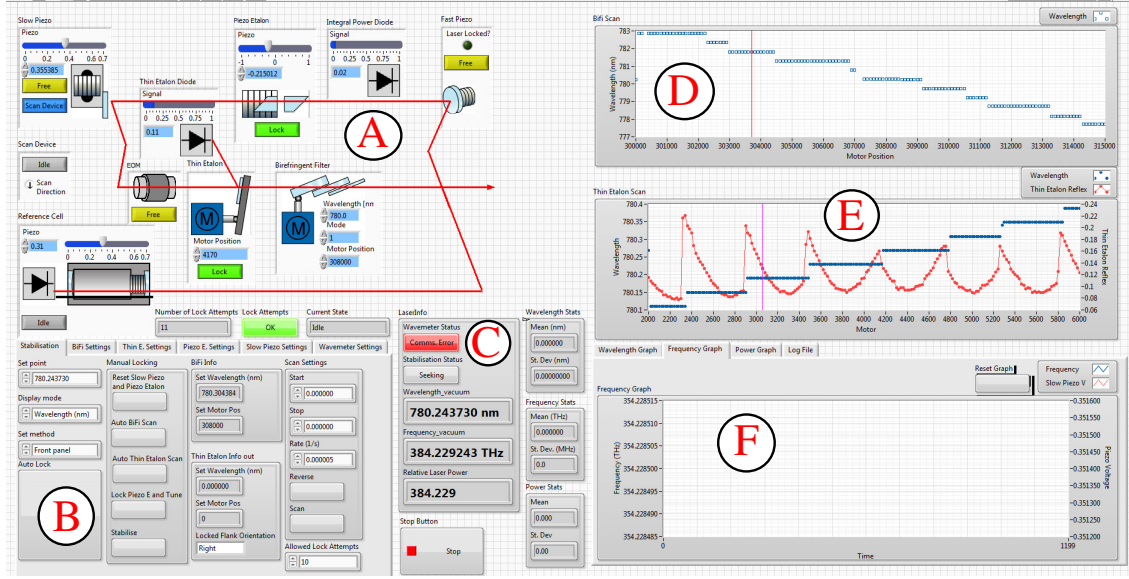


Figure 5.20: Screenshot of the laser locking program. Label A shows the controls for each optical element contained inside the Matisse laser system, B shows the auto-lock controls with settings for each tunable element, C shows the laser status as measured by the wavemeter, D shows controls for the birefringent filter scan, E shows controls for the thin etalon scan, and F shows the frequency graph.

A flowchart showing the structure of the laser locking program can be seen in figure 5.21. On start-up of the program, the wavemeter and graphs are initialised. The wavelength is measured by the wavemeter continuously for times separated by dt . The user can then shift the program into different scan states. In a BiFi scan, the motor is stepped whilst wavelength λ_i and motor positions m_i are recorded. When the motor has reached the end of its scan range, the gradient at each point is approximated as

$$\left(\frac{d\lambda}{dm}\right)_i \approx \lambda_i - \lambda_{i+1}. \quad (5.4)$$

The position where the gradient is above a user-set threshold value is recorded. These positions correspond to the boundary between laser modes, where the gradient $d\lambda/dm$ is large, as seen in figure 5.20. The wavelengths and motor positions are then split into separate arrays depending on their respective laser mode. The BiFi is then set to the mean motor position of the array with the closest wavelength to the desired wavelength. The thin etalon is scanned in a similar way, except the arrays of wavelength and motor positions are reversed before gradients are calculated. This is done to obtain positive gradients, as the transition between laser modes has a negative gradient with increasing thin etalon motor position. The piezo etalon scan checks if the current wavelength λ_{current} is within a user-set allowed deviation from the set wavelength λ_{set} . If this is true, the piezo etalon motor position is set to

$$m = m_{\text{current}} + I(\lambda_{\text{current}} - \lambda_{\text{set}})dt, \quad (5.5)$$

where m_{current} is the current motor position and I is a feedback constant to be set by the user.

When auto-locking mode is activated, the BiFi scan is initiated, followed by the thin etalon scan. The piezo etalon scan is then run in a loop until the laser deviates out of the piezo etalon's scan range. When this occurs, the BiFi scan and following scans

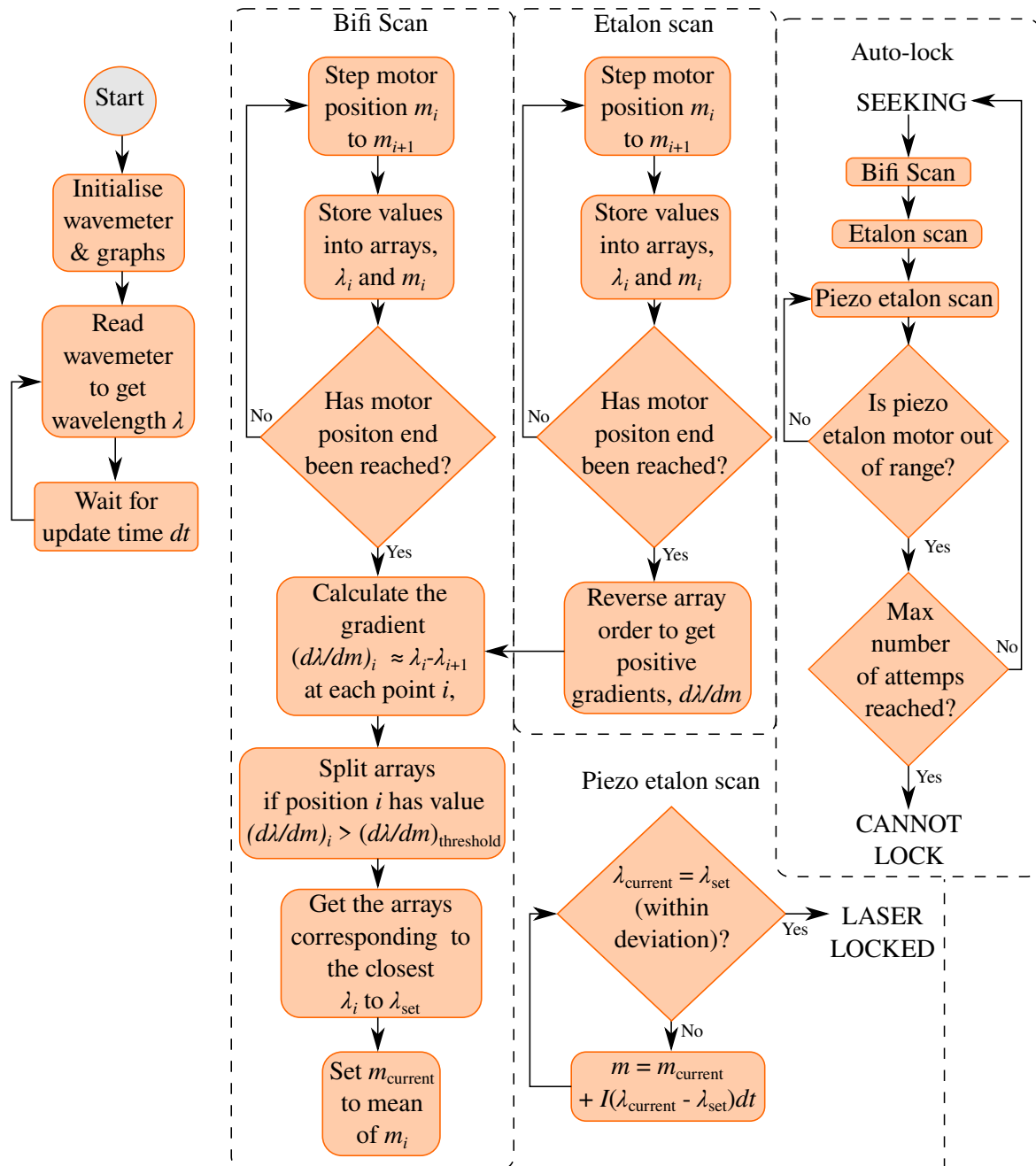


Figure 5.21: Flowchart showing the structure of the LabVIEW-based laser locking program. The wavelength is read by a wavemeter. If the wavelength drifts away from the set wavelength by a user-set amount, the auto-lock algorithm is initiated.

are initiated again until the laser locks to the set wavelength, or a maximum number of attempts has been reached, as seen in figure 5.21. The locking status is set to ‘SEEKING’ if scans are being performed, ‘CANNOT LOCK’ if the maximum number of scan attempts have failed, and ‘LASER LOCKED’ if the measured laser wavelength is within the set deviation range of the set wavelength. The locking status, wavelength, and relative laser power are shared to the main control program as network variables. These variables are then displayed and saved when running experiments.

5.8 Multi-Channel Analyser

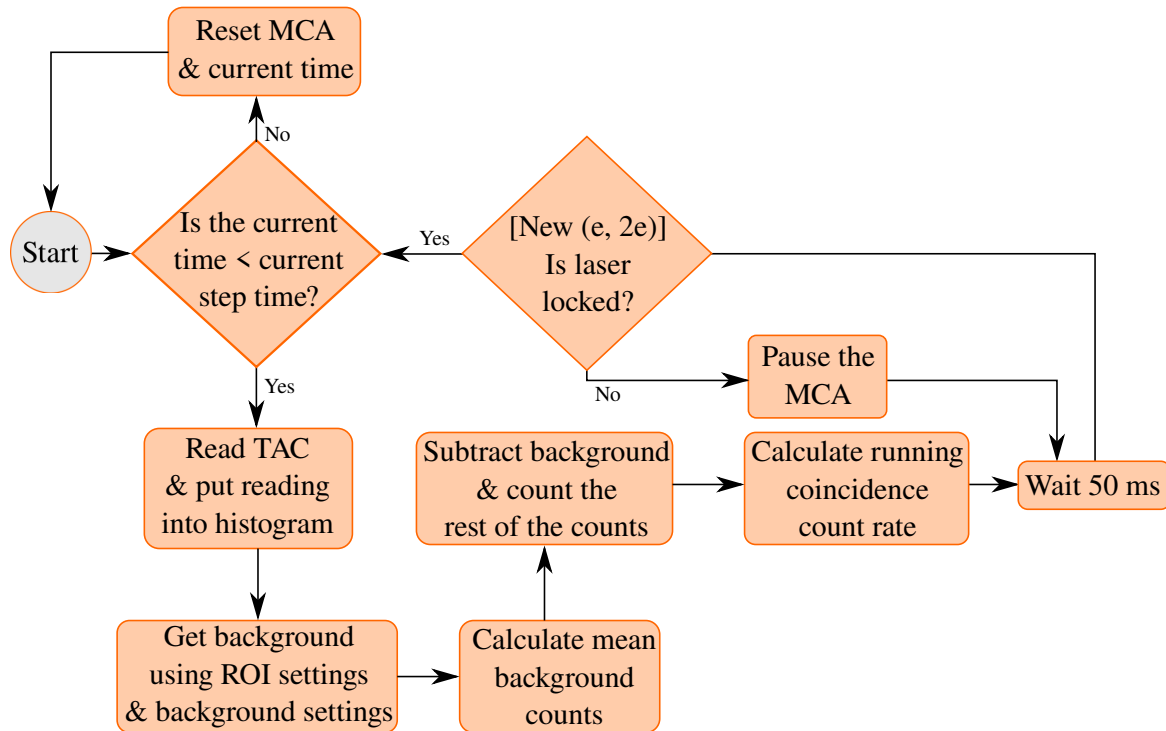


Figure 5.22: Flowchart of the LabVIEW-based multi-channel analyser. Time-to-amplitude (TAC) readings are binned into a histogram and coincidence counts are calculated using the set background range and region of interest (ROI).

The multi-channel analyser (MCA) is implemented in the LabVIEW main control program, as shown in figure 5.1. The output pulses from the TAC are used to create a histogram with a user-set bin width, number of bins, and timing scale. The bin range of the ‘background’ signal and region of interest (ROI) is set by the user and the number of coincidence counts is calculated as

$$N_C = N_{ROI} - \bar{N}_B, \quad (5.6)$$

where N_{ROI} is the number of TAC pulses within the region of interest and \bar{N}_B is the equivalent number of TAC pulses within the background region. The timing scale and delay time added by the delay generator is set so that the TAC pulse corresponding to a coincidence signal is measured in the centre of the histogram.

A flowchart showing the structure of the MCA can be seen in figure 5.22. On start-up of the main program and resetting of the MCA, the corresponding DAQ card analog input

channels are set up to read in differential mode and are triggered from the TAC's delayed valid conversion pulse. The MCA histogram is also configured to match the timing scale selected.

After this initialisation process, a timer is started and the dwell time is displayed on the front panel. If in an experiment the current dwell time is less than the current step time, analog readings from the TAC are transferred from the DAQ card's buffer to memory in the PC. The analog readings are converted to time signals and then binned in the histogram, which is displayed in the main program. Using equation 5.6, coincidence counts are then calculated in real time and a running coincidence rate is calculated and displayed on the front panel. Every 50 ms the current dwell time is checked and if larger than the step time, the MCA and timer are reset and initialised again. The coincidence counts accrued during the step time are then plotted in a graph displayed in the main program and saved to a file. If taking other analogue readings from the DAQ card, such as pressure readings, the MCA is paused and then resumed when the readings have been taken. If using the New (e, 2e), the laser locking status is checked and if the laser is not locked, the MCA is paused until the laser locking program has re-locked to the set laser wavelength.

5.9 Experiment Types & Data Handling

The different types of experiments which can be performed using the main control program are detailed in this section. Each experiment type is separated into different tabs in the program. Each experiment has a similar experimental procedure: the analysers and/or electron gun are tuned to maximise the experimental count rate before the experiment starts, the scan variable values to scan over and step time(s) are then chosen, the save file location and settings are then chosen, and then the scan is finally started.

Before a scan begins, the electron gun voltages are first tuned to peak the analyser count rates and the Faraday cup (FC) current. If the FC current decreases whilst the analyser count rates increase, the electron beam is not passing through the interaction region and into the FC. The lens voltage and deflector voltages on each analyser are then adjusted to peak the analyser count rates. This can be done manually or by using a modified Nelder-Mead (NM) algorithm [127]. The NM routine can be run under the 'NM Optimisation' tab in the main control program, as seen in figure 5.23. The user-adjusted NM routine settings are: minimum voltage change at each algorithm step, initial voltage steps, lower and upper bounds on voltages, settle and sample time, and the number of times to run the algorithm. The coefficients at each algorithm step are also displayed along with a chart of the real-time analyser count rates. Two virtual LEDs display whether the NM algorithm has finished running for each analyser.

5.9.1 Gun Energy Scan

The gun energy can be scanned whilst measuring the analyser count rates or coincidence counts. This gun energy scan can be performed under the tab labelled 'Energy Scan',

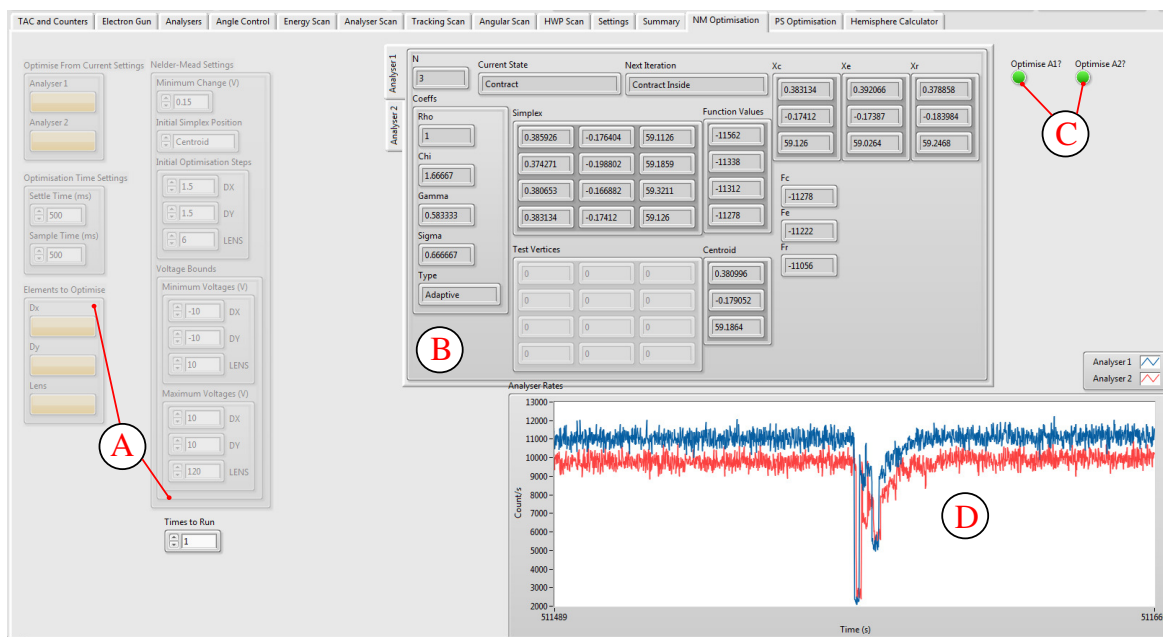


Figure 5.23: A screenshot of the Nelder-Mead (NM) optimisation tab in the main control program. Label A shows the settings for the NM optimisation routine, B shows the current NM parameters for maximising the analyser rates, C shows the status of whether the NM algorithm has optimised analyser 1 and 2, and D shows the measured analyser rates over time.



Figure 5.24: A screenshot of the gun energy scan tab in the main control program. Label A shows the scan settings: the count type for the scan and the gun energies to add to the scan. Label B shows the list of gun energies to add to the scan and C shows buttons to append to, clear, or mirror the gun energies in this list to the scan. Label D shows the gun energies to scan and the counts measured at each step. Label E shows a graph of the counts with respect to gun energy and F shows the current analyser rates.

as seen in figure 5.24. The coarse gun energy is set by the electron gun power supply and the gun fine energy is controlled by the analog output of the DAQ card. Using the gun fine energy as the scan variable restricts the scan range to ± 10 eV from the set gun coarse energy. The user inputs the gun fine voltages to scan over and then appends them to a main scan array. The time spent gathering data at each scan step is adjusted in the interface outside of the tab control, as shown in figure 5.1. At each scan step, the mean analyser rate or accumulated coincidence counts are calculated and plotted on a graph. After each step has been completed, the data is saved in the set save file.

As the incident electron energy is scanned in a gun energy scan, an inelastic spectrum of a target can be measured. This scan can be performed to find the target's spectrum of states by measuring analyser rates. Before an (e, 2e) experiment is performed, a gun energy scan is used to tune the gun energy to the ionisation potential by finding the coincidence peak, as seen in section 6.2.

5.9.2 Tracking Scan

In the main control program, the gun fine energy and the residual energy (RE) of the analysers can be scanned and tracked together whilst the analyser rates are measured. A screenshot of the controls for this tracking scan is shown in figure 5.25. The voltage for this scan is provided by the analog output of the DAQ card, which is referenced to both gun coarse and RE of the analysers. The range for the scan voltage is hence ± 10 eV. In both of the spectrometers, a manual toggle switch connects the output of the DAQ card to the RE of the analyser power supplies. The stop voltage and voltage step is input by the user to set up the scan. A table of gun energy and RE voltages to be scanned over then appears. The step time can be adjusted outside of this tab, as shown in figure 5.25. An estimated time and date for the completion of the scan is also shown here. When the user starts a scan, the mean analyser rate for each time step is measured and displayed on a graph along with the scan voltages.

A tracking scan can be used to measure the elastic spectrum of a target. This is useful to investigate phenomena such as resonances between scattering processes, as shown in section 8.2.

5.9.3 Angular Scan

The analyser angles can be varied whilst measuring either analyser rates or coincidence counts. The controls for this angular scan are found under a tab in the main control program, as shown in figure 5.26. The analyser angle configurations to scan over are set by the user by generating 'sections' of angles and then appending these sections to the main angular scan array. Section angles can be 'mirrored' by reversing the index of the section array and appending the result to the end of the array. This allows a quick way to generate a scan which performs multiple sweeps of an angular range. As the analyser angles are changed at every step, the analyser rates or coincidence counts are measured, displayed in a graph, and saved in a file. As the experimental geometry changes, the focus

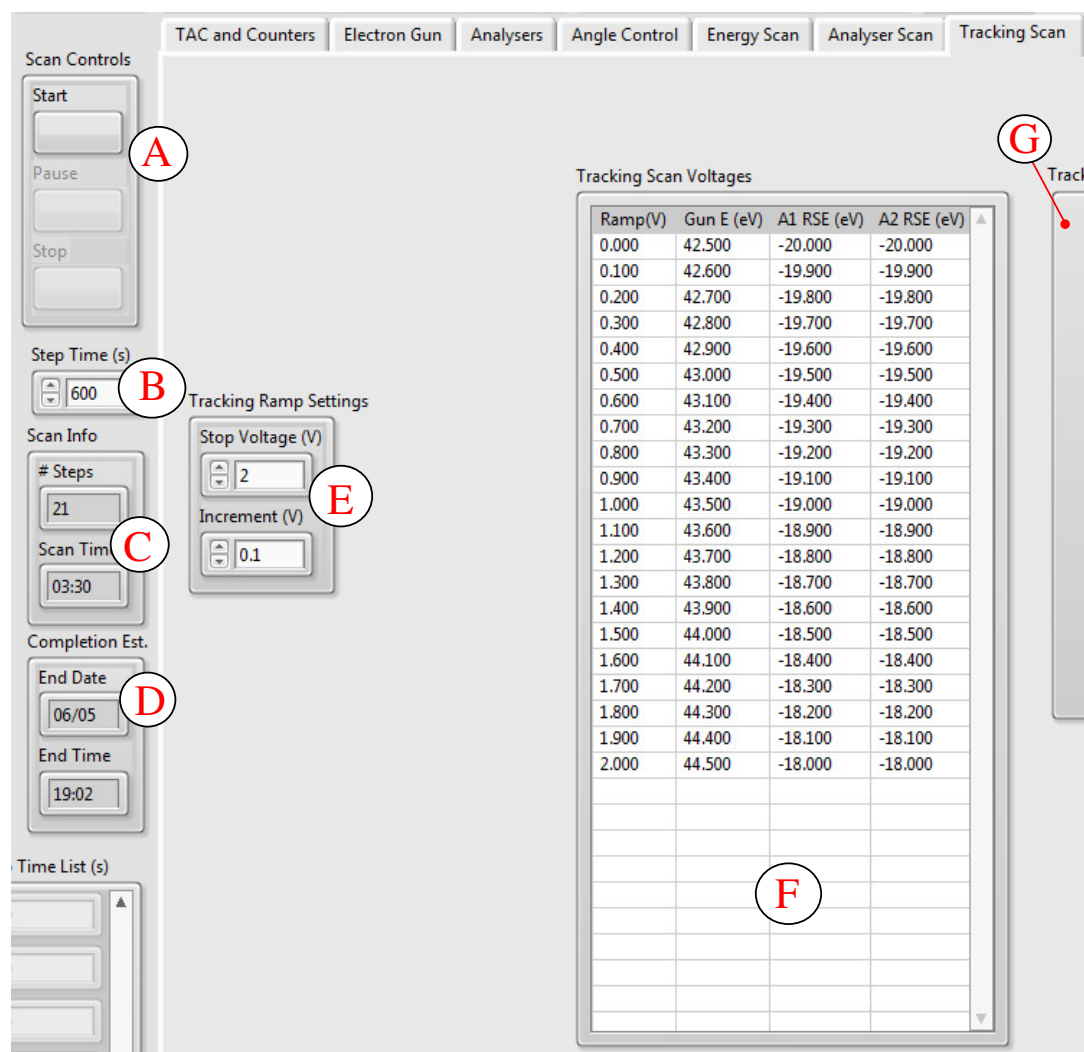


Figure 5.25: Tracking energy scan screenshot. A shows the start/stop/pause scan buttons, B shows the user-input step time, C shows the scan information, D shows an estimate for the date and time the scan is completed, E shows the tracking scan settings, F shows the tracking scan to be performed, and G shows the tracking scan graph (off-screen).

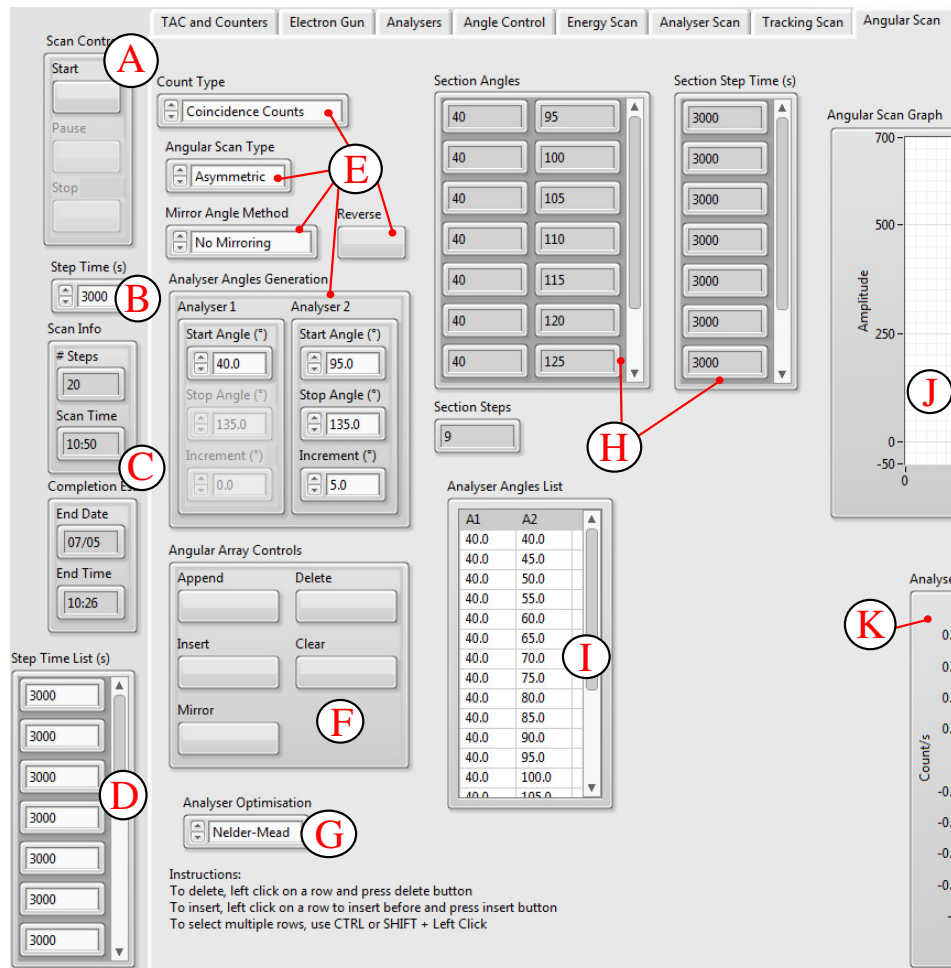


Figure 5.26: A screenshot of the angular scan tab in the main control program. Label A shows the scan start/pause/stop buttons, B shows the user-set step time, C shows the scan information, D shows a list of scan step times, E shows the user-set angular scan settings, F shows controls to modify the analyser angles scan list, G shows the optimisation routine run after every step, H shows the section angles and step times, I shows the analyser angles scan list, J shows the angular scan graph (off-screen), and K shows the analyser rates (off-screen).

of the analysers onto the interaction region varies slightly. The set analyser voltages are hence optimised at every angular step to keep experimental conditions consistent. This is done by performing a [NM](#) optimisation routine at each angular step, after the analysers have moved to their set angles but before the [MCA](#) is started.

The angular scan is used to determine the [TDCS](#) from the target. This type of experiment is used to generate data shown in chapters 6 and 7. As the angular configuration is changed, the TDCS can vary greatly (up to a factor of 10^3 in the measurements of xenon presented in chapter 6). A variable step time is hence used in this type of experiment to ensure that a significant number of counts is measured at each step. A preliminary sweep of the desired angles is performed first with a shorter constant step time and then the coincidence rate data from this preliminary experiment is used to estimate an effective step time for each angular step.

5.9.4 Half-Wave Plate Scan

When operating the New (e, 2e) spectrometer, the [HWP](#) angle can be scanned whilst analyser count rates or coincidence counts are measured. The controls for this experiment is found in the main program under the tab labelled ‘HWP Scan’, as seen in figure 5.19. A HWP scan angle array is generated from a front panel interface where the user enters a start angle, stop angle, and angle increments with a precision of 5° . At each angular step, counts are measured, plotted in a chart, and saved in a file.

Rotation of the HWP angle results in a rotation of the laser polarisation by twice the rotation angle, as noted in section 4.2. The laser polarisation angle can hence only be adjusted by 10° increments. This type of experiment therefore measures the [QDCS](#) of the target. As in an angular scan, the QDCS may vary greatly with polarisation angle, so a variable step time is used to ensure a significant number of counts is measured at each polarisation angle.

5.9.5 Data Handling

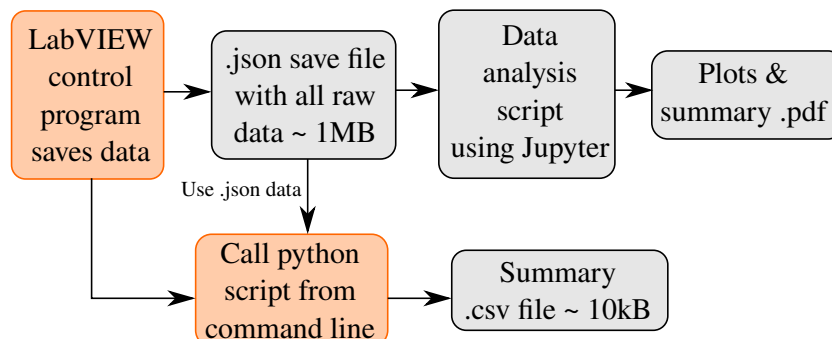


Figure 5.27: Flowchart of the data flow in an experiment. The main control program saves experimental data in a [JSON](#) file format, which is analysed in real time to produce plots and a summary page. A script is also called to generate a summary [CSV](#) file. A colour key can be found in figure 3.1.

All analyser and gun voltages, [TAC](#) readings, scan settings, count data, [NM](#) optimisation

settings, and date and time are saved in the main control program for a single scan. This generates data which is typically ~ 1 MB for an angular scan running for around a week. Figure 5.27 shows that this data is saved in a JSON file format, making the data human-readable and easily extractable for post-processing. The location of the file, target name, and notes to be saved in the file can be set in the ‘Settings’ tab of the main program. The JSON file is created at the start of a scan and data is saved to the file at every step. The save file is named as the datetime string at the start of the scan followed by the scan type (e.g. ‘GES’ for gun energy scan), for easy identification of files.

Real-time data analysis is performed using Jupyter [128] whilst the experiment is running. The experiment can then be stopped or adjusted depending on the analysed data. A primary plot and summary page is also generated for each scan.

A CSV file containing a summary of the scan data is also generated by the main program by calling a python [79] script which extracts key information from the JSON files. This summary file is easier to read and is smaller in size (~ 10 kB).

5.10 Summary

The electron spectrometer control system’s software and firmware have been detailed in this chapter. The LabVIEW main program interfaces with Arduino-controlled modules via a serial connection. The main program also interfaces with a LabVIEW laser locking program over a network connection. The main control program controls the hardware, collects all resulting data, and optimises the experiment. Additional hardware can also be added to the control system by modifying the LabVIEW program.

The general architecture of this experimental control system can be implemented in many other types of electron spectrometers, thereby enabling a range of computer-controlled measurements. Examples of different types of experiments performed using these systems have been presented, which demonstrates the capability and flexibility of the control system.

In the next chapter, new data for the TDCS of xenon is presented, which was obtained using this experimental control system on the Old (e, 2e).

Chapter 6

The Evolution of the TDCS of Xenon

New triple differential cross section (TDCS) measurements from xenon are presented in this chapter as the scattering geometry changes from coplanar to the perpendicular plane. The Old (e, 2e) spectrometer was used to make these measurements. A measurement of the binding energy spectrum of xenon was used to tune the gun energy to measure coincidence from the $5^2P_{3/2}$ ion state. Coincidence data are presented at energies of 60 eV, 80 eV, and 100 eV above the ionisation potential. These new data are compared to measurements collected for the first four noble gases and to that from xenon at lower energies. A new technique was used to measure the ratio of relative cross sections between xenon and helium using a xenon-helium mixture. With this data, absolute differential cross sections of xenon can be determined once the helium cross sections have been calculated. This work has been published in reference [66].

6.1 Introduction

The noble gases provide an excellent testing ground for $(e, 2e)$ measurements, as they are gaseous targets and so allow an atomic beam of high density to be produced easily using a gas jet. The cross section of He has been intensively investigated over a wide range of kinematic conditions and the ionisation models for this atom are now considered to be accurate [46]. The TDCS for Ne has also been measured over a range of geometries and comparative models are also found to be reasonable [132]. By contrast, calculations for Ar, Kr, and Xe are more difficult since these targets have a large number of bound electrons that may influence the interaction. Previous studies have found good agreement with coplanar $(e, 2e)$ data for these targets at high energies [133], however calculations in the low to intermediate energy regime have met with mixed success, particularly for non-coplanar geometries [36, 65, 134, 135].

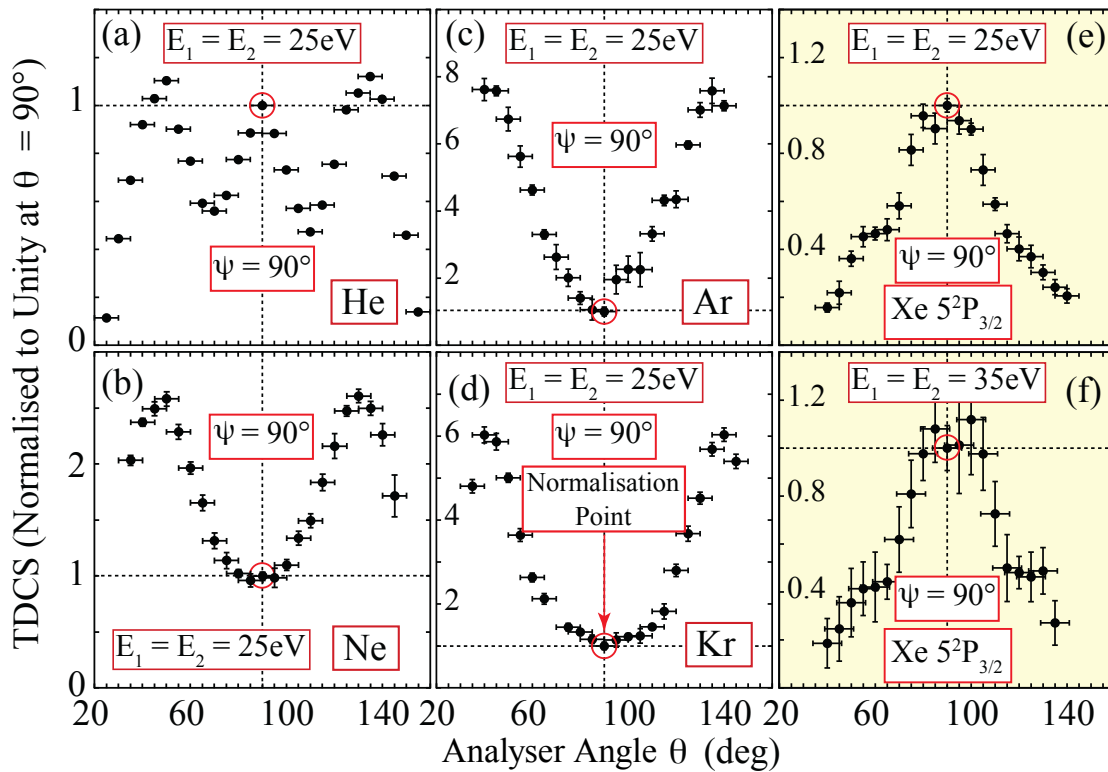


Figure 6.1: TDCS measurements for the first five noble gases in the perpendicular plane at 50 eV above the IP (a) to (e) as well as for xenon at 70 eV above the IP (f). The data are normalised to unity at an angle of 90° . Xenon does not follow the angular trend seen for the other targets. Data has been taken from reference [134].

Previous measurements from the first five noble gases in the perpendicular plane ($\psi = 90^\circ$) conducted in Manchester showed an unexpected result: xenon displayed the opposite trend to other targets at higher energies [134], as shown in figure 6.1. The TDCS for He displays a triple peak structure under these kinematic conditions, with peaks at angles of 45° , 90° , and 135° . As the atomic number increases (from Ne to Kr) a similar structure is seen, where there is a minimum in the cross section at 90° and peaks occur around 45° and 135° . It should be noted that the peaks at 45° and 135° are from the same interaction process: this is due to symmetry around the incident beam direction in this geometry.

By contrast, the TDCS for xenon under these kinematic conditions is a maximum at 90° and no additional peaks are observed at other angles. A follow up study measured the TDCS of xenon as the incident electron angle was varied from a coplanar geometry to the perpendicular plane [135]. The highest energy used in this study was $E_1 = E_2 = 20$ eV and the lowest energy was $E_1 = E_2 = 2.5$ eV. These results demonstrated that the TDCS for xenon at lower energies is similar in form to that from other noble gas targets, however as the energy was increased, clear differences were again observed in all geometries.

Several calculations for the TDCS from noble gas targets have been carried out for the geometries discussed here [36,65,136]. Purohit and co-workers [136] used a DWBA theory and included polarisation of the target as well as PCI between the outgoing electrons in their model. The calculations had mixed success and could not emulate the data over all geometries, even for the lighter targets. These authors included a Gamow factor (see chapter 1 for detail) however their results did not produce a zero cross section when $\theta_1 = \theta_2 = 0^\circ$ and 180° , as is required when PCI is included. No measurements had been carried out at that time for krypton or xenon to compare to their calculations.

A fully relativistic calculation was carried out for xenon 10 years later by the group of Stauffer and colleagues [65] following publication of data from the coplanar to perpendicular plane geometries in [135]. These authors used both a Coulomb Born calculation and a relativistic Distorted Wave Born calculation using Dirac wavefunctions. They included the static potential of the target and a Gamow factor to emulate PCI. They also included exchange interactions which result from the antisymmetric nature of the electron wavefunction under spatial and spin exchange. The model agreed with the data at higher energies in the perpendicular plane, however once again it had mixed success in all other geometries where measurements were obtained. Agreement at low energies was poor, however this was expected within the constraints of the DWBA model used. At low energies, the wave functions in the interaction are not well-approximated by distorted waves (see chapter 1).

The recent work by Whelan and co-workers [36] concentrated on measurements in the perpendicular plane for each of the noble gas targets. These authors used a non-relativistic DWBA model and included PCI through the use of both a Gamow factor as well as the factor introduced by Ward and Macek [37], both of which provide an approximation to the effect of PCI. These authors noted that the advantage of the DWBA method is that different interaction processes can effectively be switched ‘on’ or ‘off’ by replacing the distorted waves by plane waves, as noted in chapter 1. This allows different scattering mechanisms to be explored to try to understand the physical processes that are involved.

By switching these interaction processes on and off it becomes possible to link the scattering process to possible semi-classical mechanisms involved. Zhang, Whelan and Walters [137] noted that the central peak in the perpendicular plane for helium could arise from the momentum of the bound electron matching that of the incident electron, so that both their momenta cancel out in the perpendicular plane. The electrons then have to leave the interaction at a mutual angle of $\theta_1 + \theta_2 = 180^\circ$ to preserve the total momentum of the system. The peaks seen at $\theta = 45^\circ$ and 135° were then considered as being due to elastic scattering of the electron from the atom followed by a binary collision, leading to a three-peak structure as observed. Don Madison and co-workers [58] also used a DWBA model and concluded that the central peak could also be explained by a triple scattering

process. In this case, the incident electron first scatters elastically into the perpendicular plane followed by a binary collision with one of the bound electrons, then scatters elastically again to emerge at a mutual angle of 180° .

The semi-classical double and triple scattering mechanisms are attractive as they give a relatively simple explanation of the processes leading to ionisation in the perpendicular plane. Unfortunately, they do not describe the measurements well for the heavier targets, as shown in [36, 65] and in figure 6.1. A fully quantum calculation is hence required to describe the cross sections for these targets and the semi-classical description of scattering appears to break down. It is therefore unclear at present why the TDCS for xenon is so different to that found for the other targets.

The motivation of the experimental work presented in this chapter and as published in [66] was hence to provide additional data at higher energies than used previously, where DWBA models should prove to be accurate. The new data were taken from a coplanar geometry through to the perpendicular plane at energies from 60 eV to 100 eV above the ionisation potential using the Old (e, 2e) spectrometer. Again, there is a common point at the mutual angle $\theta_1 + \theta_2 = 180^\circ$, which has been used to normalise the data at a given energy to a single reference point. Since the models for ionisation of helium are now considered to be of high accuracy, additional experiments were also carried out to renormalise these new data to the helium cross section at the same outgoing energies. In this way both the relative angular cross sections and their absolute values (relative to the helium calculations of absolute cross sections) can be compared to different models.

6.2 Binding Energy Spectrum of Xenon

A measured binding energy of xenon is presented in figure 6.2. The data collected was measured by performing a gun energy scan set to measure coincidence counts. The analysers were set to equal angles of 50° and were set to detect electrons with symmetric energy 40 eV. Coincidence counts were measured using a dwell time of 300 s per 0.125 eV increment of the gun energy. The first coincidence peak corresponds to ionisation to the xenon $5^2P_{3/2}$ ionic ground state at a gun energy of 91.6 eV, resulting in a binding energy of 11.6 eV. The small, broad peak above the background at a binding energy of around 13.1 eV corresponds to the $5^2P_{1/2}$ ionic ground state. The resolution of the analysers can be seen in this spectrum with a full width at half-maximum for each state at ~ 1 eV. As the energy separation between the two ion states is larger than the resolution of the analysers, these states are well-resolved and there is little contamination between them.

From previous measurements [134], the TDCS of xenon in the perpendicular plane resulting in the $^2P_{3/2}$ and $^2P_{1/2}$ ionic ground state showed no significant differences at energies of 5 eV, 10 eV, and 15 eV above the IP. It is assumed that this is the case for higher energies as well. For the coincidence experiments presented in the following sections, the gun energy was hence set to measure coincidence from the $5^2P_{3/2}$ ionic ground state as this produces a larger signal.

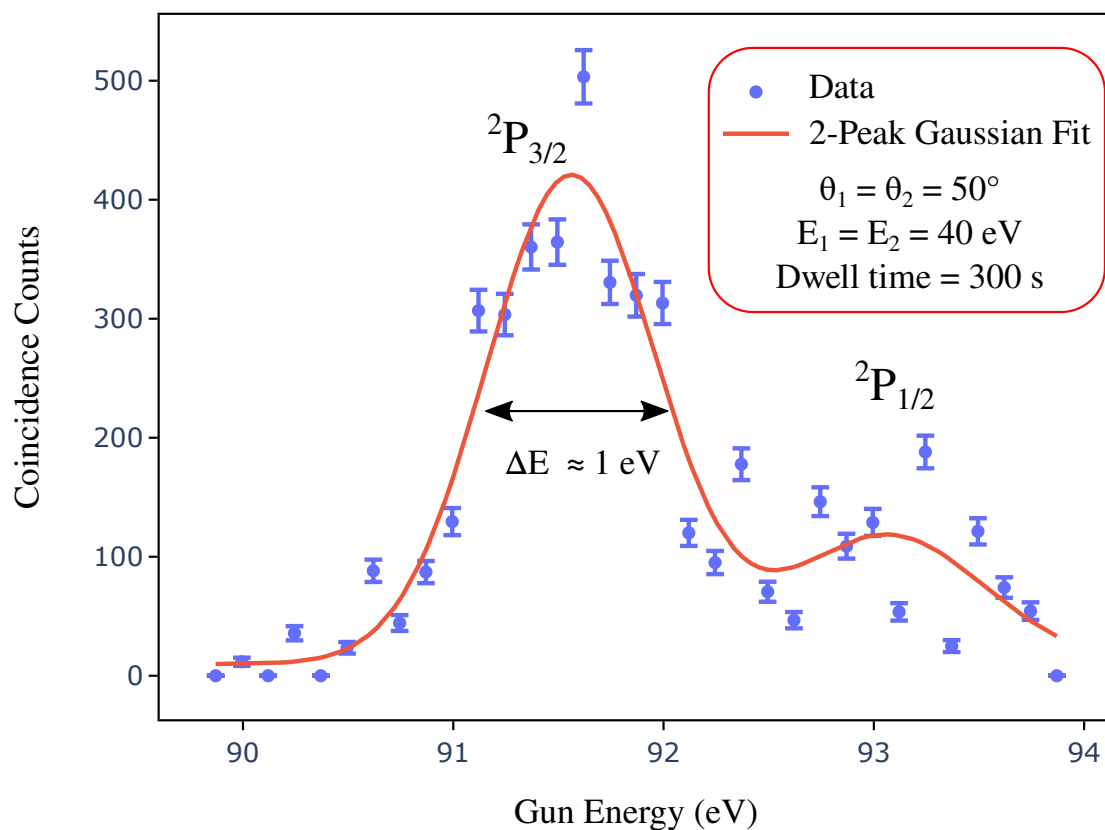


Figure 6.2: Measured binding energy spectrum for the ionisation of xenon showing the two ion ground states $5^2P_{3/2}$ and $5^2P_{1/2}$ in the coplanar geometry. The outgoing electrons detected have symmetric energies of 40 eV and are detected at equal angles of 50° . The electron gun energy increments in 0.125 eV and a dwell time of 300 s was used to gather the coincidence data. The data is fitted with a 2-peak Gaussian model with centres at 91.6 eV and 93.1 eV. The error on each measurement is taken as the square root of the coincidence counts.

6.3 The Measured TDCS from Xenon

The measured cross sections for ionisation of xenon are presented in figures 6.3 to 6.5 for incident electron energies of 60 eV, 80 eV, and 100 eV above the $5^2P_{3/2}$ ion state. For each energy, the gun angle ψ was moved from 0° to 90° in steps of 22.5° . This allows the evolution of the TDCS from a coplanar geometry to the perpendicular plane to be determined.

For each gun angle the coincidence counts were normalised to the common point of $\theta = 90^\circ$ so that a direct comparison can be made across all gun angles at each energy. This point is common to all gun angles due to symmetry, as shown in figure 1.6. A logarithmic scale is used to present these data as the TDCS varies over a large range for different angles, particularly at higher energies.

6.3.1 60 eV above the IP

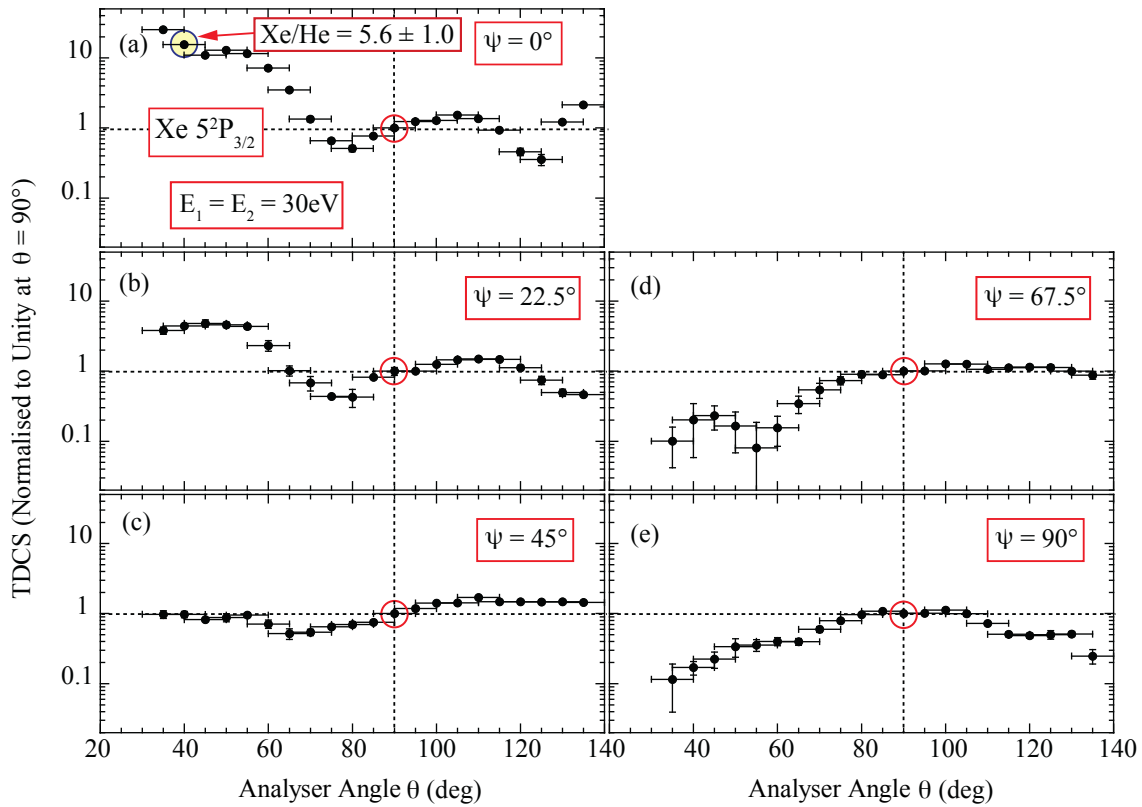


Figure 6.3: The evolution of the TDCS of xenon as the incident electron angle ψ is moved out of the plane from a coplanar geometry (a) to perpendicular to the plane (e). These data were taken with an incident energy of 60 eV above the $5^2P_{3/2}$ ion state. All measurements are inter-normalised to the 90° common point which is here set to unity. The Xe:He coincidence ratio was determined to be 5.6 ± 1.0 at an analyser angle of 40° as shown (see section 6.4 for details).

Figure 6.3 shows the measured TDCS for the lowest energy investigated of 60 eV above the IP. For the kinematics adopted in all these experiments the TDCS must be zero at both 0° and 180° due to post collisional interactions, as noted above. The coplanar TDCS hence exhibits a three peak structure with the largest peak in the forward-scattering region,

where θ is less than 90° . A local minimum can be seen at $\sim 45^\circ$ within this structure. A second peak is found at $\sim 105^\circ$ with a minimum at $\sim 80^\circ$. The cross section then decreases in this backward-scatter region ($\theta \geq 90^\circ$), a second minimum being observed at $\sim 125^\circ$. A third peak occurs at higher angles, however its position is beyond the range of the spectrometer. This third structure is larger than that at 100° but is smaller than the forward-scatter peak. The minima at around 45° and 125° are due to the momentum distribution of the bound p-electron that is ionised, as is well documented for the heavier noble gas targets [138–140].

As the gun angle is increased out of the plane the TDCS starts to flatten and becomes almost uniform with angle at $\psi = 45^\circ$, where the TDCS in the forward-scatter and back-scatter regions is approximately the same as at an angle of 90° . The mechanisms which cause the back and forward-scatter peaks are hence suppressed as the incident electron angle is moved out of the plane. At $\psi = 67.5^\circ$ the forward-scattering cross section reduces by a factor of ~ 10 and at an angle of 55° a minimum is seen (although the uncertainty is large). The statistical variation at this angle is large since the coincidence rates were only a few counts in several hours. In the perpendicular plane, where $\psi = 90^\circ$, the forward and back-scatter peaks have largely disappeared, leaving a single peak at 90° as observed previously (and as shown in figure 6.1).

6.3.2 80 eV above the IP

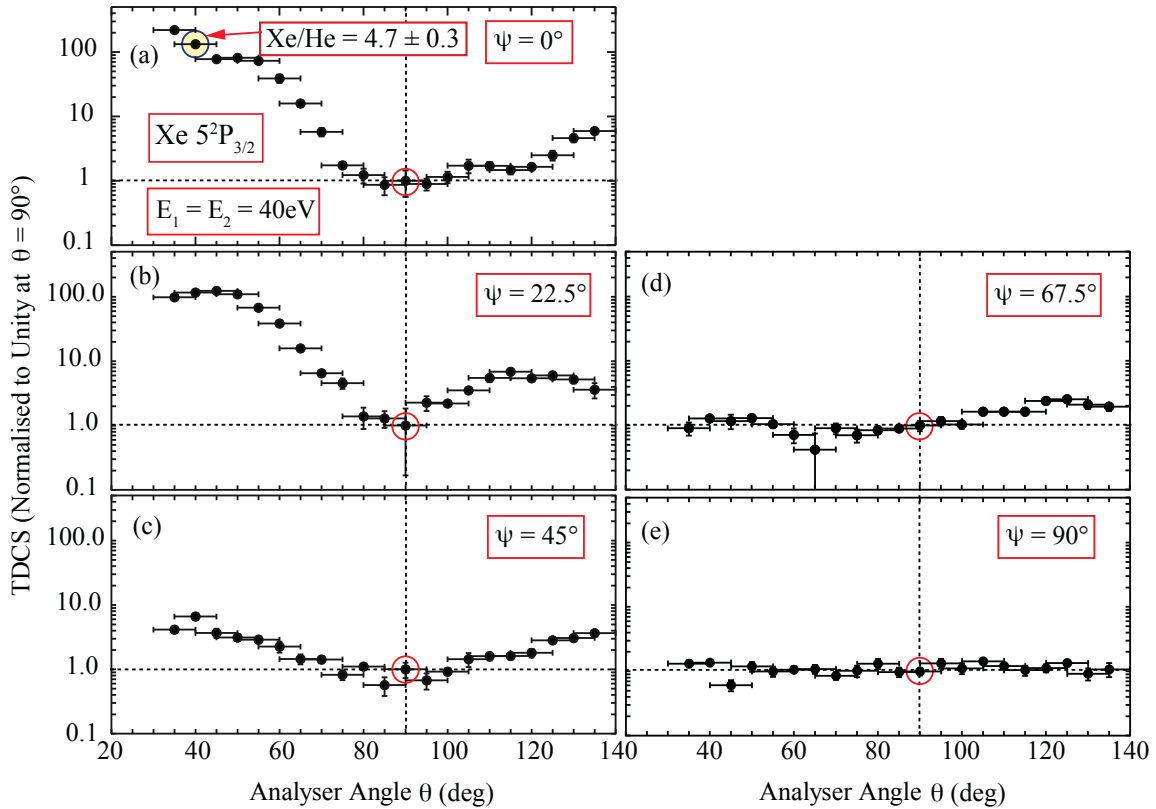


Figure 6.4: Evolution of the TDCS of xenon as ψ is moved out of the plane at an incident energy of 80 eV above the IP. All measurements are again inter-normalised to the 90° common point. The Xe:He coincidence ratio was determined to be 4.7 ± 0.3 at $\theta = 40^\circ$.

Figure 6.4 shows the evolution of the TDCS at 80 eV above the IP. The coplanar data shows a similar 3-peak structure as for 60 eV (figure 6.3). The minima due to the momentum of the bound electron at 45° and 125° are not as deep under these kinematic conditions, the second peak at around 105° being much less pronounced at this energy. The ratio between the TDCS at the 90° common point and both forward and back-scatter peaks is now much larger, with the cross section at 35° over 100 times larger than at 90° . Rosel and co-authors [141] propose that the relative cross section at 90° will reduce as the incident energy increases as expected from Rutherford scattering, where the TDCS at 90° is proportional to E_{inc}^{-2} as noted in chapter 1. The results shown here broadly follow this pattern.

As the gun angle increases out of the plane the TDCS again reduces on both sides of the 90° common point, as is found at the lower energy. When $\psi = 45^\circ$ the TDCS has a double-peaked structure with a single minimum around 90° . At the gun angle of 67.5° the TDCS again flattens and shows little change with scattering angle. The minimum at this gun angle is much less prominent and has moved to $\sim 65^\circ$. The TDCS then slowly rises to a small peak at around 125° . In the perpendicular plane when $\psi = 90^\circ$, the TDCS is almost completely flat and has no clear structure. This contrasts with the data at 50 eV, 60 eV, and 70 eV shown above, where a broad peak at 90° is observed. As discussed above, PCI forces the TDCS under these kinematics to be zero at $\theta = 0^\circ$ and 180° and so this broad feature must reduce to zero at these extreme angles, although it was not possible to measure the cross section in these regions.

6.3.3 100 eV above the IP

The results for 100 eV above the IP are shown in figure 6.5. The contrast between high and low measurements in the coplanar geometry is much greater at this energy, with the forward scatter peak at $\theta = 35^\circ$ being almost 1000 times larger than at the $\theta = 90^\circ$ point. The shape of the coplanar DCS at this energy is similar to the results at lower energies, however the second minimum at $\sim 125^\circ$ due to the momentum of the bound p-electron is no longer observed. The minimum in the DCS under these conditions is found at $\sim 90^\circ$.

As the gun angle increases to $\psi = 22.5^\circ$ the dip at 45° can no longer be seen and the TDCS reduces significantly in the forward direction, while maintaining a similar magnitude in the backward direction. The back-scatter peak has moved to 125° from $\sim 135^\circ$. At a gun angle $\psi = 45^\circ$ the forward and back-scatter peaks decrease further and the minimum moves to $\sim 95^\circ$. At $\psi = 67.5^\circ$ the TDCS again is relatively flat with small peaks of similar magnitude in both forward and backward directions (as inferred from the TDCS being zero at 0° and 180° due to PCI). When the gun is set perpendicular to the plane the TDCS now has evolved into a 3-peak structure, with peaks at $\sim 40^\circ$ and $\sim 135^\circ$ together with a small central peak at 90° . These measurements are hence similar to those of helium at lower energies, where ionisation occurs from an s-electron rather than a p-electron. One possibility for this three-peak structure is that the deep penetration into the atom that occurs in the perpendicular geometry at these energies may be probing the inner 5s electrons, rather than directly ionising an outer 5p electron. Clearly further input from theory is required to elucidate whether this could be the mechanism that is involved.

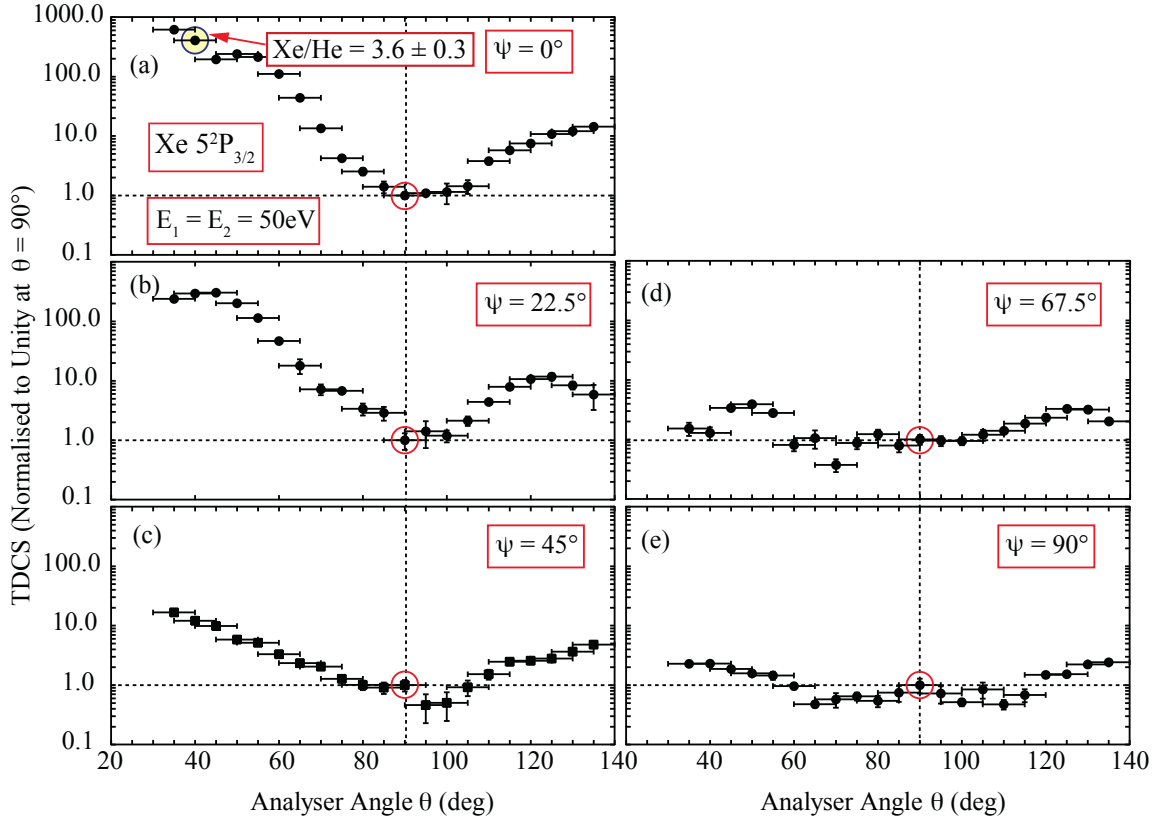


Figure 6.5: Evolution of the TDCS of xenon as ψ is moved out of the plane at an incident energy of 100 eV above the IP. All measurements are inter-normalised to the 90° common point. The Xe:He coincidence ratio is determined to be 3.6 ± 0.3 at $\theta = 40^\circ$.

6.4 Xenon-Helium Coincidence Ratio

Absolute cross section measurements are desired from coincidence experiments for direct comparison to theory, since different models can produce similar structures but they may have very different magnitudes. In practice, absolute measurements are very difficult to make at low energies and so almost all data in this energy regime are relative. The techniques adopted in Manchester allow a relative TDCS to be determined over a large angular range in three dimensions, since there is a common point at $\theta = 90^\circ$ for all gun angles. These previous experiments have not however measured absolute cross sections, due to the difficulty of defining the parameters of the experiment under low energy conditions.

A new technique has hence been adopted in the present work to map the data onto an ‘absolute’ scale, by measuring the TDCS for xenon in parallel with measurements from helium. Since the helium ionisation cross section is now modelled accurately by theory [64], the ratio of measurements from each target under the same conditions will allow these new xenon results to be placed on an absolute scale, once the TDCS of helium is calculated.

As noted in [142], the coincidence count rates measured at a given angle and energy N_C^{gas} are determined from the TDCS as well as the analyser efficiencies $\varepsilon_1, \varepsilon_2$, their solid angles of detection $\delta\Omega_1, \delta\Omega_2$, the energy resolution of the spectrometer δE_C , the tar-

get density $\nu(V)$, the electron beam density, and the interaction volume V_{int} set by the electrostatic optics. The analyser efficiencies are set by voltages on the electron optical elements within each analyser, as well as the efficiency of the channeltron detectors and pass energy of the energy selectors. The scattered electron density selected by the analysers is so low (typically around 1 fA or less) that space charge effects can be ignored within them. The incident electron beam density depends on the characteristics of the electron gun. These can change when different targets are studied, due to space charge effects that occur around the cathode and within the gun electrostatic optics. This makes it very difficult to determine the beam density under different conditions and with different targets. The gas density from the gas jet nozzle may also change for different targets, further complicating direct measurement of absolute values of the cross section.

The influence of the analyser efficiencies can be eliminated by measuring the TDCS for both helium and xenon under the same conditions, so that no changes are made to the electrostatic optics during these measurements. Any density variation of the different targets in the interaction volume can also be removed by ensuring that both targets are uniformly distributed throughout this volume. This was achieved here by feeding an equal mixture of xenon and helium into the spectrometer via a second gas feed, as shown in figure 3.3(c). Since the number density of each target is the same when injected through this feed, the vacuum chamber (and hence interaction volume) are filled with a correspondingly uniform background gas density for each target, so that $\nu_{He} = \nu_{Xe}$.

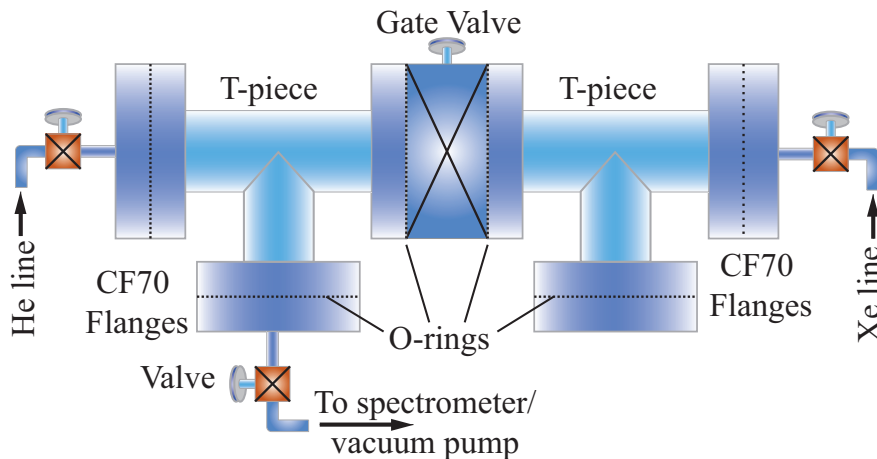


Figure 6.6: A diagram of the mixing chamber used to mix He and Xe gas into a 1:1 He-Xe mixture. The chamber is made from stainless steel with valves shown as crosses and O-rings shown as dashed lines.

To ensure an equal quantity of He and Xe gas was present in the interaction region, a mixing chamber was built to mix the two gases together before injection into the spectrometer. Figure 6.6 shows a diagram of the mixing chamber that was used. The chamber is composed of two equal-sized, stainless steel T-pieces separated by a gate valve. Inlet valves fitted to the chamber allowed He and Xe to fill individual chambers separately while the gate valve was shut. When the gate valve was opened, the two gases mixed. To ensure the mixture had an equal ratio of gases, both sides were filled to a pressure of 2 bar using the same regulator. Since each chamber had the same volume and pressure, there was hence an equal density of He and Xe atoms in each. Opening the gate valve then produced a mixed gas ratio of 1:1. A third valve fitted to one of the T-pieces allowed

the mixing chambers to be evacuated before filling. This valve was also used to redirect the gas mixture into the spectrometer via a needle valve located on the top flange.

Since the effect on the gun due to the different gases was equal (as the chamber was uniformly filled with both targets) the relative effects of space charge are also removed. The TDCS ratio hence only depends upon differences in the beam profile that occur due to changes in the energy. The energy must be changed for fixed outgoing electron energies, since He and Xe have ionisation potentials separated by ~ 13 eV. By keeping all electrostatic elements in the gun unchanged during ratio measurements, the effect on the beam radius at different energies was calculated using the modelling program SIMION [143]. The model indicated that the electron beam with current I_F had a uniform density across its profile and that the beam radius r_{gas} changed only slightly with energy. Since the target gas density is uniform throughout the spectrometer $\nu(V) = \nu_{He} = \nu_{Xe} = \nu$. The interaction volume is then set by the volume spanned by the incident electron beam as it passes through the region defined by the analyser electrostatic optics. This volume is given by $V_{int} = \pi r_{gas}^2 L_{int}$, where L_{int} is the length of the region. The coincidence rates are then given by:

$$\dot{N}_C^{Xe} = \frac{I_F \nu V_{int}}{e \pi r_{Xe}^2 I_F} (TDCS)^{Xe} \varepsilon_1 \varepsilon_2 \delta \Omega_1 \delta \Omega_2 \delta E_C \quad (6.1)$$

$$\Rightarrow (TDCS)^{Xe} = \dot{N}_C^{Xe} \frac{e}{I_F \nu L_{int}} (\varepsilon_1 \varepsilon_2 \delta \Omega_1 \delta \Omega_2 \delta E_C)^{-1} \quad (6.2)$$

similarly

$$(TDCS)^{He} = \dot{N}_C^{He} \frac{e}{I_F \nu L_{int}} (\varepsilon_1 \varepsilon_2 \delta \Omega_1 \delta \Omega_2 \delta E_C)^{-1} \quad (6.3)$$

In these experiments the analyser parameters and the beam current I_F did not change between measurements from Xe and He. The relative cross sections can hence be derived from the coincidence rates:

$$\frac{(TDCS)^{Xe}}{(TDCS)^{He}} = \frac{\dot{N}_C^{Xe} \frac{e}{I_F \nu L_{int}} (\varepsilon_1 \varepsilon_2 \delta \Omega_1 \delta \Omega_2 \delta E_C)^{-1}}{\dot{N}_C^{He} \frac{e}{I_F \nu L_{int}} (\varepsilon_1 \varepsilon_2 \delta \Omega_1 \delta \Omega_2 \delta E_C)^{-1}} \quad (6.4)$$

$$\therefore (TDCS)^{Xe} = \left(\frac{\dot{N}_C^{Xe}}{\dot{N}_C^{He}} \right) (TDCS)^{He} \quad (6.5)$$

A representative sample of the coincidence counts measured with an equal He and Xe mixture at an energy of 100 eV above the IP is shown in figure 6.7. For each 300 second run the incident energy was switched sequentially to detect coincidence counts from He and then Xe at a fixed angle of $\theta = 40^\circ$ in a coplanar geometry. The coincidence counts for Xe and He can be seen in figure 6.4(b). Over time the gas in the mixing chamber was used up as it exited into the spectrometer through the needle valve. The pressure in the mixing chamber hence decreased, leading to a corresponding decrease in the background gas pressure inside the spectrometer, shown in figure 6.7(a). This decrease in the background gas density lead to a corresponding slow decrease in coincidence counts over time. To allow for this variation, the data were re-normalised to the chamber pressure over the running time of the experiment, as shown in figure 6.7(c). The error bars are set to the square root of the counts. The large variation in the average is due to the short dwell time for each run. A short dwell time was used to keep coincidence counts high for the

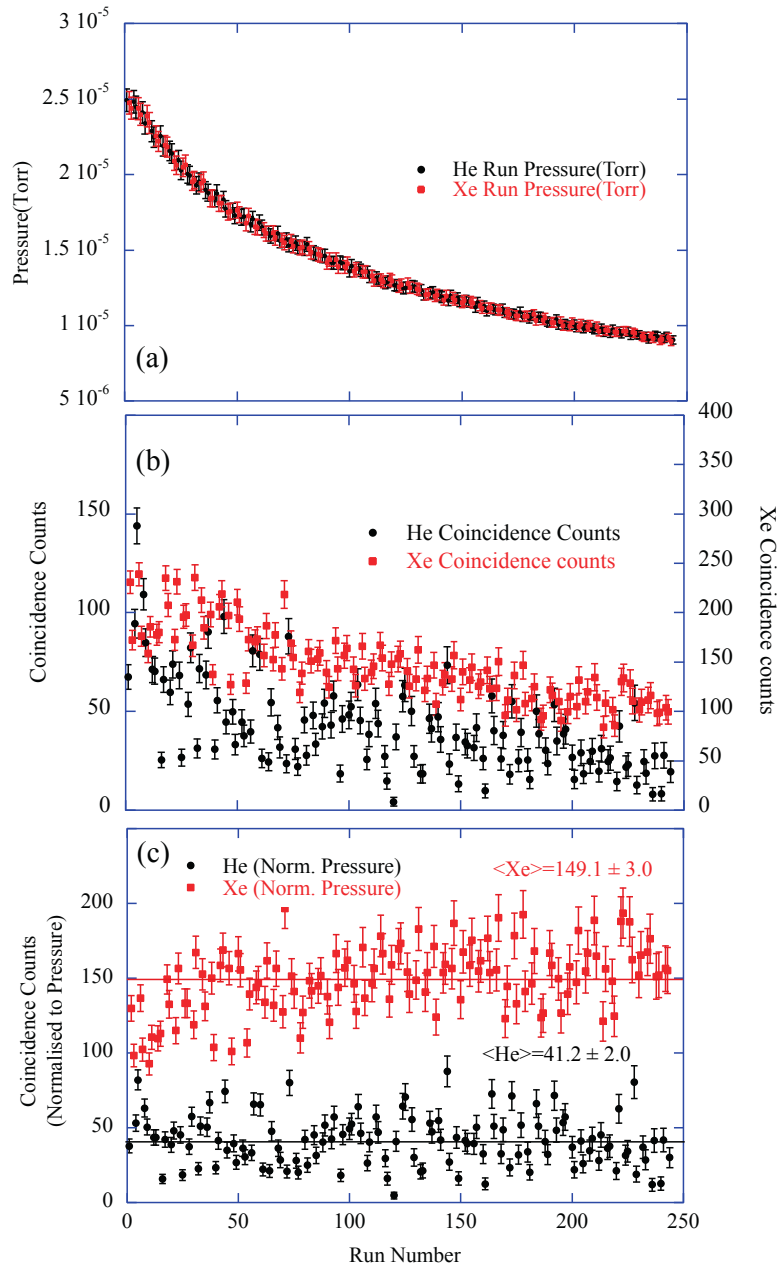


Figure 6.7: The coincidence counts as the incident electron energy is switched to sequentially detect signal from He and Xe with a uniform 1:1 mixture throughout the spectrometer. The analysers were set to detect electrons with 50 eV energy at an analyser angle of 40° in a coplanar geometry. (a) shows the measured pressure in the chamber. (b) shows the counted coincidence events in a 300 second period. (c) shows the coincidence counts normalised to pressure, where the mean coincidence counts are shown as dashed lines and are given by 149.1 ± 3.0 for Xe and 41.2 ± 2.0 for He. The uncertainties in each measurement are taken as the square root of the normalised coincidence counts

duration of the experiment, which decreases over time due to the decrease in chamber pressure. These measurements established that the He TDCS is smaller than the Xe TDCS at this angle for all energies studied here, with ratios of 5.6 ± 1.0 , 4.7 ± 0.3 , and 3.6 ± 0.3 at 60 eV, 80 eV, and 100 eV above the IP respectively. These ratios are also given in figures 6.3, 6.4 and 6.5 above.

6.5 Summary

In this chapter, the ionisation cross sections for Xe have been presented for a range of energies from 60 eV to 100 eV above the ionisation potential of the $5^2P_{3/2}$ ion state, for a range of geometries from coplanar scattering to the perpendicular plane. The outgoing electrons were selected to have equal energies and equal angles from the projection of the incident electron beam onto the detection plane. This configuration allowed all data at a given energy to be placed on a relative scale through the common normalisation point where $\theta_1 = \theta_2 = 90^\circ$. The results were then renormalised onto an ‘absolute’ scale by comparing the TDCS for Xe at $\theta = 40^\circ$ to that for He, which can be calculated accurately using collision models. It is found that at this scattering angle the TDCS for Xe is larger than that for He at all energies studied here.

The results presented in this chapter will provide a comprehensive test of different collision models for this target, at energies where calculations such as the Distorted Wave Born Approximation have proven to be reasonably accurate. The lower energy measurements at 60 eV above the ionisation potential in the perpendicular plane again show that the TDCS for Xe does not follow the trend seen in other noble gases, with a peak at $\theta = 90^\circ$ rather than a minimum. As the energy increases further to 80 eV this feature reduces to a broad flat structure. At the highest energy of 100 eV a 3-peak structure re-emerges, similar to that seen for helium at lower energies. These features suggest that the collision mechanisms in this geometry are becoming more complex and so they will provide a good test of future models.

It is unclear without further theoretical input why these structures evolve as they do, however it is evident that the ‘sequential’ collision processes discussed in the introduction cannot explain these findings. Broad flat cross sections have also been observed in the perpendicular plane for molecular targets such as CH_4 [69]. The mechanism that creates these broad structures hence appears to be related to the kinematics rather than to the target.

The TDCS at other incident angles and energies also show structural complexity that will test new calculations and models. The cross sections are seen to vary widely in magnitude, with the ratio between maximum and minimum measurements in a coplanar geometry at 100 eV being ~ 3 orders of magnitude. Since the data are placed on a relative scale for all gun angles through the common normalisation point, the results at each energy will provide an excellent test of theory as the incident beam angle changes. By linking the absolute magnitude of the cross sections to that of helium as described above, these new results will also allow further examination of the interaction processes that are occurring, and the suitability of different models and approximations when applied to this target.

In the next chapter, measurements of Ar are presented in the perpendicular plane to see if a similar broad, flat structure appears as the energy increases. These measurements also investigate the query by Whelan and co workers [36] who found a large disagreement with experiment at an incident energy 50 eV above the ionisation potential for this target.

Chapter 7

The Evolution of the TDCS of Argon

In this chapter, triple differential cross section (TDCS) measurements from argon are presented in the perpendicular plane geometry. These measurements were made using the Old (e, 2e) spectrometer. New data were obtained at energies from 40 eV to 200 eV above the ionisation potential (IP), with the scattered and ejected electrons having equal energies. These data are compared to previous measurements from 5 eV to 50 eV above the IP as well as to theoretical calculations from different models in this energy range. A significant discrepancy between the prediction of theory and experiment 50 eV above the IP was re-tested, the new experiments confirming the results from previous measurements. Additional data spanning this energy are presented which show a deep minimum in the cross section under these conditions. Results for the evolution of the cross section into the intermediate energy regime are also discussed.

7.1 Introduction

The motivation for the experimental work on argon arises from a query by Whelan and co-workers [36] who found a large disagreement between the experimental data in previous measurements of argon [134] and their models at an energy of 50 eV above the IP. By contrast, their calculations using a non-relativistic distorted wave Born approximation (DWBA) agreed reasonably well at 35 eV and 40 eV above the IP, as long as post-collisional interactions (PCI) were not included. These differences prompted the authors to suggest that the experimental results should be remeasured in this regime and that more data was required to establish if the difference was real. PCI was included through the use of both a Gamow factor and the Ward-Macek factor, as discussed in chapter 1. Both methods provide an approximation to the effect of PCI and their inclusion for argon was found to overcompensate the effects of electron-electron repulsion for the outgoing electrons. The DWBA model without inclusion of PCI hence provided the closest agreement to experiment, apart from in the regions near mutual outgoing electron angle $\phi = 0^\circ$ and 180° where PCI dominates.

Previous perpendicular plane measurements conducted in Manchester from argon were carried out from 5 eV to 50 eV above the $3^2P_{3/2}$ ion state [134]. These data are reproduced in this chapter for comparison to the new results which extend the energy to 200 eV above the IP. Data between 40 eV and 60 eV above the IP have also been obtained with a finer energy mesh than previously adopted, to explore the region of discrepancy between theory and experiment as seen in [36]. New results from 60 eV to 200 eV above the IP were also taken to establish how the TDCS varied with angle over a much wider energy range than has been carried out before.

7.2 The Measured DCS of Argon

The TDCS of Ar was measured from 5 eV to 200 eV above the IP. These results show that there is a larger than expected cross section at 50 eV above the IP so a finer scan around this energy was measured. The mutual analyser angles $\phi = \theta_1 + \theta_2$ are plotted in the following results to provide a direct comparison between the theory in [36] and measurements. It should be noted that in this geometry only the angle ϕ has meaning.

These measurements took several months to complete due to the very low count rates obtained in the perpendicular plane at higher energies. The Old (e, 2e) spectrometer was used to perform these measurements between mutual analyser angles of 70° to 270° . Due to the analyser energy resolution of ~ 1 eV it was not possible to resolve the $3^2P_{1/2}$ and $3^2P_{3/2}$ ion states and so the coincidence signals are a contribution from both states. Data was collected for 2000 s to 12,000 s for each coincidence measurement.

7.2.1 5 eV to 200 eV above the IP

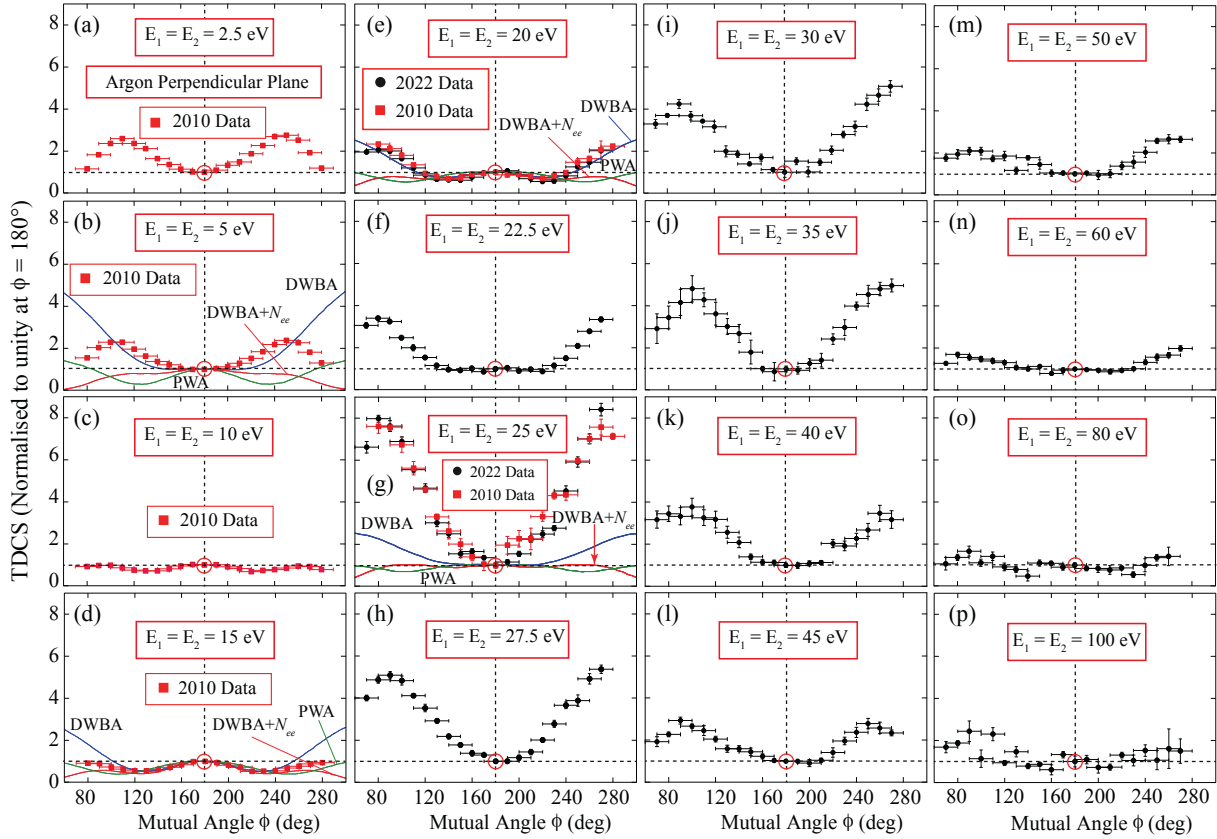


Figure 7.1: Evolution of the TDCS of argon in the perpendicular plane from (a) 5 eV above the ionisation potential to (p) 200 eV above the IP. All measurements are normalised to unity at the mutual analyser angle $\phi = 180^\circ$. The data shown as (red) squares are from measurements taken in 2010 [134], whereas those shown as (black) dots are the new measurements. The calculations of [36] are also shown.

The measured cross sections for the ionisation of argon are presented in figure 7.1 for incident electron energies from 5 eV to 200 eV above the $3^2P_{(1/2,3/2)}$ ion states [134, 144]. At each energy, the gun angle was set to $\psi = 90^\circ$ and the mutual analyser angle ϕ was adjusted in steps of 10° . The data are normalised to unity at the angle $\phi = 180^\circ$ where the analysers are opposite each other. The data are hence relative measurements for each energy. This is consistent with the previous data that has already been published for this target.

The results from [134] have also been reproduced in figure 7.1 so that a direct comparison can be made between the new measurements and the previous data. This figure also shows how the relative cross section evolves from a low incident energy 5 eV above the IP to a high energy 200 eV above the IP. The results from the calculations in [36] are also reproduced here, to allow comparison between theory and experiment. The models include the DWBA calculation with no inclusion of PCI (DWBA), the calculation *with* inclusion of PCI (DWBA + N_{ee}) and when plane waves were used instead of distorted waves (PWA). The Gamow factor N_{ee} is defined in equation 1.32. Results from these models are included for incident energies above the IP of (b) 10 eV, (d) 30 eV, (e) 40 eV and (g) 50 eV. As noted in [36] the DWBA without PCI gives the closest agreement with

the data from $\phi = 120^\circ$ to $\phi = 240^\circ$, however since PCI is not included, this calculation diverges from the data as the analysers approach each other. Inclusion of the N_{ee} factor to emulate PCI is clearly too strong an effect, since this calculation is in greater disagreement with the data, especially at low and high angles. Its inclusion does however ensure that the cross section is zero at $\phi = 0^\circ$ and $\phi = 360^\circ$, which is required for the kinematics chosen here. The plane wave approximation in general does not emulate the data at any of the energies shown here.

The most striking difference between theory and experiment can be seen at an energy of 50 eV above the IP. It is this difference that motivated the current measurements, as suggested in [36]. The new experimental data agrees well with the older measurements both at (e) 40 eV and (g) 50 eV above the IP. These results hence show that the models are missing something within the interaction at this energy, leading to this difference. To help elucidate what this mechanism may be, the cross section in this region was further explored over a finer energy grid. These data are presented in figure 7.2 and are discussed below.

Experimental measurements were also taken at higher energies as shown in panels (h) to (p), so that the evolution of the cross section could be further explored beyond previous studies. These measurements are challenging due to the very low coincidence rates that are produced in this region and so there is a reasonable degree of variation in the data. Beyond 50 eV above the IP the cross section is seen to have only a 2-peak structure with the peaks decreasing in magnitude as the energy is increased. This trend continues until at 60 eV above the IP the cross section becomes almost flat, with little angular variation as the mutual angle changes. This has also been observed in the results for xenon (see chapter 6) as well as in some molecular targets in this geometry [69] and so it appears not to be due directly to the target but due to the kinematics of the interaction. Additional calculations are hence required to explain these results.

7.2.2 Detailed Measurements around 50 eV above the IP

Figure 7.2 shows the measured TDCS over a finer energy grid than adopted in figure 7.1, so that more data in this region are available for comparison to future models. The data for $E_1 = E_2 = 20$ eV (panel (a)) shows a 3-peak structure with a small central peak at $\phi = 180^\circ$ and two additional peaks at around $\phi = 80^\circ$ and $\phi = 280^\circ$. As noted above, the TDCS must be zero at $\phi = 0^\circ$ and $\phi = 360^\circ$ and so these peak amplitudes have to decrease to zero beyond the measured data at these extremities. The DWBA model emulates the data well between $\phi = 80^\circ$ and $\phi = 280^\circ$ at this energy, but does not show the peak structure due to the lack of PCI in this model. Both the previous work from [134] and the new data are in agreement over all angles where measurements were carried out.

The new results 45 eV above the IP are shown in panel (b). The middle peak is seen to have reduced in amplitude compared to the side-peaks, with the data between 140° and 220° being relatively flat. As the energy increases to 47.5 eV above the IP (panel (c)) the central peak and flat area have largely disappeared and the TDCS in this region decreases compared to that for the side-peaks. A small increase in energy to 50 eV (panel (d)) then shows a rapid decrease in the TDCS at $\phi = 180^\circ$ compared to the maxima around $\phi = 90^\circ$

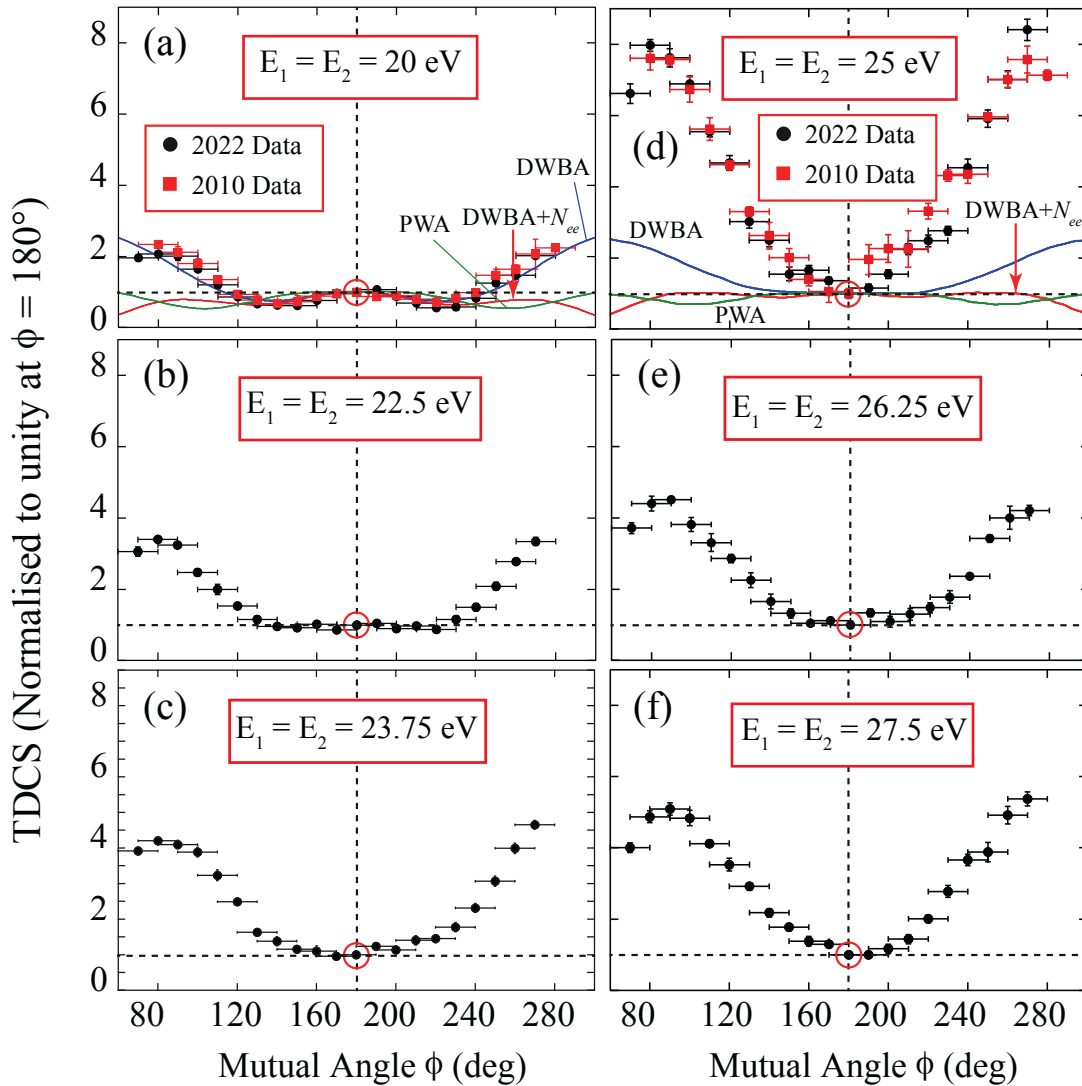


Figure 7.2: Detailed survey of the TDCS of argon in the perpendicular plane from 40 eV to 55 eV above the ionisation potential. The measurements are again normalised to unity at the mutual analyser angle of 180° . The data shown as (red) squares are from measurements taken in 2010, whereas those shown as (black) dots are the current measurements. The calculations of Whelan and co-workers [36] are shown for 40 eV and 50 eV above the IP as solid curves.

and 270° . The new data and older measurements at this energy are again in agreement. The DWBA, DWBA + N_{ee} and PWA models do not predict the data at this energy, as has been discussed above. A further increase in energy to (e) 52.5 eV and (f) 55 eV above the IP shows that the relative magnitude of the side peaks compared to the TDCS at $\phi = 180^\circ$ decreases once more. No central structure is observed at energies greater than 45 eV above the IP, as discussed above.

The large changes around $E_1 = E_2 = 25$ eV indicate that an additional process is occurring at this energy that is not included in the models. The deep minimum relative to the side peaks that is seen here may hence be due to a mechanism first reported experimentally in helium at 64.6 eV for a gun angle of 67.5° [51, 145, 146]. These helium experiments found that the TDCS decreased sharply to zero at this incident beam angle for scattered and ejected electron angles $\theta_1 = \theta_2 = 70^\circ$ (see figure 1.6). It was suggested in [51] that this deep minimum is due to quantum interference, leading to a zero in the cross section under these non-coplanar kinematic conditions. A second minimum was predicted several years later by Whelan and co-workers [147] from ionisation of the inner 2s electron in neon. This was subsequently observed experimentally in Manchester [148].

The deep minima that are found in non-coplanar ionisation cross sections have been considered theoretically by a number of authors since their discovery, as is discussed in [36]. This has led to new studies of *quantum vortices* in the wavefunctions that describe the ionisation cross sections. Macek, Briggs and co-authors [149] first explained the experimental data in [51] using this approach in 2010. Subsequent theoretical studies have been carried out since that time by a number of authors for both electron and positron impact ionisation [150–152]. These theories use a partial wave expansion to construct a total wavefunction which describes the TDCS, as discussed in chapter 1. In momentum space, there are some points where the expansion of the partial waves destructively interfere as more terms are added. This ultimately leads to a zero at the centre of a vortex in momentum space, which subsequently leads to the deep minima that are observed in the measured ionisation cross sections. The minimum found in the new experimental data presented here may hence arise due to a similar quantum vortex occurring nearby in the results presented for the ionisation of argon.

7.3 Summary

In this chapter, the ionisation cross sections for Ar have been presented over a wide range of energies from 5 eV to 200 eV above the ionisation potential of the unresolved $3^2P_{(1/2,3/2)}$ ion states. The measurements were carried out in the perpendicular plane using the Old (e, 2e) spectrometer and have now been published in [67]. The detected electrons were selected to have equal energies and the results are presented as a function of the mutual analyser angle ϕ between them. The data are presented on a relative scale with the TDCS at $\phi = 180^\circ$ set to unity at each energy. A query by Whelan and co-workers [36] about the reliability of previous data taken in 2010 [134] has now been resolved in favour of the experimental results. Further measurements over a finer energy grid have found that the TDCS in this region produces a deep minimum in the cross section that may be related to the presence of a nearby quantum vortex. Further theoretical analysis of the collision

is hence required to establish if this is the mechanism that is involved.

New data have also been presented that extends the measurements into the intermediate energy regime where models such as the Distorted Wave Born Approximation have proven to be reliable under these kinematic conditions. By providing a comprehensive survey of this region, it is hoped that the calculations can be refined, to present an accurate description of the interactions that are occurring. The TDCS at the higher energies evolves into a broad flat structure with the side lobes seen around $\phi = 90^\circ$ and 270° reducing in magnitude as the energy increases. The broad featureless cross section found at these higher energies has been observed from other targets including Xe and CH₄. The TDCS in this region may hence be dominated by the kinematic conditions, rather than by the target structure. More theoretical input is needed to resolve why the TDCS evolves in energy as is observed here.

Further measurements are underway at Manchester to explore these energy regions further, with experiments using Kr now being conducted to extend the existing perpendicular plane data into the higher energy regime.

In the next chapter, a fluorescence spectrum from the laser excitation of strontium is presented, which was preliminary work towards carrying out (e, 2e) ionisation measurements from this laser-excited target. This work was carried out in the New (e, 2e) spectrometer, since this allows easy access to the laser beams that are required. The New (e, 2e) spectrometer was calibrated using the 2^2S resonance of helium, and so this is also detailed in this chapter. Proposed experiments to measure (e,2e) cross sections from laser-aligned strontium are then outlined.

Chapter 8

Laser-Excited Strontium

This chapter presents preliminary experiments to measure laser-aligned $(e, 2e)$ from a strontium target in the New $(e, 2e)$ spectrometer. First, a fluorescence spectrum of a laser-excited strontium sample and measurements of the isotope shifts of Sr are presented. An elastic scattering spectrum over the 2^2S resonance of He is then discussed, allowing calculation of the contact potential in this spectrometer when using this target. This is necessary since deposition of the metal vapour on different electrostatic elements inside the spectrometer can change the energy of the system. It is hence important to ascertain the effects of this deposition to establish if any changes occur. The process of measuring laser-aligned $(e, 2e)$ from strontium in the New $(e, 2e)$ spectrometer is then described.

8.1 Introduction

Whilst the work presented in chapters 6 and 7 present new measurements for the triple differential cross section (TDCS) of ground state atoms, they do not directly aid in understanding the ionisation of complex *molecular* targets. The modelling of complex molecules has had poor comparison to experiment, as is the case with recent measurements of (e, 2e) cross sections from CH₄ [69], C₄H₈O [153], and C₅H₁₀O₂ [154]. Measurements of (e, 2e) from molecules ‘averages’ over all possible molecular orientations and so theoretical models must calculate the TDCS for each orientation separately and average them. This is extremely computationally intensive and so in practice has only been carried out for a few kinematic conditions and targets. Other methods (e.g. see [155]) are hence often used to approximate this averaging process. These have proven to yield a poor comparison with experiment in most cases so far studied.

Data from laser-aligned atoms can provide an alternative and excellent test of current theories by providing quadruple differential cross section (QDCS) data, as discussed in chapter 1. The first laser-aligned (e, 2e) experiments were performed in Manchester using a magnesium target in the New (e, 2e) spectrometer [71, 72]. These experiments required an operator to be present for the duration of the experiment, as the control of the laser was not synchronised to the main program. Collection of data hence needed to be stopped if the laser wavelength drifted too far from the transition wavelength and started again when the laser wavelength was re-adjusted manually by the operator. With the new experimental control system detailed in chapters 3 to 5, new laser-aligned (e, 2e) measurements can now be performed without an operator present and experimental data can be collected over a greater period of time.

A strontium target is suitable for new laser-aligned (e, 2e) measurements as it is an alkaline-earth atom with no hyperfine structure (similar to magnesium) and so can be aligned into a pure *P*-state. The temperature required to produce an atomic beam of strontium can also be reached by the New (e, 2e) atomic beam oven, as shown in chapter 3 and appendix C.

In this chapter, preliminary experiments leading to the measurements of the QDCS of strontium are presented. A fluorescence spectrum of a strontium sample is first shown, which is used to calculate the isotope shifts and relative isotope abundances of Sr. Fluorescence is also used to establish the correct laser frequency of the 1S_0 to 1P_1 transition of the most abundant isotope of Sr in this spectrometer. This depends on a number of factors including the Doppler profile of the atomic beam and the Gaussian profile of the laser beam. Measurements of the 2^2S resonance of He are also presented, allowing a measurement of the contact potential inside the New (e, 2e) spectrometer to be ascertained. The experiments required to perform laser-aligned (e, 2e) from the sample of strontium are then outlined. These (e, 2e) experiments could not be performed due to failures of the laser systems during the COVID-19 pandemic. The high-powered UV argon ion laser that was used to pump the blue dye laser (and hence obtain the necessary wavelength of ~ 461 nm) failed, following several months of shutdown of the laboratory. This laser cannot be replaced as they are no longer manufactured and so it was not possible to obtain the radiation that was required. The laser was operating during the early stage of this PhD project, which is how the results obtained in this chapter were obtained.

8.2 Fluorescence Spectrum of Strontium

The atomic beam oven was used to heat a strontium sample, producing an atomic beam which passed through the interaction region. The UV pumped blue dye laser system was used to direct blue, tunable laser light at the interaction region to laser-excite the strontium. The lens in the New (e, 2e) spectrometer, as seen in figure 3.4(c), was used to image the fluorescence from the interaction region through a CF70 window and onto a reverse biased OSD15-5T photodiode. The output of the photodiode was fed into an amplifier with controllable gain. The output of the amplifier was measured by the on-board 16-bit ADC on the DAQ card, which was connected to the main PC. The fluorescence signal was therefore measured by the photodiode voltage, which is directly proportional to the intensity under these operating conditions.

The laser frequency was tuned to the $5s^2 \ ^1S_0$ to $5s5p \ ^1P_1$ transition peak by performing a broad frequency scan near the transition frequency 325.2517 THz (460.8622 nm wavelength in vacuum) [105]. The frequency was then set to produce the maximum intensity of fluorescence, which was found to be 325.251892 THz. The atomic beam oven temperature was initially set to 500°C, as estimated by appendix C, and then tuned to maximise the fluorescence, resulting in an operational oven temperature of 650°C for these measurements.

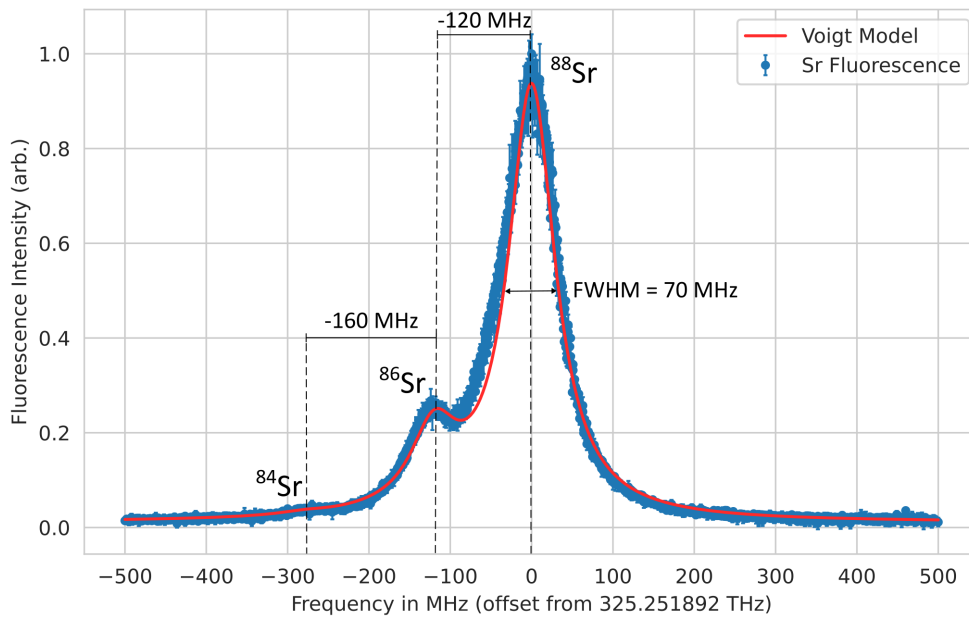


Figure 8.1: The fluorescence intensity of laser-excited strontium as the laser frequency is scanned. The fluorescence intensity is normalised to the maximum measured intensity. A 3-peak Voigt profile is fitted to the data. The isotope peaks are labelled and the isotopic shifts are calculated as: 120 MHz between ^{88}Sr and ^{86}Sr and 160 MHz between ^{86}Sr and ^{84}Sr . The amplitude of the three fitted Voigt profiles are 0.005, 0.15, 0.826 for the ^{88}Sr , ^{86}Sr , and ^{84}Sr peaks respectively. The full-width at half maximum (FWHM) of the Voigt model is 70 MHz for each peak.

The voltage on the DAQ card was then measured as the laser frequency was scanned by ± 500 MHz from the peak fluorescence frequency using the thin etalon scan. This scan was

performed multiple times and the average photodiode voltage was calculated, resulting in the averaged spectrum shown in figure 8.1. A 3-peak Voigt profile [97] is fitted to the data with a full-width at half-maximum constrained to 70 MHz, as it is determined by the resolution of the spectrometer. This allowed an easier fit of the other free parameters (amplitude, centre frequency and background) of the Voigt profiles. The spectrum has a 3-peak structure with each peak corresponding to a strontium isotope: the ^{88}Sr peak at the central frequency, the ^{86}Sr peak at -120 MHz from the central frequency, and the ^{84}Sr peak at -280 MHz away from the central frequency. The amplitude of each peak then corresponds to the relative abundance of the strontium in the sample. The position and relative amplitudes of the peaks agree well with other measurements of the fluorescence spectrum of this atom [156, 157].

8.3 Calibration using the He 2^2S Resonance

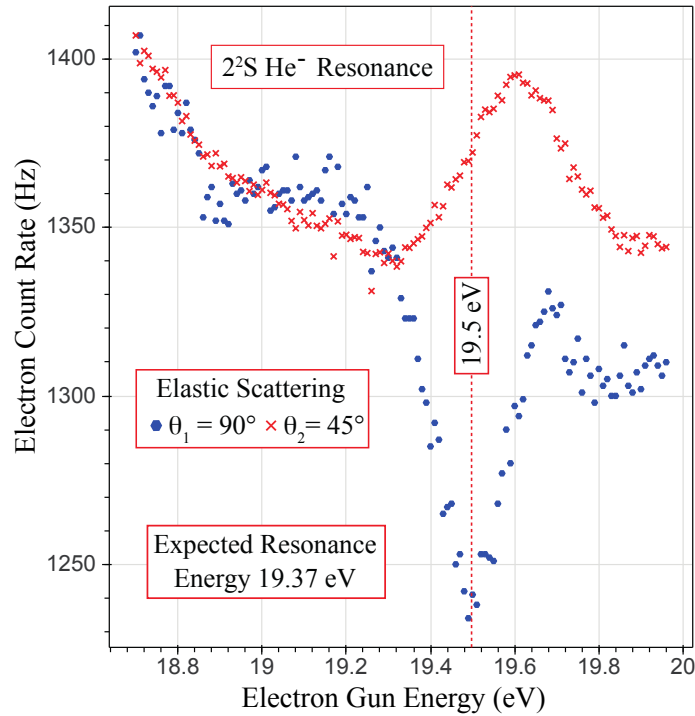


Figure 8.2: Measurement of the elastic scattering spectrum of He as the electron gun energy was scanned over the 2^2S negative ion resonance in the New (e, 2e) spectrometer. The electron energy analyser residual energy was tracked to the gun energy and the pass energy of the analysers was set to 5 eV. The analyser angles were set to $\theta_1 = 45^\circ$ and $\theta_2 = 90^\circ$ for analysers 1 and 2 respectively. The He 2^2S resonance dip is measured at 19.50 eV with the expected dip occurring at 19.37 eV [5]. The difference of 0.13 eV is the contact potential that arises due to strontium deposition.

When performing electron scattering experiments from alkali-earth atoms such as strontium, the ions produced in the interaction region may deposit and condense onto the surfaces of the spectrometer. This charged coating changes the potential difference between the electron gun and the grounded interaction region. This contact potential can be ~ 1 eV so will affect the measured ionisation potential using gun energy scans.

To calibrate the spectrometer, the contact potential can be measured by determining the energy of the elastic scattering 2^2S He^- resonance. This resonance occurs due to the interference between two scattering amplitudes. One scattering amplitude is due to the elastic scattering from neutral helium. The other is from the capture of the incident electron by the He atom forming the unstable $\text{He}^- 2^2S$ state. The subsequent state decays into the ejected electron and the neutral He atom [158, 159]. This results in resonance structures being seen in the elastic scattering cross section at an incident electron energy of 19.37 eV [4, 5]. As the resonance energy is known with high accuracy, the difference between the measured value and expected value yields the contact potential of the spectrometer. The value of the contact potential can then be used to calibrate the energy scale of the spectrometer.

The elastic spectrum of helium scanned over the 2^2S negative ion resonance, as measured by the New (e, 2e) spectrometer, can be seen in figure 8.2. The He was injected into the interaction region via the gas jet, as shown in figure 3.4(c). The spectrum was measured by using a tracking scan, as detailed in chapter 5. The differing feature profiles between the two analysers is due to the resonance cross section varying with scattering angle so only analyser 1, set to an angle of $\theta_1=90^\circ$, was used to determine the He resonance dip. To measure the He resonance precisely, the resolution of the analysers was increased by setting the pass energy of the analysers to 5 eV. Under these conditions the incident beam energy resolution dominates the width of the features. The dip is measured at 19.50 eV and therefore the contact potential is measured as +0.13 V. The contact potential can change over time and is different for various targets so calibration using the He resonance is required after every experiment.

8.4 Proposed Experiments to Measure the QDCS of Strontium

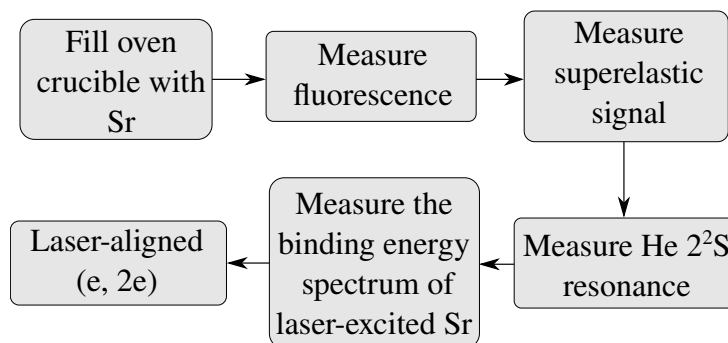


Figure 8.3: Flowchart of proposed experiment leading to performing laser-aligned (e, 2e) experiments from a strontium target and measurement of the quadruple differential cross section (QDCS).

The coincidence signal from alkali-earth targets is lower than that of gaseous targets due to a lower atomic beam density. The coincidence signal from laser-aligned alkali-earths is furthermore even smaller, as a fraction of atoms are only in the necessary laser-excited 1P_1 -state. The measurement of the QDCS of strontium therefore requires

multiple preliminary experiments to tune the experimental conditions to maximise the coincidence signal.

Figure 8.3 shows a flowchart of recommended steps to go through before performing laser-aligned (e, 2e) from strontium using the New (e, 2e) spectrometer. The atomic beam oven must first be charged by filling the crucible with strontium. As Sr reacts with oxygen strongly, care must be taken to ensure that the crucible is filled with a maximum amount of strontium and not strontium oxide. The process of charging the crucible with strontium is therefore performed in an argon-filled bag. The crucible can then be inserted into the atomic beam oven and heated to produce an atomic beam of strontium.

A fluorescence spectrum of the strontium produced by the oven can then be measured, as shown in section 8.2. To produce fluorescence, the laser beam and atomic beam must be aligned to intersect in the interaction region. Measuring the fluorescence spectrum allows the laser wavelength and the atomic beam oven temperature to be tuned to produce a maximum population of excited atoms in the interaction region. Superelastic scattering from the excited 1P_1 state of Sr can then be performed, ensuring that the electron gun, laser, and atomic beam are all aligned. The contact potential inside the spectrometer can then be calculated by measuring the elastic scattering spectrum of He over the 2^2S resonance, as shown in section 8.2. Using the calculated contact potential, the ionisation potential of the laser-excited Sr can be estimated as $IP - \hbar\omega$, where IP is the ionisation potential of the ground state and ω is the angular frequency of the laser light. A binding energy spectrum can then be measured by performing a gun energy scan, as shown in section 6.2. The gun energy can then be tuned to the energy which yields the maximum coincidence counts from the 1P_1 state of Sr.

After performing all of the preliminary experiments, laser-aligned (e, 2e) signals can be measured by performing a half-wave plate (HWP) scan. A step time of up to 2000 s per polarisation angle was used in previous laser-aligned (e, 2e) measurements [72]. In the New (e, 2e) spectrometer, the laser beam is produced by the dye laser system and run through multi-mode optical fibre, then through a polariser and half-wave plate. The beam is then retro-reflected so that the power lost by the polariser is regained by the reflected beam. This setup is likely to produce similar laser power to the previous experiments. Due to the auto laser-locking system, the experiment can be run without an operator so larger step times and longer experiment durations can be used than previously, increasing the accuracy and precision of the measured QDCS. Recent work has been carried out to fix the laser systems in the laboratory and one of the Ti:Sapphire lasers has now been configured to produce radiation at 461 nm. This beam will be used in future experiments to perform the experiments on strontium that are proposed here.

8.5 Summary

This chapter has presented a fluorescence spectrum of strontium excited from the 1S_0 ground state to the first excited 1P_1 state. The isotopic peaks were identified and the relative amplitudes of each peak were measured, showing that the dominant isotope is ^{88}Sr . These data are in good agreement with other measurements of the isotope shifts

and relative isotope abundances for strontium. If the measured spectrum is mapped to a transverse atomic velocity spectrum, the atomic beam divergence can be estimated as is done in reference [157].

A procedure for measuring the contact potential in the New (e, 2e) or Old (e, 2e) spectrometer using the He 2^2S resonance has been discussed. An elastic scattering spectrum over this resonance has been presented, resulting in the calculation of a +0.13 V contact potential in the New (e, 2e) spectrometer. The procedure to tune the New (e, 2e) spectrometer to measure the QDCS from the excited 1P_1 state of strontium has also been described.

In the following chapter, conclusions and suggestions for future research are outlined.

Chapter 9

Conclusions and Suggestions for Future Work

9.1 Conclusions

Electron-atom scattering and electron impact ionisation measurements were introduced in chapter 1. Rutherford scattering was discussed, yielding a single differential cross section which can be used to explain many scattering phenomena. More modern scattering theories were highlighted, including the Distorted Wave Born Approximation (DWBA) with the inclusion of post-collisional interactions (PCI) and the Convergent Close Coupling (CCC) theory. An (e, 2e) experiment fully characterises the electron impact ionisation process by measuring a triple differential cross section (TDCS). Current (e, 2e) theories agree well with experimental data for light elements and molecules at high energies but they do not describe well the TDCS for heavier and complex targets. Laser-aligned (e, 2e) data could aid in developing models describing the (e, 2e) of molecules.

The density matrix formalism can be used to describe the state of an atom. The equations of motion for an atom in a laser field were derived from quantum electrodynamic theory using this formalism in chapter 2. A new open-source laser-atom interaction simulator (LASED) to generate and solve the derived equations for any atom excited by continuous wave laser radiation was then detailed in this chapter. The 4^1S_0 to 4^1P_1 laser-excitation of Ca, the 3^1D_2 to 10^1P_1 laser-excitation of He, following electron-impact excitation from the 1S_0 ground state, and the laser-excitation of the Caesium D_2 transition were all simulated using LASED. This work has been published in [75].

The New (e, 2e) and Old (e, 2e) spectrometers were detailed in chapter 3. The electron gun, Faraday cup (FC), electron energy analysers, channel electron multipliers, analyser and gun power supplies and stepper motor systems were described. The atomic beam oven used in the New (e, 2e) was then detailed along with measurements of its thermal properties. The gravity-fed liquid nitrogen cold trap, gas jet and timing electronics to detect a coincidence event were also described. In chapter 4, the Matisse Ti:Sa laser system was then detailed along with the newly-built laser shielding and magnetic laser safety interlocks. A new ESP32-based laser shutter controller was also described. The

optics inside the New (e, 2e) spectrometer and the half-wave plate (HWP) rotator were then discussed.

A modular, customisable, and low-cost experimental control system for use in both spectrometers has been built. This work is published in [76]. This control system uses a LabVIEW interface which communicates with many Arduino units via USB connections. The Arduino units then control experimental hardware and can easily be re-programmed. A laser-locking program to automatically lock the Ti:Sa laser system's wavelength to a set value has also been built. This laser-locking program communicates with the main LabVIEW control program which will allow laser-aligned (e, 2e) to be performed without an experimental operator present.

New experimental data of the TDCS of xenon was presented in chapter 6. A binding energy spectrum of xenon showed that the $^2P_{3/2}$ and $^2P_{1/2}$ ion states and could be resolved due to the ~ 1 eV resolution of the spectrometer. The TDCS of xenon was then presented for ionisation to the $^2P_{3/2}$ ion state as the scattering geometry changed from coplanar to the perpendicular plane for incident electron energies of 60 eV, 80 eV, and 100 eV above the ionisation potential (IP). A new technique to map these relative cross section measurements to absolute values using a He-Xe mixture was then detailed. These new data confirmed the different trend observed in xenon compared to the other noble gases, as noted in [134]. It was also found that as the energy increases to 80 eV above the IP, the TDCS of xenon evolves into a broad, flat structure as the scattering geometry changes from the coplanar to perpendicular plane geometry. The TDCS then evolves into a 3-peak structure at 100 eV above the IP. This work is published in [66].

New measurements of the TDCS of argon were then presented in chapter 7. The motivation for collecting this data was a query made by Whelan and co-workers [36] who found a discrepancy between their calculations and previous measurements made in Manchester [134]. The TDCS of argon was measured in the perpendicular plane for energies of 40 eV to 200 eV above the IP and was collated with the previous data of the TDCS of argon from 5 eV to 50 eV above the IP. As with the xenon measurements, the TDCS evolved into a flat, broad structure as energy increased. This suggests that this behaviour is independent of target and is likely to be kinematic in origin. Further theoretical investigation is warranted here. A deep minimum in the cross section was measured for an incident electron energy of 50 eV above the IP. More detailed measurements were made around this energy to further investigate the evolution of this feature of the TDCS. This deep minimum may be due to a quantum vortex. A thorough theoretical analysis is required to validate this claim. This work is published in [67].

The fluorescence spectrum of strontium was presented in chapter 8, allowing the tuning of the laser frequency to the 5^1S_0 to 5^1P_1 transition. The contact potential in the New (e, 2e) spectrometer was measured as 0.13 V using the He 2^2S resonance. Experiments leading to the measurement of the quadruple differential cross section of Sr using the New (e, 2e) spectrometer were also outlined.

The primary aims of this project were to set up the spectrometers at Manchester to perform more sophisticated (e, 2e) experiments and to collect novel (e, 2e) data to aid in theoretical understanding of this fundamental process. It is felt that this project has been successful in both of these aims. Data collected from the ionisation of argon and

xenon have revealed new results which warrant further theoretical investigations. A laser-atom simulator has been constructed to aid in the design of (e, 2e) from laser-excited targets. The Old (e, 2e) and New (e, 2e) spectrometers have been upgraded to use a modular experimental control system which can be customised to perform a wide range of measurements.

9.2 Suggestions for Future Work

9.2.1 Improvements to LASED

The purpose of **LASED** is to be a general, easy-to-use laser-atom system simulator which can be used for any atomic system excited by laser light. Later versions of the LASED library should aim to extend its usefulness by including modelling of the interaction in magnetic fields, as well as including excitation by multiple laser beams to model multi-step excitation processes. Computation times can be reduced by carefully considering the symmetry of the system and by eliminating equations that represent density matrix elements that remain zero throughout the simulation.

More theoretical work to express the laser polarisation angle in the equations of motion would save computing time. Currently, to model a polarisation angle, the Wigner rotation matrix must be applied twice: once to rotate to the frame where the polarisation angle is zero and then again back to ensure that the time-evolved density matrix is rotated back to the original frame. This requires a lot of computational resources.

Another useful addition would be the modelling of pulsed lasers. There needs to be careful consideration of the pulse duration when modelling pulsed lasers as the derived equations of motion in section 2.2 could break down if the pulse duration is smaller or similar to the characteristic time of oscillation. If the pulse duration is large enough, the density matrix after pulse-excitation can be substituted into the next pulse cycle as an initial condition, after letting the system freely evolve over the pulse-off time.

In future versions of LASED, computationally intensive tasks could be implemented in a low-level compiled programming language such as (C++ [160] or Rust [161]) whilst still maintaining the easy-to-use python programming interface. This would greatly decrease computing time. Examples of tasks which would benefit from being implemented in a low-level language would be: generating the equations of motion and corresponding matrix A , rotation of the frame of reference, and calculation of the angular shape of the charge cloud.

9.2.2 Improvements to the (e, 2e) Spectrometers and Control System

Measurements of (e, 2e) data at Manchester can be made more reliable and precise by improving the Old (e, 2e) and New (e, 2e) spectrometers. The Ionivac ITR90 pressure

gauge has an RS-232 output which can be read using a microcontroller and an RS-232 to TTL converter so that the analogue pins on the DAQ card are only used to read the output of the TAC. This enables the MCA to not be paused when taking pressure measurements, allowing more readings of the TAC for a given time period which would increase experimental efficiency.

The electron gun supply for the Old (e, 2e) needs replacing as elements supplying the coarse gun energy and the lens voltage GL2B are not working. The New (e, 2e) spectrometer would benefit from having a computer-controlled supply for the electron gun. New designs of power supplies could include measurement of the output voltage by an ADC. This would allow adjustment of the output voltage to match the set voltage using software. Test points should also be provided to allow monitoring of all voltages with a digital voltmeter.

The New (e, 2e) cold trap must be re-filled from a dewar containing liquid nitrogen (LN_2). The dewar contains enough LN_2 to supply the cold trap for 2-3 days of continuous operation. When there is not enough LN_2 in the dewar to fully fill the cold trap, the motor for the pump will keep on spinning. If an operator is not present to manually switch off the motor, the pump can be damaged. To avoid this problem, an LN_2 monitoring system could be designed which measures the motor on-time using an Arduino. The LN_2 pump circuit can be modified to include a transistor which can switch the motor on/off, with the gate of the transistor connected to a digital output pin of the Arduino. If the pump is on for much greater than the average re-fill time, the Arduino would then send a message to the main control program to pause the experiment, until it is restarted by an operator. The Arduino could then turn off the pump by turning off its digital output to the transistor. This monitoring system would also give an estimate of how much LN_2 is left in the dewar and when to re-fill the dewar.

A higher precision ADC could be used in the New (e, 2e) analyser angle controller to measure the analyser potentiometer voltages. With a 12-bit ADC, the angular control of analysers could be a factor of four more precise than the existing 10-bit ADC. An ESP32 microcontroller could replace the Arduino, as these have on-board 12-bit ADCs, or a dedicated ADC could be used e.g. the MCP4822. Code could also be written to auto-calibrate the analyser angles and display an error message in the main program if the rotary couplers are not tight enough and start slipping.

The LabVIEW main control program is large in size and requires strict adherence to guidelines for writing 'clean' code to ensure that it is readable and executes without errors. This means that in practice, writing LabVIEW code to control new hardware takes longer than expected. The program is also difficult to debug as it is large and interconnected. To make modification of the main control program easier, new and existing code could be broken up into modular pieces of executable code in an open-source programming language (e.g. python [79]) and called from the terminal using the LabVIEW main program. This enables parallel processing of tasks to be executed in a highly modular fashion whilst keeping the LabVIEW graphical user interface. The API commands sent to the Arduino units and the checksum system could also be standardised for both Old and New (e,2e) to simplify the code.

New Faraday Cup Current Detector Design

As noted in section 3.6, the isolation amplifier in the Old (e, 2e) spectrometer's Faraday cup (FC) current detector gives an unreliable output. The electrometer which measures the FC current in the New (e, 2e) outputs a noisy signal which oscillates at mains frequency of 50 Hz. This signal could be filtered but it would make the response to sudden changes in current slow.

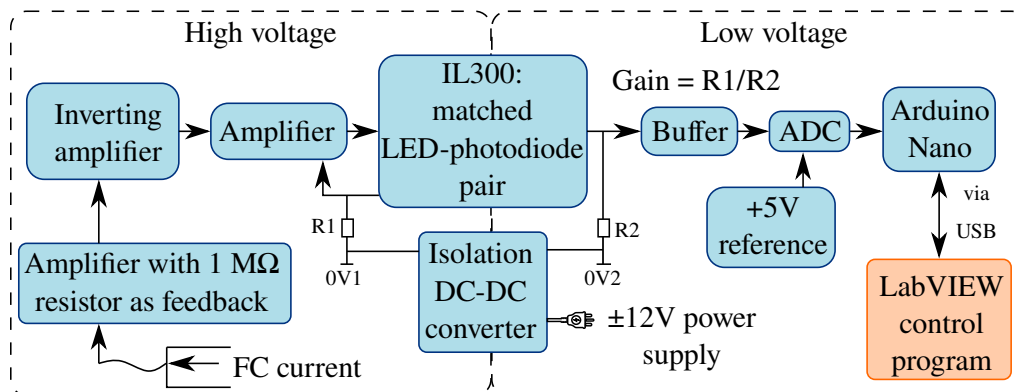


Figure 9.1: A new design for a Faraday cup current detector which uses an IL300 linear opto-coupler. A full schematic and PCB design can be found at [119]. A colour key can be found in figure 3.1.

The design of a new FC current detector is presented in figure 9.1. This design has a similar design to the Old (e, 2e) FC current detector where an amplifier with a $1\text{ M}\Omega$ feedback resistor generates 1 V for every $1\text{ }\mu\text{A}$ of FC current. An IL300 linear opto-coupler is then used to isolate the high voltage FC current signal from the low voltage digital electronics. The IL300 consists of an LED and matched photodiode-pair so that feedback from one photodiode compensates for the non-linearity of the other photodiode and the output has a linear response to input voltage. The gain of the IL300 is set by the choice of resistors R1 and R2. The output of the IL300 is then buffered and measured by an ADC. The ADC passes on this measurement to an Arduino Nano which then sends the reading to the main control program via a USB connection.

The circuit schematic and PCB design for this device is available at [119]. This device has been built and is in testing, the IL300 successfully outputs a linear voltage from μA current but the ADC failed to read the voltage. Investigation and potential modification of this design is therefore required.

An Atomic Beam Oven Temperature Controller

The atomic beam oven requires careful warming up to its operating temperature to ensure that ceramic pieces inside the oven do not break, as noted in section 3.8. An operator is therefore required to manually ramp the current supplied to the oven at the beginning of each experiment. A computer-controlled atomic beam oven power supply combined with a temperature monitoring system can be used to slowly ramp the temperature automatically. Such a system would also allow a measured temperature to be sent to the main control program and optimisation of the oven temperature to maximise count rates.

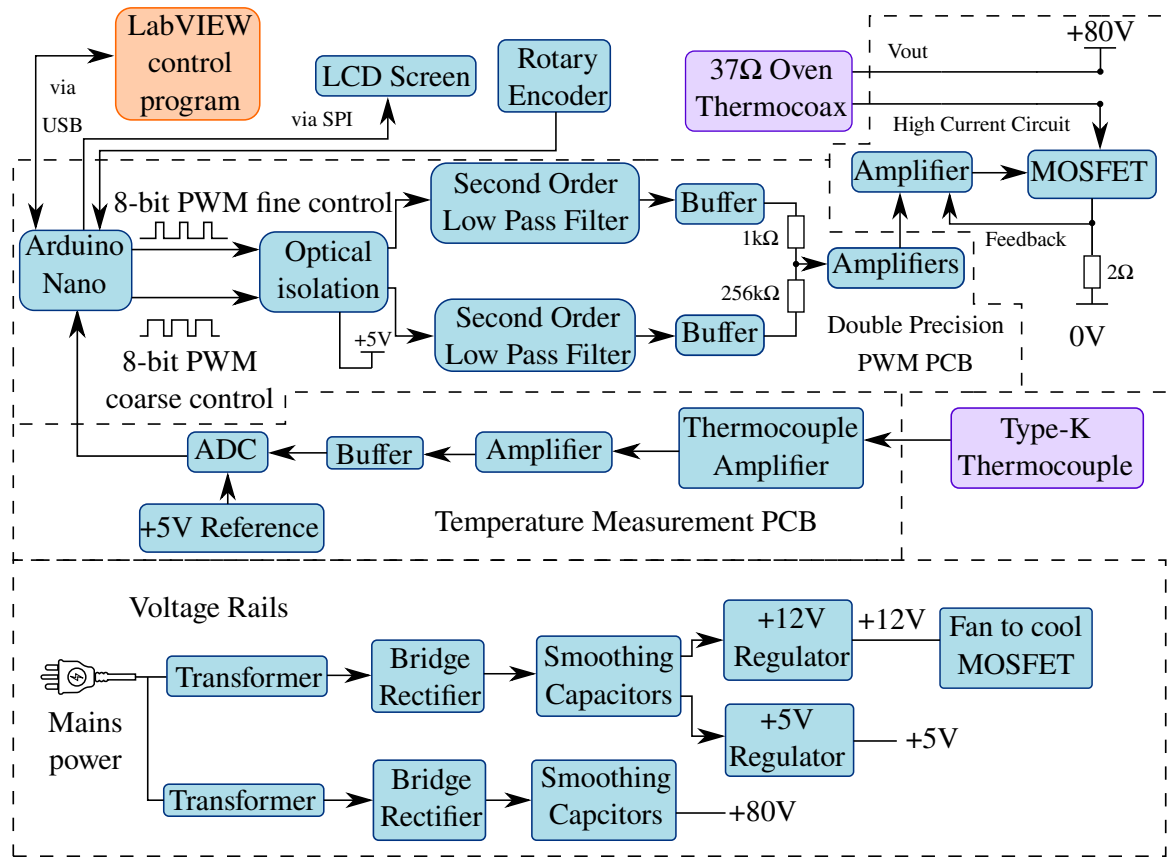


Figure 9.2: Design of an atomic beam oven temperature controller. A constant current power supply provides voltage to a $37\ \Omega$ load which corresponds to the New (e , $2e$) atomic beam oven's Thermocoax resistance. The temperature is monitored by a Type-K thermocouple and an ADC. An Arduino Nano then controls the output current of the power supply to adjust the temperature. A full schematic and PCB design can be found at [119]. A colour key can be found in figure 3.1.

The design of an atomic beam oven temperature controller is presented in figure 9.2. The control program sends a set temperature to an Arduino Nano which provides two 8-bit isolated, filtered pulse-width modulated (PWM) signals to set the current driven through a MOSFET. One PWM signal is for fine control of the current and the other is for coarse control, providing 16-bit control over the current. The drain of the MOSFET is in series with the Thermocoax of the oven and a +80 V DC voltage rail. This results in a maximum current draw of around 2.1 A through the Thermocoax in the atomic beam oven. The MOSFET is mounted on a heat sink and a +12 V DC fan is used to provide cooling. The output of the type-K thermocouple is amplified, buffered, and then fed into an ADC, which sends a voltage measurement to the Arduino. The Arduino can then relay this temperature measurement to the main control program via USB. An LCD screen displays the set and current temperature of the oven and any messages to the operator. A rotary encoder is monitored by the Arduino for manual control of the set temperature.

Circuit schematics and PCB layouts for this new design can be found at [119]. The PCBs have been made, but the parts have not been assembled onto the PCB. Further production and testing of this device is hence required.

9.2.3 Future (e,2e) Experiments

As discussed in chapters 6 and 7, the flattening of the TDCS for xenon and argon measured in the perpendicular plane occurs as energy increases. Experiments performing (e, 2e) from a krypton target may yield the same flattening and provide further evidence that this phenomena is independent of target.

Since the Ti:Sa laser is now operational and can produce wavelengths of around 460 nm, laser-aligned (e, 2e) from a strontium target can now be performed in the New (e, 2e) spectrometer. Laser-aligned (e, 2e) from a calcium target could also be performed, as the required laser wavelength is around 423 nm for excitation of the ground 4^1S_0 state to the 4^1P_1 state [105]. The atomic beam oven can also achieve the ~ 600 °C (see appendix C) required to form a calcium vapour.

Bibliography

- [1] I.E. McCarthy and E. Weigold. (e, 2e) spectroscopy. *Physics Reports*, 27(6):275–371, 1976.
- [2] N. Andersen and K. Bartschat. Complete experiments in electron-atom collisions. In *Advances in Atomic, Molecular, and Optical Physics*, volume 36, pages 1–85. Elsevier, 1996.
- [3] G.J. Schulz. Resonance in the elastic scattering of electrons in helium. *Physical Review Letters*, 10(3):104, 1963.
- [4] S. Cvejanovic and F.H. Read. A new technique for threshold excitation spectroscopy. *Journal of Physics B: Atomic and Molecular Physics (1968-1987)*, 7(10):1180, 1974.
- [5] J.N.H. Brunt, G.C. King, and F.H. Read. Resonance structure in elastic electron scattering from helium, neon and argon. *Journal of Physics B: Atomic and Molecular Physics (1968-1987)*, 10(7):1289, 1977.
- [6] G. Hon and B.R. Goldstein. Centenary of the Franck-Hertz experiments. *Annalen der Physik*, 525(12):A179–A183, 2013.
- [7] R.F. Egerton. Electron energy-loss spectroscopy in the TEM. *Reports on Progress in Physics*, 72(1):016502, 2008.
- [8] J.A. Hunt and David B. Williams. Electron energy-loss spectrum-imaging. *Ultra-microscopy*, 38(1):47–73, 1991.
- [9] P. Nozieres and D. Pines. Electron interaction in solids. characteristic energy loss spectrum. *Physical Review*, 113(5):1254, 1959.
- [10] K. Blum and H. Kleinpoppen. Electron-photon angular correlation in atomic physics. *Physics Reports*, 52(4):203–261, 1979.
- [11] N. Andersen, J.W. Gallagher, and I.V. Hertel. Collisional alignment and orientation of atomic outer shells I. Direct excitation by electron and atom impact. *Physics Reports*, 165(1-2):1–188, 1988.

- [12] B.V. Hall, Y. Shen, A.J. Murray, M.C. Standage, W.R. MacGillivray, and I. Bray. Superelastic electron scattering from laser excited rubidium at 20 eV incident energy. *Journal of Physics B: Atomic, Molecular and Optical Physics*, 37(5):1113, 2004.
- [13] R. P. Dufresne and G. Del Zanna. Modelling ion populations in astrophysical plasmas: carbon in the solar transition region. *A & A*, 626:A123, 2019.
- [14] I.A. Mironova, K.L. Aplin, F. Arnold, G.A. Bazilevskaya, R.G. Harrison, A.A. Krivolutsky, K.A. Nicoll, E.V. Rozanov, E. Turunen, and I.G. Usoskin. Energetic particle influence on the earth's atmosphere. *Space Science Reviews*, 194(1):1–96, 2015.
- [15] V.H. Chaplin, M.Konopliv, T.Simka, L.K.Johnson, R.B.Lobbia, and R.E. Wirz. *Insights from Collisional-Radiative Models of Neutral and Singly-Ionized Xenon in Hall Thrusters*. 2021.
- [16] J.A. Linnell and A.D. Gallimore. Efficiency analysis of a hall thruster operating with krypton and xenon. *Journal of Propulsion and Power*, 22(6):1402–1418, 2006.
- [17] S.E. Huber, A. Mauracher, D. Süß, I. Sukuba, J. Urban, D. Borodin, and M. Probst. Total and partial electron impact ionization cross sections of fusion-relevant diatomic molecules. *The Journal of Chemical Physics*, 150(2):024306, 2019.
- [18] L.L. Foldy and W. Tobocman. Application of formal scattering theory to many-body problems. *Physical Review*, 105(3):1099, 1957.
- [19] K. Bartschat and P.G. Burke. The R-matrix method for electron impact ionisation. *Journal of Physics B: Atomic and Molecular Physics (1968-1987)*, 20(13):3191, 1987.
- [20] C.M. Granados-Castro and L.U. Ancarani. Electron impact ionization of the outer valence orbital $1t_2$ of CH_4 . *The European Physical Journal D*, 71(3):1–10, 2017.
- [21] I. Bray and A.T. Stelbovics. Convergent close-coupling calculations of electron-hydrogen scattering. *Physical Review A*, 46(11):6995, 1992.
- [22] D.H. Madison and O. Al-Hagan. The distorted-wave Born approach for calculating electron-impact ionization of molecules. *Journal of Atomic and Molecular Physics*, 2010, 2010.
- [23] H. Geiger and E. Marsden. LXI. The laws of deflexion of a particles through large angles. *The London, Edinburgh, and Dublin Philosophical Magazine and Journal of Science*, 25(148):604–623, 1913.
- [24] E. Rutherford. The scattering of α and β particles by matter and the structure of the atom. *Philosophical Magazine*, 92(4):379–398, 2012.
- [25] G. Barton. Rutherford scattering in two dimensions. *American Journal of Physics*, 51(5):420–422, 1983.

- [26] A.N. James, K.A. Connell, and R.A. Cunningham. Energy loss fluctuations caused by Rutherford scattering. *Nuclear Instruments and Methods in Physics Research Section B: Beam Interactions with Materials and Atoms*, 53(3):349–351, 1991.
- [27] P.G. Burke and K. Smith. The low-energy scattering of electrons and positrons by hydrogen atoms. *Reviews of Modern Physics*, 34(3):458, 1962.
- [28] D.J. Griffiths and D.F. Schroeter. *Introduction to quantum mechanics*. Cambridge University Press, 2018.
- [29] J.J. Sakurai and E.D. Commins. *Modern Quantum Mechanics, Revised Edition*, 1995.
- [30] M. Cherid, A. Duguet, and A. Lahmam-Bennani. An accurate investigation of the validity of the first Born approximation to describe high-energy (e, 2e) cross sections at small and intermediate momentum transfer. *Journal of Physics B: Atomic and Molecular Physics (1968-1987)*, 20(6):L187, 1987.
- [31] D.H. Madison, R.V. Calhoun, and W.N. Shelton. Triple-differential cross sections for electron-impact ionization of helium. *Physical Review A*, 16(2):552, 1977.
- [32] R. Huby and J.R. Mines. Distorted-wave Born approximation for stripping to virtual levels. *Reviews of Modern Physics*, 37(3):406, 1965.
- [33] J. Botero and J.H. Macek. Threshold angular distributions of (e, 2e) cross sections of helium atoms. *Physical Review Letters*, 68(5):576, 1992.
- [34] J. Röder, J. Rasch, K. Jung, C.T. Whelan, H. Ehrhardt, R.J. Allan, and H.R.J. Walters. Coulomb three-body effects in low-energy impact ionization of H (1s). *Physical Review A*, 53(1):225, 1996.
- [35] A.J. Murray and F.H. Read. Low energy (e, 2e) differential cross section measurements on neon from the coplanar to the perpendicular plane geometry. *Journal of Physics B: Atomic, Molecular and Optical Physics*, 33(8):L297, 2000.
- [36] F.K. Miller, H.R.J. Walters, and C.T. Whelan. Energy-sharing (e, 2e) collisions: Ionization of the inert gases in the perpendicular plane. *Physical Review A*, 91(1):012706, 2015.
- [37] S.J. Ward and J.H. Macek. Wave functions for continuum states of charged fragments. *Physical Review A*, 49(7):1049–1056, 1994.
- [38] M. Abramowitz, I.A. Stegun, and R.H. Romer. *Handbook of mathematical functions with formulas, graphs, and mathematical tables*, 1988.
- [39] A.T. Stelbovics and T. Winata. A study of L2 approximations in atomic scattering. *Australian Journal of Physics*, 43(5):485–498, 1990.
- [40] I. Bray and D.V. Fursa. Convergent Close-Coupling Method: A “Complete Scattering Theory”? *Physical Review Letters*, 76(15):2674, 1996.

- [41] I. Bray, D.V. Fursa, A.S. Kheifets, and A.T. Stelbovics. Electrons and photons colliding with atoms: development and application of the convergent close-coupling method. *Journal of Physics B: Atomic, Molecular and Optical Physics*, 35(15):R117, 2002.
- [42] M.C. Zammit, D.V. Fursa, J.S. Savage, and I. Bray. Electron–and positron–molecule scattering: Development of the molecular convergent close-coupling method. *Journal of Physics B: Atomic, Molecular and Optical Physics*, 50(12):123001, 2017.
- [43] I.E. McCarthy and A.T. Stelbovics. Momentum-space coupled-channels optical method for electron-atom scattering. *Physical Review A*, 28(5):2693, 1983.
- [44] R. Muller-Fiedler, K. Jung, and H. Ehrhardt. Double differential cross sections for electron impact ionisation of helium. *Journal of Physics B: Atomic and Molecular Physics (1968-1987)*, 19(8):1211, 1986.
- [45] H. Ehrhardt, M. Schulz, T. Tekaats, and K. Willmann. Ionization of helium: angular correlation of the scattered and ejected electrons. *Physical Review Letters*, 22(3):89, 1969.
- [46] X. Ren, I. Bray, D.V. Fursa, J. Colgan, M.S. Pindzola, T. Pflüger, A. Senftleben, S. Xu, A. Dorn, and J. Ullrich. Electron-impact ionization of helium: A comprehensive experiment benchmarks theory. *Physical Review A*, 83(5):052711, 2011.
- [47] G.H. Wannier. The threshold law for single ionization of atoms or ions by electrons. *Physical Review*, 90(5):817, 1953.
- [48] F.H. Read. Extensions of the Wannier theory for near-threshold excitation and ionisation of atoms by electron impact. *Journal of Physics B: Atomic and Molecular Physics*, 17(19):3965, 1984.
- [49] C.E. Brion, G. Cooper, Y. Zheng, I.V. Litvinyuk, and I.E. McCarthy. Imaging of orbital electron densities by electron momentum spectroscopy—a chemical interpretation of the binary (e, 2e) reaction. *Chemical Physics*, 270(1):13–30, 2001.
- [50] J. Ullrich, R. Moshhammer, A. Dorn, R. Dörner, L.P.H Schmidt, and H. Schmidt-Böcking. Recoil-ion and electron momentum spectroscopy: reaction-microscopes. *Reports on Progress in Physics*, 66(9):1463, 2003.
- [51] A.J. Murray and F.H. Read. Evolution from the coplanar to the perpendicular plane geometry of helium (e, 2e) differential cross sections symmetric in scattering angle and energy. *Physical Review A*, 47(5):3724, 1993.
- [52] A.J. Murray, F.H. Read, and N.J. Bowring. Parametrization of low-energy symmetric (e, 2e) differential cross section measurements. *Journal of Physics B: Atomic, Molecular and Optical Physics*, 30(2):387, 1997.
- [53] J. Colgan, M.S. Pindzola, G. Childers, and M.A. Khakoo. Low-energy electron-impact single ionization of helium. *Physical Review A*, 73(4):042710, 2006.

- [54] J. Colgan, M.S. Pindzola, F. Robicheaux, C. Kaiser, A.J. Murray, and D.H. Madison. Differential cross sections for the ionization of oriented H_2 molecules by electron impact. *Physical Review Letters*, 101(23):233201, 2008.
- [55] J. Colgan, O. Al-Hagan, D.H. Madison, A.J. Murray, and M.S. Pindzola. Deep interference minima in non-coplanar triple differential cross sections for the electron-impact ionization of small atoms and molecules. *Journal of Physics B: Atomic, Molecular and Optical Physics*, 42(17):171001, 2009.
- [56] T.J. Hawley-Jones, F.H. Read, S. Cvejanovic, P. Hammond, and G.C. King. Measurements in the perpendicular plane of angular correlations in near-threshold electron impact ionization of helium. *Journal of Physics B: Atomic, Molecular and Optical Physics*, 25(10):2393, 1992.
- [57] T.J. Hawley-Jones. The Design, Construction, and Operation of an (e, 2e) Coincidence Experiment. PhD Thesis. *The University of Manchester*, 1984.
- [58] O. Al-Hagan, C. Kaiser, D. Madison, and A.J. Murray. Atomic and molecular signatures for charged-particle ionization. *Nature Physics*, 5(1):59–63, 2009.
- [59] X. Ren, A. Senftleben, T. Pflüger, A. Dorn, J. Colgan, M.S. Pindzola, O. Al-Hagan, D.H. Madison, I. Bray, D.V. Fursa, and J. Ullrich. Tracing multiple scattering patterns in absolute (e, 2e) cross sections for H_2 and He over a 4π solid angle. *Physical Review A*, 82(3):032712, 2010.
- [60] A.J. Murray, M.J. Hussey, and M. Needham. Design and characterization of an atomic beam source with narrow angular divergence for alkali-earth targets. *Measurement Science and Technology*, 17(11):3094, 2006.
- [61] M. Hussey, A.J. Murray, W.R. MacGillivray, G.C. King, and N. Bowring. Super-elastic scattering from calcium over the complete angular range using a magnetic angle changing device. In *Journal of Physics: Conference Series*, volume 88, page 012061. IOP Publishing, 2007.
- [62] M. Hussey, A. Murray, W MacGillivray, and G. King. Low energy super-elastic scattering studies of calcium over the complete angular range using a magnetic angle changing device. *Journal of Physics B: Atomic, Molecular and Optical Physics*, 41(5):055202, 2008.
- [63] T.N. Rescigno, M. Baertschy, W.A. Isaacs, and C.W. McCurdy. Collisional breakup in a quantum system of three charged particles. *Science*, 286(5449):2474–2479, 1999.
- [64] I. Bray, D.V. Fursa, A.S. Kadyrov, A.T. Stelbovics, A.S. Kheifets, and A.M. Mukhamedzhanov. Electron-and photon-impact atomic ionisation. *Physics Reports*, 520(4):135–174, 2012.
- [65] A.A. Illarionov and A.D. Stauffer. Calculation of non-coplanar electron-impact ionization of xenon. *Journal of Physics B: Atomic, Molecular and Optical Physics*, 45(22):225202, 2012.

- [66] M. Patel, M. Harvey, A. Sakaamini, and A.J. Murray. Evolution of the xenon (e, 2e) differential cross section from a coplanar geometry to the perpendicular plane in the intermediate-energy regime. *Physical Review A*, 105(3):032818, 2022.
- [67] M. Patel and A.J. Murray. Measurement of argon (e, 2e) differential cross sections in the perpendicular plane from 5 to 200 eV above the ionization threshold. *Physical Review A*, 105(4):042815, 2022.
- [68] A.I. Lozano, F. Costa, X. Ren, A. Dorn, L. Álvarez, F. Blanco, P. Limão-Vieira, and G. García. Double and triple differential cross sections for single ionization of benzene by electron impact. *International Journal of Molecular Sciences*, 22(9):4601, 2021.
- [69] M. Harvey, A. Sakaamini, M. Patel, S. Amami, D. Madison, and A.J. Murray. Triple differential cross-section measurements for electron-impact ionization of methane from a coplanar geometry to the perpendicular plane. *The Journal of Chemical Physics*, 151(19):194305, 2019.
- [70] X. Ren, T. Pflüger, S. Xu, J. Colgan, M.S. Pindzola, A. Senftleben, J. Ullrich, and A. Dorn. Strong molecular alignment dependence of H₂ electron impact ionization dynamics. *Physical Review Letters*, 109(12):123202, 2012.
- [71] K.L. Nixon and A.J. Murray. Differential cross sections for ionization of laser-aligned atoms by electron impact. *Physical Review Letters*, 106(12):123201, 2011.
- [72] K.L. Nixon and A.J. Murray. Parametrization of electron-impact ionization cross sections from laser-excited and aligned atoms. *Physical Review Letters*, 112(2):023202, 2014.
- [73] J. Pursehouse, C. Bostock, K.L. Nixon, M. Harvey, D.V Fursa, I. Bray, and A.J. Murray. Comparison of experiment and theory for superelastic electron-collision studies from laser-aligned magnesium. *Physical Review A*, 98(2):022702, 2018.
- [74] S. Jhumka, K.L. Nixon, M. Hussey, and A.J. Murray. Superelastic electron collisions with silver: Measuring the angular momentum transferred to the target during the collision. *Physical Review A*, 87(5):052714, 2013.
- [75] M. Patel, M. Harvey, and A.J. Murray. Laser-atom interaction simulator derived from quantum electrodynamics. *Physical Review A*, 105:053117, May 2022.
- [76] M. Patel, A. Sakaamini, M. Harvey, and A. J. Murray. An experimental control system for electron spectrometers using Arduino and LabVIEW interfaces. *Review of Scientific Instruments*, 91(10):103104, 2020.
- [77] Arduino [Online]. Available at: <https://www.arduino.cc/>. Accessed: [2022, May 25], 2022.
- [78] National Instruments. LabVIEW [Online]. Available at: <https://www.ni.com/en-gb/shop/labview.html>. Accessed: [2022, May 25], 2022.

- [79] Python Software Foundation. Python downloads [Online]. Available at: <https://www.python.org/downloads/> [2022, May 10], 2022.
- [80] K. Blum. *Density matrix theory and applications*, volume 64. Springer Science & Business Media, 2012.
- [81] P.M. Farrell, W.R. MacGillivray, and M.C. Standage. Quantum-electrodynamic calculation of hyperfine-state populations in atomic sodium. *Physical Review A*, 37(11):4240, 1988.
- [82] P.M. Farrell, W.R. MacGillivray, and M.C. Standage. Calculation of the optical pumping parameters for electron-superelastic-scattering experiments from the sodium $3^2P_{3/2}$ level. *Physical Review A*, 44(3):1828, 1991.
- [83] W.R. MacGillivray and M.C. Standage. Stepwise electron and laser excitation of atoms. *Physical Reports*, 168(1):1, 1988.
- [84] A.J. Murray, W.R. MacGillivray, and M. Hussey. Theoretical modeling of resonant laser excitation of atoms in a magnetic field. *Physical Review A*, 77(1):013409, 2008.
- [85] R. Loudon. *The quantum theory of light*. Oxford University Press, 2000.
- [86] J.R. Ackerhalt and J.H. Eberly. Quantum electrodynamics and radiation reaction: nonrelativistic atomic frequency shifts and lifetimes. *Physical Review D*, 10(10):3350, 1974.
- [87] R. Kubo. Stochastic Liouville Equations. *Journal of Mathematical Physics*, 4(2):174–183, 1963.
- [88] R.M. Whitley and C.R. Stroud Jr. Double optical resonance. *Physical Review A*, 14(4):1498, 1976.
- [89] P.M. Farrell and W.R. MacGillivray. On the consistency of Rabi frequency calculations. *Journal of physics A: Math. Gen.*, 28:209, 1995.
- [90] A.J. Murray, C.J. Webb, W.R. MacGillivray, and M.C. Standage. Electron-Laser Stepwise Excitation Coincidence Experiment on the 6^1P_1 State of Mercury. *Physical review letters*, 62(4):411, 1989.
- [91] M. Patel. LASED documentation [Online]. Available at: <https://lased.readthedocs.io/en/latest/> [2022, May 10], 2022.
- [92] S. Weyers, E. Aucouturier, C. Valentin, and N. Dimarcq. A continuous beam of cold cesium atoms extracted from a two-dimensional magneto-optical trap. *Optics communications*, 143(1-3):30–34, 1997.

- [93] A. Meurer, C.P. Smith, M. Paprocki, O. Čertík, S.B. Kirpichev, M. Rocklin, A. Kumar, S. Ivanov, J.K. Moore, S. Singh, T. Rathnayake, S. Vig, B.E. Granger, R.P. Muller, F. Bonazzi, H. Gupta, S. Vats, F. Johansson, F. Pedregosa, M.J. Curry, A.R. Terrel, Š. Roučka, A. Saboo, I. Fernando, S. Kulal, R. Cimrman, and A. Scopatz. Sympy: symbolic computing in python. *PeerJ Computer Science*, 3:e103, January 2017.
- [94] C.R. Harris, K.J. Millman, S.J. van der Walt, Ralf G., P. Virtanen, D. Cournapeau, E. Wieser, J. Taylor, S. Berg, N.J. Smith, R. Kern, M. Picus, S. Hoyer, M.H. van Kerkwijk, M. Brett, A. Haldane, J.F. del Río, M. Wiebe, P. Peterson, P. Gérard-Marchant, K. Sheppard, T. Reddy, W. Weckesser, H. Abbasi, C. Gohlke, and T.E. Oliphant. Array programming with NumPy. *Nature*, 585(7825):357–362, September 2020.
- [95] R. Virtanen, P. and Gommers, T.E. Oliphant, M. Haberland, T. Reddy, D. Cournapeau, E. Burovski, P. Peterson, W. Weckesser, J. Bright, S.J. van der Walt, M. Brett, K.J. and Mayorov N. Wilson, J. and Millman, A.R.J. Nelson, E. Jones, R. Kern, E. Larson, C.J. Carey, Í. Polat, E.W. Feng, Y. and Moore, J. VanderPlas, D. Laxalde, J. Perktold, R. Cimrman, I. Henriksen, E.A. Quintero, C.R. Harris, A.M. Archibald, A. H. Ribeiro, F. Pedregosa, P. van Mulbregt, and SciPy 1.0 Contributors. SciPy 1.0: Fundamental Algorithms for Scientific Computing in Python. *Nature Methods*, 17:261–272, 2020.
- [96] D. Welford, D.M. Rines, and B.J. Dinerman. Efficient TEM₀₀-mode operation of a laser-diode side-pumped Nd: YAG laser. *Optics Letters*, 16(23):1850–1852, 1991.
- [97] A.E. Siegman. *Lasers*. University science books, California USA, 1986.
- [98] A.J. Murray, W.R. MacGillivray, and M.C. Standage. Application of stepwise electron and laser excitation techniques to electron-photon correlation studies: I. theory. *Journal of Physics B: Atomic, Molecular and Optical Physics*, 23:3373–3392, 1990.
- [99] D.M. Brink, G.R. Satchler, and M. Danos. Angular momentum. *Physics Today*, 16(6):80, 1963.
- [100] L.C. Biedenharn, J.D. Louck, and P.A. Carruthers. *Angular momentum in quantum physics: theory and application*, volume 8. Addison-Wesley Reading, MA, 1981.
- [101] A.T. Masters, A.J. Murray, R. Pascual, and M.C. Standage. Multipole treatment of radiation trapping in a stepwise-excitation, electron-photon coincidence experiment. *Physical Review A*, 53(6):3884, 1996.
- [102] A. Lurio, R.L. DeZafra, and R.J. Goshen. Lifetime of the First 1P_1 State of Zinc, Calcium, and Strontium. *Physical Review*, 134(5A):A1198, 1964.
- [103] G. Risberg. Spectrum of atomic calcium CaI and extensions to analysis of CaII. *Arkiv for Fysik*, 37(3):231, 1968.

- [104] A.J. Murray and D. Cvejanovic. Low energy superelastic scattering from the 4^1P_1 state of calcium in an (e, 2e) spectrometer. *Journal of Physics B: Atomic, Molecular and Optical Physics*, 36(24):4889, 2003.
- [105] A. Kramida, Y. Ralchenko, J. Reader, and and NIST ASD Team. NIST Atomic Spectra Database (ver. 5.9), [Online]. Available at: <https://physics.nist.gov/asd> [2022, March 28]. National Institute of Standards and Technology, Gaithersburg, MD., 2021.
- [106] J.P.M. Beijers, S.J. Doornenbal, J. van Eck, and H.G.M. Heideman. A polarisation-correlation analysis of the 3^1D state of helium excited by electron impact. *Journal of Physics B: Atomic and Molecular Physics (1968-1987)*, 20(24):6617, 1987.
- [107] I. Bray. (Private Communication), 2020. Curtin University, Western Australia.
- [108] R.J. Rafac, C.E. Tanner, A.E. Livingston, and H.G. Berry. Fast-beam laser lifetime measurements of the cesium $6p^2P_{1/2,3/2}$ states. *Physical Review A*, 60(5):3648, 1999.
- [109] T. Udem, J. Reichert, T.W. Hänsch, and M. Kourogi. Absolute optical frequency measurement of the cesium D_2 line. *Physical Review A*, 62(3):031801, 2000.
- [110] E. Arimondo, M. Inguscio, and P. Violino. Experimental determinations of the hyperfine structure in the alkali atoms. *Reviews of Modern Physics*, 49(1):31, 1977.
- [111] M. Patel. LASED source code [Online]. Available at: <https://github.com/mvpmanish/LASED> [2022, May 10], 2022.
- [112] A.J. Murray. Low-cost high-speed pulsed amplifiers for electron, ion and photon detectors. *Measurement Science and Technology*, 23(10):107001, September 2012.
- [113] D. Dubbers. Simple formula for multiple mu-metal shields. *Nuclear Instruments and Methods in Physics Research Section A: Accelerators, Spectrometers, Detectors and Associated Equipment*, 243(2-3):511–517, 1986.
- [114] M.B.J. Woolf. (e, 2e) Measurements in the Perpendicular Plane. PhD Thesis. *The University of Manchester*, 1989.
- [115] J.R. Pierce. *Theory and design of electron beams*. D. Van Nostrand Company, New York, 1954.
- [116] A. Sakaamini. Electron Impact Ionization of Nitrogen and Methane. PhD Thesis. *The University of Manchester*, 2019.
- [117] K. Jost. Fringing field correction for 127 degrees and 180 degrees electron spectrometers. *Journal of Physics E: Scientific Instruments*, 12(10):1001–1005, oct 1979.
- [118] C.E. Kuyatt and J.A. Simpson. Electron monochromator design. *Review of Scientific Instruments*, 38(1):103–111, 1967.

- [119] M. Patel. Manchester atomic & molecular physics code repository. Gitlab [Online]. Available at: <https://gitlab.com/manchesteratomicphysics>. Accessed: [2022, July 6], 2022.
- [120] J. Pursehouse. Electron and photon interactions in magnesium, calcium and rubidium. PhD Thesis. *The University of Manchester*, 2017.
- [121] K.J. Ross and B. Sonntag. High temperature metal atom beam sources. *Review of Scientific Instruments*, 66(9):4409–4433, 1995.
- [122] N.M. Laurendeau. *Statistical thermodynamics: fundamentals and applications*. Cambridge University Press, 2005.
- [123] A.J. Murray and S. Atkinson. An automatic controller for filling and maintaining liquid nitrogen levels in dewars. *Measurement Science and Technology*, 15(5):N31, 2004.
- [124] Espressif. ESP32 [Online]. Available at: <https://www.espressif.com/en/products/socs/esp32>. Accessed: [2022, June 21], 2022.
- [125] J.P. Rogers and A.J. Murray. A low-cost and reliable laser shutter interlock using a software-command interface. arXiv [Online]. Available at: <https://arxiv.org/abs/2206.09858>. Accessed: [2022, July 6], 2022.
- [126] S. Chacon and B. Straub. *Pro git*. Springer Nature, 2014.
- [127] F. Gao and L. Han. Implementing the Nelder-Mead simplex algorithm with adaptive parameters. *Computational Optimization and Applications*, 51(1):259–277, 2012.
- [128] B.E. Granger and F. Pérez. Jupyter: Thinking and storytelling with code and data. *Computing in Science Engineering*, 23(2):7–14, 2021.
- [129] Spellman High Voltage Electronics Limited. Serial Protocol for the MPS Series [Online]. Available at: <https://www.spellmanhv.com/-/media/en/Products/MPS-Digital-Interface.pdf>. Accessed: [2022, July 6], 2022.
- [130] Oerlikon Leybold Vacuum GmbH. Ionivac ITR 90 Datasheet [Online]. Available at: <https://www.idealvac.com/files/manuals/Leybold-ITR90-Gauge-Specs-Data-Sheet01.pdf>. Accessed: [2022, June 26], 2008.
- [131] J.J. Moré. The Levenberg-Marquardt algorithm: implementation and theory. In *Numerical analysis*, pages 105–116. Springer, 1978.
- [132] T. Pflüger, O. Zatsarinny, K. Bartschat, A. Senftleben, X. Ren, J. Ullrich, and A. Dorn. Electron-impact ionization of neon at low projectile energy: An inter-normalized experiment and theory for a complex target. *Physical Review Letters*, 110(15):153202, 2013.

- [133] C.T. Whelan, H.R.J. Walters, A. Lahmam-Bennani, and H. Ehrhardt. *(e, 2e) & related processes*, volume 414. Springer Science & Business Media, 2012.
- [134] K.L. Nixon, A.J. Murray, and C. Kaiser. Low energy (e, 2e) studies of the noble gases in the perpendicular plane. *Journal of Physics B: Atomic, Molecular and Optical Physics*, 43(8):085202, 2010.
- [135] K.L. Nixon and A.J. Murray. Mapping the xenon (e, 2e) differential cross section from coplanar to perpendicular geometries. *Physical Review A*, 85(2):022716, 2012.
- [136] G. Purohit, A.S. Bhullar, and K.K. Sud. (e, 2e) triple differential cross sections of He, Ne, Ar, Kr and Xe atoms in coplanar to perpendicular plane geometry. *Indian Journal of Physics*, 77B(2):177–184, 2003.
- [137] X. Zhang, C.T. Whelan, and Walters H.R.J. Energy sharing (e, 2e) collision-ionisation of helium in the perpendicular plane. *J. Phys. B: At. Mol. Opt. Phys.*, 23:L173–L178, 1990.
- [138] A. Lahmam-Bennani, H.F. Wellenstein, A. Duguet, and M. Rouault. Absolute triple differential cross sections for the 3p ionisation of argon by electron impact. *Journal of Physics B: Atomic, Molecular and Optical Physics*, 16:121, 1983.
- [139] A.J. Murray, N.J. Bowring, and F.H. Read. Comparison of argon and helium (e, 2e) differential cross sections at 64.6 eV using symmetric detection energies and angles. *Journal of Physics B: Atomic, Molecular and Optical Physics*, 33:2859, 2000.
- [140] L. Avaldi, R. Camilloni, E. Fainelli, and G. Stefani. An Ar valence-shell study by asymmetric (e, 2e) experiments. *Journal of Physics B: Atomic, Molecular and Optical Physics*, 21:L359, 1988.
- [141] T. Rosel, C. Dupré, J. Roder, A. Duguet, K. Jung, A. Lahmam-Bennani, and H. Ehrhardt. Coplanar symmetric (e, 2e) cross section on helium and neon. *Journal of Physics B: Atomic, Molecular and Optical Physics*, 24(13):3059, 1991.
- [142] A.J. Murray, M.B.J. Woolf, and F.H. Read. Results from symmetric and non-symmetric energy sharing (e, 2e) experiments in the perpendicular plane. *Journal of Physics B: Atomic, Molecular and Optical Physics*, 25:3021, 1992.
- [143] Adaptas Solutions. SIMION Ion and Electron Optics Simulator [Online]. Available at: <https://simion.com/>. Accessed: [2022, July 6], 2021.
- [144] Kate L Nixon and Andrew James Murray. (e, 2e) ionization studies of the stable noble gases in a coplanar symmetric geometry. *Physical Review A*, 87:022712, 2013.
- [145] A.J. Murray and F.H. Read. Exploring the helium (e, 2e) differential cross section at 64.6 eV with symmetric scattering angles but nonsymmetric energies. *Journal of Physics B: Atomic, Molecular and Optical Physics*, 26(13):L359, 1993.

- [146] N.J. Bowring, F.H. Read, and A.J. Murray. Two-electron interference in the helium (e, 2e) differential cross section at 64.6 eV. *Journal of Physics B: Atomic, Molecular and Optical Physics*, 32:L57, 1999.
- [147] J. Rasch, C.T. Whelan, R.J. Allan, S.P. Lucey, and H.R.J. Walters. Strong interference effects in the triple differential cross section of neutral-atom targets. *Physical Review A*, 56:1379, 1997.
- [148] A.J. Murray and F.H. Read. Deep interference minima in experimental ionization differential cross sections. *Physical Review A*, 63:012714, 2000.
- [149] J.H. Macek, J.B. Sternberg, S.Y. Ovchinnikov, and J.S. Briggs. Theory of deep minima in (e, 2e) measurements of triply differential cross sections. *Physical Review Letters*, 104:033201, 2010.
- [150] F. Navarrete and R.O. Barrachina. Vortices in ionization collisions. *Nuclear instruments and methods in physics*, 369:72, 2016.
- [151] A.W. Alrowaily, S.J. Ward, and P. van Reeth. Deep minima and vortices for positronium formation in low-energy positron-hydrogen collisions. *Journal of Physics B: Atomic, Molecular and Optical Physics*, 52:205201, 2019.
- [152] C.M. DeMars, S.J. Ward, J. Colgan, S. Amami, and D.H. Madison. Deep minima in the triply differential cross section for ionization of atomic hydrogen by electron and positron impact. *Atoms*, 8:26, 2020.
- [153] E. Wang, X. Ren, M. Gong, E. Ali, Z. Wang, C. Ma, D. Madison, X. Chen, and A. Dorn. Triple-differential cross sections for (e, 2e) electron-impact ionization dynamics of tetrahydrofuran at low projectile energy. *Physical Review A*, 102(6):062813, 2020.
- [154] Y. Wang, Z. Wang, M. Gong, C. Xu, and X. Chen. Theoretical study of (e, 2e) triple differential cross sections of pyrimidine and tetrahydrofurfuryl alcohol molecules using multi-center distorted-wave method. *Chinese Physics B*, 31(1):010202, 2022.
- [155] X. Xu, M. Gong, X. Li, S.B. Zhang, and X. Chen. Theoretical study of (e, 2e) triple differential cross sections of tetrahydrofuran using multicenter distorted-wave method. *The Journal of Chemical Physics*, 148(24):244104, 2018.
- [156] S. Ye, X. Zhang, T.C. Killian, F.B. Dunning, M. Hiller, S. Yoshida, S. Nagele, and J. Burgdörfer. Production of very-high-n strontium Rydberg atoms. *Physical Review A*, 88(4):043430, 2013.
- [157] M. Schioppo, N. Poli, M. Prevedelli, S. Falke, C. Lisdat, U. Sterr, and G.M. Tino. A compact and efficient strontium oven for laser-cooling experiments. *Review of Scientific Instruments*, 83(10):103101, 2012.
- [158] K.L. Kwok and F. Mandl. A narrow resonance in the elastic scattering of electrons by helium. *Proceedings of the Physical Society (1958-1967)*, 86(3):501, 1965.

- [159] U. Fano. Effects of configuration interaction on intensities and phase shifts. *Physical Review*, 124(6):1866, 1961.
- [160] B. Stroustrup. *The C++ programming language*. Pearson Education, 2013.
- [161] S. Klabnik and C. Nichols. *The Rust Programming Language*. No Starch Press, 2019.
- [162] A. Corney. *Atomic and laser spectroscopy*. Clarendon Press Oxford, 1978.
- [163] F. Mandl. *Statistical physics*, volume 14. John Wiley & Sons, 1991.
- [164] M. Mantina, A.C. Chamberlin, R. Valero, C.J. Cramer, and D.G. Truhlar. Consistent van der Waals radii for the whole main group. *The Journal of Physical Chemistry A*, 113(19):5806–5812, 2009.
- [165] C.B. Alcock, V.P. Itkin, and M.K. Horrigan. Vapour pressure equations for the metallic elements: 298–2500k. *Canadian Metallurgical Quarterly*, 23(3):309–313, 1984.

Appendix A

Laser-Atom Interaction Calculations

A.1 Calculation of the Generalised Decay Constants

The generalised decay constants need to be calculated directly when there are vertical coherences in a laser-atom system i.e. when there is hyperfine splitting, as shown in equation 2.64. For hyperfine states, the splitting between excited energy levels is small so $\omega_{e'} \approx \omega_{e''}$. Using equation 2.55 this approximation hence leads to

$$\Gamma_{ege'g} = 2 \sum_q g_{e'g}^q g_{eg}^{q*} \pi \delta(\omega_q - \Delta_{eg}) \quad (\text{A.1})$$

and from equation 2.56 the magnitude of the generalised decay constant can be calculated by

$$|\Gamma_{ege'g}| = \sqrt{\Gamma_{eg} \Gamma_{e'g}}. \quad (\text{A.2})$$

The sign of the generalised decay constant is calculated by considering the coupling coefficients. The coupling coefficients are generally complex

$$g_{e'g}^q = |g_{e'g}^q| e^{i\alpha} \quad (\text{A.3})$$

$$g_{eg}^q = |g_{eg}^q| e^{i\zeta} \quad (\text{A.4})$$

and the half-Rabi frequency can be written in terms of phase and amplitude terms, so that

$$\begin{aligned} \Omega_{e'g}^q &= g_{e'g}^q \langle a_L(0) \rangle = |g_{e'g}^q| e^{i\alpha} \langle a_L(0) \rangle e^{i\beta} \\ &= |g_{e'g}^q| \langle a_L(0) \rangle e^{i(\alpha+\beta)} \end{aligned} \quad (\text{A.5})$$

and similarly

$$\Omega_{eg}^q = |g_{eg}^q| \langle a_L(0) \rangle e^{i(\zeta+\beta)}. \quad (\text{A.6})$$

Since the half-Rabi frequencies are defined here as being real, it follows that

$$\alpha + \beta = n\pi \quad (\text{A.7})$$

$$\zeta + \beta = m\pi \quad (\text{A.8})$$

where n and m are integers. If equation A.7 is subtracted from A.8 it is found that

$$e^{i(\alpha-\zeta)} = e^{i(n-m)\pi} = \begin{cases} +1, & \text{if } n - m \text{ even} \\ -1, & \text{if } n - m \text{ odd.} \end{cases} \quad (\text{A.9})$$

Hence if Ω_{eg}^q and $\Omega_{e'g}^q$ have the same sign then $(n-m)$ is even and if they have the opposite sign then $(n-m)$ is odd. This can be related to the calculated coupling coefficients using equation 2.53 so that

$$\Gamma_{ege'g} = \begin{cases} +|\Gamma_{ege'g}|, & \text{if } C_{eg}^q C_{e'g'}^q > 0 \\ -|\Gamma_{ege'g}|, & \text{if } C_{eg}^q C_{e'g'}^q < 0. \end{cases} \quad (\text{A.10})$$

A.2 Calculation of the Half-Rabi Frequency

The half-Rabi frequency can be written as

$$\Omega_{eg}^L = g_{eg}^{L*} \langle a_L^\dagger(0) \rangle, \quad (\text{A.11})$$

where L is the mode of the laser representing the polarisation and wave vector. By substituting 2.23 into equation A.11, the half-Rabi frequency can be written as

$$\Omega_{eg}^L = i \sqrt{\frac{\omega_L}{2\epsilon_0 \hbar V}} \boldsymbol{\epsilon}_L \cdot \mathbf{D}_{eg} \langle a_L^\dagger(0) \rangle, \quad (\text{A.12})$$

where ω_L is the frequency of the laser and $\boldsymbol{\epsilon}_L$ is the polarisation vector of the laser mode L . The expectation value of the initial laser field operator can be written as

$$\langle a_L^\dagger(0) \rangle = \sqrt{N_L} e^{i\alpha}, \quad (\text{A.13})$$

where the definition of the product of the creation and annihilation operators is used here $a_L^\dagger a_L = N_L$, N_L is the number of photons in the field mode L , and α is the phase. By using the expressions for the energy of a photon $E_L = \hbar\omega_L$ in field mode L and the intensity of the corresponding laser field $I_L = N_L \hbar\omega_L c / V$, the half-Rabi frequency can be written in terms of the laser intensity. Now, by substituting equation A.13 into equation A.12 the half-Rabi frequency can be expressed as

$$\begin{aligned} \Omega_{eg}^L &= i \sqrt{\frac{I_L}{2\epsilon_0 \hbar^2 c}} \boldsymbol{\epsilon}_L \cdot \mathbf{D}_{eg} e^{i\alpha} \\ &= \sqrt{\frac{I_L}{2\epsilon_0 \hbar^2 c}} \boldsymbol{\epsilon}_L \cdot \mathbf{D}_{eg} e^{i(\alpha + \frac{\pi}{2})} \end{aligned} \quad (\text{A.14})$$

Now, the scalar product $\hat{\boldsymbol{\epsilon}}_L \cdot \mathbf{D}_{e'g'}$ must be considered. \mathbf{D}_{eg} describes the dipole matrix element between atomic states $|e\rangle$ and $|g\rangle$ and can be defined as

$$\begin{aligned} \mathbf{D}_{eg} &= \langle e | \mathbf{D} | g \rangle \\ &= \langle F' m_{F'} | \mathbf{D} | F m_F \rangle, \end{aligned} \quad (\text{A.15})$$

where the states $|e\rangle$ and $|g\rangle$ are described by eigenstates $|F'm_{F'}\rangle$ and $|Fm_F\rangle$ respectively. A circular basis can be defined where the unit vectors $\hat{\mathbf{e}}_q$ are represented by [162]

$$\hat{\mathbf{e}}_0 = \hat{\mathbf{e}}_x \quad (\text{A.16})$$

$$\hat{\mathbf{e}}_{\pm 1} = \frac{1}{\sqrt{2}}(\hat{\mathbf{e}}_x \pm i\hat{\mathbf{e}}_y). \quad (\text{A.17})$$

The laser polarisation can be conveniently expressed in this circular basis so that the unit vectors $\hat{\mathbf{e}}_q$ are the unit vectors for linear polarisation $q = 0$, σ^+ polarisation $q = +1$, and σ^- polarisation $q = -1$. If the dipole matrix element is also described in this basis so that the unit vectors are $\hat{\mathbf{d}}_{q'}$, then the scalar product of the two vectors is $\hat{\mathbf{e}}_q \cdot \hat{\mathbf{d}}_{q'} = \delta_{qq'}$ and the scalar product is only non-zero when the laser polarisation aligns with the atomic dipole. Therefore, the scalar product can be written as

$$\hat{\mathbf{e}}_q \cdot \mathbf{D}_{eg} = C_{eg}^L ||D||, \quad (\text{A.18})$$

where $||D||$ is the reduced dipole matrix element and the coefficient C_{eg}^L incorporates the coupling between laser field polarisation L and the atomic dipole matrix element \mathbf{D}_{eg} . The reduced dipole matrix element can be calculated by applying the selection rules for electric dipoles and relating this to the natural lifetime τ by [85]

$$||D|| = \langle L' = 1 ||D|| L = 0 \rangle = \sqrt{\frac{3\epsilon_0 \hbar \lambda^3}{8\pi^2 \tau}}, \quad (\text{A.19})$$

where λ is the wavelength of the transition from state $|e\rangle$ to $|g\rangle$.

The coupling coefficients C_{eg}^L can be calculated by applying the Wigner-Eckart theorem [80] so that the dipole operator matrix element can be expanded in the circular basis as [89]

$$\langle F' m_{F'} | \mathbf{D}_{eg} | F m_F \rangle = (-1)^{F' - m_{F'} + q} \begin{pmatrix} F' & 1 & F \\ -m_{F'} & q & m_F \end{pmatrix} \langle F' ||D_q|| F \rangle, \quad (\text{A.20})$$

where $\begin{pmatrix} F' & 1 & F \\ -m_{F'} & q & m_F \end{pmatrix}$ is a Wigner-3j symbol. Applying state reduction formulae to equation A.20 yields a computable expression

$$\begin{aligned} C_{eg}^q &= \langle F' m_{F'} | \mathbf{D}_{eg} | F m_F \rangle \\ &= (-1)^{\frac{q(1+q)}{2} + F' + F + J' + J + I' + L' + S' - m_{F'} + 1} \\ &\quad \times \sqrt{(2F' + 1)(2F + 1)(2J' + 1)(2J + 1)(2L' + 1)} \\ &\quad \times \begin{pmatrix} F' & 1 & F \\ -m_{F'} & q & m_F \end{pmatrix} \begin{Bmatrix} J' & F' & I' \\ F & J & 1 \end{Bmatrix} \begin{Bmatrix} L' & J' & S' \\ J & L & 1 \end{Bmatrix}, \end{aligned} \quad (\text{A.21})$$

where $\begin{Bmatrix} J' & F' & I' \\ F & J & 1 \end{Bmatrix}$ and $\begin{Bmatrix} L' & J' & S' \\ J & L & 1 \end{Bmatrix}$ are Wigner-6j symbols.

The half-Rabi frequency can now be calculated by substituting equation A.18 and A.19

into equation A.14 to yield

$$\begin{aligned}
\Omega_{eg}^L &= C_{eg}^L \sqrt{\frac{I_L}{2\epsilon_0 \hbar^2 c}} \|D\| e^{i(\alpha + \frac{\pi}{2})} \\
&= C_{eg}^L \sqrt{\frac{I_L}{2\epsilon_0 \hbar^2 c}} \sqrt{\frac{3\epsilon_0 \hbar \lambda^3}{8\pi^2 \tau}} \\
&= C_{eg}^L \sqrt{\frac{3\lambda^3 I_L}{8\pi \hbar c \tau}}, \tag{A.22}
\end{aligned}$$

where the phase term $e^{i(\alpha + \frac{\pi}{2})}$ has been incorporated into the optical coherences by adding the phase to the slowly varying operator phase term described by equation 2.43.

A.2.1 The Half-Rabi Frequency in a Circular Basis

When linear polarised light is incident upon an atomic target in the natural frame, where the incident laser beam direction is along the quantisation axis, the laser field needs to be considered as a coherent sum of right-hand circular (σ^+) and left-hand circular (σ^-) light. In the equations of motion for this laser-atom system, it is necessary to consider the linear driving field in terms of this circular basis.

The half-Rabi frequency can be defined using equation A.14

$$\Omega_{eg}^L = i \sqrt{\frac{I_L}{2\epsilon_0 \hbar^2 c}} \boldsymbol{\epsilon}_L \cdot \mathbf{D}_{eg} e^{i\alpha}, \tag{A.23}$$

where the dipole moment is defined as

$$\mathbf{D}_{eg} = -\langle e | q_e \mathbf{r} | g \rangle. \tag{A.24}$$

Here q_e is the elementary charge constant. To express the dipole moment in a circular basis, the vector \mathbf{r} can be expanded in Cartesian coordinates as $\mathbf{r} = r^x \hat{\mathbf{e}}_x + r^y \hat{\mathbf{e}}_y + r^z \hat{\mathbf{e}}_z$ and equations A.16 and A.17 can be used to express \mathbf{r} in a circular basis

$$\begin{aligned}
\mathbf{r} &= r^{-1} \hat{\mathbf{e}}_{-1} + r^0 \hat{\mathbf{e}}_0 + r^{+1} \hat{\mathbf{e}}_{+1} \\
&= \frac{r^{-1}}{\sqrt{2}} (\hat{\mathbf{e}}_x - i \hat{\mathbf{e}}_y) + r^0 \hat{\mathbf{e}}_z - \frac{r^{+1}}{\sqrt{2}} (\hat{\mathbf{e}}_x + i \hat{\mathbf{e}}_y). \tag{A.25}
\end{aligned}$$

Now, defining the polarisation vector of the incident laser radiation $\hat{\boldsymbol{\epsilon}}_L$ along the x-axis, the half-Rabi frequency can be written as

$$\begin{aligned}
\Omega_{eg}^{\pi_x} &= -e^{i(\alpha + \frac{\pi}{2})} \sqrt{\frac{I_L}{2\epsilon_0 \hbar^2 c}} \hat{\mathbf{e}}_x \cdot \langle e | q_e (r^{-1} \hat{\mathbf{e}}_{-1} + r^0 \hat{\mathbf{e}}_0 + r^{+1} \hat{\mathbf{e}}_{+1}) | g \rangle \\
&= -e^{i(\alpha + \frac{\pi}{2})} \sqrt{\frac{I_L q_e^2}{2\epsilon_0 \hbar^2 c}} (\langle e | r^{-1} \hat{\mathbf{e}}_x \cdot \hat{\mathbf{e}}_{-1} | g \rangle + \langle e | r^0 \hat{\mathbf{e}}_x \cdot \hat{\mathbf{e}}_0 | g \rangle + \langle e | r^{+1} \hat{\mathbf{e}}_x \cdot \hat{\mathbf{e}}_{+1} | g \rangle) \\
&= -e^{i(\alpha + \frac{\pi}{2})} \sqrt{\frac{I_L q_e^2}{4\epsilon_0 \hbar^2 c}} (\langle e | r^{-1} | g \rangle - \langle e | r^{+1} | g \rangle) \\
&= e^{i(\alpha + \frac{\pi}{2})} \sqrt{\frac{I_L}{4\epsilon_0 \hbar^2 c}} (D_{eg}^{-1} - D_{eg}^{+1}). \tag{A.26}
\end{aligned}$$

Now, consider purely circularly polarised light. In this case the half-Rabi frequency is

$$\begin{aligned}
\Omega_{eg}^{\pm 1} &= -e^{i(\alpha + \frac{\pi}{2})} \sqrt{\frac{I_L}{2\epsilon_0 \hbar^2 c}} \hat{\mathbf{e}}_{\pm 1} \cdot \langle e | q_e (r^{-1} \hat{\mathbf{e}}_{-1} + r^0 \hat{\mathbf{e}}_0 + r^{+1} \hat{\mathbf{e}}_{+1}) | g \rangle \\
&= -e^{i(\alpha + \frac{\pi}{2})} \sqrt{\frac{I_L q_e^2}{2\epsilon_0 \hbar^2 c}} (\langle e | r^{\pm 1} | g \rangle) \\
&= -e^{i(\alpha + \frac{\pi}{2})} \sqrt{\frac{I_L}{2\epsilon_0 \hbar^2 c}} D_{eg}^{\pm 1}.
\end{aligned} \tag{A.27}$$

Therefore, we can compare equations [A.26](#) and [A.27](#) to obtain an expression for linearly polarised light in the natural frame

$$\Omega_{eg}^{\pi_x} = \frac{1}{\sqrt{2}} (\Omega_{eg}^{-1} - \Omega_{eg}^{+1}). \tag{A.28}$$

Appendix B

LASED Installation & Benchmarking

B.1 Installation of LASED

Installation of LASED requires the user to install the python programming language, which can be downloaded at [79]. It is recommended to download and install the latest source release of python. Once python has been installed, the command “pip3 install LASED” must be input to the terminal and run. This will install LASED and all dependencies.

B.2 Computation Time

n (Number of Energy Levels)	Execution Time (s)
4	0.833
6	0.855
8	2.50
24	283
36	2270
48	8570

Table B.1: A table to show execution times using LASED to simulate the time evolution of laser-atom systems with varying number of energy levels. 501 time steps were simulated from 0 to 500 ns with a laser intensity of 100 mW/mm², π -polarised light, and no Gaussian or Doppler averaging. For $n \geq 24$ the simulated systems have hyperfine structure.

LASED aims to model an arbitrary atom-laser system as defined by the user. By designing LASED to be as general as possible, the computing time increases rapidly with the number of substates in the system. At the same time, LASED aims to be efficient and usable with low-powered machines on any operating system. The python language was hence chosen for its development as this is open source and can be run on a wide range of different platforms.

To illustrate the computation time on a standard PC, table B.1 shows the execution time for atomic systems which have a varying number of substates. These computations were performed using an Intel i5-3320M central processing unit (CPU) operating at 2.60 GHz with 8 GB of random access memory (RAM) using a Linux operating system. The computing times are dominated by populating the matrices at small n as this operation takes time $\mathcal{O}n^2$, due to the size of the matrix scaling by n^2 . As the number of n increases, the dominant computational operation becomes the matrix multiplication itself, as this has a higher order computational time of $\mathcal{O}n^3$ [94].

Appendix C

Knudsen Number Calculations

To parameterise different flow regimes for atomic beams, the Knudsen number can be defined as

$$K = \frac{\lambda}{L}, \quad (\text{C.1})$$

where λ is the mean free path of an atom in the beam and L is the characteristic length scale for which the flow regime is defined. The mean free path of an atom moving through a stationary collection of atoms with number density n and effective cross-sectional area of collision A is given by [163]

$$\lambda = \frac{1}{nA}. \quad (\text{C.2})$$

For an atomic beam however, the atoms are not stationary and the expression for the mean free path must be modified to take into account the movement of atoms in the ensemble. A Maxwell-Boltzmann distribution of velocities in the atomic beam can be assumed as

$$f(v) = \left(\frac{m}{2\pi kT}\right)^{\frac{3}{2}} 4\pi v^2 e^{-\frac{mv^2}{2kT}}, \quad (\text{C.3})$$

where v is the magnitude of the velocity of an atom in the beam, T is the temperature of the beam, and m is the mass of the atom. For two atoms with velocities \mathbf{v} and \mathbf{v}' , the average relative velocity is given by

$$\begin{aligned} \bar{v}_{\text{rel}}^2 &= \langle (\mathbf{v} - \mathbf{v}')^2 \rangle \\ &= \int d^3\mathbf{v} \int d^3\mathbf{v}' (\mathbf{v} - \mathbf{v}')^2 f(\mathbf{v}) f(\mathbf{v}') \\ &= \langle v^2 \rangle - 2\langle \mathbf{v} \cdot \mathbf{v}' \rangle + \langle v'^2 \rangle. \end{aligned} \quad (\text{C.4})$$

Since any two atoms travelling in a beam are uncorrelated, $\langle \mathbf{v} \cdot \mathbf{v}' \rangle = 0$ and $\langle v^2 \rangle = \langle v'^2 \rangle$ which leads to the simplification of equation C.4 so that $\bar{v}_{\text{rel}} = \sqrt{2}\sqrt{\langle v^2 \rangle}$. This indicates that the number of collisions between atoms is a factor of $\sqrt{2}$ higher than when the atoms are stationary. Equation C.2 can be modified to take into account the increased number of collisions so that the mean free path of an atom in an atomic beam is then given by

$$\lambda = \frac{1}{\sqrt{2}nA}. \quad (\text{C.5})$$

For a beam composed of one atomic species, the effective cross-sectional area can be approximated as

$$A = \pi d^2, \quad (\text{C.6})$$

where d is the ‘diameter’ of the atomic species in the beam. Assuming that the beam behaves under the ideal gas law, the number density of atoms is given by

$$n = \frac{P}{kT}, \quad (\text{C.7})$$

where P is the pressure and k is Boltzmann’s constant. Combining equations C.5, C.6, and C.7 yields an expression for the mean free path which can be substituted into equation C.1 to obtain a calculable expression for the Knudsen number

$$K = \frac{kT}{\sqrt{2}\pi d^2 L P_{\text{vap}}}, \quad (\text{C.8})$$

where the pressure P has been replaced with the vapour pressure of the atomic gas P_{vap} . For an atomic beam, a Knudsen number of approximately 1 gives the maximum flow rate which can be achieved, as discussed in chapter 3. Equation C.8 can therefore be used to calculate the Knudsen number as a function of the oven temperature for the metal atom targets used in these experiments. This can then be used to estimate the operational oven temperature which can be used for a particular target and oven configuration.

The Knudsen number as a function of temperature has been calculated in the next sections for calcium, magnesium, and strontium targets. The characteristic length scale L is taken to be the nozzle length of the New (e, 2e) atomic beam oven and is measured by calipers as 20.1 ± 0.1 mm. For each calculation, the Van der Waals diameter [164] is taken to be the parameter d in equation C.8. The vapour pressure for each metal can be calculated from [165]

$$\log(P_{\text{vap}}) = A + BT^{-1} + C\log(T), \quad (\text{C.9})$$

where A , B , and C are experimentally determined coefficients [165].

The operational oven temperature calculated from using equation C.8 and setting $K = 1$ is an underestimate of the oven temperature which produces the maximum atomic beam flux, as seen in chapter 8. This is likely to be due to the discrepancy in the measured temperature and the actual temperature that the atoms flow through the nozzle of the oven.

C.1 Calcium

The data for calculating the Knudsen number for calcium is shown in table C.1 and the Knudsen number variation with temperature is shown in figure C.1. By assuming that $K \sim 1$ gives optimum operating conditions, it is seen that an oven temperature of around 575 °C is optimal for calcium atoms from the New (e, 2e) atomic beam oven.

Parameter	Value	Unit	Source
Diameter of calcium, d_{Ca}	462	pm	[164]
A	15.133	atm	[165]
B	-9517	atm.K	[165]
C	-1.403	atm/log(K)	[165]

Table C.1: Coefficients of vapour pressure and the atomic diameter of calcium.

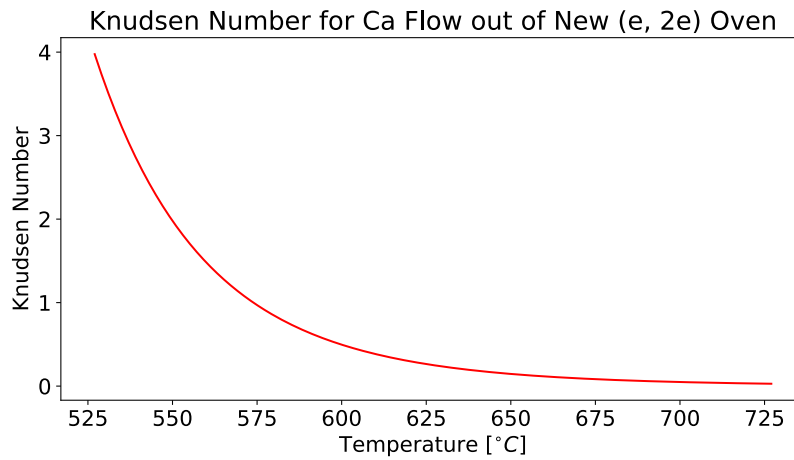


Figure C.1: Knudsen number variation with the New (e, 2e) atomic beam oven temperature for Ca.

C.2 Magnesium

The data for calculating the Knudsen number for magnesium is shown in table C.2 and the Knudsen number variation with temperature is shown in figure C.2. An initial oven temperature of around 450 °C is hence seen to be the best temperature to create an atomic beam of Mg from the New (e, 2e) oven.

Parameter	Value	Unit	Source
Diameter of magnesium, d_{Mg}	173	pm	[164]
A	13.495	atm	[165]
B	-7813	atm.K	[165]
C	-0.8253	atm/log(K)	[165]

Table C.2: Coefficients of vapour pressure and the atomic diameter of magnesium.

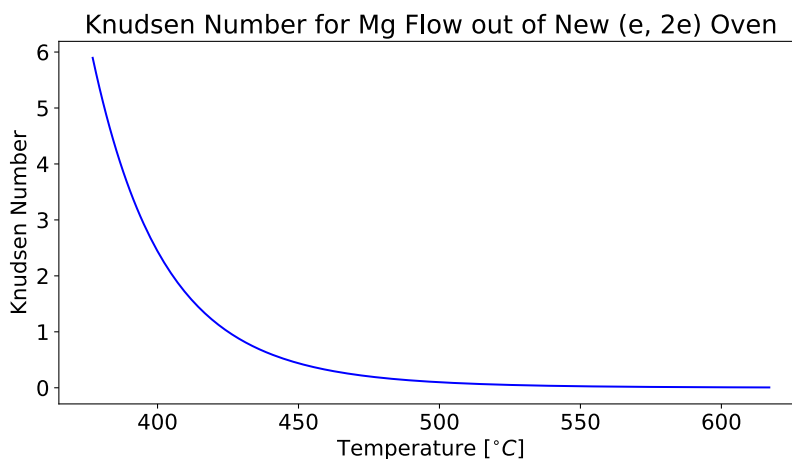


Figure C.2: Knudsen number variation with the New (e, 2e) atomic beam oven temperature for Mg.

C.3 Strontium

The data for calculating the Knudsen number for strontium is shown in table C.3 and the Knudsen number variation with temperature is shown in figure C.3. For this target, an oven temperature of around 500 °C produces a Knudsen number of 1.

Parameter	Value	Unit	Source
Diameter of strontium, d_{Sr}	498	pm	[164]
A	9.226	atm	[165]
B	-8572	atm.K	[165]
C	-1.1926	atm/log(K)	[165]

Table C.3: Coefficients of vapour pressure and the atomic diameter of strontium.

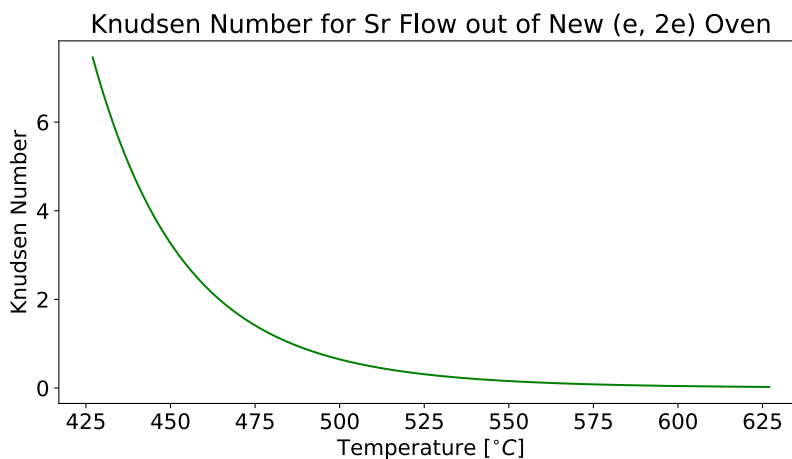


Figure C.3: Knudsen number variation with the New (e, 2e) atomic beam oven temperature for Sr.

Appendix D

Control Software

D.1 ASCII characters

A table of the decimal and hexadecimal values of the first 128 ASCII characters is found in figure D.1. These values are used to calculate the checksums in the LabVIEW-Arduino communication protocol, as detailed in chapter 5.

Decimal	Hexidecimal	Binary	Character	Decimal	Hexidecimal	Binary	Character	Decimal	Hexidecimal	Binary	Character
0	0	0	[NULL]	48	30	110000	0	96	60	1100000	`
1	1	1	[START OF HEADING]	49	31	110001	1	97	61	1100001	a
2	2	10	[START OF TEXT]	50	32	110010	2	98	62	1100010	b
3	3	11	[END OF TEXT]	51	33	110011	3	99	63	1100011	c
4	4	100	[END OF TRANSMISSION]	52	34	110100	4	100	64	1100100	d
5	5	101	[ENQUIRY]	53	35	110101	5	101	65	1100101	e
6	6	110	[ACKNOWLEDGE]	54	36	110110	6	102	66	1100110	f
7	7	111	[BELL]	55	37	110111	7	103	67	1100111	g
8	8	1000	[BACKSPACE]	56	38	111000	8	104	68	1101000	h
9	9	1001	[HORIZONTAL TAB]	57	39	111001	9	105	69	1101001	i
10	A	1010	[LINE FEED]	58	3A	111010	:	106	6A	1101010	j
11	B	1011	[VERTICAL TAB]	59	3B	111011	;	107	6B	1101011	k
12	C	1100	[FORM FEED]	60	3C	111100	<	108	6C	1101100	l
13	D	1101	[CARRIAGE RETURN]	61	3D	111101	=	109	6D	1101101	m
14	E	1110	[SHIFT OUT]	62	3E	111110	>	110	6E	1101110	n
15	F	1111	[SHIFT IN]	63	3F	111111	?	111	6F	1101111	o
16	10	10000	[DATA LINK ESCAPE]	64	40	1000000	@	112	70	1110000	p
17	11	10001	[DEVICE CONTROL 1]	65	41	1000001	A	113	71	1110001	q
18	12	10010	[DEVICE CONTROL 2]	66	42	1000010	B	114	72	1110010	r
19	13	10011	[DEVICE CONTROL 3]	67	43	1000011	C	115	73	1110011	s
20	14	10100	[DEVICE CONTROL 4]	68	44	1000100	D	116	74	1110100	t
21	15	10101	[NEGATIVE ACKNOWLEDGE]	69	45	1000101	E	117	75	1110101	u
22	16	10110	[SYNCHRONOUS IDLE]	70	46	1000110	F	118	76	1110110	v
23	17	10111	[ENG OF TRANS. BLOCK]	71	47	1000111	G	119	77	1110111	w
24	18	11000	[CANCEL]	72	48	1001000	H	120	78	1111000	x
25	19	11001	[END OF MEDIUM]	73	49	1001001	I	121	79	1111001	y
26	1A	11010	[SUBSTITUTE]	74	4A	1001010	J	122	7A	1111010	z
27	1B	11011	[ESCAPE]	75	4B	1001011	K	123	7B	1111011	{
28	1C	11100	[FILE SEPARATOR]	76	4C	1001100	L	124	7C	1111100	
29	1D	11101	[GROUP SEPARATOR]	77	4D	1001101	M	125	7D	1111101	}
30	1E	11110	[RECORD SEPARATOR]	78	4E	1001110	N	126	7E	1111110	~
31	1F	11111	[UNIT SEPARATOR]	79	4F	1001111	O	127	7F	1111111	[DEL]
32	20	100000	[SPACE]	80	50	1010000	P				
33	21	100001	!	81	51	1010001	Q				
34	22	100010	"	82	52	1010010	R				
35	23	100011	#	83	53	1010011	S				
36	24	100100	\$	84	54	1010100	T				
37	25	100101	%	85	55	1010101	U				
38	26	100110	&	86	56	1010110	V				
39	27	100111	'	87	57	1010111	W				
40	28	101000	(88	58	1011000	X				
41	29	101001)	89	59	1011001	Y				
42	2A	101010	*	90	5A	1011010	Z				
43	2B	101011	+	91	5B	1011011	[
44	2C	101100	,	92	5C	1011100	\				
45	2D	101101	-	93	5D	1011101]				
46	2E	101110	.	94	5E	1011110	^				
47	2F	101111	/	95	5F	1011111	_				

Figure D.1: The first 128 ASCII characters and their corresponding decimal, hexadecimal, and binary values.

D.2 Tables of API commands

The application programming interface (API) of the Arduino-based analyser angle controller systems and analyser power supplies used in the Old (e, 2e) and New (e, 2e) spectrometers are found in tables D.1 and D.2 respectively. The API for the gun power supply in the Old (e, 2e) is found in table D.3.

Serial Command	Apparatus	Action
ID	New & Old (e, 2e)	Print "SC" to the serial line
SC1	New & Old (e, 2e)	Enable checksum
SC0	New & Old (e, 2e)	Disable checksum
nSS	New & Old (e, 2e)	Stop analyser
nGV	New & Old (e, 2e)	Read and get potentiometer voltage
nGA	New & Old (e, 2e)	Read pot voltage and get current angle
nGS	New & Old (e, 2e)	Get moving status
nGH	New (e, 2e)	Read and get the home flag
nGO	New (e, 2e)	Read and get the opto-interrupter flag
nGF	Old (e, 2e)	Get the opto-interrupter flags
nGP	New & Old (e, 2e)	Get the set angle
nGR	New & Old (e, 2e)	Get the current rate
nSP{}	New & Old (e, 2e)	Set the set angle
nSZ{}	Old (e, 2e)	Set the number of steps to move
nSR{}	New & Old (e, 2e)	Set the max rate
nSM{}	Old (e, 2e)	Set the max rate
nSr{}	New & Old (e, 2e)	Set the minimum rate
nSm{}	Old (e, 2e)	Set the minimum rate
nSA{}	New & Old (e, 2e)	Set the maximum acceleration
nSa{}	New (e, 2e)	Set the minimum acceleration
nSE{}	New (e, 2e)	Set the maximum angle
nSF{}	New (e, 2e)	Set the minimum angle
nSJ{}	New (e, 2e)	Set the jerk
nSh{}	New (e, 2e)	Set the home angle
nSC	New (e, 2e)	Set calibration mode
nSH	New (e, 2e)	Put in HOMING mode
nSc{}	Old (e, 2e)	Set the crash angle
nSO	Old (e, 2e)	Set check optos

Table D.1: Arduino-controlled analyser stepper API. The '{}' are not included in the sent serial command but indicate that the numbers after the command are read by the Arduino and used in the corresponding action. The 'n' at the beginning of the serial command denotes a number which the user enters which denotes the analyser to move e.g. '1GV' gets the potentiometer voltage from analyser 1.

Serial Command	Apparatus	Action
ID	New & Old (e, 2e)	Prints "AN" to the serial line
SVRE{}	New & Old (e, 2e)	Sets residual energy voltage
SVLE{}	New & Old (e, 2e)	Sets lens voltage
SVDX{}	New & Old (e, 2e)	Sets x-deflectors voltages
SVDY{}	New & Old (e, 2e)	Sets y-deflectors voltages
SVAM{}	New & Old (e, 2e)	Sets analyser mean voltage
SVIH{}	New & Old (e, 2e)	Sets inner hemisphere voltage
SVOH{}	New & Old (e, 2e)	Sets outer hemisphere voltage
GVAE	New & Old (e, 2e)	Get all voltages
GMAE	New & Old (e, 2e)	Get all voltages
GVRE	New & Old (e, 2e)	Get residual energy voltage
GVLE	New & Old (e, 2e)	Get lens voltage
GVDX	New & Old (e, 2e)	Get x-deflectors voltages
GVDY	New & Old (e, 2e)	Get y-deflectors voltages
GVAM	New & Old (e, 2e)	Get analyser mean voltage
GVIH	New & Old (e, 2e)	Get inner hemisphere voltage
GVOH	New & Old (e, 2e)	Get outer hemishere voltage
SC1	New (e, 2e)	Enables checksum
SC0	New (e, 2e)	Disables checksum
SDRE{}	Old (e, 2e)	Set the residual energy DAC value
LOCK1	Old (e, 2e)	Lock manual controls
LOCK0	Old (e, 2e)	Unlock manual controls

Table D.2: Arduino-controlled electron energy analyser power supplies [API](#). The '{}' are not apart of the serial command but indicate that the numbers after the command are read by the Arduino and used in the corresponding action.

Serial Command	Action
ID	Print "EG" to the serial line
SVGF{}	Set gun fine voltage
SVGC{}	Set gun coarse voltage
SVGR{}	Set the grid voltage
SVAN{}	Set the anode voltage
SV1B{}	Set the voltage of lens GL1B
SV1X{}	Set the voltage of deflectors GD1X
SV1Y{}	Set the voltage of deflectors GD1Y
SV1C{}	Set voltage of lens GL1C
SV2X{}	Set the voltage of deflectors GD2X
SV2Y{}	Set the voltage of deflectors GD2Y
SV2B{}	Set the voltage of lens GL2B
SV3X{}	Set the voltage of deflectors GD3X
SV3Y{}	Set the voltage of deflectors GD3Y
GVAE	Get all set voltages

Table D.3: Old (e, 2e) Arduino-controlled electron gun power supply [API](#). The '{}' are not apart of the serial command but indicate that the numbers after the command are read by the Arduino and used in the corresponding action.